

2003

## Multinuclear NMR studies of relaxor ferroelectrics

Donghua Zhou

*College of William & Mary - Arts & Sciences*

Follow this and additional works at: <https://scholarworks.wm.edu/etd>



Part of the [Condensed Matter Physics Commons](#)

---

### Recommended Citation

Zhou, Donghua, "Multinuclear NMR studies of relaxor ferroelectrics" (2003). *Dissertations, Theses, and Masters Projects*. Paper 1539623422.

<https://dx.doi.org/doi:10.21220/s2-xsb9-p144>

This Dissertation is brought to you for free and open access by the Theses, Dissertations, & Master Projects at W&M ScholarWorks. It has been accepted for inclusion in Dissertations, Theses, and Masters Projects by an authorized administrator of W&M ScholarWorks. For more information, please contact [scholarworks@wm.edu](mailto:scholarworks@wm.edu).

# Multinuclear NMR Studies of Relaxor Ferroelectrics

---

A Dissertation

Presented to

The Faculty of the Department of Physics

The College of William & Mary in Virginia

In Partial Fulfillment

Of the Requirements for the Degree of

Doctor of Philosophy

---

by


Donghua Zhou

2003

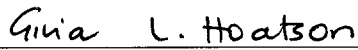
# APPROVAL SHEET

This dissertation is submitted in partial fulfillment of  
the requirements for the degree of

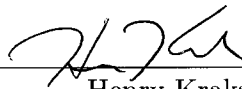
Doctor of Philosophy

  
Donghua Zhou

Approved, March 2003

  
\_\_\_\_\_

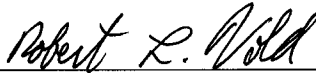
Gina L. Hoatson  
Advisor

  
\_\_\_\_\_

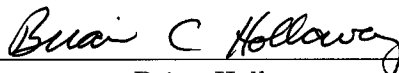
Henry Krakauer

  
\_\_\_\_\_

Kenneth G. Petzinger

  
\_\_\_\_\_

Robert L. Vold  
Department of Applied Science

  
\_\_\_\_\_

Brian Holloway  
Department of Applied Science

*To my parents and Lingjin...*

# Table of Contents

<b>Acknowledgments</b>	<b>viii</b>
<b>List of Tables</b>	<b>ix</b>
<b>List of Figures</b>	<b>xii</b>
<b>Abstract</b>	<b>xiii</b>
<b>1 Introduction</b>	<b>2</b>
<b>2 NMR Spectroscopy</b>	<b>4</b>
2.1 Precessing Magnetization and NMR Signal . . . . .	6
2.2 Density Matrix . . . . .	8
2.3 NMR Spectrometer . . . . .	11
2.4 Relaxation Times . . . . .	13
2.5 Recovery Times and Spin Echo . . . . .	15
2.6 Summary . . . . .	17
<b>3 Chemical Shift Interaction</b>	<b>18</b>

3.1	Chemical Shielding and Chemical Shifts . . . . .	19
3.2	Static Spectra . . . . .	21
3.3	Magic-Angle Spinning Spectra . . . . .	23
3.4	Total Suppression of Spinning Sidebands . . . . .	26
3.5	Phase Adjusted Spinning Sidebands . . . . .	28
3.6	Summary . . . . .	34
<b>4</b>	<b>Electric Quadrupole Interaction</b>	<b>36</b>
4.1	Quadrupolar Nuclei and Quadrupolar Interaction . . . . .	36
4.2	Perturbation Expansion of Energy Levels and Transition Frequencies . . . . .	47
4.3	Quadrupole Spectra of Polycrystalline Materials . . . . .	49
4.4	The Quest to Remove Anisotropy . . . . .	57
4.5	Prototype Experiment and Theory of MQMAS . . . . .	60
4.6	Pure Absorption Lineshape . . . . .	66
4.7	Extraction of Parameters and Site Populations . . . . .	74
4.8	Axes of Distributions . . . . .	76
4.9	“Dream” Transformation . . . . .	76
4.10	Summary . . . . .	79
<b>5</b>	<b>Perovskite Relaxor Ferroelectrics</b>	<b>81</b>
5.1	Ferroelectrics . . . . .	81
5.2	Relaxor Ferroelectrics . . . . .	82
5.3	Origins of Relaxor Behaviors . . . . .	85
5.4	NMR Studies on PMN-PSN Solid Solutions . . . . .	90

<b>6</b>	<b>Niobium NMR Studies of PMN-PSN</b>	<b>94</b>
6.1	High Field and Fast Speed MAS NMR . . . . .	95
6.2	MAS NMR Results . . . . .	96
6.3	Spectral Assignments . . . . .	100
6.4	Models of cation disorder . . . . .	106
6.5	Higher Resolution Needed: 3QMAS NMR . . . . .	112
6.6	3QMAS Results . . . . .	114
6.7	Fit of 3QMAS Spectra . . . . .	125
6.8	Conclusions . . . . .	127
<b>7</b>	<b>Scandium NMR Studies of PMN-PSN</b>	<b>131</b>
7.1	MAS . . . . .	133
7.2	3QMAS . . . . .	136
7.3	Conclusion . . . . .	142
<b>8</b>	<b>Lead NMR Studies of PMN-PSN</b>	<b>143</b>
8.1	Experimental Setting . . . . .	145
8.2	Static and MAS spectra, and $T_1$ Measurements . . . . .	147
8.3	2D-PASS: Isotropic Chemical Shift . . . . .	149
8.4	Measurement of the shortest Pb-O bond length . . . . .	153
8.5	Lead displacement models . . . . .	155
8.6	2D-PASS: Anisotropic Chemical Shift . . . . .	158
8.7	Pb-O bonding environments . . . . .	160
8.8	Conclusion . . . . .	162

<b>9 Conclusion</b>	<b>164</b>
<b>A Rotation Matrices</b>	<b>167</b>
<b>B Coherence Transfer Pathway and Phase Cycling</b>	<b>169</b>
B.1 Traditional Scheme . . . . .	170
B.2 Simplification of Phase Cycling . . . . .	172
B.3 Summary . . . . .	172
<b>Bibliography</b>	<b>175</b>



## ACKNOWLEDGMENTS

I would like to express my gratitude to my advisors Drs. Gina L. Hoatson and Robert L. Vold for their guidance and patience. Their quality to pursue perfection has deeply influenced me. All the committee members are thanked for spending time reading and commenting on my dissertation. Dr. Henry Krakauer and Dr. Shiwei Zhang are thanked for several helpful discussions. Bill Brouwer read many chapters and corrected my English. I highly appreciate the generous help and friendship from colleagues in the NMR lab: Dr. Dariya (Dasha) Malyarenko, Yana Goddard, Dr. Jørgen Kristensen, Dr. Sixun Zheng, Bill Brouwer, Elizabeth Slonaker, Jason Gammon, and Xin Zhao.

Many people outside the department deserve my thanks. Dr. Peter K. Davies in the University of Pennsylvania made this work possible by providing us well characterized relaxor ferroelectric samples. It was with Drs. Dominique Massiot and Franck Fayon in CNRS, France, Gina and Bob started this project during their sabbatical (September 2000 to March 2001). Dr. Massiot generously allowed us to use his spectral analyzing software DMFIT and Dr. Fayon commented the  $^{93}\text{Nb}$  3QMAS and  $^{207}\text{Pb}$  2D-PASS manuscripts. Dr. Zhehong Gan in NHMFL, Florida patiently assisted Gina and Donghua in acquiring  $^{93}\text{Nb}$  and  $^{45}\text{Sc}$  spectra using the 19.6 Tesla spectrometer.

My wife Lingjin took good care of me so that I was able to focus on this project. I would like to thank her for her love, dedication, patience, and support.

# List of Tables

2.1	Magnetic properties . . . . .	5
3.1	Delays between pulses for 2D-PASS sequence . . . . .	31
3.2	Improved phase cycling for 2D-PASS . . . . .	33
4.1	Quadrupole moments . . . . .	44
4.2	Sternheimer factors . . . . .	45
4.3	Essential coefficients of MQMAS and STMAS . . . . .	64
4.4	NMR parameters for the three sites in Na <sub>2</sub> SO <sub>3</sub> . . . . .	74
6.1	Deconvolution parameters of MAS spectra . . . . .	100
6.2	Random site prediction and experimental results . . . . .	110
6.3	NMR parameters for the narrow peak and the two broad peaks . . . . .	117
7.1	Decomposition parameters for <sup>45</sup> Sc MAS spectra . . . . .	135
8.1	Gaussian fit parameters for the isotropic projections . . . . .	153
8.2	Parameters of unique direction model . . . . .	157

# List of Figures

2.1	Creation of $B_1$ field . . . . .	7
2.2	Free induction decay and spectrum . . . . .	8
2.3	An NMR spectrometer . . . . .	12
2.4	$T_1$ measurement using saturation comb . . . . .	14
2.5	Spin echo pulse sequence . . . . .	16
3.1	Static and MAS $^{207}\text{Pb}$ NMR spectra of $\text{PbSO}_4$ . . . . .	23
3.2	Example of 2D-PASS spectrum . . . . .	29
3.3	2D-PASS pulse sequence . . . . .	30
3.4	2D-PASS $^{207}\text{Pb}$ NMR spectra of $\text{PbSO}_4$ . . . . .	34
4.1	Static powder pattern of first order quadrupole interaction . . . . .	50
4.2	Static and MAS powder patterns of second order quadrupole interaction . .	52
4.3	$^{23}\text{Na}$ static and MAS spectra of sodium oxalate . . . . .	54
4.4	The singularities of second order quadrupole lineshapes . . . . .	55
4.5	Extracting NMR parameters from MAS spectrum . . . . .	57
4.6	A prototype two pulse MQMAS sequence . . . . .	61

4.7	MQMAS spectral processing . . . . .	62
4.8	Lineshapes in 2D spectra . . . . .	68
4.9	MQMAS pulse sequence with whole-echo detection . . . . .	69
4.10	Amplitude modulation with Z-filter . . . . .	71
4.11	$^{23}\text{Na}$ spectra of $\text{Na}_2\text{SO}_3$ . . . . .	73
4.12	Fitting the three sites in $\text{Na}_2\text{SO}_3$ 3QMAS and MAS spectra . . . . .	75
4.13	“Dream transformation” of 3QMAS spectra . . . . .	78
5.1	Generic perovskite structure . . . . .	83
5.2	Temperature dependence of dielectric constant . . . . .	83
5.3	X-ray diffraction spectra . . . . .	91
5.4	TEM images of PMN-PSN . . . . .	92
5.5	Dielectric constants for PMN-PSN . . . . .	93
6.1	$^{93}\text{Nb}$ MAS spectra of PMN . . . . .	97
6.2	The seven narrow peaks . . . . .	98
6.3	Constrained deconvolution of PMN MAS spectra . . . . .	99
6.4	Deconvolution of PMN-PSN MAS spectra . . . . .	101
6.5	Perovskite structure and B-lattice . . . . .	102
6.6	The twenty-eight nBn configurations . . . . .	104
6.7	Comparison of MAS spectra of PMN and Pyrochlore . . . . .	105
6.8	Random site predictions . . . . .	111
6.9	$^{93}\text{Nb}$ 3QMAS spectra for PMN-PSN . . . . .	114
6.10	Lineshape fits for a slice of PMN 3QMAS spectrum . . . . .	116

6.11	$^{93}\text{Nb}$ quadrupole products for scandium-deficient nBn configurations . . . .	118
6.12	Oxygen octahedral distortions of two configurations . . . . .	119
6.13	Isotropic chemical shifts and quadrupole products of the narrow peaks . . .	120
6.14	Assignments according to 3QMAS . . . . .	123
6.15	Fit the PMN 3QMAS spectrum . . . . .	127
7.1	$^{45}\text{Sc}$ MAS spectra . . . . .	133
7.2	Decomposition of $^{45}\text{Sc}$ MAS spectra . . . . .	134
7.3	$^{45}\text{Sc}$ 3QMAS spectra . . . . .	137
7.4	Schematic 3QMAS spectra of PMN-PSN . . . . .	140
8.1	Static and MAS $^{207}\text{Pb}$ spectra . . . . .	147
8.2	Lead relaxation time $T_1$ . . . . .	148
8.3	$^{207}\text{Pb}$ 2D-PASS spectrum of PMN . . . . .	149
8.4	Isotropic projections of $^{207}\text{Pb}$ 2D-PASS spectra . . . . .	151
8.5	Tetragonal structure of $\text{PbTiO}_3$ . . . . .	154
8.6	Shell distribution model for Pb displacements . . . . .	156
8.7	Unique direction model for Pb displacements . . . . .	158
8.8	Correlation between anisotropic and isotropic chemical shifts . . . . .	159
8.9	The temperature dependence of the $\delta_{22}$ . . . . .	160
B.1	A two pulse MQMAS sequence . . . . .	170

## ABSTRACT

Multinuclear NMR of  $^{93}\text{Nb}$ ,  $^{45}\text{Sc}$ , and  $^{207}\text{Pb}$  has been carried out to study the structure, disorder, and dynamics of a series of important solid solutions: perovskite relaxor ferroelectric materials  $(1-x)\text{Pb}(\text{Mg}_{1/3}\text{Nb}_{2/3})\text{O}_3-x\text{Pb}(\text{Sc}_{1/2}\text{Nb}_{1/2})\text{O}_3$  (PMN-PSN).

First, important interactions (including chemical shielding anisotropy and quadrupole interactions) and relevant NMR techniques such as magic-angle spinning (MAS), triple-quantum MAS (3QMAS), and two-dimensional phase-adjusted spinning side-bands (2D-PASS) are introduced.

$^{93}\text{Nb}$  NMR investigations of the local structure and cation order/disorder are presented as a function of PSN concentration,  $x$ . The superb fidelity and accuracy of 3QMAS allows us to make clear and consistent assignments of spectral intensities to the 28 possible nearest B-site neighbor (nBn) configurations,  $(N_{\text{Mg}}, N_{\text{Sc}}, N_{\text{Nb}})$ , where each number ranges from 0 to 6 and their sum is 6. For most of the 28 possible nBn configurations, isotropic chemical shifts and quadrupole product constants have been extracted from the data. The seven configurations with only larger cations,  $\text{Mg}^{2+}$  and  $\text{Sc}^{3+}$  (and no  $\text{Nb}^{5+}$ ) are assigned to the seven observed narrow peaks, whose deconvoluted intensities facilitate quantitative evaluation of, and differentiation between, different models of B-site (chemical) disorder. The “completely random” model is ruled out and the “random site” model is shown to be in qualitative agreement with the NMR experiments. To obtain quantitative agreement with observed NMR intensities, the random site model is slightly modified by including unlike-pair interaction energies.

To date,  $^{45}\text{Sc}$  studies have not been as fruitful as  $^{93}\text{Nb}$  NMR because the resolution is lower in the  $^{45}\text{Sc}$  spectra. The lower resolution of  $^{45}\text{Sc}$  spectra is due to a smaller span of isotropic chemical shift (40 ppm for  $^{45}\text{Sc}$  vs. 82 ppm for  $^{93}\text{Nb}$ ) and to the lack of a fortuitous mechanism that simplifies the  $^{93}\text{Nb}$  spectra; for  $^{93}\text{Nb}$  the overlap of the isotropic chemical shifts of 6-Sc and 6-Nb configurations results in the alignment of all the 28 configurations along only seven quadrupole distribution axes.

Finally we present variable temperature  $^{207}\text{Pb}$  static, MAS, and 2D-PASS NMR studies. Strong linear correlations between isotropic and anisotropic chemical shifts show that Pb-O bonds vary from more ionic to more covalent environments. Distributions of Pb-O bond lengths are also quantitatively described. Such distributions are used to examine two competing models of Pb displacements; the shell model and the unique direction model. Only the latter model is able to reproduce the observed Pb-O distance distribution.

## Multinuclear NMR Studies of Relaxor Ferroelectrics

# Chapter 1

## Introduction

Nuclear Magnetic Resonance (NMR) is a powerful spectroscopic technique that provides information about the structure and dynamics of matter on the molecular level. After the discovery of NMR in bulk materials in 1945 by Edward M. Purcell, Henry C. Torrey, and Robert V. Pound and independently by Felix Bloch, William W. Hansen, and Martin E. Packard, NMR has been continuously undergoing tremendous advances: from continuous wave to pulse Fourier transform NMR, from one dimension to multiple dimensions, from one nucleus to several coupled nuclei, and from static to spinning solid samples at the so-called magic angle. The range of its applications have been extended beyond physics, to chemistry, geology, biology, and medicine. Three Nobel prizes have been awarded to NMR works, testifying that NMR is still very vigorous after a half century: the 1952 physics prize was awarded jointly to Bloch and Purcell for their discovery of NMR; the 1991 chemistry prize was awarded to Richard R. Ernst for his contributions to the development of the methodology of high resolution NMR (especially FT NMR and multi-dimension NMR); half of the 2002 the chemistry prize was awarded to Kurt Wüthrich for his development of NMR spectroscopy for determining the three-dimensional structure of biological macromolecules in solution.



In this work NMR is used to study relaxor ferroelectric ceramics, whose important applications in electronics and optics include, but are not limited to, capacitors, nonvolatile memories, medical ultrasound generators and receivers, high frequency speakers, displacement transducers, accelerometers, voltage transformers, gas ignitors, flash protection goggles, and optical memories and displays. The local structures and short-range order/disorder of these materials are crucial for their special properties. However, X-ray diffraction is of limited use since there is little or no long range order. NMR is an powerful tool to study local structures and disorder; this work proves that NMR is able to shed valuable light on the understanding of the microscopic origin of the properties of relaxor ferroelectrics.

Chapter 2 introduces the basics of NMR spectroscopy. Chapter 3 focuses on chemical shielding effects, which may be used to probe the surrounding electronic wave function; techniques such as magic-angle spinning (MAS) and two-dimensional phase-adjusted spinning sidebands (2D-PASS) are introduced to achieve high resolution and to obtain the chemical shielding (or shift) tensor. Chapter 4 focuses on the quadrupole interaction, where the nuclei are used to probe the local electric field gradients; techniques such as MAS and multi-quantum MAS (MQMAS) are described. Chapter 5 introduces the properties of the relaxor ferroelectrics, it also reviews the endeavors made to understand these materials from other fields such as X-ray and neutron diffraction, electron microscopy, and computational modelling. Chapter 6 describes the  $^{93}\text{Nb}$  MAS and 3QMAS studies of a series of relaxor ferroelectrics,  $(1-x)\text{PbMg}_{1/3}\text{Nb}_{2/3}\text{O}_3-x\text{PbSc}_{1/2}\text{Nb}_{1/2}\text{O}_3$  (PMN-PSN); local structure and quantitative information on cation disorder is obtained. Chapter 7 describes the  $^{45}\text{Sc}$  MAS and 3QMAS studies of PMN-PSN. Finally, chapter 8 describes the study of local structures by  $^{207}\text{Pb}$  static, MAS, and 2D-PASS NMR.

## Chapter 2

# NMR Spectroscopy

NMR spectroscopy involves the manipulation and detection of nuclear magnetization. The nuclear magnetic moment ( $\boldsymbol{\mu}$ ) of a nucleus is proportional and collinear to the quantized spin angular momentum ( $\mathbf{I}\hbar$ ),

$$\boldsymbol{\mu} = \gamma\hbar\mathbf{I}, \quad (2.1)$$

where  $\hbar = 1.0545727 \times 10^{-34}$  J·s is Planck's constant and  $\gamma$  is the magnetogyric ratio. Only those nuclei with non-zero spin quantum number have magnetization and can be detected. If  $A$  (mass number) and  $Z$  (charge number) of a nucleus are both even, then the nucleus has  $I = 0$ ; for example,  $^{12}\text{C}$ ,  $^{16}\text{O}$ , and  $^{32}\text{S}$ . If  $A$  is even and  $Z$  odd, the nucleus has integral spin; for example,  $^2\text{H}$  and  $^{14}\text{N}$  have  $I = 1$ . If  $A$  is odd, then the nucleus has half-integral spin; e.g.  $^1\text{H}$  and  $^{13}\text{C}$  have  $I = 1/2$ , and  $^{17}\text{O}$  has  $I = 5/2$ . The spin quantum number, magnetogyric ratio, and natural abundance of several nuclei are listed in Table 2.1.

In an external magnetic field  $\mathbf{B}_0$ , the potential energy of orientation of a nuclear moment splits into  $2I + 1$  Zeeman levels,

$$E_m = -\boldsymbol{\mu} \cdot \mathbf{B}_0 = -\gamma\hbar m B_0, \quad (2.2)$$

where the magnetic quantum number  $m$  takes values  $-I, -I + 1, \dots, I - 1, I$ . The energy

**Table 2.1:** Magnetic properties of a few nuclei [109].

Nucleus	$I$	$\gamma$ ( $10^7$ rad·T <sup>-1</sup> s <sup>-1</sup> )	Freq. (MHz) <sup>a</sup>	Abund. (%)	Receptivity <sup>b</sup>
<sup>1</sup> H	1/2	26.7522128	300	99.985	1.0
<sup>2</sup> H	1	4.10662791	46.05	0.015	0.00000145
<sup>13</sup> C	1/2	6.728284	75.44	1.10	0.000175
<sup>17</sup> O	5/2	-3.62808	40.67	0.038	0.0000111
<sup>23</sup> Na	3/2	7.0808493	79.36	100	0.0927
<sup>25</sup> Mg	5/2	-1.63887	18.36	10.0	0.000268
<sup>45</sup> Sc	7/2	6.5087973	72.88	100	0.302
<sup>93</sup> Nb	9/2	6.5674	73.43	100	0.488
<sup>207</sup> Pb	1/2	5.58046	62.76	22.1	0.00201

<sup>a</sup> The resonance frequency at 7.0459800 Tesla.

<sup>b</sup> The receptivity is proportional to the cube of  $\gamma$  times the natural abundance.

difference between two adjacent levels is  $\Delta E = h\nu_0$ , where

$$\nu_0 = \frac{\gamma B_0}{2\pi} \quad (2.3)$$

is the Larmor frequency. When excited by radio-frequency (rf) irradiation, the atoms will resonate, or absorb energy at this frequency. The detected resonance frequency identifies the kind of atom and the other atoms to which it is connected in the molecule. The molecular structure can be determined by measuring all of the frequencies.

The system is at finite temperature; thus spin populations of these levels are not equal but are instead distributed according to the Boltzmann law of statistical mechanics  $N_m = N \exp(-E_m/kT)$ , where  $N$  is the total number of spins. The net macroscopic magnetization is

$$M = N\gamma\hbar \frac{\sum_{m=-I}^{m=I} m \exp(\gamma\hbar m B_0/kT)}{\sum_{m=-I}^{m=I} \exp(\gamma\hbar m B_0/kT)}. \quad (2.4)$$

For proton  $\gamma\hbar/k = 0.002\text{K/Tesla}$ , therefore the ratio  $\gamma\hbar B_0/kT$  is always small for currently achievable static magnetic fields ( $\leq 45$  Tesla) at temperatures above 1K. This suffices to per-

mit a linear expansion of the Boltzmann exponential (“high temperature” approximation) to obtain

$$M = \frac{N\gamma^2\hbar^2 I(I+1)B_0}{3kT}. \quad (2.5)$$

At room temperature in an 7 Tesla magnetic field, there are only about 50 more protons in the spin-up state than those in the spin-down state out of a total  $10^6$  protons. It is this tiny population difference that is responsible for the entire NMR signal.

This chapter only covers a few aspects of NMR spectroscopy. For more information these textbooks are good sources [1, 45, 95, 39, 75, 79, 81, 89].

## 2.1 Precessing Magnetization and NMR Signal

In a static field  $\mathbf{B}_0$ , the nuclear magnetic moment precesses at an angular velocity

$$\omega_0 = -\gamma B_0, \quad (2.6)$$

its magnitude is  $2\pi$  times the Larmor frequency. For positive  $\gamma$ , the negative  $\omega_0$  means the magnetic moment precesses clockwise around  $-\mathbf{B}_0$ . The macroscopic magnetization also undergoes the same precession. To effectively perturb the system, a small magnetic field  $2B_1 \cos(\omega_{rf}t + \phi_0)$  oscillating at a frequency very close to the Larmor frequency ( $\omega_{rf} \sim \omega_0$ ) is applied perpendicular to  $\mathbf{B}_0$  (Fig. 2.1). Since negative frequency doesn’t have special meaning in electronics, the signed  $\omega_{rf}$  here should be interpreted as its absolute value when used in the sense of electronics. This field consists of two oppositely rotating circular magnetic fields,  $B_1 \exp(i\omega_{rf}t)$  and  $B_1 \exp(-i\omega_{rf}t)$  (drop  $\phi_0$  here and below). The component  $B_1 \exp(-i\omega_{rf}t)$  has an angular velocity of about  $2\omega_0$  relative with the precessing spin, this

component barely affects the nuclear spin. The other component  $B_1 \exp(i\omega_{rf}t)$  rotates at an angular velocity very close to the Larmor precession and can thus cause stimulated absorption of energy. It is convenient to change to a frame rotating at speed  $\omega_{rf}$  with the laboratory frame. In this rotating frame, the  $B_1$  field appears static and it exerts a torque to bring the magnetic moment toward the  $x'y'$  plane at an angular velocity

$$\omega_1 = \gamma B_1, \quad (2.7)$$

as depicted Fig. 2.1. Usually the rf irradiation is turned off after time  $\tau_{\pi/2}$ , which satisfies  $\omega_1 \tau_{\pi/2} = \pi/2$ , the magnetic moment is tipped onto the  $x'y'$  plane; this rf pulse is referred to as  $\pi/2$  or  $90^\circ$  pulse. Viewed from the laboratory frame, the magnetic moment precesses in the  $x'y'$  plane at the Larmor frequency. This causes the magnetic flux in the coil to change with time and induce a voltage. This voltage is detected and amplified to provide the NMR signal.

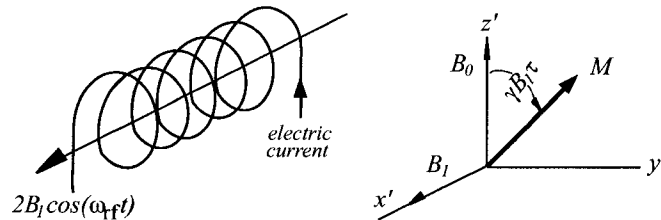


**Figure 2.1:** Creation of  $B_1$  field in the laboratory frame (left) and the effect of rf pulse in the rotating frame (right). In the rotating frame, the axis labels are primed.

The acquired signal in time domain, which is usually called the free induction decay (FID), is shown Fig. 2.2. The corresponding frequency domain spectrum is obtained by Fourier transformation. The FID may be expressed as

$$S(t) = S_0 e^{i\Omega t - t/T_2^*}, \quad (2.8)$$

where  $t \geq 0$ , the relative precession frequency in the rotating frame is defined as  $\Omega = \omega_0 - \omega_{rf}$ , and  $T_2^*$  is the transverse relaxation time which shall be described shortly in section 2.4. By carrying out a Fourier transform  $\int S(t) \exp(-i\omega t) dt$  the frequency domain spectrum is

$$I(\omega) = S_0[a(\omega) + id(\omega)], \quad (2.9)$$

where

$$a(\omega) = \frac{R}{(\Omega - \omega)^2 + R^2}, \quad d(\omega) = \frac{\Omega - \omega}{(\Omega - \omega)^2 + R^2}, \quad (2.10)$$

and  $R = 1/T_2^*$  is the transverse relaxation rate. Both the real and imaginary components of the spectrum are plotted in Fig. 2.2. The real, absorptive component is narrow and it has a full-width of  $2/T_2^*$  at the half-maximum. The imaginary, dispersive component has much wider linewidth; serious overlap occurs if there is more than one resonance peak. Therefore, the absorption lineshape provides better resolution and is usually presented.

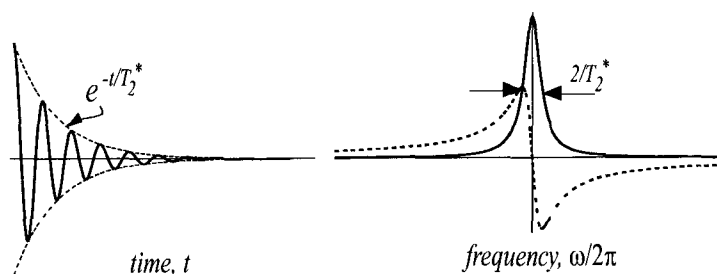


**Figure 2.2:** Free induction decay with envelope (left) and spectra (right). The real spectrum is narrow and absorptive (solid) and the imaginary spectrum is wide and dispersive (dashed). The full-width at half-height of the absorption line is  $2/T_2^*$ .

## 2.2 Density Matrix

In an NMR experiment, to theoretically describe the time evolution of an ensemble of nuclear spins, the quantum mechanic density matrix formalism is necessary. In a mixed

ensemble, the expectation value of an arbitrary operator  $\mathcal{O}$  is

$$\overline{\langle \mathcal{O} \rangle} = \sum_i \omega_i \langle \psi_i | \mathcal{O} | \psi_i \rangle, \quad (2.11)$$

where  $\omega_i$  is the fractional population of the state  $\psi_i$ . Define the density matrix as

$$\rho = \sum_i \omega_i |\psi_i\rangle \langle \psi_i| \quad (2.12)$$

with the matrix elements given by

$$\langle \psi_k | \rho | \psi_j \rangle = \sum_i \omega_i \langle \psi_k | \psi_i \rangle \langle \psi_i | \psi_j \rangle. \quad (2.13)$$

Using the closure relation the expectation value in Eq. (2.11) becomes

$$\begin{aligned} \overline{\langle \mathcal{O} \rangle} &= \sum_{ijk} \omega_i \langle \psi_i | \psi_j \rangle \langle \psi_j | \mathcal{O} | \psi_k \rangle \langle \psi_k | \psi_i \rangle \\ &= \sum_{ijk} \omega_i \langle \psi_k | \psi_i \rangle \langle \psi_i | \psi_j \rangle \langle \psi_j | \mathcal{O} | \psi_k \rangle \\ &= \sum_{jk} \langle \psi_k | \rho | \psi_j \rangle \langle \psi_j | \mathcal{O} | \psi_k \rangle \\ &= Tr(\rho \mathcal{O}), \end{aligned} \quad (2.14)$$

where  $Tr$  means evaluating the trace.

In the Zeeman representation, the diagonal elements  $\rho_{ii}$  of the density matrix are populations of the eigenstates. Off diagonal elements  $\rho_{ij}$  ( $i \neq j$ ) describe the phase coherence of the spins and

$$p = m_i - m_j \quad (2.15)$$

is called the order of the coherence, where  $m_i$  and  $m_j$  are the magnetic quantum numbers of the  $|\psi_i\rangle$  and  $|\psi_j\rangle$  states, respectively. Only the  $\pm 1$ -quantum coherence can be directly

detected due to the selection rules; conventionally the  $-1$ -quantum coherence is detected in NMR. However, multi-quantum coherence may be indirectly detected in multi-dimensional NMR experiments (such as 2D-PASS and MQMAS experiments in Chapters 3 and 4 respectively). In an multi-pulse NMR experiment, a specific coherence transfer pathway needs to be selected; the guidelines for the pathway selection are described in Appendix B.

The time evolution of the density matrix is determined by the Liouville-von Neumann equation,

$$\frac{d\rho}{dt} = i[\rho, H], \quad (2.16)$$

and the Hamiltonian  $H$  usually consists of the large and time independent Zeeman interaction  $H_z$  and other interactions denoted by  $H_1$ ;

$$H = H_z + H_1. \quad (2.17)$$

The classic rotating frame is equivalent to the interaction representation in quantum mechanics, where the density matrix and  $H_1$  become

$$\begin{aligned} \tilde{\rho} &= e^{iH_z t} \rho e^{-iH_z t}, \\ \tilde{H}_1 &= e^{iH_z t} H_1 e^{-iH_z t}, \end{aligned} \quad (2.18)$$

and the equation of evolution in the interaction representation is

$$\frac{d\tilde{\rho}}{dt} = i[\tilde{\rho}, \tilde{H}_1] \quad (2.19)$$

For simplicity, we drop the tilde and imply working in the interaction representation; also the



subscript of  $H_1$  is dropped. The Liouville-von Neumann equation may be solved iteratively,

$$\rho(t) = \rho(0) + i \int_0^t [\rho(0), H(t')] dt' - \int_0^t dt' \int_0^{t'} [[\rho(0), H(t'')], H(t')] dt'', \quad (2.20)$$

where orders higher than the second are truncated. However, for numerical simulation it is better to use the propagator formalism,

$$\rho(t) = U(t, 0)\rho(0)U^\dagger(t, 0), \quad (2.21)$$

where  $U(t, 0)$  is the unitary propagator responsible for the spin dynamics in the period from 0 to  $t$ . The propagator is defined as

$$U(t, 0) = \hat{T} \exp \left\{ -i \int_0^t H(t') dt' \right\} \quad (2.22)$$

with  $\hat{T}$  being the Dyson time-ordering operator for Hamiltonians containing non-commuting components. In practice this is usually evaluated by a simple time-ordered product

$$U(t, 0) = \prod_{j=0}^{n-1} \exp\{-iH(j\Delta t)\Delta t\}, \quad (2.23)$$

where  $n$  is the number of infinitesimal time intervals  $\Delta t$  during which the Hamiltonian may be considered time independent. The exponentials are evaluated by diagonalization of the matrix representation of the Hamiltonian. A versatile simulation program for solid-state NMR spectroscopy, SIMPSON, is becoming popular [8].

## 2.3 NMR Spectrometer

An NMR spectrometer must be capable of manipulating rf pulse and detecting nuclear magnetization. Major components of a modern pulsed NMR spectrometer are shown in

Figure 2.3: superconducting magnet, probe, frequency synthesizer, pulse programmer, RF transmitter, receiver, digitizer, and computer.

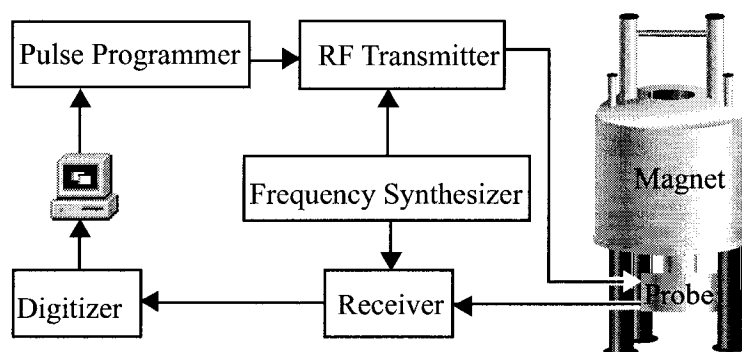


**Figure 2.3:** An NMR spectrometer.

The NMR magnet provides a strong, stable (0.01 ppm/hour for a 7 Tesla OXFORD magnet), and extremely homogenous (0.1 ppm half-height line width with superconducting shims for given sample volume) magnetic field into which the sample is placed. The strength of the NMR spectrometer is typically specified in terms of the resonance frequency for proton expressed in MHz. The highest static magnetic field achieved to date is 45 T in the National High Magnetic Field Lab (NHMFL), Tallahassee, FL. Once in operation, this magnet, which is a hybrid of electro- and superconducting types, uses nearly 70% of the electric power in the city of Tallahassee. Superconducting magnets are desirable since after being energized they consume no electric power. Both Oxford Instruments and Bruker BioSpin have recently commercialized their highest field superconducting 900 MHz (21.1 T) magnets.

The NMR probe holds the sample and is placed in the bore of the magnet. The probe also contains one or two coils for irradiating the sample with rf energy and for detecting the very weak nuclear signal from the sample. There are special probes, such as those capable of variable temperature, of rotating the sample around an axis making a fixed or variable

angle with the static field. One of the latest inventions for liquid state NMR spectroscopy is the cryogenic probe. With the electronics working at low temperature, the reduced thermal noise allows high sensitivity to be achieved.

The NMR console consists of pulse programmer, rf transmitter, frequency synthesizer, receiver, and digitizer. It generates and controls rf pulses used to excite the sample in the probe. The console also receives and amplifies the very weak signals coming back from the probe.

NMR spectrometers also rely on computers and software for the control of the various pulse sequences and the collection, processing, and storage of the NMR data. The NMR signals are subjected to complex digital signal processing algorithms including the Fourier Transform to convert the time domain FIDs into frequency domain spectra for interpretation.

## 2.4 Relaxation Times

In a static magnetic field, the magnetization is quantized and oriented along the  $z$ -direction (parallel to the field). A  $\pi/2$  pulse results in zero longitudinal magnetization,  $M_z = 0$ . After the rf perturbation is removed, the nuclear spins release energy to the surrounding environment and  $M_z$  recovers according to,

$$M_z(t) = M_0(1 - e^{-t/T_1}), \quad (2.24)$$

and  $T_1$  is the time constant. In reality, non-exponential recovery may also be observed. Given long enough time, thermal equilibrium will be re-established and the longitudinal magnetization returns to its equilibrium value,  $M_z(\infty) = M_0$ .

Similarly, the decay of transverse magnetization is called transverse relaxation. After a  $\pi/2$  pulse the transverse magnetization decays toward its thermal equilibrium value of zero. Inevitably, the transverse relaxation time is shorter than the longitudinal relaxation time. In addition, factors like field inhomogeneity, dipolar coupling, chemical shift anisotropy, and quadrupole interaction cause components of the transverse magnetization to fan out, producing additional dephasing mechanisms for the *net* transverse magnetization. The contribution from field inhomogeneity is characterized by the time constant  $T_2'$  ( $\sim 1/\gamma\Delta B$ ). Symbol  $T_2$  is used to denote the intrinsic time constant arising from all other factors. The overall effective relaxation time  $T_2^*$  is calculated according to

$$\frac{1}{T_2^*} = \frac{1}{T_2} + \frac{1}{T_2'} \quad (2.25)$$

In nonviscous liquids, fast motion averages out all the anisotropic interactions, resulting in  $T_2 \cong T_1$ . However in solids (and some liquids),  $T_2$  is much shorter than  $T_1$ .

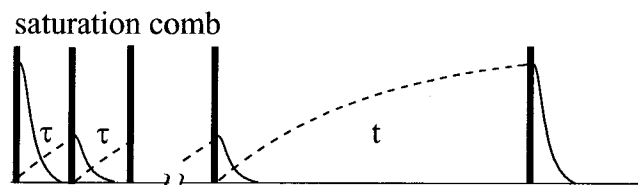


**Figure 2.4:**  $T_1$  measurement using saturation comb. The saturation comb consists of 4-20  $\pi/2$  pulses separated by interval  $\tau$ ,  $T_2^* < \tau \ll T_1$ . A reading  $\pi/2$  pulse is then applied after delay  $t$ . Solid curves denote the decay of transverse magnetization and the dashed curves denotes the regrowth of longitudinal magnetization.

For solids  $T_1$  can be measured using the saturation sequence shown in Fig. 2.4. A number of  $\pi/2$  pulses are applied with such short time intervals that the the system is unable to release energy to surroundings and finally the populations of all energy states become equal; this saturation comb sets the magnetization to zero. To achieve efficient

saturation, the interval  $\tau$  between two pulses should satisfy  $T_2^* < \tau \ll T_1$ . Another  $\pi/2$  pulse is applied after a delay  $t$ , and the signal is then acquired. The signal  $M(t)$  obeys

$$M(t) = M_0(1 - e^{-t/T_1}). \quad (2.26)$$

$M(t)$  is measured at a set of  $t$  values and then  $T_1$  is obtained by fitting the data with the above equation. The  $^{207}\text{Pb}$  relaxation times for relaxor ferroelectric materials satisfy the condition  $T_2^* \ll T_1$  and the saturation sequence is used for  $T_1$  measurement in Chapter 8.

The more general strategy to measure  $T_1$  is the  $\pi - \pi/2 - acquisition$  inversion recovery sequence for which the magnetization recovers as

$$M(t) = M_0 \left( 1 - 2e^{-t/T_1} \right). \quad (2.27)$$

However, for materials with long  $T_1$  this strategy is time consuming since at least  $5T_1$  after the acquisition is needed to allow the magnetization to return to  $M_0$  before the next round of pulsing and acquisition.

## 2.5 Recovery Times and Spin Echo

For samples with very short  $T_2^*$  the FID decays very fast. Acquiring such an FID is difficult because of the electronic “deadtime” problem associated with each pulse. During deadtime no signal is detectable due to several factors: (1) The receiver, which is designed to detect and amplify microvolt NMR signals, is paralyzed by the diode limited 0.5 volt leak-through of the transmitter excitation pulse(s); the leak-through voltage needs time to decay to below the weak micro-volt NMR signal (rf ringing down problem). (2) Acoustic standing wave,

which is established by an rf pulse in conductive probe components in the magnetic field, is converted back to an rf radiation by the reciprocal mechanism and interferes with the NMR signal (acoustic ringing down problem).

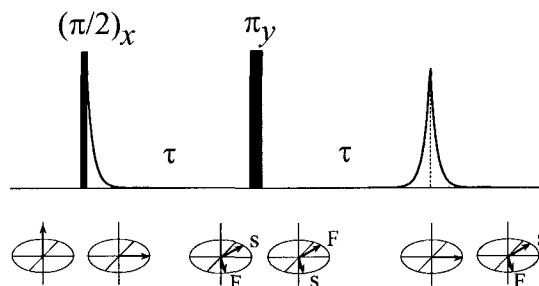


**Figure 2.5:** Spin echo pulse sequence and vector diagrams to monitor the magnetization. ‘S’ stands for magnetization species with slow Larmor precession, ‘F’ stands for fast precession.

The deadtime problem is usually solved by using spin echo techniques. In the pulse sequence shown in Fig. 2.5, a  $\pi_y$  pulse is applied after the initial  $(\pi/2)_x$  pulse with time interval  $\tau$ ; the subscripts denote the phases of the applied pulses:  $x$  for  $\phi_0 = 0$  and  $y$  for  $\phi_0 = \pi/2$ . The  $\pi_y$  pulse refocuses the decayed FID after time  $\tau$ ; the mechanism of refocusing is illustrated in the vector diagrams. For simplicity, suppose the magnetization consists of only two components, one with slow precession speed, another with fast speed. The  $(\pi/2)_x$  pulse brings the magnetization onto the  $y$  axis. The components then fan out (or dephase); the fast component move clockwise while the slow component moves counter-clockwise. Their vector sum, the transverse magnetization, decays. The  $\pi_y$  pulse flips the two components by  $180^\circ$  around the  $-y$  axis, and then each component continues its journey in its original direction. As a result, the two components come closer and at time  $\tau$  after the second pulse, they meet to give a maximum magnetization. Then they part and the magnetization decays. By choosing  $\tau$  longer than the deadtime, the above mentioned

problems are avoided. Spin echoes have become important components in many sequences for solid state NMR spectroscopy.

## 2.6 Summary

This chapter introduces NMR spectroscopy from both a classic description of the precessing magnetization and a quantum mechanic density matrix description. The construction of a modern NMR spectrometer is also briefly covered. The methods of relaxation time measurement are described. The saturation comb method will be used to measure the  $^{207}\text{Pb}$  longitudinal relaxation time for relaxor ferroelectric materials in Chapter 8. The important spin echo concept is also introduced. This solves the dead time problem and can be combined with MQMAS and 2D-PASS sequences that appear in later chapters.

## Chapter 3

# Chemical Shift Interaction

Consider a nucleus subject to a static external magnetic field  $\mathbf{B}_0$ . The local magnetic field ( $\mathbf{B}$ ) it interacts with differs from  $\mathbf{B}_0$ , since the external field is shielded by the surrounding electrons. This “chemical shielding” has both diamagnetic and paramagnetic contributions. The diamagnetic shielding is described in terms of Lenz’s law; the electrons circulating around the nucleus induce a small field *opposite* to the applied field. The paramagnetic shielding is associated with excited electronic states and results in a small field *along* the applied field. Formal theory of the chemical shielding interaction can be found in Slichter’s book [95].

The chemical shielding interaction is influenced by surrounding atoms and chemical bonds. Therefore, the nuclei can be used to probe the chemical environment. One classic example is the proton NMR spectrum of ethyl alcohol ( $\text{CH}_3\text{-CH}_2\text{-OH}$ ), which is composed of three set of peaks with different chemical shifts. These are assigned to methyl, methylene, and hydroxyl protons and have integrated intensities proportional to the number of protons in each site, i.e., 3:2:1.



### 3.1 Chemical Shielding and Chemical Shifts

The local field experienced at the nucleus is given by

$$\mathbf{B} = (1 - \sigma)\mathbf{B}_0, \quad (3.1)$$

where  $\sigma$  is the shielding tensor. It is possible to choose a principal axes system (PAS) where only the diagonal components are nonzero. These diagonal components  $\sigma_{11}$ ,  $\sigma_{22}$ , and  $\sigma_{33}$  are often expressed relative to a standard in terms of chemical shift (or “antishielding”)  $\delta_{11}$ ,  $\delta_{22}$ , and  $\delta_{33}$  (in ppm):  $\delta = 10^6(\sigma_{\text{std}} - \sigma)$ , with  $\sigma_{\text{std}}$  as the shielding tensor for a standard reference material. For  $^1\text{H}$  and  $^{13}\text{C}$ , the standard sample is usually liquid tetramethylsilane (TMS). In liquids, the anisotropy of the chemical shielding is eliminated by averaging due to fast isotropic molecular reorientation. Therefore,  $\sigma_{\text{std}}$  reduces to  $(1/3)\text{trace}(\sigma_{\text{std}})\mathbf{I}$ , where  $\mathbf{I}$  is the identity matrix. Usually we set  $\sigma_{\text{std}} = 0$ , thus  $\delta = -10^6\sigma$ . Instead of directly using the principle elements  $\delta_{11}$ ,  $\delta_{22}$ , and  $\delta_{33}$  to characterize the chemical shift anisotropy (CSA), it is convenient to define the isotropic chemical shift ( $\delta_{\text{iso}}$ ), the span ( $\Omega$ , which measures the full frequency coverage), and the skew ( $\kappa$ , which measures the deviation from axial symmetry),

$$\begin{aligned} \delta_{\text{iso}} &= \frac{\delta_{11} + \delta_{22} + \delta_{33}}{3}, \\ \Omega &= \delta_{11} - \delta_{33}, \\ \kappa &= \frac{3}{\Omega}(\delta_{22} - \delta_{\text{iso}}). \end{aligned} \quad (3.2)$$

Also by convention,

$$\delta_{11} \geq \delta_{22} \geq \delta_{33} \quad (\sigma_{11} \leq \sigma_{22} \leq \sigma_{33}), \quad (3.3)$$

to ensure  $\Omega \geq 0$  and  $-1 \leq \kappa \leq +1$  ( $\kappa = -1$  when  $\delta_{22} = \delta_{33}$  and  $\kappa = +1$  when  $\delta_{22} = \delta_{11}$ ).

However, it is important to be aware of another convention and to be able to convert between the two. This earlier convention uses the anisotropic chemical shift  $\delta_{\text{aniso}}$  instead of the span  $\Omega$ , and the asymmetry parameter  $\eta$  instead of the skew  $\kappa$ ,

$$\begin{aligned}\delta_{\text{aniso}} &= \delta_{33} - \delta_{\text{iso}}, \\ \eta &= \frac{\delta_{11} - \delta_{22}}{\delta_{33} - \delta_{\text{iso}}},\end{aligned}\tag{3.4}$$

where the three components should be so sorted  $|\delta_{33} - \delta_{\text{iso}}| \geq |\delta_{22} - \delta_{\text{iso}}| \geq |\delta_{11} - \delta_{\text{iso}}|$  as to ensure  $0 \leq \eta \leq 1$ . This ordering places  $\delta_{11}$  between  $\delta_{22}$  and  $\delta_{33}$ , and closer to  $\delta_{22}$ . In the case of axial symmetry ( $\eta = 0$ ), notations  $\delta_{\parallel} = \delta_{33}$  and  $\delta_{\perp} = \delta_{11} = \delta_{22}$  are also used widely in the literature. The formulas to convert them to the first convention are,

$$\begin{aligned}\Omega &= |\delta_{\text{aniso}}| \frac{3 + \eta}{2}, \\ \kappa &= \text{Sign}(\delta_{\text{aniso}}) \frac{3\eta - 3}{3 + \eta}.\end{aligned}\tag{3.5}$$

And the inverse relations are,

$$\begin{aligned}\delta_{\text{aniso}} &= -\text{Sign}(\kappa) \Omega \frac{3 + |\kappa|}{6}, \\ \eta &= \frac{3 - 3|\kappa|}{3 + |\kappa|}.\end{aligned}\tag{3.6}$$

The second convention will be used in this thesis. But adding to the chaos of two conventions, we may find in the literature a slightly different definition of  $\eta$  for the second convention [cf Eq. (3.4)],

$$\eta = \frac{\delta_{22} - \delta_{11}}{\delta_{33} - \delta_{\text{iso}}},\tag{3.7}$$

with ordering of components  $|\delta_{33} - \delta_{\text{iso}}| \geq |\delta_{11} - \delta_{\text{iso}}| \geq |\delta_{22} - \delta_{\text{iso}}|$ . The principal components  $\delta_{11}$  and  $\delta_{22}$  are swapped in the two definitions of  $\eta$ .

### 3.2 Static Spectra

The chemical shielding Hamiltonian is

$$H_{\text{CS}} = \gamma \hbar \mathbf{I} \sigma \mathbf{B}_0. \quad (3.8)$$

The chemical shielding interaction is small ( $\sim$ kHz) compared to the Zeeman interaction ( $\sim$ 100 MHz) and can be treated as a perturbation. To the first order, the terms  $\sigma_{xz}$  and  $\sigma_{yz}$  in the Hamiltonian that do not commute with  $I_z$  may be dropped (secular approximation with  $\mathbf{B}_0$  in  $z$  direction in the LAB frame). Thus the Hamiltonian becomes

$$H_{\text{CS}} = \gamma \hbar I_z \sigma_{zz} B_0. \quad (3.9)$$

To ease coordinate transformations, a traceless chemical shift tensor is defined,

$$\tilde{\delta} = \delta - \delta_{\text{iso}}. \quad (3.10)$$

As a scalar,  $\delta_{\text{iso}}$  is the same in any frame. From  $\tilde{\delta}$ , we further construct a second rank irreducible spherical tensor (valid for any frame),

$$\begin{aligned} f_0 &= \tilde{\delta}_{33}, \\ f_{\pm 1} &= \mp \sqrt{\frac{2}{3}} (\tilde{\delta}_{13} \pm i \tilde{\delta}_{23}), \\ f_{\pm 2} &= \sqrt{\frac{2}{3}} \left[ \frac{1}{2} (\tilde{\delta}_{11} - \tilde{\delta}_{22}) \pm i \tilde{\delta}_{12} \right]. \end{aligned} \quad (3.11)$$

In the PAS frame, these reduce to

$$\begin{aligned} f_0^P &= \delta_{\text{aniso}}, \\ f_{\pm 1}^P &= 0, \\ f_{\pm 2}^P &= \eta \delta_{\text{aniso}} / \sqrt{6}. \end{aligned} \tag{3.12}$$

The components in the PAS frame (P) are conveniently transformed into the laboratory frame (L) by Wigner rotation matrix  $\mathcal{D}^2(\Omega_{PL})$  through Euler angles  $\Omega_{PL} = (\alpha, \beta, \gamma)$  (Appendix A),

$$f_m^L = \sum_{m'=-2}^2 \mathcal{D}_{m'm}^2(\Omega_{PL}) f_{m'}^P. \tag{3.13}$$

Immediately we have

$$\tilde{\delta}_{zz}^L = f_0^L = \delta_{\text{aniso}} \left[ \frac{3 \cos^2 \beta - 1 + \eta \sin^2 \beta \cos 2\alpha}{2} \right], \tag{3.14}$$

and

$$\delta_{zz}^L = \delta_{\text{iso}} + \delta_{\text{aniso}} \left[ \frac{3 \cos^2 \beta - 1 + \eta \sin^2 \beta \cos 2\alpha}{2} \right]. \tag{3.15}$$

In a powder sample, the crystallites are randomly oriented. The orientation dependence of the chemical shift [Eq. (3.15)] results in anisotropic lineshape with two edges and a peak at frequencies equal the three principal values  $\delta_{11}$ ,  $\delta_{22}$ , and  $\delta_{33}$ . An example of static powder pattern of crystalline  $^{207}\text{Pb}$  for  $\text{PbSO}_4$  is shown in Fig. 3.1. The chemical shift parameters can be extracted from the lineshape, these are  $\delta_{\text{iso}} = -3607(\pm 5)$  ppm,  $\delta_{\text{aniso}} = -317(\pm 5)$  ppm,  $\eta = 0.6(\pm 0.1)$ . These parameters agree within experimental error with literature values  $\delta_{\text{iso}} = -3611$  ppm,  $\delta_{\text{aniso}} = -317$  ppm,  $\eta = 0.6$  [116].

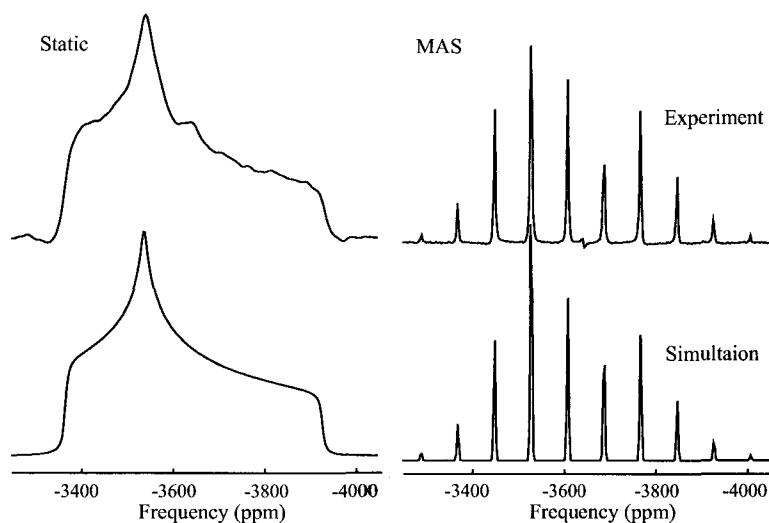


**Figure 3.1:** Experimental and simulated static and MAS  $^{207}\text{Pb}$  NMR spectra of  $\text{PbSO}_4$  at 7 T. The scaling for each sub-figure is exactly the same. The static spectrum was acquired with recycle delay 30 s, dwell time  $20 \mu\text{s}$ , and 1312 scans. The MAS spectrum was acquired with a sample spinning rate of 5.0 kHz, recycle delay 30 s, dwell time  $10 \mu\text{s}$ , and 1168 scans. Spectra were simulated with  $\delta_{\text{iso}} = -3607$  ppm,  $\delta_{\text{aniso}} = -317$  ppm,  $\eta = 0.55$ , and MAS FWHH of 0.3 kHz. Chemical shifts are referenced with respect to tetramethyl lead in toluene.

### 3.3 Magic-Angle Spinning Spectra

Typically the chemical shift anisotropy lineshapes of several nonequivalent crystalline (or molecular) sites overlap and this makes assignment and structural interpretation difficult. It is thus desirable to remove the anisotropy to recover the structural information contained in the isotropic chemical shifts. The removal of anisotropy occurs naturally in liquids due to fast isotropic molecular reorientation (section 3.1). We apply the idea of coherent averaging to solids by rotating a sample at the so-called “magic-angle”  $\theta_m = 54.7^\circ$  (the zero point of the function  $3 \cos^2 \theta - 1$ ) with respect to the external magnetic field. Magic-angle spinning (MAS) averages out all second rank tensor interactions. If the sample rotation frequency  $\nu_R = \omega_R/2\pi$  greatly exceeds the span of the lineshape, a single narrow line is observed for each site. However, if spinning speed is less than or comparable to the anisotropic linewidth,

many spinning sidebands are observed (separated by  $\omega_R/2\pi$ ). If the sample spinning is slow, these narrow lines have an envelope close to the static lineshape. An example of MAS powder pattern split into spinning sidebands is shown in Fig. 3.1 for  $\text{PbSO}_4$ .

The intensities of the sidebands can be calculated rigorously using the following MAS theory. The irreducible spherical tensor can be written as

$$f_m^L = \sum_{m'=-2}^2 \mathcal{D}_{m'm}^2(\Omega_{RL}) \sum_{m''=-2}^2 \mathcal{D}_{m''m'}^2(\Omega_{PR}) f_{m''}^P, \quad (3.16)$$

where Euler angles  $\Omega_{PR} = (\alpha, \beta, \gamma)$  translate the PAS frame to rotor frame (R), and Euler angles  $\Omega_{RL} = (\omega_R t, \arccos(1/\sqrt{3}), 0)$  translate the rotor frame to LAB frame. For simplicity we drop the time-independent isotropic part, so the observed frequency (in Hz,  $\omega_L/10^6$  factor since  $f_0^L$  is in ppm) is

$$\begin{aligned} \omega(t) &= \frac{f_0^L \omega_L}{10^6} \\ &= C_1 \cos(\omega_R t + \gamma) + S_1 \sin(\omega_R t + \gamma) \\ &\quad + C_2 \cos(2\omega_R t + 2\gamma) + S_2 \sin(2\omega_R t + 2\gamma), \end{aligned} \quad (3.17)$$

where the four coefficients  $C_i, S_i, i = 1, 2$  are functions of the orientation of the PAS and rotor frames  $(\alpha, \beta)$ . In some situations, it is more convenient to use an equivalent form,

$$\omega(t) = \tilde{C}_1 \cos(\omega_R t) + \tilde{S}_1 \sin(\omega_R t) + \tilde{C}_2 \cos(2\omega_R t) + \tilde{S}_2 \sin(2\omega_R t), \quad (3.18)$$

where the four coefficients  $\tilde{C}_i, \tilde{S}_i, i = 1, 2$  are functions of  $(\alpha, \beta, \gamma)$  [91].

For a single crystallite, the MAS time domain signal is

$$s(t) = e^{i \int_0^t \omega(t') dt'} = e^{i\Phi(t)} e^{-i\Phi(0)}, \quad (3.19)$$

with phase

$$\begin{aligned}\Phi(\alpha, \beta, \gamma + \omega_R t) &= \int \omega(\alpha, \beta, \gamma + \omega_R t) dt \\ &= \frac{1}{2\omega_R} [2\tilde{C}_1 \sin(\omega_R t) - 2\tilde{S}_1 \cos(\omega_R t) + \tilde{C}_2 \sin(2\omega_R t) - \tilde{S}_2 \cos(2\omega_R t)].\end{aligned}\quad (3.20)$$

The phase is proportional to  $1/\omega_R$ , thus increased spinning speed reduces the anisotropic effects. In order to focus on the time dependence, we define

$$g(\alpha, \beta, \gamma + \omega_R t) = e^{i\Phi(\alpha, \beta, \gamma + \omega_R t)}, \quad (3.21)$$

thus the signal [Eq. (3.19)] becomes

$$s(t) = g^*(\gamma)g(\gamma + \omega_R t), \quad (3.22)$$

where the arguments  $\alpha$  and  $\beta$  are dropped for clarity. At integer rotor periods,  $Nt_R = 2N\pi/\omega_R$  ( $N = 0, 1, \dots$ ), magnetizations of all crystals refocus [ $s(Nt_R) = 1$ , independent of orientation] thus a train of rotational echoes forms in the FID. Because of this periodicity, the spectrum in the frequency domain can only have intensities at  $\omega_R$  and its harmonics  $N\omega_R$ . The intensity for the  $N$ th sideband is

$$\begin{aligned}I_N(\alpha, \beta, \gamma) &= g^*(\gamma) \int_0^{t_R} g(\gamma + \omega_R t) e^{-iN\omega_R t} \frac{dt}{t_R}, \\ &= g^*(\gamma) e^{iN\gamma} \int_0^{2\pi} g(\gamma') e^{-iN\gamma'} \frac{d\gamma'}{2\pi}, \\ &= g^*(\gamma) e^{iN\gamma} G_N(\alpha, \beta),\end{aligned}\quad (3.23)$$

where  $\gamma' = \gamma + \omega_R t$  and

$$G_N(\alpha, \beta) = \int_0^{2\pi} g(\gamma') e^{-iN\gamma'} \frac{d\gamma'}{2\pi}. \quad (3.24)$$

This sideband intensity is for a single crystal or crystallite, and is a complex valued function.

For powder samples, the next step is to integrate over  $\gamma$ ,

$$I_N(\alpha, \beta) = \int_0^{2\pi} I_N(\alpha, \beta, \gamma) \frac{d\gamma}{2\pi} = G_N^*(\alpha, \beta) G_N(\alpha, \beta). \quad (3.25)$$

It is real and positive. The observed  $N$ th sideband intensity of a powder sample,

$$\mathcal{I}_N = \int_0^{2\pi} d\alpha \int_0^\pi I_N(\alpha, \beta) \sin \beta d\beta, \quad (3.26)$$

is a function of  $C_i, S_i$ , ( $i = 1, 2$ ); the integrations over  $\alpha$  and  $\beta$  preserve the real and positive property (consult Schmidt-Rohr's book for a rigorous proof [91]).

From the intensities of these sidebands, the principal values of the chemical shift tensor can be calculated. Hertzfeld and Berger [56] plot  $\mathcal{I}_N/\mathcal{I}_0$  contour maps for the first few sidebands with regard to two variables  $\rho$  and  $\mu$ ,

$$\begin{aligned} \rho &= \frac{\sigma_{11} + \sigma_{33} - 2\sigma_{22}}{\sigma_{33} - \sigma_{11}} = \kappa, \\ \mu &= \frac{\omega_L(\sigma_{33} - \sigma_{11})}{\omega_R} = \frac{\Omega \omega_L}{10^6 \omega_R}. \end{aligned} \quad (3.27)$$

For instance, suppose we have experimental  $\mathcal{I}_1/\mathcal{I}_0$  and  $\mathcal{I}_2/\mathcal{I}_0$  values, then the crossing point of the two contour lines determine  $\rho_0$  and  $\mu_0$ . Another approach is to use computer programs (e.g. DMFIT [74]) to simulate MAS CSA spectra and fit experimental data by inspection.

### 3.4 Total Suppression of Spinning Sidebands

Although spinning sidebands contain information on chemical shift anisotropy, they crowd the spectra and complicate spectral assignments. Spectra at more than one spinning speed



are often acquired to differentiate isotropic peaks from sidebands. However, confusion is unavoidable if there are too many inequivalent sites. Moreover, the distribution of intensity among the sidebands results in low sensitivity for large CSA.

From these considerations, it seems advantageous to suppress the sidebands and effectively achieve the infinite spinning speed limit spectra. In 1982, Dixon proposed the Total Suppression of Sidebands (TOSS) sequence, which consists of four appropriately spaced  $\pi$  pulses, to achieve total suppression of spinning sidebands [37]. The sidebands are suppressed by inhibiting rotational echoes from forming. The TOSS signal can be expressed as

$$s(t) = g(\gamma + \omega_R t). \quad (3.28)$$

At no point in time do the magnetizations from all the different crystallites coherently refocus, thus no rotational echoes will form [cf Eq. (3.22)]. The sideband intensity of a single crystallite is [cf Eq. (3.23)]

$$I_N(\alpha, \beta, \gamma) = e^{i\gamma N} G_N(\alpha, \beta). \quad (3.29)$$

For a powder sample, the  $\gamma$ -averaged intensity is

$$I_N(\alpha, \beta) = G_N(\alpha, \beta) \int_0^{2\pi} e^{i\gamma N} \frac{d\gamma}{2\pi} = G_N(\alpha, \beta) \delta_{N,0}, \quad (3.30)$$

where  $\delta_{N,0}$  is Kronecker delta. Thus only the center band is preserved and all the sidebands are removed.

The centerband intensity for ordinary MAS is the  $(\alpha, \beta)$ -averaged  $G_N^*(\alpha, \beta)G_N(\alpha, \beta)$ , which is always real and positive. However, the TOSS intensity, which is the averaged  $G_N(\alpha, \beta)$ , could be complex. This is one disadvantage of the TOSS method.

### 3.5 Phase Adjusted Spinning Sidebands

TOSS achieves high resolution at the expense of important chemical shift anisotropy information. Is it possible to preserve the anisotropic information and at the same time achieve high resolution? In 1995 an excellent solution was introduced—2D-PASS (two-Dimensional Phase-Adjusted Spinning Sidebands), by Antzutkin, Shekar and Levitt [7] on the basis of Dixon's other remarkable method, PASS [36, 37]. The 2D-PASS separates sidebands by their order along the  $\omega_1$  dimension, while the  $\omega_2$  dimension consists of both isotropic and anisotropic shifts. The original spectrum of L-tyrosine hydrochloride is reproduced from Antzutkin et. al. in FIG. 3.2. A simple shearing transformation removes the anisotropy in the  $\omega_2$  dimension so that anisotropic and isotropic shifts are cleanly separated along two orthogonal axes. (An example of shearing transformation is shown at the end of this section.)

The pulse sequence for 2D-PASS is shown in FIG. 3.3. Following the initial  $\pi/2$  pulse, five  $\pi$  pulses are applied at times  $\zeta_i$  ( $i = 1 \dots 5$ ). The period 0–T, which is called PASS element, is divided into six intervals  $\tau_i$  ( $i = 1 \dots 6$ ). Usually,  $T = t_R$ , but integer number of rotor periods may be added to  $\tau_5$  and  $\tau_6$  in order to create spin echoes [41]. Data acquisition starts immediately after the PASS element. Application of a  $\pi$  pulse inverts the sign of precession frequency. Therefore, the effective phase for the isotropic part, which should remain unchanged at the end of PASS element (to ensure that  $\omega_1$  dimension contains

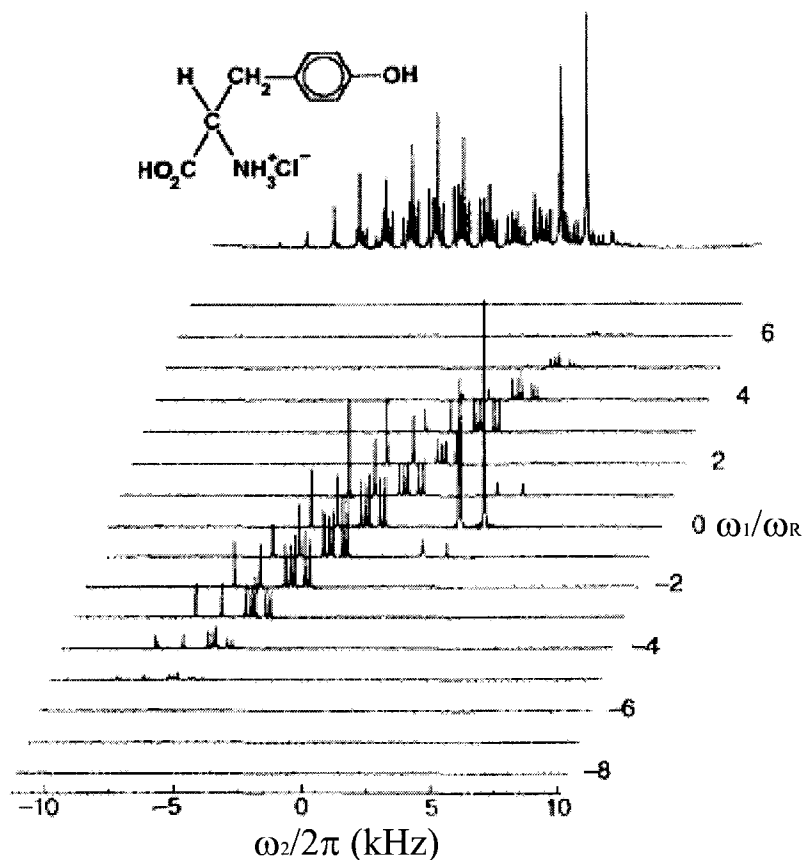


**Figure 3.2:** Example spectrum of 2D-PASS from Antzutkin et al. [7]. Top:  $^{13}\text{C}$  MAS spectrum of L-tyrosine hydrochloride powder at sample spinning speed of 1030 Hz, 3888 transients were collected. Bottom: 2D-PASS spectrum showing the separation of sidebands in the  $\omega_1$  dimension. The  $\omega_1$  slices are labeled with the order of sideband. Sixteen  $t_1$  increments were taken, each with 243 transients. (Notice the frequencies are labeled in the opposite direction to NMR convention.)

only the anisotropy), is

$$\begin{aligned}
 0 &= \omega_{\text{iso}}[(\tau_6 + \tau_4 + \tau_2) - (\tau_5 + \tau_3 + \tau_1)] \\
 &= \omega_{\text{iso}}[T + 2 \sum_{n=1}^5 (-1)^n \zeta_n].
 \end{aligned} \tag{3.31}$$

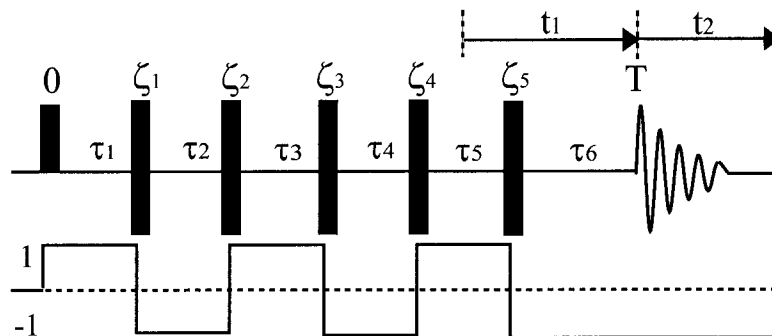


**Figure 3.3:** Pulse sequence and coherence pathway for 2D-PASS experiments. The initial  $\pi/2$  pulse is followed by five appropriately spaced  $\pi$  pulses.

For the anisotropic part, the effective phase at  $t_2$  is

$$\begin{aligned} \Psi &= -\int_0^{\zeta_1} \omega(t) dt + \int_{\zeta_1}^{\zeta_2} \omega(t) dt - \int_{\zeta_2}^{\zeta_3} \omega(t) dt + \int_{\zeta_3}^{\zeta_4} \omega(t) dt - \int_{\zeta_4}^{\zeta_5} \omega(t) dt + \int_{\zeta_5}^{T+t_2} \omega(t) dt \\ &= \Phi(T+t_2) - 2\Phi(\zeta_5) + 2\Phi(\zeta_4) - 2\Phi(\zeta_3) + 2\Phi(\zeta_2) - 2\Phi(\zeta_1) + \Phi(0). \end{aligned} \quad (3.32)$$

The same phase can be created by a free evolution (without rf pulses) starting from an effective time  $t_1$  before the end of the period  $T$ ,

$$\Psi = \Phi(T+t_2) - \Phi(T-t_1). \quad (3.33)$$

We define  $\Theta = \omega_R(T-t_1)$ , which is dubbed the “pitch” by Dixon [36]. The above two

equations, with definition of  $\Phi(t)$  in Eq. (3.20), yield

$$\begin{aligned}
& \tilde{C}_1 \left[ 2 \sum_{n=1}^5 (-1)^n \sin(\omega_R \zeta_n) + \sin(\Theta) \right] \\
& - \tilde{S}_1 \left[ 2 \sum_{n=1}^5 (-1)^n \cos(\omega_R \zeta_n) + \cos(\Theta) + 1 \right] \\
& + \frac{\tilde{C}_2}{2} \left[ 2 \sum_{n=1}^5 (-1)^n \sin(2\omega_R \zeta_n) + \sin(2\Theta) \right] \\
& - \frac{\tilde{S}_2}{2} \left[ 2 \sum_{n=1}^5 (-1)^n \cos(2\omega_R \zeta_n) + \cos(2\Theta) + 1 \right] = 0.
\end{aligned} \tag{3.34}$$

This equation is valid for any orientation, therefore all four expressions in square brackets must vanish. These four equations plus Eq. (3.31) are solved to obtain the five  $\zeta_i$  (and hence  $\tau_i$ ) values for a given  $\Theta$ . Listed in Table 3.1 are solutions for  $\Theta$  increment of  $t_R/16$ .

**Table 3.1:** Delays between pulses for 2D-PASS sequence shown in FIG. 3.3.

Increment	$\Theta/2\pi$	$\tau_1/t_R$	$\tau_2/t_R$	$\tau_3/t_R$	$\tau_4/t_R$	$\tau_5/t_R$	$\tau_6/t_R$
1	0.00000	0.16667	0.16667	0.16667	0.16667	0.16667	0.16667
2	0.06250	0.18989	0.17512	0.15541	0.17615	0.15470	0.14873
3	0.12500	0.21668	0.17874	0.14270	0.18365	0.14062	0.13761
4	0.18750	0.24453	0.17549	0.12896	0.18947	0.12651	0.13504
5	0.25000	0.26915	0.16096	0.11573	0.19608	0.11511	0.14297
6	0.31250	0.28147	0.12931	0.11053	0.21004	0.10800	0.16065
7	0.37500	0.26731	0.09195	0.13166	0.22798	0.10102	0.18008
8	0.43750	0.23472	0.07687	0.17459	0.22846	0.09069	0.19467
9	0.50000	0.20979	0.08043	0.20978	0.20979	0.08043	0.20978
10	0.56250	0.19467	0.09069	0.22846	0.17459	0.07687	0.23472
11	0.62500	0.18008	0.10102	0.22798	0.13166	0.09195	0.26731
12	0.68750	0.16065	0.10800	0.21005	0.11052	0.12931	0.28147
13	0.75000	0.14297	0.11511	0.19608	0.11574	0.16095	0.26915
14	0.81250	0.13504	0.12651	0.18947	0.12896	0.17549	0.24453
15	0.87500	0.13761	0.14062	0.18365	0.14270	0.17875	0.21667
16	0.93750	0.14874	0.15469	0.17615	0.15541	0.17512	0.18989

The signal can be written as

$$\begin{aligned} s(t_1, t_2) &= e^{i\Psi} e^{i\omega_{\text{iso}} t_2} e^{-\lambda(T+t_2)} \\ &= g^*(\gamma + \omega_R(T - t_1)) g(\gamma + \omega_R(T + t_2)) e^{i\omega_{\text{iso}} t_2} e^{-\lambda(T+t_2)}. \end{aligned} \quad (3.35)$$

The signal is periodic with the rotor period  $t_R$  in both dimensions, and thus intensities appear only at multiples of  $\omega_R$ . For simplicity, ignoring the relaxation and isotropic factors, double Fourier transformation of the signal gives the intensity

$$I_{M,N} = \int e^{-iM\omega_R t_1} \frac{dt_1}{t_R} \int s(t_1, t_2) e^{-iN\omega_R t_2} \frac{dt_2}{t_R}. \quad (3.36)$$

With substitutions  $\gamma' = \gamma + \omega_R(T - t_1)$  and  $\gamma'' = \gamma + \omega_R(T + t_2)$ ,

$$\begin{aligned} I_{M,N}(\alpha, \beta, \gamma) &= e^{i(N-M)(\gamma + \omega_R T)} \int \frac{d\gamma'}{2\pi} e^{iM\gamma'} g^*(\gamma') \int \frac{d\gamma''}{2\pi} e^{-iN\gamma''} g(\gamma'') \\ &= e^{i(N-M)(\gamma + \omega_R T)} G_M^*(\alpha, \beta) G_N(\alpha, \beta). \end{aligned} \quad (3.37)$$

Averaging over  $\gamma$  gives

$$I_{M,N}(\alpha, \beta) = \int I_{M,N}(\alpha, \beta, \gamma) \frac{d\gamma}{2\pi} = \delta_{M,N} I_N(\alpha, \beta), \quad (3.38)$$

with  $I_N$  defined in Eq. (3.23). The Kronecker  $\delta_{M,N}$  means that sideband of order  $N$  only appear in the  $N$ th  $\omega_1$  slice. And the intensity of the sideband is the same as in the conventional MAS spectrum.

To reduce pulse imperfections and to select the coherence pathway  $0 \rightarrow +1 \rightarrow -1 \rightarrow +1 \rightarrow -1 \rightarrow +1 \rightarrow -1$ , Antzoukin et al. [7] independently phase cycle the  $\pi$  pulses in three

step of  $2\pi/3$ . This results in long phase cycling of 243 total steps even without considering the four-step (of  $\pi/2$ ) cycling of the initial  $\pi/2$  pulse. In fact, it can be reduced to only three steps, as in Table 3.2. The simplification has been made by cycling the first three and the last two  $\pi$  pulses in a coordinated way,

$$\begin{aligned}\phi_1 - \phi_2 + \phi_3 &= 0^\circ \text{ (or } 360^\circ), \\ -\phi_4 + \phi_5 &= 0^\circ ,\end{aligned}\tag{3.39}$$

where  $\phi_i$  ( $i = 1, 2, \dots, 5$ ). The same coherence transfer pathway is selected by both the original and this simplified phase-cycling schemes. The new phase cycle saves experiment time (see Appendix B). Four-step cycling of the  $\pi/2$  pulse can also be used to further remove imperfections. Even with four-step cycling, there are only twelve steps in total!

**Table 3.2:** Improved phase cycling for  $\pi$  pulses in 2D-PASS (unit in  $2\pi/3$ ).

$\phi_1$	$\phi_2$	$\phi_3$	$\phi_4$	$\phi_5$
0	0	0	0	0
1	2	1	1	1
2	1	2	2	2

Direct Fourier transformations along both dimensions result in a spectrum where sidebands (and centerband) belonging to one site are distributed along a diagonal line (using the same unit for both dimensions), see Fig. 3.4(a). In fact, the  $\omega_1$  dimension contains only anisotropic shifts, while the  $\omega_2$  dimension contains both isotropic and anisotropic shifts. A shearing transformation is usually applied so that the  $\omega_2$  dimension contains only isotropic shifts. Now sidebands belonging to one site are parallel to  $\omega_1$  axis and the isotropy and anisotropy are fully separated [see Fig. 3.4(b)]. The separation of the isotropic shift gives

high resolution, while the separation of anisotropy preserves valuable information of chemical shielding tensor elements. Antzugin et al. [7] perform the shearing transformation by multiple left shifts. Left shift by an integer number of points, however, introduces errors due to insufficient digital resolution. The problem can be solved using “fractional left shift” and this is accomplished by linear phase correction in the time domain. First, inverse FT in the  $\omega_2$  dimension; for each slice, multiply  $e^{-iM\omega_R t_2}$ , with sideband order  $M$ ; then the second FT with respect to  $t_1$  is applied.

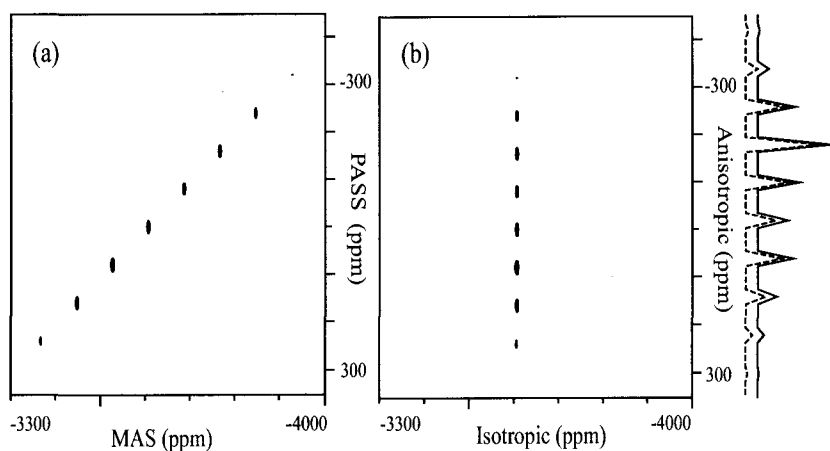


**Figure 3.4:** 2D-PASS  $^{207}\text{Pb}$  NMR spectra of  $\text{PbSO}_4$  at 7 T. The sample spinning speed was 5.0 kHz, recycle delay was 30 s, dwell time was 20  $\mu\text{s}$ , and 180 scans for each pitch increment. No shearing transformation was applied to spectrum in (a); spectrum in (b) was sheared. Slice taken at  $\delta_{\text{iso}} = -3607$  ppm (solid line) was simulated with  $\delta_{\text{aniso}} = -317$  ppm,  $\eta = 0.55$ , and MAS fwhm of 30 Hz (dotted line). Chemical shifts are reported with respect to tetramethyl lead in toluene.

### 3.6 Summary

The chemical shielding tensor of a nucleus measures the local magnetic fields created by electron density of molecular or crystal surroundings. In the beginning of this chapter, the origin of chemical shielding interaction was briefly introduced. The chemical shield-



ing tensor is characterized by isotropic and anisotropic chemical shifts. For chemical shift anisotropy, the two conventions— $\Omega$ ,  $\kappa$  versus  $\delta_{\text{aniso}}$ ,  $\eta$ —are described and conversion formulas are provided. For powder samples, both static and MAS lineshapes are calculated starting from the chemical shift Hamiltonian; this allows fit to experimental spectra and extraction of the principal elements of the chemical shielding tensor. The 2D-PASS technique separates isotropic chemical shift into the  $x$ -dimension and the anisotropic pattern of spinning sidebands into the  $y$ -dimension; this achieves high resolution and at the same time obtains all principal elements of the shielding tensor. For disordered materials such as the relaxor ferroelectric  $(1-x)\text{PbMg}_{1/3}\text{Nb}_{2/3}\text{O}_3 - x\text{PbSc}_{1/2}\text{Nb}_{1/2}\text{O}_3$  we are going to study in Chapter 8, both static and MAS  $^{207}\text{Pb}$  spectra have such low resolution that they could not provide much insight into local structures. Only the high-resolution  $^{207}\text{Pb}$  2D-PASS experiments prove to be indispensable for the study of such disordered materials.

## Chapter 4

# Electric Quadrupole Interaction

### 4.1 Quadrupolar Nuclei and Quadrupolar Interaction

As we noted in chapter 2, most elements have nuclear magnetic moments as a result of non-zero nuclear spin and thus in principle are detectable through NMR spectroscopy. Chapter 3 concentrated on the chemical shift effects arising from the interactions between the magnetic moments and the local magnetic fields. In addition, most of these magnetically active elements possess electric quadrupole moments arising from a nonspherically symmetric nuclear electronic charge distribution. Reorientation of a spherical nucleus in a surrounding electric field does not change the electrostatic energy. Nuclei with spin  $I = 0$ , having no preferred nuclear orientation at all, possess no electric quadrupolar moment. Moreover, flipping spins of  $I = 1/2$  does not change the charge distribution, and therefore, such nuclei do not display the quadrupolar effect either. Only  $I > 1/2$  nuclei can have quadrupole moments. By classifying the 103 elements according to the spin of their isotopes, we find that there are only twelve having  $I = 0$  isotopes, 25 elements having  $I = 1/2$  isotopes, and 71 having  $I \geq 1$  isotopes. Of these 71 elements 69 have isotopes with half integer spin  $n + 1/2$ , ( $n = 1, 2, \dots$ ). That is to say, two-thirds of the elements have nuclear quadrupole

moments. These elements are ubiquitous in materials and are especially important in minerals, ceramics, semiconductors, catalysts, and polymers. Obviously, it is very important to understand and investigate the effects of quadrupolar interactions in solid state NMR.

The significance of electric quadrupole moments for solid state or chemical physics is that they allow us to use the nuclei as microscopic probes for exploring the internal electric field gradients (EFGs). This is completely analogous with the use of nuclear magnetic moments for probing internal magnetic fields (via the chemical shift interaction). It is impossible to produce any appreciable gradients by direct external means, but a strong gradient can arise from internal fields, which are produced by the electric charge distribution near the nucleus. These are sensitive to subtle distortions and dynamics of the charge distribution.

Experimental NMR techniques can be divided into two main areas depending on the magnitude of the quadrupolar interaction. If the interaction is extremely large, nuclear resonance experiments can be performed at zero or very low applied magnetic field; comprehensive review of this field nuclear quadrupolar resonance (NQR) is beyond the scope of this work but is provided in reference [29]. On the other hand, the alternative high field NMR studies for which the Zeeman interaction is much larger than the quadrupole interaction will be discussed in detail. The 1957 review of quadrupolar interaction by Cohen and Reif has been found very helpful [23] in preparing section 4.1.1.

#### 4.1.1 Quadrupole Hamiltonian

Consider a nucleus subject to a electrostatic potential,  $V(\mathbf{x})$ . The electric charge  $Ze$  of the nucleus is distributed over the nuclear volume with a density  $\rho(\mathbf{x})$ . The electrostatic

Hamiltonian is expressed as an integral over the nuclear volume,

$$H_Q = \int \rho(\mathbf{x})V(\mathbf{x})d^3\mathbf{x}. \quad (4.1)$$

Expanding the potential in a Taylor's series about the center of mass of the nucleus gives

$$H_Q = \int d^3\mathbf{x}\rho(\mathbf{x}) \left\{ V_0 + \sum_j \left( \frac{\partial V}{\partial x_j} \right)_0 x_j + \frac{1}{2} \sum_{j,k} \left( \frac{\partial^2 V}{\partial x_j \partial x_k} \right)_0 x_j x_k + \dots \right\}, \quad (4.2)$$

where  $x_j$  ( $j = 1, 2, 3$ ) stands for  $x, y$  or  $z$ , the quantities with subscript 0 are evaluated at  $\mathbf{x} = 0$  and can thus be taken out of the integral. Therefore

$$H_Q = ZeV_0 + \sum_j P_j \left( \frac{\partial V}{\partial x_j} \right)_0 + \frac{1}{2} \sum_{j,k} \left( \frac{\partial^2 V}{\partial x_j \partial x_k} \right)_0 + \dots, \quad (4.3)$$

with the expectation values of:

$$\begin{aligned} & \text{the nuclear charge } \int \rho(x)d^3x = Ze, \\ & \text{the electric dipole moment } \int \rho(x)x_j d^3x \equiv P_j, \\ & \text{and the electric quadrupole moment } \int \rho(x)x_j x_k d^3x \equiv Q'_{jk}. \end{aligned} \quad (4.4)$$

The first term in Eq. (4.3) is simply the electrostatic energy of a point nucleus and can be neglected since it does not depend on the nuclear size, shape, or orientation. The second term for the electric dipole moment *vanishes* for two reasons. Firstly, in the definition of the electric dipole moment  $x_j$  has opposite sign in opposite octants. Secondly, the nuclear charge distribution has inversion symmetry  $\rho(\mathbf{x}) = \rho(-\mathbf{x})$ . This symmetry, which is equivalent to the probability density quantum-mechanically, arises from the parity conservation of the

ground state wave function upon reversing the signs of all the nuclear coordinates. From a semi-classical point of view, during times where outside fields have effect, the nucleons are in rapid precession about the direction of the nuclear spin. The time average charge distribution thus has cylindrical symmetry. This also implies mirror symmetry with the reflection plane passing through the center of mass, perpendicular to the rotation axis. Thus the average distribution has inversion symmetry, which also implies a vanishing octupole term. Therefore, Eq. (4.3) is simplified as

$$H_Q = \frac{1}{2} \sum_{jk} Q'_{jk} V_{jk} + \text{hexadecapole term} + \dots, \quad (4.5)$$

where

$$V_{jk} \equiv \frac{\partial^2 V}{\partial x_j \partial x_k} \quad (4.6)$$

is called the electric field gradient (EFG) though strictly speaking it is the negative of this.

Now let us estimate the order of magnitude of each of the expansion terms in Eq. (4.3). For hydrogen, the first term  $ZeV_0 \sim ke^2/a_0 = 4.35 \times 10^{-18}$  J, or equivalently  $6.5 \times 10^{15}$  Hz, where  $k = 8.988 \times 10^9$  J m C<sup>-2</sup> is Coulomb's constant and  $a_0 = 0.529$  Å is the Bohr radius of hydrogen. The quadrupole term  $Q'_{jk}(\partial^2 V/\partial x_j \partial x_k) \sim er_n^2(e/a_0^3) = eV_0(r_n/a_0)^2$ , where  $r_n \sim 10^{-14}$  m is the nuclear radius. This is of the order of  $10^{-8}$  of the electrostatic energy; i.e., 65 MHz. And similarly, the hexadecapole term is  $10^{-8}$  times the quadrupole term (of the order of 0.65 Hz) and this is so small that it is usually neglected.

The quadrupole tensor  $Q'_{jk}$  is symmetric by definition, and therefore it has at most six independent components. It is possible to reduce the number of independent components

to five by replacing the tensor with a traceless version

$$Q_{jk} = 3Q'_{jk} - \delta_{jk} \sum_i Q'_{ii}, \quad (4.7)$$

where  $\delta_{jk} = 1$  for  $j = k$  and vanishes otherwise. The second term on the right hand side is independent of the nuclear orientation and can be ignored since a nuclear orientation dependence is necessary in order to observe hyperfine structure or nuclear resonance. Therefore, we now have

$$H_Q = \frac{1}{6} \sum_{jk} Q_{jk} V_{jk}. \quad (4.8)$$

It is possible to further reduce the number of independent components to a single term. As mentioned above, the rapid precession creates a time average distribution cylindrically symmetric about the nuclear spin, along the direction of  $x_3$ . By symmetry, the off-diagonal elements of the quadrupole tensor vanish and  $Q_{11} = Q_{22}$ . But  $Q_{11} + Q_{22} + Q_{33} = 0$ , hence  $Q_{11} = Q_{22} = -Q_{33}/2$ . As a result, the quadrupole moment tensor is expressed in terms of its largest principal component,  $Q_{33}$ .

In quantum mechanical terms, the rapid precession of the nuclear charges about the spin direction means that  $I$  is a “good” quantum number; it is thus a suitable basis. We are interested in constant spin  $I$  since the energy required is too high to change the nuclear spin quantum number. Using the theorem that the matrix elements of traceless, second-rank, symmetric tensors are proportional [86], we have

$$\langle m' | Q_{jk} | m \rangle = C \langle m' | \frac{3}{2} (I_j I_k + I_k I_j) - \delta_{jk} \mathbf{I}^2 | m \rangle, \quad (4.9)$$

where  $C$  is some constant, and  $\mathbf{I}^2 = I_1^2 + I_2^2 + I_3^2$ . The constant  $C$  can be related to the nuclear electric quadrupole moment  $Q$ , which is the expectation value (measured in unit of

proton charge  $e$ ) of  $Q_{33}$  in the state with  $m = I$ . That is,

$$eQ \equiv \langle I | Q_{33} | I \rangle . \quad (4.10)$$

$Q$  has the dimensions of area and is customarily measured in barns ( $10^{-28} \text{ m}^2$ ). The constant

$$C = eQ/I(2I - 1) \quad (4.11)$$

is determined by comparing Eq. (4.9) ( $m = m' = I$ ) and Eq. (4.10). Combining Eqs. (4.8) and (4.9), the Hamiltonian becomes

$$\langle m' | H_Q | m \rangle = \frac{eQ}{6I(2I - 1)} \sum_{jk} \langle m' | \frac{3}{2}(I_j I_k + I_k I_j) - \delta_{jk} \mathbf{I}^2 | m \rangle V_{jk} . \quad (4.12)$$

The nuclear quadrupole moment  $Q$  has a classical equivalent,

$$eQ \equiv \int \rho(\mathbf{x})(3z^2 - r^2)d^3\mathbf{x} . \quad (4.13)$$

This definition highlights the fact that the quadrupole moment measures the departure from the spherical symmetry of the nuclear charge distribution. If  $Q = 0$ , the distribution is in spherical symmetry;  $Q > 0$  if the distribution is elongated along the spin axis like a cigar and  $Q < 0$  if the distribution is flattened like a pancake.

The quadrupole interaction vanishes if the potential  $V$  arises from a spherical or cubic charge distribution. In this situation, the off-diagonal elements of the field gradient tensor are zero and the three diagonal elements are equal,  $V_{xx} = V_{yy} = V_{zz}$ . Then  $H_Q$  in Eq. (4.8) is proportional to the trace of  $Q$  tensor, which vanishes by definition in Eq. (4.7).

Further, the diagonal elements of the gradient tensor also vanish at the center of symmetry. The potential  $V$  satisfies the Laplace equation  $\nabla^2 V = V_{xx} + V_{yy} + V_{zz} = 0$  at the nuclear center since the potential arises from charges other than that of the nucleus; while the three diagonal elements are all equal, accordingly, the only solution is that they are all zero. The Laplace equation implies that the field gradient tensor is also traceless.

In order to conveniently relate it to selection rules, the Hamiltonian may be expressed in terms of raising and lowering operators. Assisted by the Laplace equation ( $\nabla^2 V = 0$ ), we obtain

$$H_Q = \frac{eQ}{4I(2I-1)} [(3I_z^2 - \mathbf{I}^2)V_0 + (I_+ I_z + I_z I_+)V_{-1} + (I_- I_z + I_z I_-)V_1 + I_+^2 V_{-2} + I_-^2 V_2] , \quad (4.14)$$

where

$$\begin{aligned} V_0 &= V_{zz} , \\ V_{\pm 1} &= V_{xz} \pm iV_{yz} , \\ V_{\pm 2} &= \frac{1}{2}(V_{xx} - V_{yy}) \pm iV_{xy} . \end{aligned} \quad (4.15)$$

It is always possible to choose a principal axes system (PAS) where only the diagonal elements of the symmetric field gradient tensor  $V_{ij}$  are nonzero. Moreover, the diagonal elements satisfy the Laplace equation,  $\nabla^2 V = 0$ , and thus only two parameters are needed to characterize the field gradient: the principal field gradient component  $q_{zz}$  and asymmetry



parameter  $\eta$  are defined as

$$\begin{aligned} eq_{zz} &= V_{zz}, \\ \eta &= \frac{V_{xx} - V_{yy}}{V_{zz}}. \end{aligned} \quad (4.16)$$

If we orient the principal axes so that the  $z$  direction has maximum (magnitude) gradient, and the  $x$  direction minimum (also magnitude), then the value of  $\eta$  lies in the range 0 to 1.

The Hamiltonian in the principal axes system thus simplifies to

$$H_Q = \frac{e^2 q Q}{4I(2I - 1)} [(3I_z^2 - \mathbf{I}^2) + \eta(I_x^2 - I_y^2)]. \quad (4.17)$$

#### 4.1.2 Determination of the Field Gradient from NMR Experiments

To use quadrupole nuclei as microscopic probes of the charge distributions and gradients in crystals requires both the experimental measurement and theoretical prediction of the  $q_{zz}$  and  $\eta$  values.

In NMR experiments, we measure the asymmetry parameter  $\eta$ , and the quadrupole coupling constant is (in frequency units)

$$C_Q = \frac{e^2 q_{zz} Q}{h}, \quad (4.18)$$

where  $h$  is Planck's constant. Accordingly, the field gradient is calculated as

$$eq_{zz} = \frac{h C_Q}{e Q} = 4.1357 \times 10^{19} \frac{C_Q [\text{MHz}]}{Q [\text{barn}]} \text{V} \cdot \text{m}^{-2} = 1.3795 \times 10^{13} \frac{C_Q [\text{MHz}]}{Q [\text{barn}]} \text{esu} \cdot \text{cm}^{-3}. \quad (4.19)$$

The ESU equivalence is also provided for convenient conversion from older literature.

For most quadrupole isotopes, the nuclear quadrupole moments  $Q$  are determined by a variety of experiments including, but not limited to, atomic beam, Coulomb excitation reorientation, Laser resonance, muonic X-ray hyperfine structure, NQR, and NMR [98]. These values are well documented [98, 42]; nuclear quadrupole moments for several nuclei are given in Table 4.1.

**Table 4.1:** Quadrupole moments [98, 42].

Nucleus	$Q$ [barn]
$^2\text{H}$	+0.002860(15)
$^6\text{Li}$	-0.00083(8)
$^{17}\text{O}$	-0.02578
$^{23}\text{Na}$	+0.1006(20)
$^{25}\text{Mg}$	+0.201(3)
$^{45}\text{Sc}$	-0.22 (1)
$^{93}\text{Nb}$	-0.32 (2)

However, even if  $Q$  were known exactly, the principle value of the electric field gradient tensor ( $q_{zz}$ ) calculated in Eq. (4.19) is not a direct measure of the field gradient created by the surrounding charges; the field gradient a nucleus experiences is amplified by deformation of its ionic core. The undistorted close shell core has spherical symmetry and thus does not exert a field gradient at the nucleus. It is the  $r^{-3}$  dependence of the gradient ( $r$  is the distance from a charge to the nucleus) that causes the deformed core (very close to the nucleus) to have important effects on the final field gradient experienced by the nucleus [95]. The combined effect of all electrons is described by the *Sternheimer antishielding* factor ( $\gamma_\infty$ );

$$eq = eq_0(1 - \gamma_\infty), \quad (4.20)$$

where  $q_0$  is the field gradient due to charges other than those of the center ion. The factor

is either positive (shielding) or negative (anti-shielding) and can be large (typical values given in Table 4.2).

The Sternheimer anti-shielding factor is difficult to calculate with high accuracy. Values also depend on the states of the same ion (free or in crystal). Several approaches have been applied to calculating the Sternheimer factor; discrepancies in these results are due to both computation details and the initial assumptions. The most recent and complete work for free ions with atomic numbers ranging from 2 to 94 was done in 1995 within the framework of the local density approximation (LDA) [54]. Though not as complete, another work has been performed for around thirty ions in crystals as well as in the free state [90].

**Table 4.2:** Sternheimer factors of ions.

Ion	$\gamma_\infty$ free <sup>a</sup>	$\gamma_\infty$ free <sup>b</sup>	$\gamma_\infty$ crystal <sup>b</sup>
Li <sup>+</sup>	0.262	0.249	0.255
O <sup>2-</sup>	0.0892	–	–13.785
Na <sup>+</sup>	–5.59	–5.261	–5.452
Mg <sup>2+</sup>	–3.76	–3.503	–4.118
Sc <sup>3+</sup>	–13.6	–11.388	–23.104
Rb <sup>+</sup>	–52.3	–47.664	–52.781
Sr <sup>2+</sup>	–40.4	–38.893	–47.828
Y <sup>3+</sup>	–34.8	–31.020	–51.985
Zr <sup>4+</sup>	–31.1	–	–
Nb <sup>5+</sup>	–29.5	–	–49 <sup>c</sup>

<sup>a</sup> Gusev, Reznik, and Tsitrin [54].

<sup>b</sup> Schmidt, Sen, Das and others [90], except for the Nb<sup>5+</sup> entry.

<sup>c</sup> This work, see section 4.1.2.

### 4.1.3 Calculations of Electric Field Gradients

We have described the experimental approach for determining the electric field gradients.

On the other hand, it is also possible to compute the electronic structure and then calculate the EFG, with available crystal structure data. The conventional point-charge-model

approach is based on point-charge embedded in a background charge density that is broken into uniform component [33] and undulating components [57]. The slow convergence of the sum over the point charges is solved by introducing an auxiliary convergence function that separates the original sum into a rapidly converging sum in real space and a rapidly converging sum in the reciprocal space [34]. The polarizability of the core of the center atom is accounted for by the Sternheimer factors.

Another more rigorous approach calculates the EFG by local density approximation (LDA) using an extended general potential Linearized Augmented Plane Wave Method (LAPW) [94]. This includes the core polarization effects in the full potential calculations.

#### 4.1.4 Case Study of Potassium Niobate

The EFG at the niobium site in potassium niobate ( $\text{KNbO}_3$ ) presents itself as an interesting case study. The crystal structure of this ferroelectric material is well studied [112]. It undergoes an orthorhombic to rhombohedral phase transition at  $-50^\circ\text{C}$ . NQR study of  $^{93}\text{Nb}$  shows  $C_Q = 23.1$  MHz and  $\eta = 0.80$  at  $20^\circ\text{C}$  (orthorhombic), and  $C_Q = 16.0$  MHz and  $\eta = 0.0$  at  $-196^\circ\text{C}$  (rhombohedral) [25]. The difference in the asymmetry parameter ( $\eta$ ) values is readily understood by considering the orthorhombic structure to be obtained from the cubic structure by elongation along the face diagonal, and the rhombohedral by elongation along the body diagonal. In the orthorhombic phase, if the principal  $z$ -axis of the EFG tensor is chosen to be orthogonal to the rhombohedral face, then inequivalent  $x$ - and  $y$ -axes result in a non-zero asymmetry parameter  $\eta$ ; for the rhombohedral phase, if the  $z$ -axis is chosen to be the body diagonal, then the  $x$ - and  $y$ -axes are equivalent and result in a zero asymmetry parameter,  $\eta = 0$ .

Using conversion factors [Eq. (4.19)] and the measured quadrupole moment  $Q = -0.32$  barn, the field gradient is  $eq_{zz} = 2.99 \times 10^{21}$  V/m<sup>2</sup> at 20 °C. A simple point-charge-model calculation yields  $q_0 = 6 \times 10^{19}$  V/m<sup>2</sup> [25]. Since  $\gamma_\infty$  has not been specifically calculated for niobium in crystal state, taking  $\gamma_\infty = -29.5$  for the free Nb<sup>5+</sup> ion yields  $eq_{zz} = 1.8 \times 10^{21}$  V/m<sup>2</sup> [Eq. (4.20)]. Thus calculation predicts the same order of magnitude as the experimental value, but with large error. However, the  $\gamma_\infty$  values in a crystal are very different from those of a free ion. We may estimate  $\gamma_\infty$  in crystal from the data available; substitution  $eq_{zz} = 2.99 \times 10^{21}$  V/m<sup>2</sup> and  $eq_0 = 6 \times 10^{19}$  V/m<sup>2</sup> into Eq. (4.20) gives  $\gamma_\infty = -49$  for Nb<sup>5+</sup> in crystal. This value is very reasonable if we compare values for elements in the same period Rb<sup>+</sup>, Sr<sup>2+</sup>, and Y<sup>3+</sup> (see the last column of Table 4.2).

At the lower temperature of  $-196^\circ$ , the gradient is  $eq_{zz} = 2.07 \times 10^{21}$  V/m<sup>2</sup>. A recent LDA LAPW calculation for this phase gives  $eq_{zz} = 2.9 \times 10^{21}$  V/m<sup>2</sup> [94], the agreement is good but could be better.

## 4.2 Perturbation Expansion of Energy Levels and Transition Frequencies

The Hamiltonian for Zeeman and quadrupole interactions is

$$H = H_z + H_Q. \quad (4.21)$$

In a strong magnetic field,  $|H_z| \gg |H_Q|$  and we may treat the quadrupole interaction as a perturbation to the Zeeman energy levels. With the quadrupole frequency defined as

$$\nu_Q \equiv \frac{3C_Q}{2I(2I-1)}, \quad (4.22)$$

the first and second order perturbation corrections to the energy levels are [23],

$$\begin{aligned}
 E_m^{(1)} &= h(\nu_Q/6)f_0[3m^2 - I(I+1)], \\
 E_m^{(2)} &= -h(\nu_Q^2/12\nu_L)m\{f_{+1}^L f_{-1}^L[4I(I+1) - 8m^2 - 1] \\
 &\quad + f_{+2}^L f_{-2}^L[2I(I+1) - 2m^2 - 1]\},
 \end{aligned} \tag{4.23}$$

with the dimensionless field gradients expressed in terms of second rank irreducible spherical tensor components in the laboratory frame,

$$\begin{aligned}
 f_0^L &= (1/eq)V_0, \\
 f_{\pm 1}^L &= \mp(1/eq)\sqrt{\frac{2}{3}}V_{\pm 1}, \\
 f_{\pm 2}^L &= (1/eq)\sqrt{\frac{2}{3}}V_{\pm 2}.
 \end{aligned} \tag{4.24}$$

In the PAS system, the corresponding tensor components have the simplest form

$$\begin{aligned}
 f_0^P &= 1, \\
 f_{\pm 1}^P &= 0, \\
 f_{\pm 2}^P &= \eta/\sqrt{6}.
 \end{aligned} \tag{4.25}$$

The components in the principal (P) axis system are conveniently transformed into the laboratory (L) system by Wigner rotation matrices (see Appendix A) through Euler angles

$$\Omega_{PL} = (\alpha_{PL}, \beta_{PL}, \gamma_{PL}),$$

$$f_m^L = \sum_{m'=-2}^2 D_{m'm}^2(\Omega_{PL})f_{m'}^P. \tag{4.26}$$

The  $f_{+1}^L f_{-1}^L$  and  $f_{+2}^L f_{-2}^L$  terms are products of Wigner matrices and therefore can be

written as a linear arrangement of Wigner matrices (up to order 4) [6],

$$E_m^{(2)} = -h(\nu_Q^2/9\nu_L) \sum_{n=0}^2 \sum_{i=-n}^n C_{2n}(m, I) B_{2i}^{2n}(\eta) D_{2i,0}^{2n}(\alpha_{PL}, \beta_{PL}, \gamma_{PL}) \quad (4.27)$$

with

$$C_0(m, I) = 2m[I(I+1) - 3m^2], \quad C_2(m, I) = 2m[8I(I+1) - 12m^2 - 3],$$

$$C_4(m, I) = 2m[18I(I+1) - 34m^2 - 5],$$

$$B_0^0 = -(3 + \eta^2)/20, \quad B_0^2 = (\eta^2 - 3)/56, \quad B_{\pm 2}^2 = \sqrt{6}\eta/56,$$

$$B_0^4 = (18 + \eta^2)/560, \quad B_{\pm 2}^4 = 3\sqrt{10}\eta/560, \quad B_{\pm 4}^4 = \sqrt{70}\eta^2/1120.$$

Since the second subscript of the Wigner matrix element is zero, the energy levels do not depend on the angle  $\gamma_{PL}$ . The angles  $(\beta_{PL}, \alpha_{PL})$  are the polar and azimuthal angles defining the orientation of the external magnetic field  $\mathbf{B}_0$  in the PAS.

## 4.3 Quadrupole Spectra of Polycrystalline Materials

### 4.3.1 First Order Static Powder Patterns

When observed in the laboratory frame, the frequency arising from quadrupole interaction depends on crystal orientation. For the first order quadrupole effect,  $f_0^L$  is calculated as [see Eq. (4.26)]

$$f_0^L = \frac{3 \cos^2 \beta_{PL} - 1 + \eta \sin^2 \beta_{PL} \cos 2\alpha_{PL}}{2}. \quad (4.28)$$

By Eq. (4.23) the frequency of transition  $m \leftrightarrow m - 1$  is (where the subscripts on the Euler angles have been omitted for clarity)

$$\nu_m^{(1)} = -\nu_Q \frac{3 \cos^2 \beta - 1 + \eta \sin^2 \beta \cos 2\alpha}{2} (m - 1/2). \quad (4.29)$$

Powder integration over the unit sphere yields the characteristic first order quadrupole lineshape shown in Fig. 4.1.

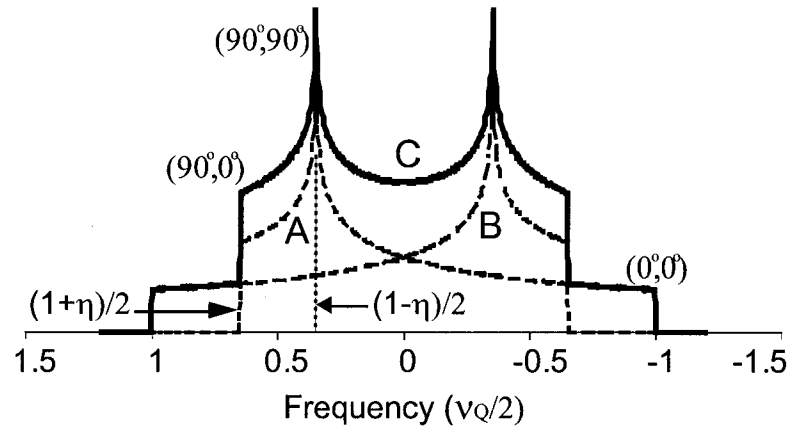


**Figure 4.1:** Static powder pattern of first order quadrupole interaction for spin  $I = 1$  nuclei, simulated with  $\eta = 0.3$ . Line A arises from transition  $1 \leftrightarrow 0$ ; while B arises from  $0 \leftrightarrow -1$ ; the overall lineshape C (solid line) is the sum of A and B. Frequency is in unit of  $\nu_Q/2$ . The discontinuities of the lineshape are labeled with their corresponding values of  $(\beta, \alpha)$ , which are the polar and azimuthal angles describing the orientation of the external  $\mathbf{B}_0$  field in principal axes system. The frequencies of the three discontinuities are  $(1 + \eta)/2$  for the point  $(90^\circ, 0^\circ)$ ,  $(1 - \eta)/2$  for  $(90^\circ, 90^\circ)$ , and  $-1$  for  $(0^\circ, 0^\circ)$ .

### 4.3.2 Second Order Static Powder Patterns

For a half-integer spin quadrupolar nucleus, a symmetric transition  $m \leftrightarrow -m$  is free of the first order quadrupole effect because of the  $3m^2 - I(I+1)$  spin dependence of the energy  $E_m^{(1)}$  [Eq. (4.23)]; only the second order effect needs to be considered. From the  $E_m^{(2)}$  expression



in Eq. (4.27), the central transition ( $1/2 \leftrightarrow -1/2$ ) frequency can be expressed as

$$\nu_{1/2}^{(2)} = (\nu_Q^2/9\nu_L)C_0(1/2, I) \left[ -\frac{3 + \eta^2}{10} + G(\alpha, \beta) \right], \quad (4.30)$$

with

$$\begin{aligned} G(\alpha, \beta) = & \frac{1}{160} [(138 - 19\eta^2 + 60\eta \cos 2\alpha + 45\eta^2 \cos 4\alpha) \\ & + (-900 + 30\eta^2 + 480\eta \cos 2\alpha - 90\eta^2 \cos 4\alpha) \cos^2 \beta \\ & + (810 + 45\eta^2 - 540\eta \cos 2\alpha + 45\eta^2 \cos 4\alpha) \cos^4 \beta]. \end{aligned}$$

Function  $G(\alpha, \beta)$  averages to zero (over all orientations), and the bary center (center of mass/gravity) of the lineshape is

$$\nu_{1/2}^{(2)} = -(\nu_Q^2/9\nu_L)C_0(1/2, I) \frac{3 + \eta^2}{10}. \quad (4.31)$$

The maximum and minimum frequencies are

$$\begin{aligned} \nu_{\min} &= -(\nu_Q^2/9\nu_L)C_0(1/2, I)(1 + \eta), \\ \nu_{\max} &= -(\nu_Q^2/9\nu_L)C_0(1/2, I) \frac{(3 + \eta)^2}{16}. \end{aligned} \quad (4.32)$$

Thus the frequencies span the range

$$\Delta = (\nu_Q^2/9\nu_L)C_0(1/2, I) \frac{\eta^2 + 22\eta + 25}{16}. \quad (4.33)$$

Powder integration over the unit sphere yields the lineshapes shown in Fig. 4.2.

### 4.3.3 Second Order Powder Patterns of Rotating Samples

If the sample spins with angular speed  $\omega_R$  around an axis tilted from the static magnetic field ( $\mathbf{B}_0$ ) by  $\theta$ , the dimensionless field gradient is obtained by first transforming from

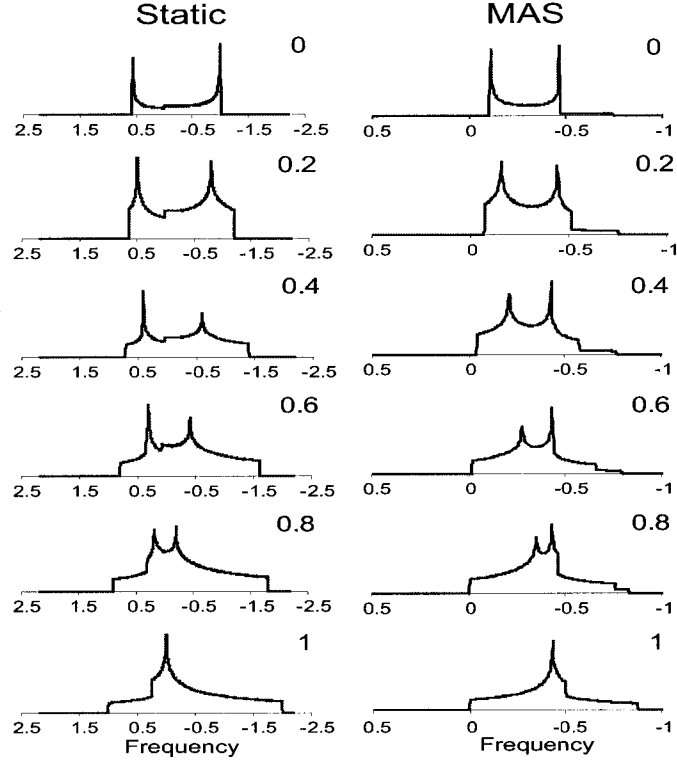


**Figure 4.2:** The central transition powder patterns of second order quadrupole interaction, with asymmetry parameter values  $\eta = 0, 0.2, 0.4, 0.6, 0.8$  and  $1$ . Frequency is normalized in unit of  $(\nu_Q^2/9\nu_L)C_0(1/2, I)$ . Left column: static spectra; right column: magic-angle spinning spectra. Note the scales differ by a factor of 3.3.

the principal (P) to rotor (R) fixed axes, defined by Euler angles  $\Omega_{PR} = (\alpha_{PR}, \beta_{PR}, \gamma_{PR})$ , followed by transforming from the rotor fixed to laboratory (L) fixed axes with Euler angles  $\Omega_{RL} = (\omega_R t, \theta, \gamma)$ . The energy is independent of  $\gamma$ , so  $\gamma$  can be set to zero without loss of generality. (We have seen in the end of section 4.2 that for static samples, the second order energy contribution is independent on  $\gamma_{PL}$ .) The energy becomes

$$E_m^{(2)} = -h(\nu_Q^2/9\nu_L) \sum_{n=0}^2 \sum_{i=-n}^n \sum_{j=-n}^n C_{2n}(m, I) B_{2i}^{2n}(\eta) D_{2i,j}^{2n}(\alpha_{PR}, \beta_{PR}, \gamma_{PR}) D_{j,0}^{2n}(\omega_R t, \theta, 0) \quad (4.34)$$

In the infinite spinning speed limit, the spinning sidebands disappear; thus only the  $j = 0$  term survives,

$$E_m^{(2)} = -h(\nu_Q^2/9\nu_L) \{ C_0 B_0^0 + [B_0^2 d_{00}^2(\beta_{\text{PR}}) + 2B_2^2 d_{20}^2(\beta_{\text{PR}}) \cos(2\alpha_{\text{PR}})] C_2 d_{00}^2(\theta) \\ + [B_0^4 d_{00}^4(\beta_{\text{PR}}) + 2B_2^4 d_{20}^4(\beta_{\text{PR}}) \cos(2\alpha_{\text{PR}}) + 2B_4^4 d_{40}^4(\beta_{\text{PR}}) \cos(4\alpha_{\text{PR}})] C_4 d_{00}^4(\theta) \} , \quad (4.35)$$

where  $d_{ij}^n$  are the reduced Wigner matrix elements (see Appendix A).

If the angle is chosen such that  $\theta = \theta_M = \arccos(1/\sqrt{3})$ , the “magic angle”, then  $d_{00}^2(\theta_M) = 0$  and the contribution from the second term vanishes; on the other hand,  $d_{00}^4(\theta_M) = -7/18$  and therefore the third term is scaled by a factor of 7/18. Finally, the second order energy levels are,

$$E_m^{(2)} = -(\nu_Q^2/9\nu_L) \left[ -C_0(m, I) \frac{3 + \eta^2}{20} + C_4(m, I) F(\alpha, \beta) \right] , \quad (4.36)$$

with

$$F(\alpha, \beta) = \frac{1}{11520} [(-54 - 3\eta^2 + 60\eta \cos 2\alpha - 35\eta^2 \cos 4\alpha) \\ + (540 + 30\eta^2 - 480\eta \cos 2\alpha + 70\eta^2 \cos 4\alpha) \cos^2 \beta \\ + (-630 - 35\eta^2 + 420\eta \cos 2\alpha - 35\eta^2 \cos 4\alpha) \cos^4 \beta] ,$$

where the subscripts PR on the Euler angles have been omitted for clarity. For half integer quadrupolar nuclei ( $I > 1/2$ ), the central transition ( $1/2 \leftrightarrow -1/2$ ) frequency is

$$\nu_{1/2}^{(2)} = (\nu_Q^2/9\nu_L) C_0(1/2, I) \left[ -\frac{3 + \eta^2}{10} + 36F(\alpha, \beta) \right] , \quad (4.37)$$

where, the equality  $C_4(1/2, I) = 18C_0(1/2, I)$  has been used to simplify the expression. The function  $F(\alpha, \beta)$  averages to zero, therefore, the bary center of the lineshape is the same as

that of the static powder pattern [see Eq. (4.31)]. The minimum and maximum frequencies are given by

$$\begin{aligned}\nu_{\min} &= -(\nu_Q^2/9\nu_L)C_0(1/2, I)\frac{6+\eta^2}{8}, \\ \nu_{\max} &= -(\nu_Q^2/9\nu_L)C_0(1/2, I)\frac{3(1-\eta)^2}{28}.\end{aligned}\quad (4.38)$$

The frequencies span the range

$$\Delta = (\nu_Q^2/9\nu_L)C_0(1/2, I)\frac{(\eta+6)^2}{56}.\quad (4.39)$$

Comparing this to Eq. (4.33), we find the MAS spectrum is 2.43 ( $\eta = 0$ ) to 3.43 ( $\eta = 1$ ) times narrower than the static spectrum.

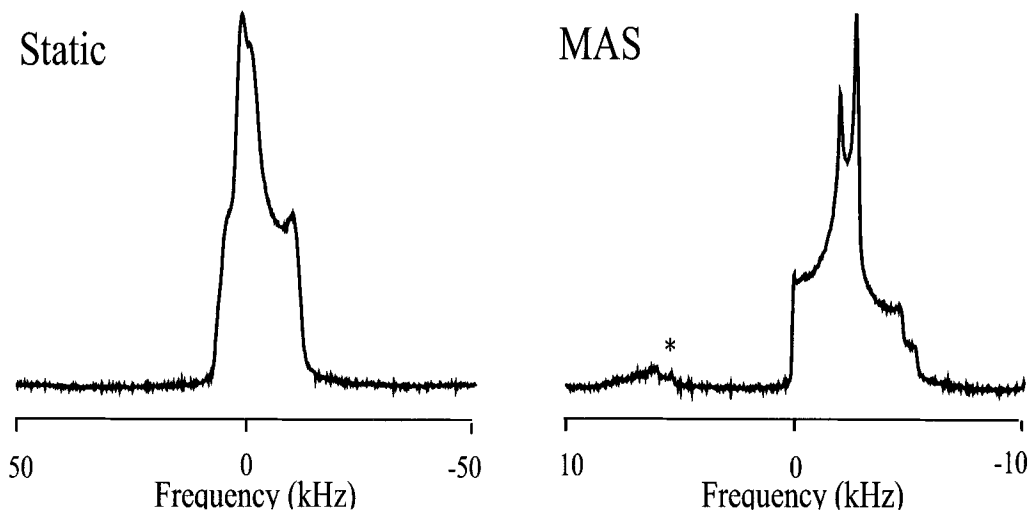


**Figure 4.3:**  $^{23}\text{Na}$  static and MAS spectra of sodium oxalate at 7 Tesla.  $^{23}\text{Na}$  resonance is at 79.374 MHz, aqueous NaCl was used as chemical shift reference, RF strength  $\nu_1=100$  kHz, pulse duration  $1.25 \mu\text{s}$ , recycle delay 10 s, 500 scans. The sample was spinning at 8 kHz, spinning sideband is marked by star.

Powder integration over the unit sphere yields the lineshapes shown in the right column

of Fig. 4.2. Experimental static and MAS  $^{23}\text{Na}$  spectra of sodium oxalate ( $\text{Na}_2\text{C}_2\text{O}_4$ ) are shown in Fig. 4.3.

#### 4.3.4 Characteristic Points of Powder Lineshapes

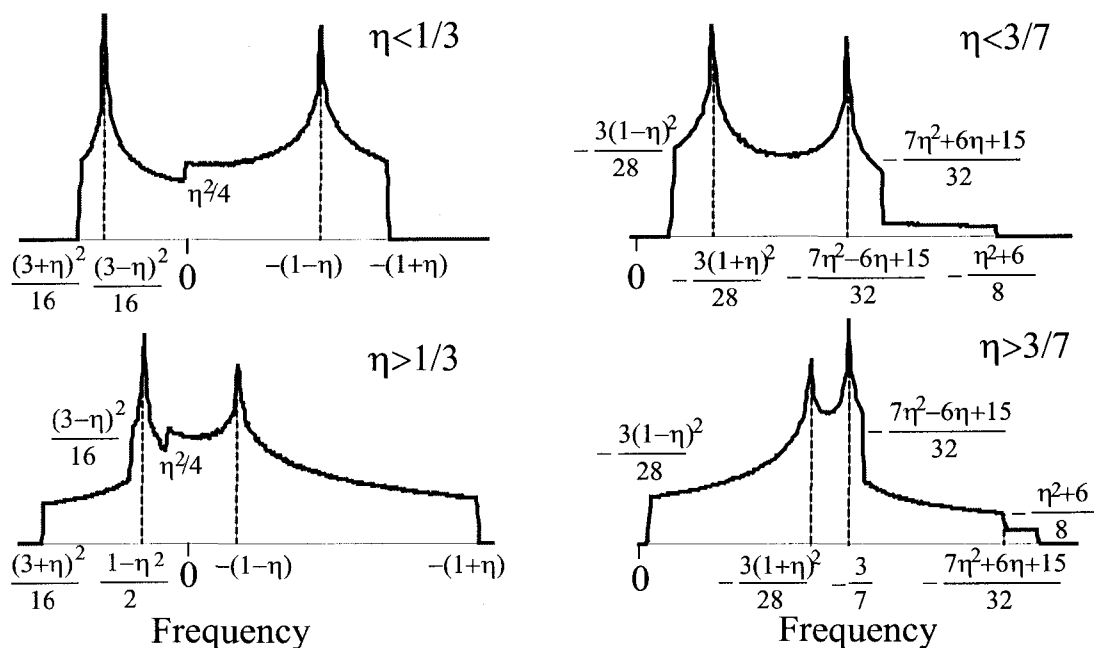


**Figure 4.4:** The shoulders and singularities in central transition powder patterns of second order quadrupole interaction. Frequency is in unit of  $(\nu_Q^2/9\nu_L)C_0(1/2, I)$ . Left: static; right: MAS.

All the frequency functions given in Eqs. (4.29), (4.30), and (4.37) depend explicitly on the orientation variables  $(\beta, \alpha)$ , succinctly  $\nu = \nu(\mu, \alpha)$  with  $\mu \equiv \cos \beta$ . In the neighborhood of an extrema, i.e., a certain point  $(\mu_i, \alpha_i)$  where

$$\left. \frac{\partial \nu}{\partial \mu} \right|_{(\mu_i, \alpha_i)} = \left. \frac{\partial \nu}{\partial \alpha} \right|_{(\mu_i, \alpha_i)} = 0, \quad (4.40)$$

the frequency-orientation surface is very flat. This means that a very large area of  $(\mu, \alpha)$

contributes to a very narrow range of frequencies. Therefore, at this frequency  $\nu(\mu_i, \alpha_i)$  the spectrum shows a discontinuity; either a shoulder or a peak. Furthermore, if  $(\mu_i, \alpha_i)$  is a minimum (or maximum), then the lineshape has a shoulder at  $\nu(\mu_i, \alpha_i)$ ; if a saddle point, the lineshape displays a peak (singularity).

For the first order quadrupole lineshape, the three critical points are indicated as  $(\beta, \alpha)$  orientations  $(90^\circ, 90^\circ)$ ,  $(0^\circ, 0^\circ)$ , and  $(90^\circ, 0^\circ)$  in Fig. 4.1. For the second order quadrupole lineshapes of both static and spinning samples, these critical points are shown in Fig. 4.4. If the asymmetry parameter  $\eta < \eta_0$ , there are five characteristic shoulders and singularities, otherwise there are six. The critical values are  $\eta_0 = 1/3$  for a static pattern, and  $\eta = 3/7$  for a MAS pattern.

The characteristic discontinuities can be used to extract NMR parameters from experimental spectra. Theoretically, only three points are required to solve for the three parameters: isotropic chemical shift  $\delta_{\text{iso}}^{\text{CS}}$ , quadrupole coupling constant  $C_Q$ , and the asymmetry parameter  $\eta$ . However, if more points can be identified, the average values and error estimation can be obtained from several sets of solutions. Usually the (negative) second order derivative spectra (SODS) have better sensitivity to these characteristic singularities. A peak in a normal spectra appears as a much narrower peak in SODS, and a shoulder appears as a zero-crossing point. SODS are particularly useful if the spectra are broadened. The  $^{23}\text{Na}$  MAS spectrum of sodium oxalate is shown in Fig. 4.5, five characteristic points are matched (marked by small circles) to give parameter values;  $C_Q = 2.52(0.02)$  MHz,  $\eta = 0.74(0.03)$ ,  $\delta_{\text{iso}}^{\text{CS}} = 2.0(0.5)$  ppm. A MAS spectrum, simulated using these average parameters and then apodized with 60 Hz lorentzian broadening, matches the experimental spectrum very well. These parameters agree well with the literature values  $\delta_{\text{iso}}^{\text{CS}} = 1$  ppm,

$C_Q = 2.6(0.1)$  MHz,  $\eta = 0.7(0.1)$  [76] and  $C_Q = 2.43$  MHz,  $\eta = 0.77$  [115].

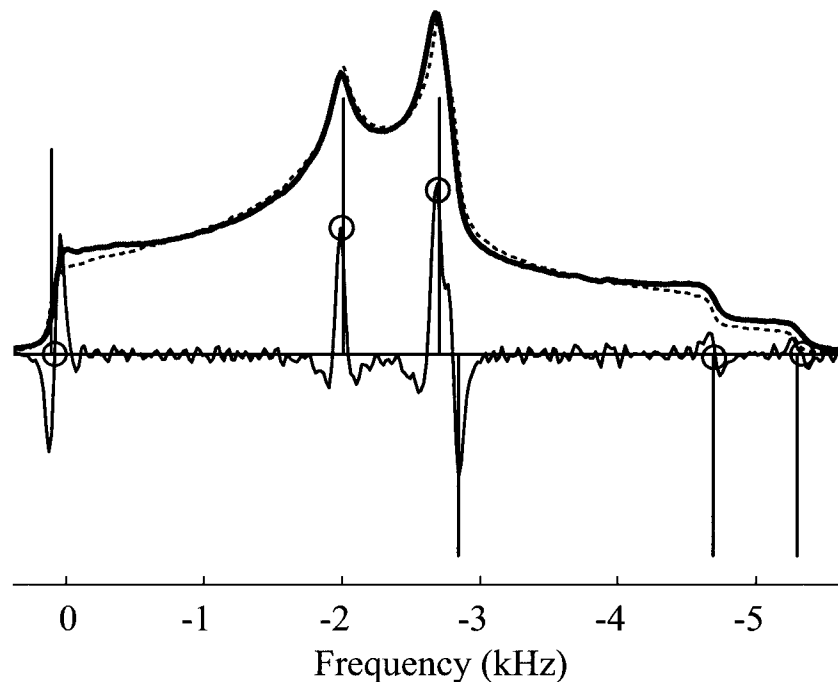


**Figure 4.5:** Extracting NMR parameters from MAS spectrum. The experimental  $^{23}\text{Na}$  MAS spectrum of sodium oxalate (bold solid line, see experimental conditions in Fig. 4.3) is compared to the simulated one (dotted line) with parameters determined from matching the four characteristic points (marked by circle). The (negative) second derivative of experimental spectrum (solid thin line) helps to determine the characteristic points more accurately. The “sticks” mark the characteristic points of simulated spectrum. The analysis is performed with a custom Matlab GUI *lineshape2quad*.

#### 4.4 The Quest to Remove Anisotropy

For the central transition of a half-integer quadrupolar nucleus, second order anisotropy broadens the resonance lines. Many experiments have been designed to remove this anisotropy and to achieve higher resolution.

The crystal-orientation dependent frequencies (or energy levels) contain  $d_{00}^2(\theta)$  and

$d_{00}^4(\theta)$  terms [see Eq. (4.35)]. There is no angle  $\theta$  that eliminates both terms simultaneously ( $54.74^\circ$  for  $d_{00}^2(\theta) = 0$ ;  $30.56^\circ$  or  $70.12^\circ$  for  $d_{00}^4(\theta) = 0$ ); this means spinning the sample at a single fixed axis can never completely eliminate the second order quadrupolar anisotropy.

To solve this problem, double rotation (DOR) [88] and dynamic-angle spinning (DAS) [69, 77] were introduced in 1988. The DOR spinner module consists of two rotors: the large outer rotor (20 mm diameter) at  $54.7^\circ$  with  $\mathbf{B}_0$  spins slowly (e.g. 400 Hz), and the small inner rotor (5 mm diameter) at  $30.6^\circ$  with  $\mathbf{B}_0$  spins fast (e.g. 2000 Hz). Both orientational dependent terms are averaged out under these double rotation conditions. The DAS rotor spins  $N$  rotor cycles at  $\theta_1 = 37.38^\circ$  and then  $N$  cycles at  $\theta_2 = 79.19^\circ$ . Since the two angles fulfill the conditions  $d_{00}^2(\theta_1) = -d_{00}^2(\theta_2)$ , and  $d_{00}^4(\theta_1) = -d_{00}^4(\theta_2)$  the two terms cancel.

However, both DOR and DAS have limitations besides the challenge and cost in building such special, intricate probes. In DOR, the spinning speed of the outer rotor is limited to about 1 kHz and as a result the many spinning sidebands obscure the interpretation of spectra. In a DAS experiments, during the time ( $\sim 36$  ms) required for switching the spinner axis, the magnetization is stored along the static field  $\mathbf{B}_0$  to quench its evolution. The finite switching time makes DAS unsuitable for species having fast spin-lattice relaxation ( $T_1 < 100$  ms).

In 1993, variable angle spinning (VAST) was proposed to completely remove the anisotropy for spin  $I = 3/2$  nuclei [6]. VAST makes use of the unique  $C_2(3/2, 3/2) = 0$  to eliminate the  $d_{00}^2$  term by choosing the  $+3/2 \leftrightarrow -3/2$  transition, and of  $d_{00}^4(70.12^\circ) = 0$  to eliminate the term by setting the spinner axis at  $70.12^\circ$ . In addition to the removal of anisotropy, the chemical shift separation is tripled (compared to the central transition). The triple-



quantum transition is directly excited by a strong RF pulse at  $3\nu_L$  and then observed at this “overtone” frequency.

The application of the VAST method is obviously limited by the requirement  $I = 3/2$ , since only for this spin  $C_2(3/2, 3/2) = 0$ . Moreover, spinning the sample at an angle other than the magic-angle preserves the broadening arising from chemical shift anisotropy and dipolar interactions. Therefore, this method is only useful to  $I = 3/2$  nuclei experiencing small CSA and dipolar interactions.

In 1995, Frydman and Harwood proposed multi-quantum magic angle spinning (MQMAS), an experiment which can be performed in conventional MAS probes [44, 76]. MQMAS completely removes the anisotropy in the indirect dimension. The central idea is to eliminate phase accumulation of the  $d_{00}^4$  term by correlating the multi-quantum (MQ) coherence ( $m \leftrightarrow -m$ ) in the evolution period with the single-coherence ( $+1/2 \leftrightarrow -1/2$ ) in the detection period. Spinning at the magic-angle eliminates the  $d_{00}^2$  term.

MQMAS presents a new horizon to NMR spectroscopists: the half-integer quadrupolar nuclei, which occupy two-thirds of the periodic table, are now routinely accessible. Great efforts have been made to achieve pure absorption mode and high sensitivity. The quest for pure absorption mode has spawned whole-echo detection, split- $t_1$ , and z-filter [73, 14, 5]; high sensitivity methods include optimization of the strength and duration of RF pulses [4], the rotation-induced adiabatic coherence transfer pulse sequence (RIACT) [113], rotor synchronized detection in the indirect dimension [72, 3], double frequency sweeps (DFS) [64], fast amplitude modulation of the pulses (FAM) [104, 70, 71, 50] and the so called “fast spinning gives transfer enhancement at rotary resonance” (FASTER) [105].

In 2000, satellite transition MAS (STMAS) was proposed by Gan [46]. STMAS is similar

in concept to MQMAS, but the MQ coherence in MQMAS is replaced by the excitation of one satellite transition (ST). The ST excitation efficiency is higher than MQ excitation efficiency, and consequently higher sensitivity is expected. However, STMAS is “dirtier” than MQMAS for four reasons. Firstly, in MQMAS, the effect of the first order quadrupole interaction is completely suppressed by choosing a symmetric coherence pathway; in STMAS this effect is suppressed only by spinning at the magic-angle. Therefore, a tiny misset in the magic-angle allows a large first order effect to leak through. Secondly, for very large quadrupole coupling constants, STMAS is affected by the third order quadrupole effect. Thirdly, in practice a long ( 40  $\mu$ s) soft pulse is applied to saturate the central transition (CT) before the STMAS sequence. However, the saturation does not always work perfectly and this results in a CT-CT diagonal ridge that interferes with the ST-CT correlation signal. Finally, for spin  $I > 3/2$  there are several satellite transitions ( $5/2 \leftrightarrow 3/2$ ,  $3/2 \leftrightarrow 1/2$  for  $I = 5/2$ ), and their coexistence complicates the spectra and analysis.

In conclusion, MQMAS appears at present to be the superior method when working with half-integer quadrupole nuclei.

## 4.5 Prototype Experiment and Theory of MQMAS

### 4.5.1 Prototype Experiment

A prototype MQMAS pulse sequence involves the application of two RF pulses (Fig. 4.6). Multi-quantum (MQ) coherence of order  $p$  (of the symmetric transition  $m \leftrightarrow -m$ ,  $p = -2m$ ) and single-quantum coherence of order  $-1$  (of the transition  $1/2 \leftrightarrow -1/2$ ) are selected in the evolution period  $t_1$  and detection period  $t_2$ , using appropriate phase cycling (the rules

of choosing a coherence pathway and examples for MQMAS sequences can be found in Appendix B). For a FID with given  $t_1$ , an echo forms at  $t_2 = Kt_1$ , where  $K$  is a constant determined by the quantum numbers  $m$  and  $I$  of the nuclei. Two-dimensional time domain data is obtained by acquiring a number of one-dimensional FIDs in which the evolution time  $t_1$  is incremented by  $\Delta t_1$ . The two-dimensional frequency spectra are obtained by double Fourier transformation; first along the directly detected dimension ( $t_2 \rightarrow \nu_2$ ) and then along the indirectly detected dimension ( $t_1 \rightarrow \nu_1$ ). This is shown schematically in Fig. 4.7 (A→B→E). However, we will see shortly that a shearing transformation is usually inserted between the two Fourier transformations, (see A→B→C→D Fig. 4.7).

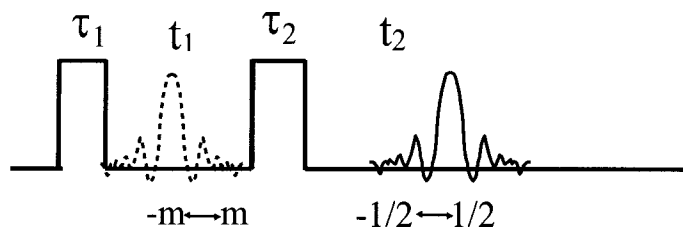


**Figure 4.6:** A prototype two pulse MQMAS sequence. Echo signal (solid line) and/or anti-echo signal (dotted line) form when the appropriate coherence pathway is chosen.

#### 4.5.2 Frequency Formulas and Shear Transformation

Under MAS conditions, the frequency of the symmetric ( $m \leftrightarrow -m$ ) transition is [see Eq. (4.36)]

$$\nu_m = 2m\nu_L\delta_{\text{iso}}^{\text{CS}} + (2\nu_Q^2/9\nu_L) \left[ -C_0(m, I)\frac{3+\eta^2}{20} + C_4(m, I)F(\alpha, \beta) \right], \quad (4.41)$$

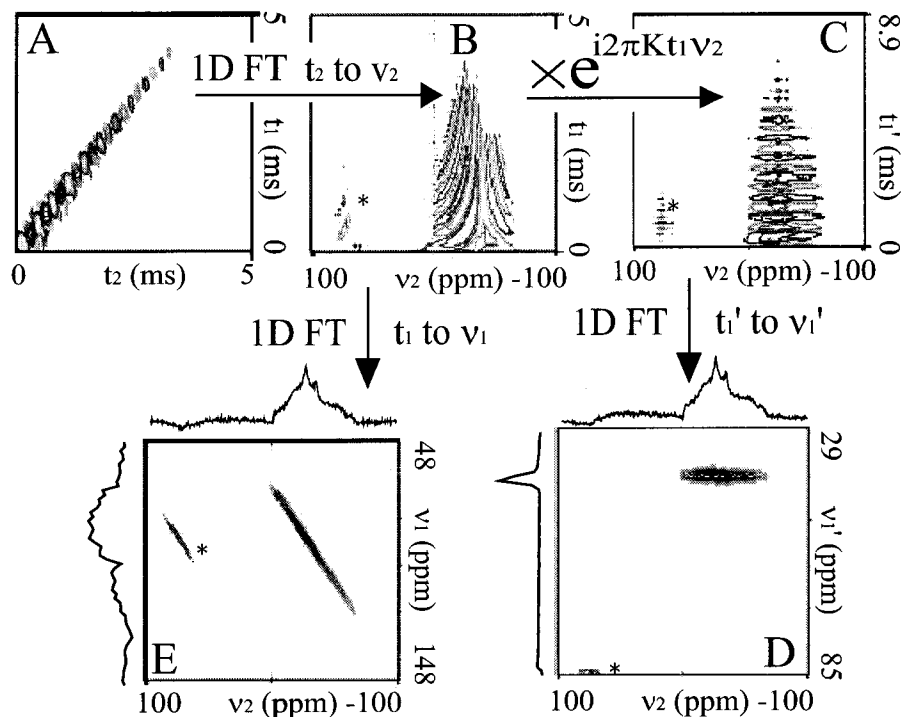


**Figure 4.7:** MQMAS spectral processing. (A) 3QMAS time domain signal of  $^{23}\text{Na}$  in  $\text{Na}_2\text{C}_2\text{O}_4$  at 7 Tesla. Prototype 2-pulse sequence is used with  $-3 \rightarrow -1$  coherence pathway. RF strength  $\nu_1 = 89$  kHz, pulse widths  $\tau_1 = 8 \mu\text{s}$ ,  $\tau_2 = 1.8 \mu\text{s}$ , full sweep widths  $sw_2 = 16$  kHz,  $sw_1 = 8$  kHz, spinning speed 8 kHz, recycle delay 2 s, 480 scans for each 1D FID. (B) 1D FT in direct dimension of signal A; the result is called an interferogram. (C) Shear transformation. (D) 1D FT in indirect dimension; spectrum is shown with projections along each axis. Vertical axis is rescaled in C and D as a result of shear transformation. Vertical dimension of D and E is adjusted by adding their respective full sweep widths ( $sw_1$  and  $sw_1'$ ) to account for the frequency aliasing. Spinning sideband is marked by star.

where  $\delta_{\text{iso}}^{\text{CS}}$  is the isotropic chemical shift. Expressed in ppm with respect to the Larmor frequency, it becomes

$$\begin{aligned}
 \delta_m &= 2m\delta_{\text{iso}}^{\text{CS}} + \frac{2 \times 10^6 \nu_Q^2}{9\nu_L^2} \left[ -C_0(m, I) \frac{3 + \eta^2}{20} + C_4(m, I) F(\alpha, \beta) \right] \\
 &= 2m\delta_{\text{iso}}^{\text{CS}} - AP_Q^2 \left[ \frac{C_0(m, I)}{C_0(1/2, I)} - \frac{C_4(m, I)}{C_4(1/2, I)} \cdot \frac{360F(\alpha, \beta)}{3 + \eta^2} \right] \\
 &= 2m\delta_{\text{iso}}^{\text{CS}} + K_{\text{Sym}0} \delta_{\text{iso}}^{2Q} + K_{\text{Sym}4} \delta_{\text{aniso}}^{2Q}, \quad (4.42)
 \end{aligned}$$

with

$$A = \frac{3 \times 10^5 C_0(1/2, I)}{[2I(2I - 1)]^2 \nu_L^2}, \quad P_Q = C_Q \sqrt{1 + \eta^2/3}, \quad \delta_{\text{iso}}^{2Q} = -AP_Q^2,$$

$$\delta_{\text{aniso}}^{2Q} = AP_Q^2 \frac{360F(\alpha, \beta)}{3 + \eta^2}, \quad K_{\text{Sym}0} = \frac{C_0(m, I)}{C_0(1/2, I)}, \quad K_{\text{Sym}4} = \frac{C_4(m, I)}{C_4(1/2, I)}.$$

The quantity  $P_Q$  is called the quadrupole product.  $C_0, C_2, C_4, K_{\text{Sym}0}, K_{\text{Sym}4}$  and several other relevant variables are compiled in Table 4.3 for spin  $I = 3/2, 5/2, 7/2$  and  $9/2$ . For the central ( $+1/2 \leftrightarrow -1/2$ ) transition,  $K_{\text{Sym}0} = K_{\text{Sym}4} = 1$  and the frequency is simply

$$\delta_{1/2} = \delta_{\text{iso}}^{\text{CS}} + \delta_{\text{iso}}^{2Q} + \delta_{\text{aniso}}^{2Q}. \quad (4.43)$$

The signal may be expressed as

$$S(t_1, t_2) = S_0 e^{(i\omega_m - R_1)t_1} e^{(i\omega_{1/2} - R_2)t_2}, \quad (4.44)$$

where  $S_0$  is a quantity related to spin populations and the efficiency of the pulse sequence,  $\omega_m = 2\pi\nu_m$  and  $\omega_{1/2} = 2\pi\nu_{1/2}$ , with  $R_1$  and  $R_2$  as phenomenological relaxation rates. The phase is

$$\phi(t_1, t_2) = \omega_m t_1 + \omega_{1/2} t_2. \quad (4.45)$$

At  $t_2^e = -K_{\text{Sym}4} t_1$  the phase is independent of  $\delta_{\text{aniso}}^{2Q}$ . All spins are in-phase at this moment and an echo forms. For convenience, we define

$$K = -K_{\text{Sym}4},$$

$$k = |K|, \quad (4.46)$$

**Table 4.3:** Essential coefficients of MQMAS and STMAS.

$m$	$C_0^a$	$C_2^a$	$C_4^a$	$K_{\text{Sym}0}^b$	$K_{\text{Sym}4}^b$	$K_{\text{iso}}^{\text{CS}c}$	$K_{\text{iso}}^{2Qc}$	$K_{\text{Sat}0}^d$	$K_{\text{Sat}4}^d$
$I = 3/2$									
1/2	3	24	54	1	1	0	0	1	1
3/2	-9	0	-42	-3	-7/9	17/8	-5/4	-2	-8/9
$I = 5/2$									
1/2	8	64	144	1	1	0	0	1	1
3/2	6	120	228	3/4	19/12	17/31	-10/31	-1/8	7/24
5/2	-50	-40	-300	-25/4	-25/12	85/37	-50/37	-7/2	-11/6
$I = 7/2$									
1/2	15	120	270	1	1	0	0	1	1
3/2	27	288	606	9/5	101/45	17/73	-10/73	2/5	28/45
5/2	-15	240	330	-1	11/9	17/10	-1	-7/5	-23/45
7/2	-147	-168	-966	-49/5	-161/45	238/103	-140/103	-22/5	-12/5
$I = 9/2$									
1/2	24	192	432	1	1	0	0	1	1
3/2	54	504	1092	9/4	91/36	17/127	-10/127	5/8	55/72
5/2	30	600	1140	5/4	95/36	85/131	-50/131	-1/2	1/18
7/2	-84	336	168	-7/2	7/18	119/25	-14/5	-19/8	-9/8
9/2	-324	-432	-2232	-27/2	-31/6	85/37	-50/37	-5	-25/9

<sup>a</sup>  $C_0(m, I)$ ,  $C_2(m, I)$ , and  $C_4(m, I)$  are defined in Eq. (4.27).

<sup>b</sup>  $K_{\text{Sym}0}$  and  $K_{\text{Sym}4}$  are defined in Eq. (4.42).

<sup>c</sup>  $K_{\text{iso}}^{\text{CS}}$  and  $K_{\text{iso}}^{2Q}$  are defined in Eq. (4.50).

<sup>d</sup>  $K_{\text{Sat}0} = \frac{C_0(m, I) - C_0(m-1, I)}{C_0(1/2, I) - C_0(-1/2, I)}$ , and  $K_{\text{Sat}4} = \frac{C_4(m, I) - C_4(m-1, I)}{C_4(1/2, I) - C_4(-1/2, I)}$  are defined for STMAS with satellite transition  $m \leftrightarrow m - 1$ .

so that the time for an echo is

$$t_2^e = Kt_1. \quad (4.47)$$

If  $K < 0$ , the echo forms at negative  $t_2$ , and it is called an ‘‘anti-echo’’. Negative  $t_2$  cannot be accessed directly. However, it can be detected by shifting the time origin of  $t_2$  using the spin-echo technique (Chapter 2).

Both  $\delta_m$  and  $\delta_{1/2}$  contain the anisotropic term  $\delta_{\text{aniso}}^{2Q}$ . Therefore in the 2D spectrum obtained without a shearing transformation, both dimensions are anisotropic. The projections onto both horizontal and vertical axes are very broad and the contour shows a ridge

of slope  $K_{\text{Sym4}} = -7/9$  as shown in Fig. 4.7.E. However, a shearing transformation may be applied so that the vertical dimension is free of anisotropy. As seen in Fig. 4.7.D, the projection onto the vertical axis is very narrow and the ridge is parallel to the horizontal dimension. The shearing transformation essentially extends the evolution time to the echo center by defining

$$t'_1 = t_1 + t_2^e = (1 + K)t_1. \quad (4.48)$$

Operationally the time extension is fulfilled by multiplying a  $t_1$ -dependent first order phase factor,  $e^{i2\pi K t_1 \nu_2}$ , immediately after the first Fourier transformation with respect to the directly detected  $t_2$  dimension ( see Fig. 4.7.B and Fig. 4.7.C). After the second Fourier transformation (along the  $t'_1$  dimension) the  $\nu'_1$  dimension is isotropic (Fig. 4.7.D). Thus we may call this the “isotropic dimension” and label it with  $\nu_{\text{id}}$  (or  $\delta_{\text{id}}$ );  $\nu_2$  is the original MAS dimension, and we may label it with  $\nu_{1/2}$  (or  $\delta_{1/2}$ ).

The factor  $1 + K$  also applies to increment in the indirect dimension,  $\Delta t_1$ , and it leads to the re-scaling of the spectral width

$$sw'_1 = \frac{1}{(1 + K)\Delta t_1} = \frac{sw_1}{1 + K}.$$

This formula has different values for echo and anti-echo pathways since their  $K$  values have opposite signs. However, in some experiments both pathways are detected simultaneously (this is the so-called amplitude modulation seen in the Z-filter sequence, which will be described in detail in the next section). The simple solution is to use  $k$ , the absolute value of  $K$ . Therefore,

$$sw'_1 = \frac{sw_1}{1 + k}, \text{ and } t'_1 = t_1(1 + k). \quad (4.49)$$

With the shearing transformation, the frequency formula for the isotropic dimension is

$$\delta_{\text{id}} = \frac{K\delta_{1/2} + \delta_m}{1+k} = K_{\text{iso}}^{\text{CS}}\delta_{\text{iso}}^{\text{CS}} + K_{\text{iso}}^{2Q}\delta_{\text{iso}}^{2Q} = K_{\text{iso}}^{\text{CS}}\left(\delta_{\text{iso}}^{\text{CS}} - \frac{10}{17}\delta_{\text{iso}}^{2Q}\right), \quad (4.50)$$

with

$$K_{\text{iso}}^{\text{CS}} = \frac{2m+K}{1+k} = \frac{1}{1+k} \frac{34m(4m^2-1)}{36I(I+1)-27},$$

$$K_{\text{iso}}^{2Q} = \frac{K_{\text{Sym}0}+K}{1+k} = -\frac{1}{1+k} \frac{20m(4m^2-1)}{36I(I+1)-27},$$

and the relation

$$K_{\text{iso}}^{\text{CS}} = -\frac{17}{10}K_{\text{iso}}^{2Q}$$

is independent of  $I$ . With Eq. (4.50), we may determine the ppm reference for the isotropic dimension. We do not need to consider the quadrupole effect here; therefore the chemical shift value (ppm) for the center of the isotropic axis ( $\delta_{\text{id}}^{\text{C}}$ ) is related to that for the MAS axis ( $\delta_{1/2}^{\text{C}}$ ),

$$\delta_{\text{id}}^{\text{C}} = K_{\text{iso}}^{\text{CS}}\delta_{1/2}^{\text{C}}. \quad (4.51)$$

## 4.6 Pure Absorption Lineshape

### 4.6.1 Dispersion Problem

The Fourier transformation of a 1D FID consists of both absorption (real) component,  $a(\omega)$ , and dispersion (imaginary) component,  $d(\omega)$  (see Chapter 2). Conventionally the narrower absorption component is presented. However, in a two-dimension spectrum, both the real and imaginary components contain contributions from both absorption and dispersion. Subsequent 1D FTs along the two dimensions of the signal  $S(t_1, t_2)$  [Eq. (4.44)], the spectrum



is

$$\begin{aligned} S(\omega_1, \omega_2) &= S_0[a_1(\omega_1) + id_1(\omega_1)][a_2(\omega_2) + id_2(\omega_2)] \\ &= S_0\{[a_1(\omega_1)a_2(\omega_2) - d_1(\omega_1)d_2(\omega_2)] + i[a_1(\omega_1)d_2(\omega_2) + d_1(\omega_1)a_2(\omega_2)]\}, \end{aligned} \quad (4.52)$$

where

$$a_i(\omega_i) = \frac{R_i}{(\omega_i - \omega_{0i})^2 + R_i^2} \text{ and } d_i(\omega_i) = \frac{\omega_{0i} - \omega_i}{(\omega_i - \omega_{0i})^2 + R_i^2}, \quad i = 1, 2$$

with  $R_1$  and  $R_2$  being relaxation rates for the  $m \leftrightarrow -m$  and  $1/2 \leftrightarrow -1/2$  coherences, respectively, and for MQMAS experiments,  $\omega_{01} = \omega_m$ ,  $\omega_{02} = \omega_{1/2}$ .

The pure absorption lineshape  $a_1(\omega_1)a_2(\omega_2)$  is very clean: it is positive everywhere and clearly defined (Fig. 4.8.A). On the other hand, the pure dispersion lineshape  $-d_1(\omega_1)d_2(\omega_2)$  has two negative and two positive lobes, and spreads over a large area (Fig. 4.8.B). Thus the pure absorption lineshape has much higher resolution. The real part of the the spectrum,  $a_1(\omega_1)a_2(\omega_2) - d_1(\omega_1)d_2(\omega_2)$ , is a hybrid of both pure dispersion and absorption lineshapes, which results in a distortion known as “phase twist” (Fig. 4.8.C). Phase twist causes overlap between different resonance sites and should be avoided. The pure absorption mode spectra are obviously superior. There are two approaches to obtaining absorption mode spectra: whole-echo detection and amplitude modulation.

#### 4.6.2 Solution One: Whole-Echo Detection

The dispersion component  $d(\omega)$  can be eliminated if the signal,

$$S(t) = e^{i\omega_0 t - R|t|}, \quad (4.53)$$

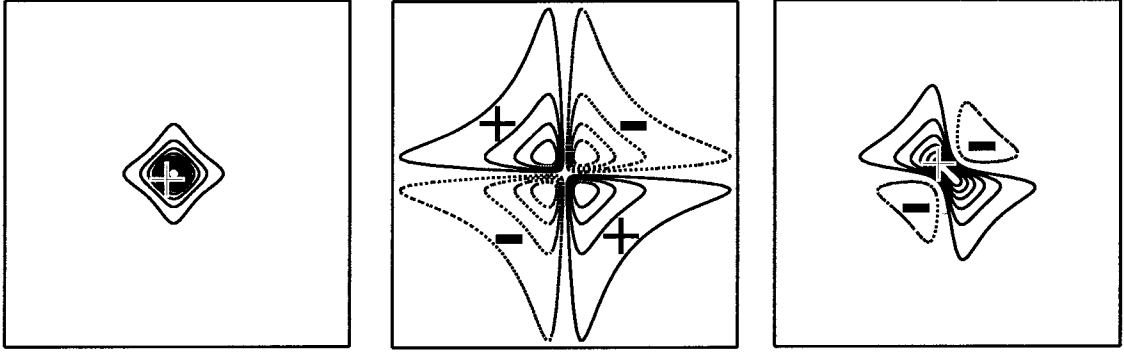


**Figure 4.8:** Lineshapes in 2D spectra. (A) Pure absorption  $a_1(\omega_1)a_2(\omega_2)$ . (B) Pure dispersion  $-d_1(\omega_1)d_2(\omega_2)$ . (C) Mixed phase  $a_1(\omega_1)a_2(\omega_2) - d_1(\omega_1)d_2(\omega_2)$ .

is considered from time  $t = -\infty$  (notice  $|t|$  instead of  $t$ ). Since the Fourier transform over the range from negative to positive infinity has only pure absorption mode,

$$S(\omega) = \int_{-\infty}^{\infty} e^{i\omega_0 t - R|t|} e^{-i\omega t} dt = \frac{2R}{(\omega - \omega_0)^2 + R^2} = 2a(\omega). \quad (4.54)$$

A spin-echo signal with sufficiently large time shift is of the form in Eq. (4.53); the signal is (approximately, due to relaxation) symmetric around the echo top. The signal starts with zero magnitude, thus the lower limit of the integration may be extended to negative infinity. If we incorporate a spin-echo into our prototype 2-pulse sequence, a time shift  $\tau$  is introduced to allow for the detection of whole-echo. Then we have the signal

$$S(t_1, \tilde{t}_2) = S_0 e^{(i\omega_m - R_1)t_1} e^{i\omega_{1/2}\tilde{t}_2 - R_2|\tilde{t}_2|}, \quad (4.55)$$

where  $\tilde{t}_2 = t_2 - \tau$ . The spectrum (with phase correction  $e^{-i\omega_2\tau}$ ) is

$$\begin{aligned} S(\omega_1, \omega_2) &= S_0 [a_1(\omega_1) + id_1(\omega_1)] * 2a_2(\omega_2) \\ &= 2S_0 [a_1(\omega_1)a_2(\omega_2) + id_1(\omega_1)a_2(\omega_2)], \end{aligned} \quad (4.56)$$

whose real component is purely absorptive.

The MQMAS sequence with whole-echo (or anti-echo) detection is shown in Fig. 4.9. The coherence pathway is  $p \rightarrow +1 \rightarrow -1$ , with the sign of  $p$  appropriately chosen to form an echo (solid line) or an antiecho (dotted line). The FID is shifted by  $\tau$ , which is equal to the delay between the second and third pulses. The third pulse is a  $\pi$  pulse with very low RF power, which is selective for the central transition. The flip angle of the last nominal soft  $\pi$  pulse should be  $\pi/(I + 1/2)$  for solid samples, if the  $\pi$  pulse is calibrated with a liquid sample.

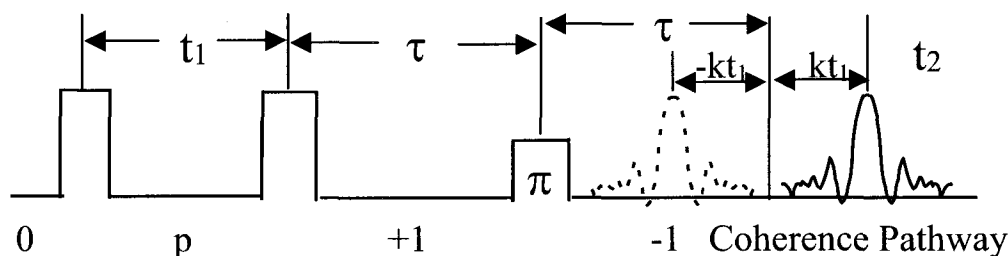


**Figure 4.9:** MQMAS pulse sequence with whole-echo detection. Echo (solid line) and/or anti-echo (dotted line) signals form by appropriately phase-cycling.

### 4.6.3 Solution Two: Amplitude Modulation and Z-filter

In the whole-echo detection approach, the dispersion problem is solved by effectively extending the lower limit of the Fourier integration to negative infinity. The same principle of limit extension applies to the amplitude modulation approach. In this approach, both  $\pm p$  coherences are selected during evolution. The recorded signal is proportional to  $\cos(\omega_m t_1)$  ( $e^{i\omega_m t_1} + e^{i\omega_{-m} t_1}$ , with  $\omega_m = -\omega_{-m}$ ) hence “amplitude modulation”, as opposed to  $e^{i\omega_m t_1}$  of single coherence, which is phase modulation. The extension to negative time becomes

clear by re-writing

$$e^{i\omega - mt_1} = e^{i\omega_m(-t_1)}. \quad (4.57)$$

It seems we may simply use the prototype two-pulse sequence with the difference that both  $\pm p$  are now selected during the evolution. There is a problem, however, in that the  $+p \rightarrow -1$  and  $-p \rightarrow -1$  pathways have different transfer efficiencies, since the coherence transfer efficiency of a pulse also depends on absolute value of  $\Delta p$ , the difference in order between the final and initial coherences. The larger  $|\Delta p|$  is, the less efficient the transfer.  $|\Delta p| = 1 + p$  for  $+p \rightarrow -1$  and  $|\Delta p| = p - 1$  for  $-p \rightarrow -1$  (for convenience,  $p$  is set positive here and in all cases when both coherences are selected). Thus the two exponential terms,  $e^{i\omega_m t_1}$  and  $e^{i\omega - mt_1}$ , are not added with equal proportion and therefore the signal is not purely amplitude modulated.

The solution is to use a “Z-filter” one the multi-coherences before converting them to the detectable  $-1$  coherence, as indicated in Fig. 4.10. If the zeroth order coherences are selected during filtering, it is not difficult to show that both pathways ( $0 \rightarrow \pm p \rightarrow 0 \rightarrow -1$ ) have equal transfer amplitudes and pure amplitude modulation is achieved. To be efficient, the last pulse must be a selective  $\pi/2$  pulse for the central transition.

Amplitude modulated spectra can not discern the sign of  $\omega_1$  (the indirectly detected dimension) since the signal is phase insensitive. Hypercomplex data are collected to restore the sign by alternating the preparation phase  $\phi^{prep}$  of the first pulse between 0 and  $\pi/2p$ . The  $p$  coherence experiences a phase shift of  $-p\phi^{prep}$ . Therefore, a recorded signal is  $90^\circ$  out of phase with the previous slice, and sign sensitivity is restored.

The processing of hypercomplex MQMAS data consists of several steps: separation of echo and anti-echo, Fourier transformation with respect to  $t_2$  for both echo and anti-echo,

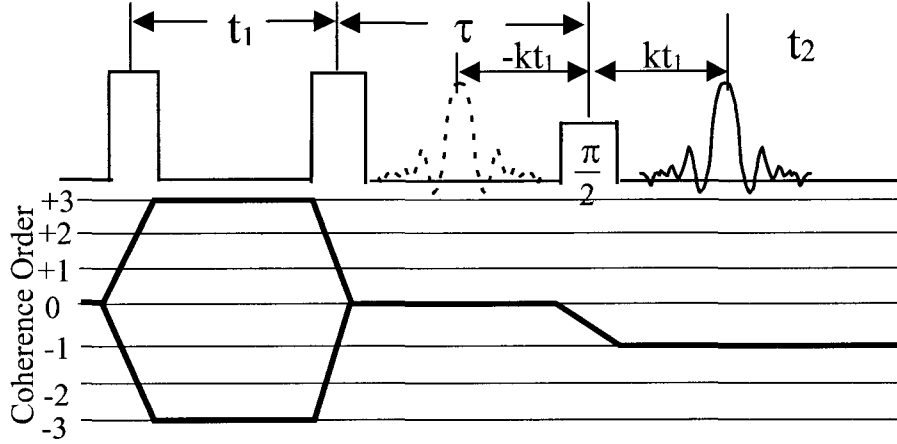


**Figure 4.10:** Amplitude modulation with Z-filter. Echo signal is solid line, anti-echo dotted line. The coherence transfer pathways  $0 \rightarrow \pm 3 \rightarrow 0 \rightarrow -1$  are selected.

performing a shearing transformation as required, FT along  $t'_1$ , reverse the  $\omega_1$  axis for the spectra with  $+p$  coherence, and finally sum the two spectra. An exhaustive description follows. Let  $S_X$  and  $S_Y$  be the signal generated with preparation phase 0 and  $\pi/2p$ , respectively,

$$\begin{aligned} S_X(t_1, t_2) &= S_0[e^{i\omega_{-p}t_1} + e^{i\omega_p t_1}]e^{-R_1 t_1} e^{(i\omega_{-1} - R_2)t_2}, \\ S_Y(t_1, t_2) &= S_0[e^{i\omega_{-p}t_1} e^{i\pi/2} + e^{i\omega_p t_1} e^{-i\pi/2}]e^{-R_1 t_1} e^{(i\omega_{-1} - R_2)t_2}, \end{aligned} \quad (4.58)$$

where the resonance frequencies are subscripted with their coherence order and  $p$  is again positive for convenience. Now combine the two signals as

$$\begin{aligned} S_+(t_1, t_2) &= S_X(t_1, t_2) + iS_Y(t_1, t_2) = 2S_0 e^{(i\omega_p - R_1)t_1} e^{(i\omega_{-1} - R_2)t_2}, \\ S_-(t_1, t_2) &= S_X(t_1, t_2) - iS_Y(t_1, t_2) = 2S_0 e^{(i\omega_{-p} - R_1)t_1} e^{(i\omega_{-1} - R_2)t_2}. \end{aligned} \quad (4.59)$$

$S_+$  is anti-echo for  $I = 3/2$  and echo for  $I > 3/2$ , while  $S_-$  is vice versa. After FT along  $t_2$

and shearing transformation,

$$\begin{aligned} S_+(t'_1, \omega_2) &= 2S_0 e^{[i(K_p\omega_2 + \omega_p) - R_1]t'_1/(1+k)} [a_2(\omega_2) + id_2(\omega_2)], \\ S_-(t'_1, \omega_2) &= 2S_0 e^{[i(K_{-p}\omega_2 + \omega_{-p}) - R_1]t'_1/(1+k)} [a_2(\omega_2) + id_2(\omega_2)], \end{aligned} \quad (4.60)$$

with the scaled variable  $t'_1$  defined in Eq. (4.49). Only the exponential terms are involved in the FT along  $t'_1$ ,

$$\begin{aligned} FT(e^{[i(K_p\omega_2 + \omega_p) - R_1]t'_1/(1+k)}) &= \frac{R_1 + i[(\omega_p + K_p\omega_2)/(1+k) - \omega'_1]}{R_1^2 + [\omega'_1 - (\omega_p + K_p\omega_2)/(1+k)]^2}, \\ FT(e^{[i(K_{-p}\omega_2 + \omega_{-p}) - R_1]t'_1/(1+k)}) &= \frac{R_1 + i[(\omega_{-p} + K_{-p}\omega_2)/(1+k) - \omega'_1]}{R_1^2 + [\omega'_1 - (\omega_{-p} + K_{-p}\omega_2)/(1+k)]^2}. \end{aligned} \quad (4.61)$$

If the sign of  $\omega_1$  is reversed in the first equation and this is added to the second, then the imaginary parts cancel because  $K_p = -K_{-p}$  and  $\omega_p = -\omega_{-p}$ . Finally, restoring the factors omitted previously, the spectra is

$$S(\omega'_1, \omega_2) = 4S_0 \frac{R_1}{\omega'_1 - (\omega_{-p} + K_{-p}\omega_2)/(1+k)]^2 + R_1^2} [a_2(\omega_2) + id_2(\omega_2)]. \quad (4.62)$$

The real component of the spectrum gives a pure absorption lineshape.

In order to verify the experimental setup and data processing are set up correctly, the  $^{23}\text{Na}$  3QMAS spectrum of sodium sulfite ( $\text{Na}_2\text{SO}_3$ ) was acquired using the Z-filter sequence (Fig. 4.11.B). Sodium sulfite has three non-equivalent crystal sites and is ideal for demonstrating the progressive resolution improvements of static, MAS, and MQMAS techniques. One broad peak is observed in the static spectrum. A tiny glitch on top of the lineshape is the only hint of the existence of multiple sites (Fig. 4.11.A). At 8 kHz spinning speed the MAS spectrum is able to partially resolve the three inequivalent sites.

However, the third site ( $S_3$ ) is superimposed on the other two and it is difficult to discern the characteristic features (Fig. 4.11.A). Thus the quadrupolar and chemical shift parameters cannot be accurately determined for this site. In the 3QMAS spectrum, the three sites are clearly resolved and site-specific parameters may be trivially extracted. Projection onto the MAS dimension gives the MAS spectrum; projection onto the isotropic dimension has high resolution for the three sites.

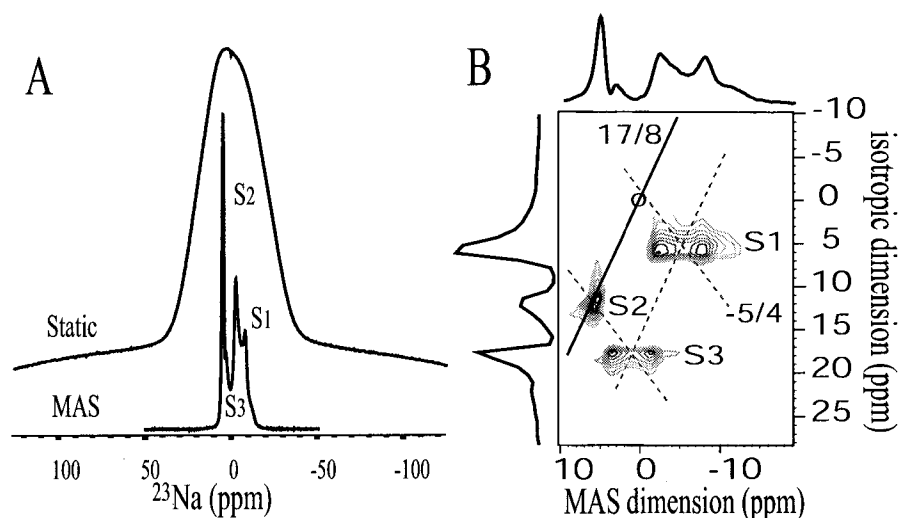


**Figure 4.11:**  $^{23}\text{Na}$  spectra of  $\text{Na}_2\text{SO}_3$  at 7 T ( $^{23}\text{Na}$  frequency reference is 79.374 MHz for aqueous NaCl). (A) For the static spectrum, full sweep width  $sw = 20$  kHz, RF strength  $\nu_1 = 100$  kHz, pulse duration is  $1.25 \mu\text{s}$ , 512 complex data points, 500 scans, recycle delay 2 s. For the MAS spectrum, all are the same except for  $sw = 8$  kHz, and the spinning speed  $\nu_R = 8$  kHz. (B) For the 3QMAS spectrum,  $sw = 8$  kHz in the direct dimension,  $t_1$  increment is  $125 \mu\text{s}$ ,  $\nu_1 = 89$  kHz for the first and second pulses,  $\nu_1 = 3.125$  kHz for the last pulse, pulse durations are 6, 2.6 and  $40 \mu\text{s}$  respectively for the three pulses, the delay between the second and third pulses is 1 ms (this is eight times the rotor period), 512 complex data points in a 1D FID, 128 slices are acquired by incrementing  $t_1$  in every other pass, 240 scans for each slice, recycle delay 1 s,  $\nu_R = 8$  kHz. The slope  $K_{\text{iso}}^{\text{CS}} = 17/8$  is for the  $\delta_{\text{iso}}^{\text{CS}}$  distribution axis, the slope  $K_{\text{iso}}^{2Q} = -5/4$  is for the  $\delta_{\text{iso}}^{2Q}$  distribution axis (see section 4.8). For all three spectra, no line broadening is applied.

## 4.7 Extraction of Parameters and Site Populations

Since averaging over all crystal orientations results in  $\langle \delta_{\text{aniso}}^{2Q} \rangle = 0$ , the bary center (or center of mass) of the lineshape in the MAS dimension is

$$\langle \delta_{1/2} \rangle = \delta_{\text{iso}}^{\text{CS}} + \delta_{\text{iso}}^{2Q} \quad (4.63)$$

by powder integration of Eq. (4.43). The coordinates for the “mass center” of a 2D-MQMAS spectrum are  $(\langle \delta_{1/2} \rangle, \delta_{\text{id}})$ . The isotropic shifts are calculated from Eqs. (4.63) and (4.50),

$$\begin{aligned} \delta_{\text{iso}}^{\text{CS}} &= \frac{1}{27} (10 \langle \delta_{1/2} \rangle + 17 \frac{\delta_{\text{id}}}{K_{\text{iso}}^{\text{CS}}}), \\ \delta_{\text{iso}}^{2Q} &= \frac{17}{27} (\langle \delta_{1/2} \rangle - \frac{\delta_{\text{id}}}{K_{\text{iso}}^{\text{CS}}}). \end{aligned} \quad (4.64)$$

The quadrupole product  $P_Q$  can be extracted by using the relation  $\delta_{\text{iso}}^{2Q} = -AP_Q^2$  [Eq. (4.42)]. For the 3QMAS spectrum shown in Fig. 4.11, the mass center coordinates (in ppm) for the three sites are (-5.8, 5.3) for  $S_1$ , (5.4, 11.5) for  $S_2$ , and (1.0, 18.0) for  $S_3$ . With  $I = 3/2$  and  $\nu_L = 79.374$  MHz, we calculate  $A = 3.97$  ppm·MHz<sup>-2</sup> and  $K_{\text{iso}}^{\text{CS}} = 17/8$ . The extracted parameters are listed in Table 4.4. One should be reminded that this method is subject to errors, since coordinates of the mass center are determined by visual inspection.

**Table 4.4:** NMR parameters for the three sites in Na<sub>2</sub>SO<sub>3</sub> using different methods.

Site	Mass Center			Line Fitting				
	$\delta_{\text{iso}}^{\text{CS}}$ <sup>a</sup>	$\delta_{\text{iso}}^{2Q}$	$P_Q$	$\delta_{\text{iso}}^{\text{CS}}$	$C_Q$	$\eta$	$\delta_{\text{iso}}^{2Q}$	$P_Q$
1	0.6	-5.29	1.16	-0.1	1.15	0.1	-5.25	1.15
2	5.4	0.0	0.0	6.0	0.35	0	-0.49	0.35
3	5.7	-4.8	1.10	6.0	1.13	0.2	-5.16	1.14

<sup>a</sup>  $\delta_{\text{iso}}^{\text{CS}}$  and  $\delta_{\text{iso}}^{2Q}$  are in ppm, and  $C_Q$  and  $P_Q$  are in MHz.



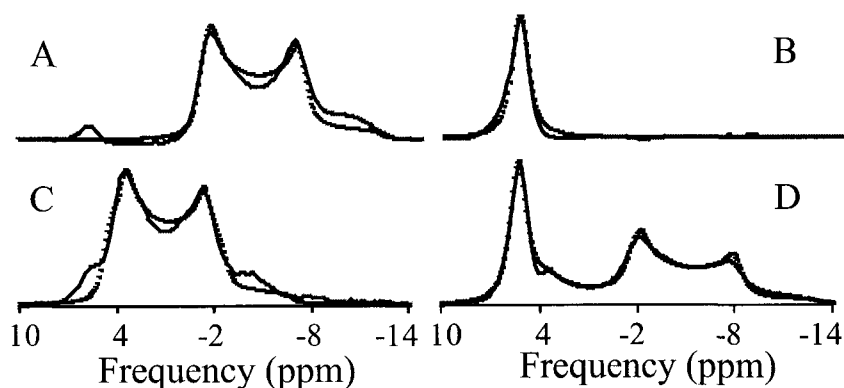


**Figure 4.12:** Line fitting (dotted line) of the three sites in  $\text{Na}_2\text{SO}_3$  3QMAS and MAS spectra (solid line). (A) Site 1 of 3QMAS, simulation parameters  $(\delta_{\text{iso}}^{\text{CS}}/\text{ppm}, C_Q/\text{MHz}, \eta) = (-0.1, 1.15, 0.1)$ , exponential broadening (EM) 50 Hz. (B) Site 2 of 3QMAS, simulation parameters  $(6, 0.35, 0)$ , EM 69 Hz. (C) Site 3 of 3QMAS, simulation parameters  $(6, 1.13, 0.2)$  EM 40 Hz, (D) Fit the MAS spectrum by adding the above three simulated components with weight 48%, 31%, and 21% respectively.

More accurate values may be obtained by fitting to the lineshape of each site, which for this simple crystalline material is well-resolved in the 3QMAS spectrum. The best fits are shown in Fig. 4.12.A-C. However, the accuracy of parameters for site 2 is low. Site 2 has a very small quadrupolar coupling constant and narrow lineshape and as a result the characteristic discontinuities are not seen. The asymmetry parameter  $\eta$  cannot be determined at all, and it is simply set to zero. These values agree with literature values [76] and this confirms that our experiments, data processing, and fitting procedures are all working well.

The next step is to obtain the relative site populations. The excitation efficiency of the MQMAS depends on the magnitude of  $C_Q$ , RF strength  $\nu_1$ , and sample spinning speed  $\nu_R$ , therefore, the MQMAS intensities are not a faithful indicator of population. We have to turn to the MAS spectrum where excitation is more uniform. With the interaction parameters obtained by analyzing 3QMAS spectrum, we fit the MAS spectrum and obtain

the population ratio 5:3:2 for the three sites (Fig. 4.12.D).

## 4.8 Axes of Distributions

The two axes, with slopes  $17/8$  and  $-5/4$ , are drawn in Fig. 4.11.B. They correspond to the numerical factors  $K_{\text{iso}}^{\text{CS}}$  and  $K_{\text{iso}}^{2Q}$  [defined in Eq. (4.50) and listed in Table 4.3] with  $I = 3/2$  and  $m = 3/2$ .  $K_{\text{iso}}^{\text{CS}}$  describes the distribution of isotropic chemical shifts  $\delta_{\text{iso}}^{\text{CS}}$ , that is to say, if several sites have same EFG ( $P_Q$ ) but different  $\delta_{\text{iso}}^{\text{CS}}$ , then their mass centers are distributed along an axis with this slope; sites 1 and 3 of  $\text{Na}_2\text{SO}_3$  roughly satisfy these conditions.  $K_{\text{iso}}^{2Q}$  describes the distribution of  $\delta_{\text{iso}}^{2Q}$ , i.e., if several sites have the same  $\delta_{\text{iso}}^{\text{CS}}$  but different  $P_Q$ , then their mass centers align along an axis of this slope; sites 2 and 3 of  $\text{Na}_2\text{SO}_3$  roughly qualify.

These distribution axes are better appreciated when MQMAS is applied to amorphous materials. Typically these materials have continuous values of  $\delta_{\text{iso}}^{\text{CS}}$  and/or  $P_Q$  and no individual site may be identified in the MQMAS spectra. These two slopes are helpful when describing whether there are distributions of parameters  $\delta_{\text{iso}}^{\text{CS}}$ ,  $P_Q$ , or both. Many examples will be seen in the  $^{93}\text{Nb}$  3QMAS study of the disordered solid solution of PMN-PSN (be presented in Chapters 6 and 7.

## 4.9 “Dream” Transformation

In the usual presentation of MQMAS spectra with skew transformation, the MAS dimension consists of three parts,  $\delta_{\text{iso}}^{\text{CS}}$ ,  $\delta_{\text{iso}}^{2Q}$ , and  $\delta_{\text{aniso}}^{2Q}$ ; the isotropic dimension consists of the first two. One is entitled to ask: may we we improve the means of separation? One might hope

to put  $\delta_{\text{iso}}^{\text{CS}}$  along one axis, the 2nd order quadrupole effects (both  $\delta_{\text{iso}}^{2Q}$  and  $\delta_{\text{aniso}}^{2Q}$ ) along an orthogonal axis—just as in a 2D nutation spectrum. Wonderful this would be, but it is unachievable. It is equivalent to the impossibility of solving two equations to obtain three unknowns. We have to settle for a compromise: the  $x$ -axis becomes a mixture of  $\delta_{\text{iso}}^{\text{CS}}$  and  $\delta_{\text{aniso}}^{2Q}$  and the  $y$ -axis a mixture of  $\delta_{\text{iso}}^{2Q}$  and  $\delta_{\text{aniso}}^{2Q}$ . It is achieved by “brute-force” shearing of the ordinary MQMAS spectrum.

From Eqs. (4.43) and (4.50), we solve for

$$\begin{aligned}\delta_{\text{iso}}^{\text{CS}} &= \frac{\delta_{\text{id}} - K_{\text{iso}}^{2Q} \delta_{1/2}}{K_{\text{iso}}^{\text{CS}} - K_{\text{iso}}^{2Q}} + \frac{K_{\text{iso}}^{2Q} \delta_{\text{aniso}}^{2Q}}{K_{\text{iso}}^{\text{CS}} - K_{\text{iso}}^{2Q}} = \frac{10\delta_{1/2} + 17\delta_{\text{id}}/K_{\text{iso}}^{\text{CS}}}{27} - \frac{10}{27}\delta_{\text{aniso}}^{2Q}, \\ \delta_{\text{iso}}^{2Q} &= \frac{\delta_{\text{id}} - K_{\text{iso}}^{\text{CS}} \delta_{1/2}}{K_{\text{iso}}^{2Q} - K_{\text{iso}}^{\text{CS}}} + \frac{K_{\text{iso}}^{\text{CS}} \delta_{\text{aniso}}^{2Q}}{K_{\text{iso}}^{2Q} - K_{\text{iso}}^{\text{CS}}} = \frac{17\delta_{1/2} - 17\delta_{\text{id}}/K_{\text{iso}}^{\text{CS}}}{27} - \frac{17}{27}\delta_{\text{aniso}}^{2Q}.\end{aligned}\quad (4.65)$$

We then define two variables

$$\begin{aligned}\tilde{\delta}_{\text{iso}}^{\text{CS}} &\equiv \delta_{\text{iso}}^{\text{CS}} + \frac{10}{27}\delta_{\text{aniso}}^{2Q} = \frac{10\delta_{1/2} + 17\delta_{\text{id}}/K_{\text{iso}}^{\text{CS}}}{27}, \\ \tilde{\delta}_{\text{iso}}^{2Q} &\equiv \delta_{\text{iso}}^{2Q} + \frac{17}{27}\delta_{\text{aniso}}^{2Q} = \frac{17\delta_{1/2} - 17\delta_{\text{id}}/K_{\text{iso}}^{\text{CS}}}{27}.\end{aligned}\quad (4.66)$$

For each equation, the RHS of the last equal sign describes how to map from the sheared-representation to the “dream” representation. We can set  $\tilde{\delta}_{\text{iso}}^{\text{CS}}$  as the  $x$ -axis and  $\tilde{\delta}_{\text{iso}}^{2Q}$  as the  $y$ -axis, with the bary centers  $\langle \tilde{\delta}_{\text{iso}}^{\text{CS}} \rangle = \delta_{\text{iso}}^{\text{CS}}$ , and  $\langle \tilde{\delta}_{\text{iso}}^{2Q} \rangle = \delta_{\text{iso}}^{2Q}$ ;  $sw$  (full spectral width) and  $\delta^C$  (ppm value of the axis center) need to be adjusted accordingly,

$$\begin{aligned}\tilde{sw}_2 &= \frac{10sw_2 + 17sw'_1/|K_{\text{iso}}^{\text{CS}}|}{27}, \quad \tilde{sw}_1 = \frac{17sw_2 + 17sw'_1/|K_{\text{iso}}^{\text{CS}}|}{27}, \\ \tilde{\delta}_2^C &= \frac{10\delta_{1/2}^C + 17\delta_{\text{id}}^C/K_{\text{iso}}^{\text{CS}}}{27}, \quad \tilde{\delta}_1^C = \frac{17\delta_{1/2}^C - 17\delta_{\text{id}}^C/K_{\text{iso}}^{\text{CS}}}{27} = 0,\end{aligned}\quad (4.67)$$

where  $sw'_1$  is defined in Eq. (4.49) and  $\delta_{id}^C = K_{iso}^{CS} \delta_{1/2}^C$  is defined in Eq. (4.51). In this representation, the ridge for each site has a slope of 17/10, regardless of the values for  $I$  and  $m$ . An example of this transformation is shown in Fig. 4.13 for the  $\text{Na}_2\text{SO}_3$  3QMAS spectrum. Now the values of  $(\delta_{iso}^{CS}, \delta_{iso}^{2Q})$  can be directly obtained from the mass centers directly:  $S_1$   $(-0.9, -5.2)$ ,  $S_2$   $(5.6, 0)$ , and  $S_3$   $(5.8, -5.2)$  ppm (cf Table 4.4).

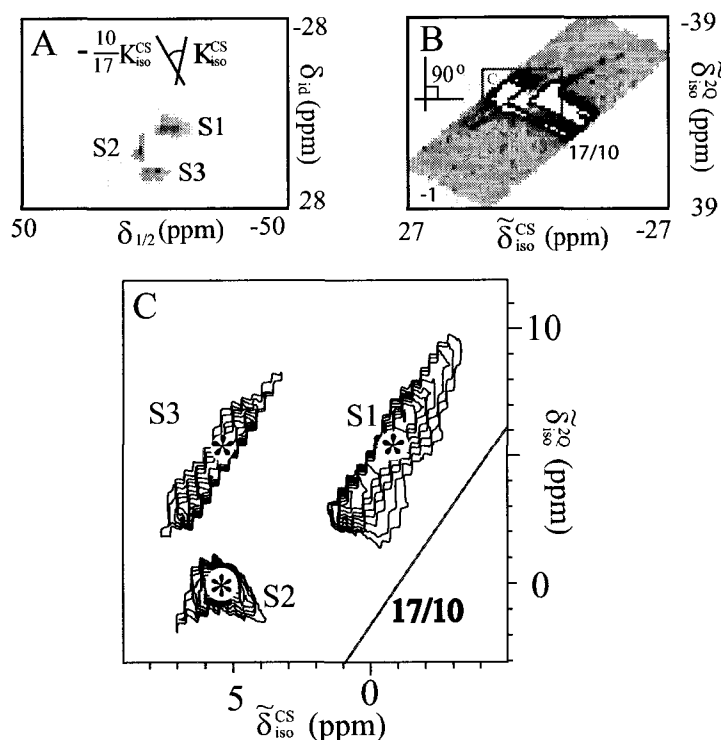


**Figure 4.13:** “Dream transformation” on  $^{23}\text{Na}$  3QMAS of  $\text{Na}_2\text{SO}_3$  (Fig. 4.11.B). (A) Whole 3QMAS spectrum ( $sw_2 = 8$  kHz,  $sw'_1 = 4.5$  kHz) (B) whole transformed spectra ( $sw''_2 = 4296$  Hz,  $sw'_1 = 6370$  Hz), low intensity contour plot is applied to show the “brute-force” feature of this transformation: the spectrum does not fill the whole window. (C) magnified view of the three sites, with centers of mass marked by stars.

One may notice that the contours of the “dream transformed” spectrum are not smooth (see Fig. 4.13.C). This is because the grid size changes during the transformation and in the “brute force” approach, several nearby points may fall into a same new grid, while some

new grids may contain no corresponding old grid point. A “soft transformation” is able to build a one to one map. This is possible since a shift in the frequency domain is equivalent to a linear phase correction in the time domain. However, this is practically difficult to achieve especially for a two-dimensional spectra. Since the theoretical frequency range is  $f_N/2$  to  $-f_N/2$  (where,  $f_N$  is the Nyquist frequency) but in all commercial software the range is  $f_N/2$  to  $-f_N/2 + f_N/N$  (where  $N$  is the number of points), this results in phase error each time doing inverse Fourier transform. Phase distortion is observed in the “soft transformed” spectra. This problem might be finally solved in the future by complicated phase compensation.

## 4.10 Summary

The electric field gradients (EFG) can be measured by NMR via quadrupolar interaction and provide structural information on atomic scale. The quadrupolar interaction energy has been treated as a perturbation to the Zeeman interaction up to the the second order. Polycrystalline NMR lineshapes have been analyzed for both static and spinning samples. Half-integer quadrupolar nuclei are of special interest since they form two-thirds of the periodic table, and especially include  $^{93}\text{Nb}$  ( $I = 9/2$ ),  $^{45}\text{Sc}$  ( $I = 7/2$ ), and  $^{25}\text{Mg}$  ( $I = 5/2$ ) in the relaxor ferroelectric  $(1-x)\text{PbMg}_{1/3}\text{Nb}_{2/3}\text{O}_3 - x\text{PbSc}_{1/2}\text{Nb}_{1/2}\text{O}_3$  we are going to study. For these inhomogeneous and chemically disordered relaxor ferroelectric materials, there are a large number of inequivalent microscopic configurations that result in overlapping NMR lineshapes. For example in the  $^{93}\text{Nb}$  MAS spectra, only seven narrow and two broad peaks are resolved out of the 28 possible nearest B-site neighbor (nBn) configurations (see Chapter

6). The situation is worse in  $^{45}\text{Sc}$  MAS spectra, where only two overlapping lineshapes may be identified out of the 28 nBn configurations (see Chapter 7)! This insufficient spectral resolution is a big hurdle to spectral assignment and NMR parameter extraction. The two-dimensional triple-quantum MAS (3QMAS) has higher resolution than MAS and will ease the tasks of spectral assignment and parameter extraction (Chapters 6 and 7).

## Chapter 5

# Perovskite Relaxor Ferroelectrics

### 5.1 Ferroelectrics

*Ferroelectrics* are materials possessing permanent polarization that can be reversed in direction by an external electric field. They are named by analogy with ferromagnetic materials such as iron (ferrum). Ferroelectric ceramics and single crystals have become a very important class of materials. Their applications in electronics and optics include, but are not limited to, capacitors, nonvolatile memories, medical ultrasound generators and receivers, high frequency speakers, displacement transducers, accelerometers, voltage transformers, gas ignitors, flash protection goggles, and optical memories and displays [87, 78, 80, 99].

Among the 32 crystal point groups, 21 do not have a center of symmetry [16, 87]. These have one or more principal axes. Except for point group  $O$  (or 432), the remaining 20 non-centrosymmetric point groups exhibit *piezoelectric* effects along the principal axes. Piezoelectrics are crystals, for example quartz, capable of producing positive electric charge on one side and negative charge on the other proportional to the mechanical pressure exerted on them. Conversely, these crystals deform in proportion to an applied electric field. Among

the 20 groups exhibiting piezoelectric effects 10 have more than one principal axes. The electric dipole moments along different axes cancel each other, thus these crystals show no net macroscopic polarization. The remaining 10 groups, which have an unique principal axis, possess spontaneous polarization and are called *polar* for this reason. The magnitude of the spontaneous polarization depends upon temperature. In BaTiO<sub>3</sub> for example, the polarization decreases as temperature goes up, it drops to zero above the Curie point ( $T_C = 120$  °C). Therefore, polar crystals are also called *pyroelectrics* [63, 87]. *Ferroelectrics* are a subgroup of pyroelectrics with the additional requirement that the spontaneous polarization can be reversed by an electric field. The reversibility is attributable to the fact that the polar structure of a ferroelectric crystal is a slight distortion from a nonpolar structure [63].

## 5.2 Relaxor Ferroelectrics

The ferroelectric BaTiO<sub>3</sub> belongs to the perovskite family, whose name is inherited from the mineral CaTiO<sub>3</sub>. Perovskites have pseudo-cubic structure and the general formula ABO<sub>3</sub>, see Figure 5.1. In fact, many compounds in the perovskite family are ferroelectrics, such as PbTiO<sub>3</sub>, KNbO<sub>3</sub>, KTaO<sub>3</sub> [62]. The ferroelectrically active B-cations usually have small ionic radius, high valence state, and no outer *d*-electron (e.g. Ti<sup>4+</sup>, Zr<sup>4+</sup>, Nb<sup>5+</sup>, Ta<sup>5+</sup>, and W<sup>6+</sup>) [21].

Some perovskites, where more than one type of cation occupies equivalent crystallographic sites, possess relaxor behavior; these materials show a broad diffuse and dispersive phase transition on cooling below the frequency-dependent dielectric-maximum temperature  $T_m(\omega)$ . Their root-mean-square (RMS) polarization ( $\sqrt{P^2}$ ) persists to a temperature



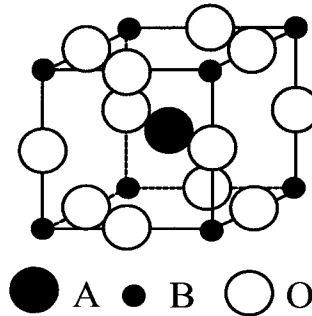


**Figure 5.1:** Generic perovskite structure,  $ABO_3$ .

( $T_D$ ) well above the  $T_m$ , while their mean polarization decreases to zero at a temperature ( $T_f$ ) well below  $T_m$  as shown in Figure 5.2. At low temperatures, these materials show a dielectric hysteresis loop. However, on heating the hysteresis loop gradually becomes thinner and finally degenerates into just nonlinearity. The degeneration of the hysteresis loop indicates that the material loses remnant polarization at high temperature [26, 27].

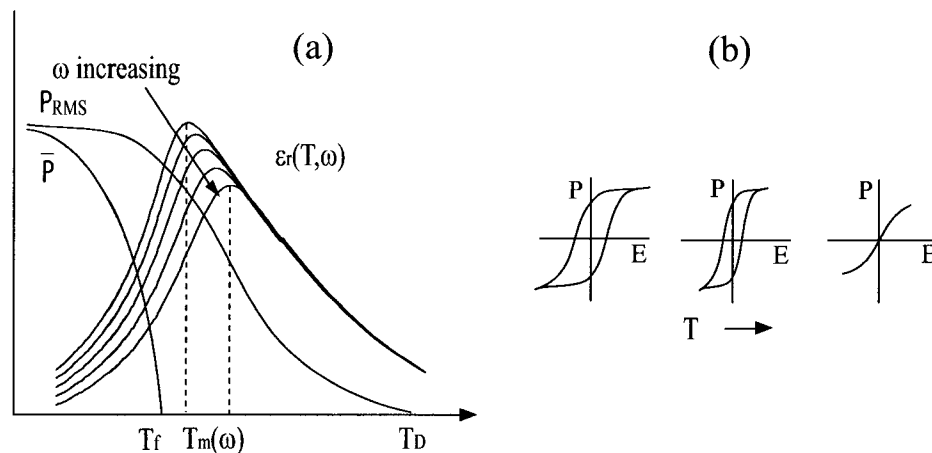


**Figure 5.2:** (a) Generic temperature dependence of dielectric constant and mean and RMS polarizations for a relaxor ferroelectric, with frequency range often in 100 Hz – 1 MHz. (b) Decay of hysteresis loop.

Perovskite relaxor ferroelectrics can be classified according to the crystallographic site(s) which have variable composition. In  $PbZr_xTi_{1-x}O_3$  (PZT),  $PbMg_{1/3}Nb_{2/3}O_3$  (PMN),  $PbSc_{1/2}Nb_{1/2}O_3$  (PSN),  $PbSc_{1/2}Ta_{1/2}O_3$  (PST),  $PbIn_{1/2}Nb_{1/2}O_3$  (PIN) the B-sites are

complex, in  $\text{Pb}_{1-x}\text{La}_{2x/3}\text{TiO}_3$  (PLT) the A-sites are complex, and in  $\text{K}_{1/3}\text{Pb}_{2/3}\text{Zn}_{2/9}\text{Nb}_{7/9}\text{O}_3$  (KPZN) and  $(\text{Pb}_{1-x}\text{La}_x)(\text{Zr}_{1-y}\text{Ti}_y)_{1-x/4}\text{V}_{x/4}^{\text{B}}\text{O}_3$  (PLZT) both A- and B-sites are complex. In the formula of PLZT,  $\text{V}^{\text{B}}$  denote vacancies on B-sites; while for  $(\text{Pb}_{1-x}\text{La}_x)_{1-x/2}(\text{Zr}_{1-y}\text{Ti}_y)\text{V}_{x/2}^{\text{A}}\text{O}_3$ , the A-sites have vacancies. The actual PLZT material may contain both types of vacancy.

Relaxor ferroelectrics have superior dielectric, electromechanical and piezoelectric properties, some of which are exhibited by the most widely used solid-solutions of PMN and  $\text{PbTiO}_3$  (PMN-PT). The Curie point ranges between  $-10^\circ\text{C}$  (PMN) and  $490^\circ\text{C}$  (PT). Solid-solutions with composition 0.65PMN-0.35PT, which is at the morphotropic phase boundary (MPB) between rhombohedral and tetragonal phases, make excellent piezoelectric transducers. Compositions with a Curie point near room temperature (e.g. 0.9PMN-0.1PT) are attractive for producing capacitors since they have large dielectric constants ( $\epsilon_r = 20,000\text{--}35,000$ ) and low dependence on temperature and applied electric field. PMN-PT with similar compositions are also attractive for strain actuator applications, where their electrostrictive effect is employed. The electrostrictive effect has a quadratic dependence on polarization (and hence the dielectric constant  $\epsilon_r$  and the applied electric field  $E$  as  $P = \epsilon_0\epsilon_r E$ , where  $\epsilon_0$  is the permittivity of vacuum) rather than the linear dependence in the piezoelectric effect [87]. This effect is found in all insulators although it is usually too small ( $10^{-5}\text{--}10^{-7}$  strain %) for any practical purpose. However due to their large dielectric constants, these relaxor ferroelectrics may achieve strains comparable to piezoelectrics (0.1 strain %). If they are operated at temperatures between  $T_f$  and  $T_D$  (see Figure 5.2), the hysteresis losses are minimized and the materials return to zero displacement when the applied voltage is suddenly withdrawn.

In addition to the perovskite ferroelectrics, there are some tungsten bronzes which also show relaxor behavior;  $\text{Sr}_{1-x}\text{Ba}_x\text{Nb}_2\text{O}_6$  (SBN) and  $\text{Pb}_{1-x}\text{Ba}_x\text{Nb}_2\text{O}_6$  (PBN) [27].

## 5.3 Origins of Relaxor Behaviors

### 5.3.1 Phenomenological Models

Although relaxor ferroelectrics have been studied intensively, the physical origin of relaxor behavior remains an open question. Two possible mechanisms that may contribute are the reorientation of local polarization and the motion of boundaries between polar regions. To account for the first mechanism, three views have been proposed regarding the nature of relaxors; spin glasses, a ferroelectric state broken into microregions, and a combination of both.

Relaxor ferroelectrics are often described as spin glasses with interacting polar clusters [101]. This explains many behaviors; the dielectric relaxation that is reflected in the frequency dispersion of dielectric maxima temperatures  $T_m(\omega)$  [101, 51], the collapse of macroscopic polarization near the freezing temperature ( $T_f$ , see Figure 5.2) on heating [101], the deviations from the Curie-Weiss relationship [102], the decreases of dielectric constant and increases of the dielectric-maximum temperature on increasing external electric field [52], and the difference between field cooled and zero field-cooled dielectric susceptibilities [24]. Blinc et al. have found that the shape of the local polarization distribution function is very different from dipolar or quadrupolar glasses, but agrees very well with the form predicted by their new glassy model—spherical random bond-random field model (SRBRF) [11, 82, 83].

Westphal et al. challenged these glassy models with evidences of Barkhausen jumps of microdomains during low-T poling and a ferroelectric anomaly of the dielectric permittivity that occurs slightly above  $T_f$  with moderate poling field [108]; they proposed that the relaxor state consists of nanoscale ferroelectric domains under the influence of quenched random electric fields.

Noticing both the glassy and ferroelectric features of the relaxors, Vugmeister and Rabitz proposed to explicitly include in their model, which is able to explain many bulk properties, a distribution of local fields and a distribution of relaxation times characterizing cluster reorientations [106, 107]. In this model, the physical origin of localized dipole moments is claimed to be the off-center shift of ions even at high temperature. In highly polarizable dielectrics such as  $\text{KTaO}_3$  and  $\text{SrTiO}_3$ , the large values of the localized dipole moment induced by an off-center ion are associated with the polarization cloud (cluster) formed by the simultaneous displacements of the other atoms adjacent to a given off-center ion. The collective dynamics in these crystals is caused by the modification of dipole-dipole interactions due to the effect of the spatial dispersion of lattice permittivity. In relaxor ferroelectrics, the concept of clusters is more complicated because the interactions between the off-center ions are unknown. Practically the distributions of local fields and relaxation times are imposed to distinguish the relaxors from conventional ferroelectrics.

To account for the second mechanism of moving boundaries, Glazounov and Tagantsev have proposed a “breathing” model to explain polarization response of relaxors [47]. Charge disorder/fluctuation induces internal random fields, which act as pinning centers for the polar region boundaries. Thus the internal random fields determine the pattern of polar regions when no external field is applied. On the application of an AC electric field, the

boundaries of polar regions vibrate like breathing lungs. This model may explain many properties including the frequency dispersion.

### 5.3.2 Microscopic Pictures

A correct quantitative understanding of the microscopic cation order/disorder is essential to evaluate existing theories or to build new phenomenological models that are capable of describing bulk properties. On a microscopic scale, the diffuse phase transitions in relaxor ferroelectrics are usually attributed to the compositional fluctuations [26]. The compositional fluctuations are thought to lead to different Curie points which results in the broadening of the dielectric peak. In the relaxor PMN ( $\text{PbMg}_{1/3}\text{Nb}_{2/3}\text{O}_3$ ), the compositional fluctuations arise from the coexistence of the two B cations,  $\text{Mg}^{2+}$  and  $\text{Nb}^{5+}$ . Initially the two types of cations were considered to be distributed completely random (CR model) on the B-lattice [96, 59]. However, compositional fluctuation by itself does not lead necessarily to dispersion; some type of ordering seems necessary. Selected-area electron diffraction and high resolution electron microscopy (HREM) studies of PMN reveal NaCl type nanodomains (2-5 nm) dispersed in a disordered matrix [66, 60, 22]. These nanodomains consist of alternating planes of B-cations (labelled  $\beta'$  and  $\beta''$ ) along the [111] direction. The non-stoichiometric 1:1 ordering is believed to be the result of interplay between long-range Coulomb interactions and short-range interactions related to the covalency of the Pb-O bonds [19]. These effects have been investigated using several computational models [17, 18, 53, 114].

In PMN, the  $\beta''$  sites are assumed to be exclusively occupied by  $\text{Nb}^{5+}$ ; unfortunately, neutron and X-ray diffraction provide no direct experimental information on the compo-

sition of the  $\beta'$  sites. This leads to several competing B-site ordering models which differ in their description of the  $\beta'$  site composition [22]. For example in PMN, the space charge model (SC) requires the ferroelectrically “inactive”  $\text{Mg}^{2+}$  and ferroelectrically “active”  $\text{Nb}^{5+}$  layers to be interleaved [22]. While in the random site model (RS), pure  $\text{Nb}^{5+}$  layers and mixed planes (of randomly distributed  $\text{Mg}^{2+}$  and the remaining  $\text{Nb}^{5+}$ ) are interleaved [22]. A consequence of the SC model is that the charges are unbalanced and this should inhibit the growth of large ordered domains. Indeed for PMN, extended thermal treatment does not result in any increase in the domain size or degree of ordering [31]. This absence of increase has been used to support the SC model [22]. However, in solid solutions of  $\text{Pb}(\text{Mg}_{1/3}\text{Ta}_{2/3})\text{O}_3$  (PMT) and 5-25 mol%  $\text{PbZrO}_3$  (PZ), Akbas et al. report that extended thermal treatment at elevated temperature causes the domain size and degree of ordering to increase substantially (from 20% volume in small ordered domains of 2-3 nm, to 95% volume in large domains of size about 100 nm) [2]. Such pronounced domain coarsening contradicts the SC model and supports the random site model, where charge-neutrality is maintained regardless of domain size. Akbas et al. further suggest that in PMN, the absence of increase in domain size is the result of the order-disorder transition temperature being too low for ions to diffuse [31, 30].

Domain growth studies on PMT-PZ solid-solutions also clearly show that nanolevel phase separation and compositional segregation are not necessarily required for relaxor behavior in the PMN-type perovskite ferroelectrics. For PMT-5 mol% PZ, the annealed samples (100 nm ordered domains) have very similar dielectric response as the as-sintered samples (2-3 nm domains); both are relaxors. Thus for this type of perovskites, relaxor properties are attributed to the random distribution of different B-cations in the  $\beta'$  sites.

This supports the random site model because in this model, there is inherent B-site disorder regardless of the domain size [2].

Lead scandium tantalate  $\text{PbSc}_{1/2}\text{Ta}_{1/2}\text{O}_3$  (PST) represents another type of perovskites in which the two B-cations have 1:1 stoichiometry. Long range order in PST-type perovskites needs to be frustrated in order for relaxor behavior to be observed. Disordered PST consists of nanodomains and is a relaxor ferroelectric. While the annealed PST, which has large domains, is a normal ferroelectric [26]. Here, unlike the case of PMT-PZ, disorder is absent in the annealed PST.

Phenomenological models may be evaluated on the basis of microscopic descriptions. The glassy models explicitly requires the coexistence of chemically ordered and disordered nanodomains, as is observed in PMN. Therefore, the relaxor properties in the fully ordered PMT-PZ, which are comprised of large domains [2], cannot be described by these models. The model of ferroelectric states broken into microdomains was also developed for PMN. This assumes space charge B-site ordering where the strong random electric fields are caused by the 1:1 ordered nanodomains that carry negative charges. The model of Vugmeister and Rabitz does not explicitly depend on the formation of nanodomains and seems applicable to both PMN and coarsened PMT-PZ. The “breathing” model does not depend on the the existence of nanodomains, since charge fluctuations and polar regions can be realized even in non-stoichiometrically well-ordered materials, such as PMT-PZ.

The “unknown” interactions between the off-center ions in the phenomenological model of Vugmeister and Rabitz was actually described by Chen et al. in 1996 [21], two years before the proposal of the model. Collective displacements of ions are traced back to the special nature of the  $\text{Pb}^{2+}$  ion. It is not unusual for  $\text{Pb}^{2+}$  ion to be off-centered in order to

accommodate the lone-pair electrons. The strong Pb-O covalent bond, together with the B-O covalent bond and the Coulombic repulsion between  $\text{Pb}^{2+}$  and B-cation, causes  $\text{Pb}^{2+}$  and B cations to move together in “lockstep”. While the size difference among different types of B-cations tends to break this collective movement. The bigger cation ( $\text{B}_{>}$ ) pushes six surrounding  $\text{O}^{2-}$  ions outward, enlarging the cavities formed by three  $\text{O}^{2-}$  ions and inducing  $\text{Pb}^{2+}$  to move toward  $\text{B}_{>}$ . This breaks the correlation of displacement between  $\text{Pb}^{2+}$  and the smaller cations ( $\text{B}_{<}$ ), freeing  $\text{B}_{<}$  to rattle around its ideal position. The preference of  $\text{Pb}^{2+}$  to be close to  $\text{B}_{>}$  is the driving force for the 1:1 ordering. However, for PMN-type perovskites, the bonding preference of 1:1 ordering is incompatible with the 1:2 stoichiometry, therefore a frustrated state with only incomplete order is inevitably formed.

## 5.4 NMR Studies on PMN-PSN Solid Solutions

Currently there is no agreement on which model is best suited to describe B-site ordering. The displacements and dynamics of  $\text{Pb}^{2+}$  cations may also play a very important role in determining material properties. We are thus motivated to investigate the B-site ordering and  $\text{Pb}^{2+}$  dynamics using solid state NMR in lead-based complex B-site perovskite relaxor ferroelectrics. Solid state NMR is an excellent tool in studying structural order/disorder and dynamics. With multi-nuclear and variable temperature (VT) NMR studies, we aim to quantitatively describe the local disorder and dynamics and establish the connection to macroscopic relaxor behavior.

The PMN-PSN  $[(1-x)\text{PbMg}_{1/3}\text{Nb}_{2/3}\text{O}_3 - x\text{PbSc}_{1/2}\text{Nb}_{1/2}\text{O}_3]$  solid solutions are chosen for our NMR studies. The two end-members, PMN and PSN, represent two types of per-



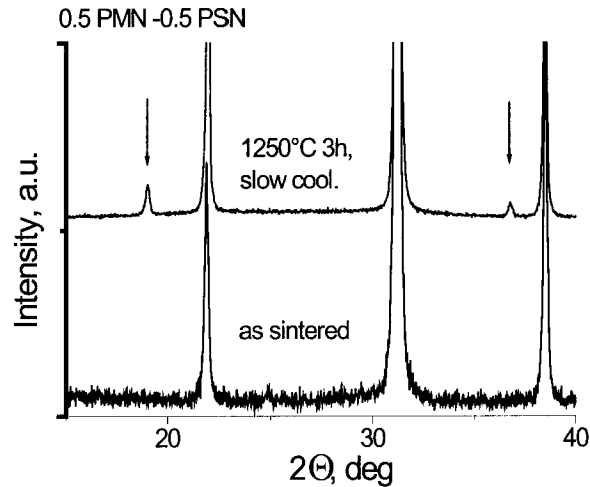


**Figure 5.3:** X-ray diffraction spectra of 0.5PMN–0.5PSN. The  $[111]_{1:1}$  long range ordering results in the  $(1/2,1/2,1/2)$  supercell reflection (indicated with vertical arrows) in the annealed sample, while it is absent in the as sintered sample [31].

ovskites with 1:2 and 1:1 B-cation stoichiometries, respectively. It is essential to use carefully prepared samples whose bulk properties have been well characterized by standard methods. The PMN-PSN ceramics studied were synthesized by Davies et al. who characterized them using X-ray diffraction (XRD), transmission electron microscopy (TEM), and frequency dependent dielectric measurements [31]. These measurements were performed on two sets of materials: “disordered”, which were simply the as-sintered samples, and “ordered”, which were obtained through prolonged annealing (24 hours, 1250 °C) followed by a slow cooling (10 °C/hour to 900 °C). Long-range ordering is revealed by XRD as the  $(1/2,1/2,1/2)$  supercell reflection; this is observed in the annealed samples and is absent in the as sintered samples (see Figure 5.3). In the TEM, the disordered samples show very limited cation order in small domains (2-3 nm) for all concentrations  $x$ . For  $x > 0.1$ , slow, high temperature annealing promotes ordering and increases domain size; the largest ordered domains

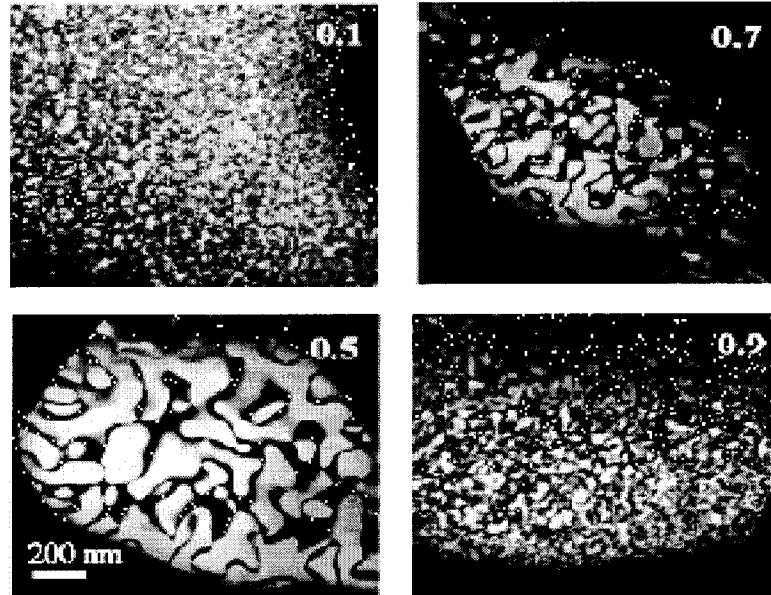


**Figure 5.4:** TEM images of  $(1-x)\text{PMN}-x\text{PSN}$  solid solutions as a function of concentration  $x$ . Domains are seen in the ordered samples [31].

( $\sim 200$  nm) are observed at  $x \sim 0.5$  (see Figure 5.4). The increased compositional order is attributed to the size, charge, and electronegativity differences between the  $\text{Nb}^{5+}$  and  $\text{Mg}^{2+}/\text{Sc}^{3+}$  ions. Dielectric results indicate that relaxor ferroelectric behavior is observed for all compositions in the disordered samples and for  $x < 0.5$  in well-ordered samples. Ordered samples with high scandium concentrations exhibit normal ferroelectric behavior, with the crossover from relaxor to normal ferroelectric behavior occurring at concentrations  $0.5 < x < 0.6$  (see Figure 5.5).

In chapter 6 we present  $^{93}\text{Nb}$  MAS and 3QMAS NMR studies, which show that a modified random site model provides the best description of the B-site ordering. In chapter 7 we present  $^{45}\text{Sc}$  MAS and 3QMAS studies. Then in chapter 8 we present variable temperature  $^{207}\text{Pb}$  static, MAS, and 2D-PASS. These lead to a quantitative description of the

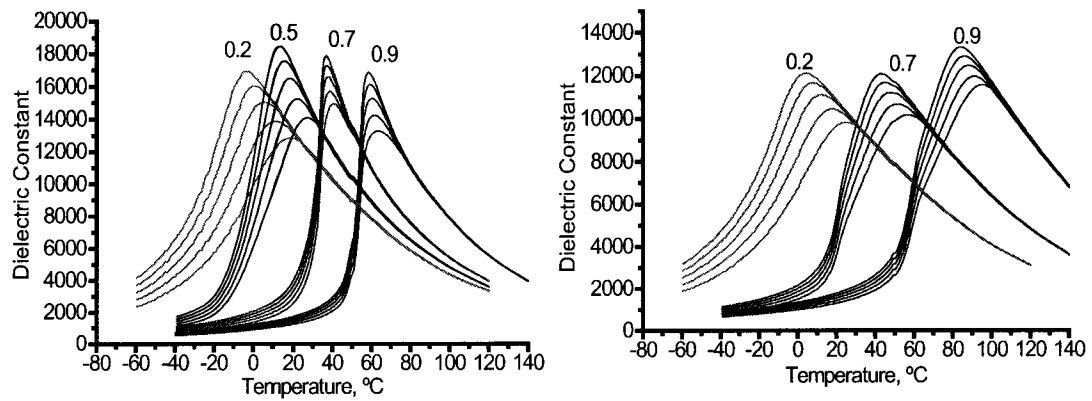


**Figure 5.5:** Dielectric constant measured at various frequencies (100 Hz–1 MHz) as function of temperature for ordered (left) and disordered (right) samples [31].

distribution of lead ion distortion and dynamics.

## Chapter 6

# $^{93}\text{Nb}$ NMR Studies of PMN-PSN

This chapter describes  $^{93}\text{Nb}$  NMR investigations of the local structure and cation order/disorder in solid solutions of  $(1 - x)\text{Pb}(\text{Mg}_{1/3}\text{Nb}_{2/3})\text{O}_3 - x\text{Pb}(\text{Sc}_{1/2}\text{Nb}_{1/2})\text{O}_3$  (PMN-PSN), as a function of PSN concentration,  $x$ . Magic-angle spinning (MAS) NMR of  $^{93}\text{Nb}$  has been used to quantitatively describe the cation order/disorder [58] and high-resolution 3-quantum MAS (3QMAS) NMR has been used to refine the spectral assignments [117].

There are only a few NMR studies of relaxor ferroelectrics [48, 28, 85, 43]. Glinchuk et al. have studied the PMN-PSN system using stationary samples at low magnetic fields (5.7 and 7 T) where the low spectral resolution precludes definitive conclusions on B-site ordering [48]. Cruz et al. have performed magic-angle spinning (MAS) and three-quantum MAS (3QMAS)  $^{93}\text{Nb}$  NMR on PMN at 9.4 T field [28]. Shore and co-workers present nutation experiments on PMN, and nutation (at 9.4 T) and MAS (at 14 T) on PMN-PT ( $\text{PbTiO}_3$ ) solid solutions [85, 43]. All  $^{93}\text{Nb}$  MAS spectra reported for PMN-PT have one narrow and one broad line. The broad peak is believed to arise from at least two overlapping lineshapes. Shore et al. associate these three components with cubic, axial and rhombic symmetry of nearest B-site neighbor environments, respectively [43]. The high resolution in our study allow us to assign spectra according to the 28 possible nearest B-site (nBn)

neighbor configurations.

## 6.1 High Field and Fast Speed MAS NMR

In  $^{93}\text{Nb}$  MAS experiments on PMN-PSN, the dominant interactions are the isotropic chemical shift and second order quadrupolar coupling, which have been described in Chapters 3 and 4, respectively. When expressed in ppm, the former ( $\delta_{\text{iso}}^{\text{CS}}$ ) is independent of magnetic field, while both the isotropic shift ( $\delta_{\text{iso}}^{2\text{Q}}$ ) and anisotropic broadening ( $\delta_{\text{aniso}}^{2\text{Q}}$ ) of the quadrupolar interaction are inversely proportional to the square of the magnetic field [Eqs. (4.42) and (4.43)]. This means that higher magnetic fields result in better spectral resolution. In an attempt to optimize the spectral resolution, MAS experiments have been performed at high magnetic fields (14 and 19.6 T) using MAS probes capable of very fast spinning ( $\nu_R = 30\text{--}35$  kHz). For the PMN-PSN solid solutions, seven narrow lines and two broad features are resolved. This allows, for the first time, the assignment of specific nearest B neighbor (nBn) configurations and quantitative comparison of experimental results with predictions of competing models of B-Site ordering.

Single pulse  $^{93}\text{Nb}$  MAS spectra were collected at three magnetic fields, 9.4, 14, and 19.6 T (proton frequencies of 400, 600, and 833 MHz respectively). Spectral resolution at 9.4 T was not satisfactory and only MAS spectra collected at 14 and 19.6 Tesla were analyzed in detail. For the experiments at 9.4 T, the  $^{93}\text{Nb}$  Larmor frequency  $\nu_L = 97.95$  MHz, rotor diameter was 4 mm, sample spinning speed  $\nu_R = 12$  kHz, rf field strength  $\nu_1 = 50$  kHz, pulse duration  $t_p = 1$   $\mu\text{s}$ , and relaxation delay  $d = 50$  ms. For experiments at 14 T,  $\nu_L = 146.9$  MHz, rotor diameter was 2.5 mm,  $\nu_R = 34$  kHz,  $\nu_1 = 50$  kHz,  $t_p = 1$   $\mu\text{s}$ , and  $d$

= 200 ms. For experiments at 19.6 T,  $\nu_L = 203.0$  MHz, rotor diameter was 2 mm,  $\nu_R = 35$  kHz,  $\nu_1 = 71$  kHz,  $t_p = 0.7$   $\mu$ s, and  $d = 100$  ms. Typically the number of scans acquired was 3000, the full spectral width was 1 MHz (dwell time 1  $\mu$ s), 4096 complex data points were collected, and NbCl<sub>5</sub> in acetonitrile was used as the chemical shift reference ( $\delta_{\text{iso}}^{\text{CS}} = 0$  ppm).

Spectra collected at 14 T were processed using Bruker XWIN software, with 100 Hz exponential multiplication, Fourier transformation, and phase correction of both zeroth and first order. Spectra collected at 19.6 T were processed using NMRPIPE [35], with three points left shift, ten points backward linear prediction, followed by 100 Hz exponential multiplication, Fourier transformation, and zeroth order phase correction. Both sets of spectra were then imported into Dominique Massiot's program DMFIT [74], base line corrected using cubic splines method, and the central transition ( $+1/2 \leftrightarrow -1/2$ ) was systematically deconvoluted into component lines.

## 6.2 MAS NMR Results

At both 14 and 19.6 T, the central transition of the <sup>93</sup>Nb MAS spectra of PMN consists of one sharp and one broad peak (see FIG. 6.1), in agreement with the literature [28, 43]. Field dependent shifts are observed for both peaks and the linewidth of the broad peak is substantially narrower at the higher field. The second order quadrupolar interaction depends on the strength of magnetic field. Thus from the field dependent shift, the quadrupolar product  $P_Q$  may be estimated. For example, between 14 and 19.6 Tesla the observed 5 ppm shift of the sharp peak in PMN spectra yields an crude estimate of the quadrupole product

$P_Q = 13$  MHz.

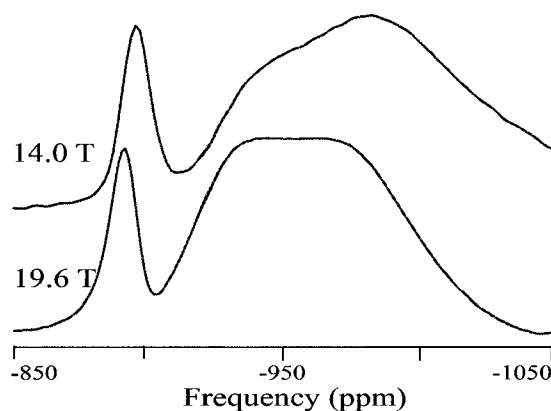


**Figure 6.1:**  $^{93}\text{Nb}$  MAS spectra of PMN collected at 14 T, with magic angle spinning speed  $\nu_R = 34$  kHz, and at 19.6 T with  $\nu_R = 35$  kHz.

Varying the magnetic field from 14 to 19.6 T causes the MAS lineshape of the broad peak to change appreciably; the former has a slanted top, while the latter is squarer. This suggests that the broad peak has at least two underlying components. The overall lineshape of the broad peak can only be reproduced if distributions of both chemical shift and quadrupolar parameters are used. Presumably these result from random local electric field gradient environments intrinsic B-site disorder. At the present resolution, it is only possible to distinguish two broad components, one at lower frequency ( $D_1$ ) and the other at higher frequency ( $D_2$ ).

The central transitions of  $^{93}\text{Nb}$  MAS spectra are shown in Fig. 6.2 for several PSN concentrations. Careful comparison of the spectra at all concentrations at both fields reveals seven narrow peaks in addition to the two distributions. The positions of these narrow peaks change very little with concentration, and their positions are separated by about 14 ppm. They are labeled from low to high frequencies as 0 through 6 (assignments are presented in

section 6.3).

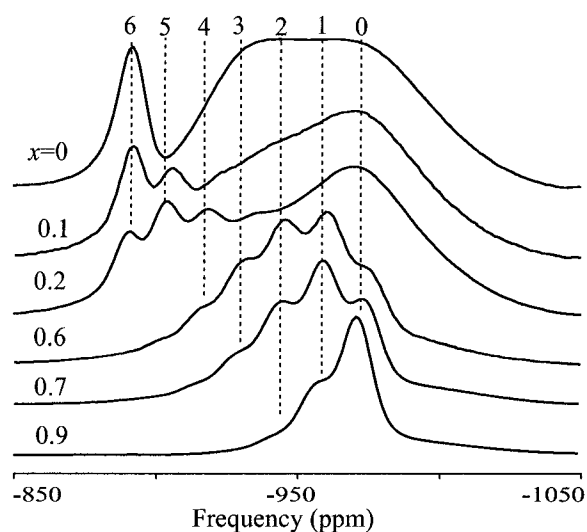


**Figure 6.2:** The seven narrow peaks in  $^{93}\text{Nb}$  MAS spectra for  $(1-x)$  PMN- $x$  PSN separated by 14 ppm approximately. Spectra are collected at 19.6 T, with sample spinning speed 35 kHz. Except for  $x = 0.0$ , all the samples are well-ordered materials.

The program DMFIT [74] was used to deconvolute the central transition MAS line-shapes. The seven narrow peaks were simulated by simple lineshapes; 50% gaussian and 50% lorentzian. Depending on the concentration of the sample, one ( $D_1$ , high  $x$ ) or two broad lines ( $D_1$  and  $D_2$ , low  $x$ ) were necessary to represent the intensities that are not reproduced by the gaussian/lorentzian lines. In the deconvolution, these broad lines include gaussian distributions of both isotropic chemical shifts and quadrupolar coupling constants. (See Table 6.1.)

The deconvolutions of PMN MAS spectra at both 14 and 19.6 T are shown in Fig. 6.3. Considerable care has been taken to obtain consistent parameters at both magnetic fields. The distribution  $D_1$  has mean  $\mu(\delta_{\text{iso}}^{\text{CS}}) = -953$  ppm, standard deviation  $\sigma(\delta_{\text{iso}}^{\text{CS}}) = 10.9$  ppm,  $\mu(\nu_Q) = 1190$  kHz,  $\sigma(\nu_Q) = 163$  kHz, and its asymmetry parameter is set to  $\eta = 0.4$



which gives good fits for both fields. D<sub>2</sub> has  $\mu(\delta_{\text{iso}}^{\text{CS}}) = -919.5$  ppm,  $\sigma(\delta_{\text{iso}}^{\text{CS}}) = 12.9$  ppm,  $\mu(\nu_Q) = 1015$  kHz,  $\sigma(\nu_Q) = 214$  kHz, and  $\eta = 0$ .

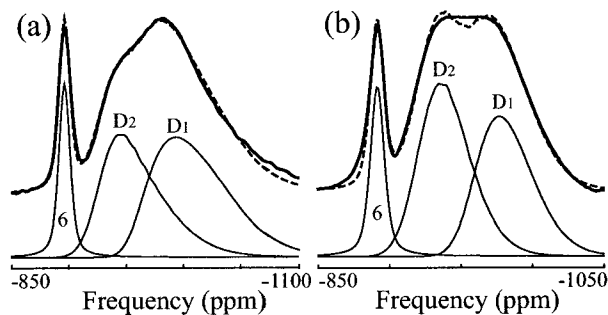


**Figure 6.3:** Constrained deconvolution of PMN MAS spectra at 14 T (a) and 19.6 T (b). Bold solid line is the experimental MAS spectrum, thin solid lines are deconvoluted components 6, D<sub>1</sub>, and D<sub>2</sub>, and dashed line is the sum of all components. (See fitting parameters in Table 6.1.)

For PMN-PSN solid solutions, deconvolutions were performed on three sets of MAS spectra; disordered samples at 14 T, disordered samples at 19.6 T, and ordered samples at 19.6 T. The parameters for broad components are very similar to those derived for PMN; very small adjustment of the mean values of the isotropic chemical shift,  $\mu(\delta_{\text{iso}}^{\text{CS}})$ , is allowed, which varies from  $-953$  to  $-951$  ppm for D<sub>1</sub>, and from  $-922$  to  $-919.5$  ppm for D<sub>2</sub>, which is essentially within the experimental error. Examples of the deconvolutions are shown in Fig. 6.4 for concentrations  $x = 0.2$  and  $0.7$ . Very good fits are achieved for all spectra with deviation being greatest for the spectrum of the  $x = 0.2$  disordered sample at 14 T (Fig. 6.4.a). It is necessary to use both broad components D<sub>1</sub> and D<sub>2</sub> for low PSN concentrations ( $x = 0, 0.1, \text{ and } 0.2$ ), but only D<sub>1</sub> is need for high concentrations ( $x = 0.6, 0.7, \text{ and } 0.9$ ). The quantitative results of the constrained deconvolution are summarized in Table 6.1.

**Table 6.1:** Deconvolution parameters of MAS spectra for  $(1-x)$ PMN- $x$ PSN solid solutions.

x	disordered, 14 T					disordered, 19.6 T					ordered, 19.6 T					
	0	0.2	0.6	0.7	0.9	0	0.2	0.6	0.7	0.9	0.1	0.2	0.6	0.7	0.9	
0 <sup>a</sup>	center (ppm)		-983.3	-982.2	-978.8			-975.1	-975.1	-971.4			-975.4	-974.2	-971.5	
	fwhm (ppm)		14.0	18.1	22.0			16.0	13.0	16.0			13.0	13.0	13.0	
	I (%)		6.3	12.8	37.4			6.3	6.4	27.7			8.4	16.9	52.5	
1	center (ppm)		-968.5	-966.8	-964.5			-960.3	-960.2	-957.0			-960.6	-959.2	-956.7	
	fwhm (ppm)		17.6	21.3	20.0			16.0	17.9	16.0			14.3	14.3	14.3	
	I (%)		19.4	29.7	10.9			17.5	23.7	15.0			21.7	31.5	25.4	
2	center (ppm)		-952.2	-950.8	-948.5			-945.1	-944.3	-942.0			-945.1	-943.6	-941.7	
	fwhm (ppm)		19.9	18.9	18.0			17.8	18.6	16.0			15.7	15.7	15.7	
	I (%)		25.9	19.7	3.3			23.2	22.4	7.0			24.8	23.6	5.0	
3	center (ppm)		-936.5	-936.0				-930.0	-928.9				-929.6	-928.9		
	fwhm (ppm)		17.4	20.4				19.3	17.0				17.0	17.0		
	I (%)		13.2	10.3				19.1	9.2				18.2	10.9		
4	center (ppm)	-924.1	-921.9	-921.3			-918.0	-915.0	-915.0		-919.0	-917.5	-915.1	-914.1		
	fwhm (ppm)	14.4	15.6	15.0			15.7	15.7	15.7		15.3	15.3	15.3	15.3		
	I (%)	5.4	5.4	2.5			6.3	6.4	2.7		2.4	7.0	7.0	2.9		
5	center (ppm)	-911.0	-908.0	-908.0			-904.2	-902.0	-902.0		-904.9	-903.5	-901.2	-901.2		
	fwhm (ppm)	14.9	16.0	17.8			15.2	15.2	14.3		13.7	13.7	13.7	13.7		
	I (%)		10.3	1.4	1.2			10.6	2.9	0.5		8.5	11.3	2.7	0.7	
6	center (ppm)	-895.5	-896.3				-891.0	-890.0	-887.0			-890.6	-890.0	-887.4	-887.4	
	fwhm (ppm)	12.0	17.0				12.0	15.5	15.5			12.0	12.0	12.0	12.0	
	I (%)	13.0	9.0				14.8	7.3	1.4			11.7	7.7	1.2	0.3	
D <sub>1</sub> <sup>b</sup>	I (%)	48.4	39.8	28.4	23.9	48.4	39.9	42.8	23.2	35.1	50.3	44.8	45.4	16.0	13.1	17.2
D <sub>2</sub> <sup>c</sup>	I (%)	38.6	35.6				45.3	33.0				32.6	28.6			

<sup>a</sup> Narrow components 0-6 are simple superpositions of 50% gaussian and 50% lorentzian. Error limits for both peak centers and fwhm (full width at half maximum) are estimated to be  $\pm 0.5$  ppm.

<sup>b</sup> D<sub>1</sub> is the first broad component with gaussian distributions of both  $\delta_{\text{iso}}^{\text{CS}}$  and  $\nu_Q$ . The mean  $\mu(\delta_{\text{iso}}^{\text{CS}})$  is allowed to vary between  $-953$  and  $-951$  ppm, standard deviation  $\sigma(\delta_{\text{iso}}^{\text{CS}}) = 10.9$  ppm,  $\mu(\nu_Q) = 1190$  kHz,  $\sigma(\nu_Q) = 163$  kHz, and the asymmetry parameter is fixed at  $\eta = 0.4$ .

<sup>c</sup> D<sub>2</sub> is the second broad component with distributions.  $\mu(\delta_{\text{iso}}^{\text{CS}})$  is from  $-922$  to  $-919.5$  ppm,  $\sigma(\delta_{\text{iso}}^{\text{CS}}) = 12.9$  ppm,  $\mu(\nu_Q) = 1015$  kHz,  $\sigma(\nu_Q) = 214$  kHz, and the asymmetry parameter is fixed at  $\eta = 0$ .

### 6.3 Spectral Assignments

We assign components of  $^{93}\text{Nb}$  MAS spectra according to the nearest B-site neighbor (nBn) configurations. This provides the most detailed description of local cation ordering in relaxor ferroelectrics to date. The solid solutions PMN-PSN have perovskite structure  $\text{ABO}_3$  (Fig. 6.5), with A on the cube center, B on the eight corners, and  $\text{O}^{2-}$  in the middle of the edges.  $\text{Pb}^{2+}$  cations sit on A sites, while B sites are occupied by three types of cations,  $\text{Mg}^{2+}$ ,  $\text{Sc}^{3+}$ , and  $\text{Nb}^{5+}$ . For a central  $\text{Nb}^{5+}$  B cation, the nearest neighbors are six oxygen ions (octahedral), next nearest neighbors are eight  $\text{Pb}^{2+}$  (hexahedral), and the next next nearest

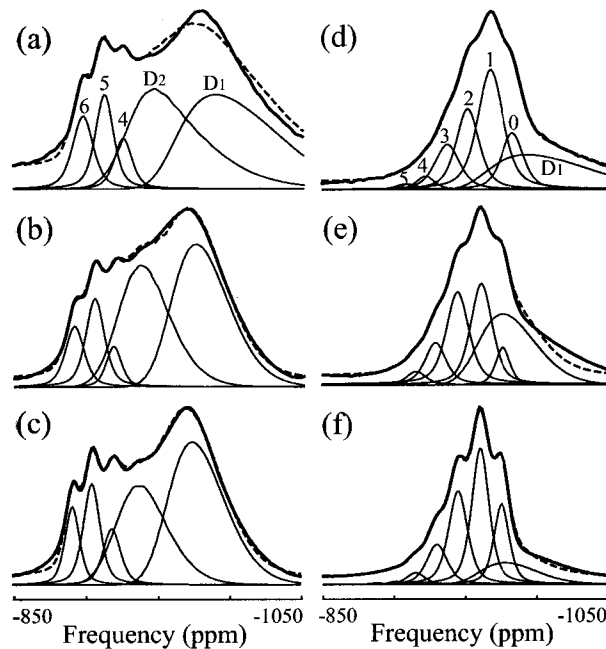


**Figure 6.4:** Deconvolution of MAS spectra for  $(1 - x)\text{PMN}-x\text{PSN}$  solid solutions. (a)  $x = 0.2$  disordered sample at 14 T. (b)  $x = 0.2$  disordered sample at 19.6 T. (c)  $x = 0.2$  ordered sample at 19.6 T. (d)  $x = 0.7$  disordered sample at 14 T. (e)  $x = 0.7$  disordered sample at 19.6 T. (f)  $x = 0.7$  ordered sample at 19.6 T. In each of (a-f), the bold solid line is the experimental spectrum, thin solid lines are decomposed components 0 – 6,  $D_1$ , and  $D_2$ , and the dashed line is the sum of all components. The dashed line in several graphs is barely visible because of the good fit. All fitting parameters are given in Table 6.1.

neighbors are six other B cations (octahedral) that we call nearest B neighbors (nBn). The first two shells are the same for each central B cation. However, the composition of the third shell varies ( $B = \text{Mg}^{2+}$ ,  $\text{Sc}^{3+}$ , and  $\text{Nb}^{5+}$ ). The valence charge, size and electronegativity are different for these B cations:  $\text{Mg}^{2+}$  (ionic radius 0.72 Å, Pauling scale electronegativity 1.31),  $\text{Sc}^{3+}$  (0.745 Å, 1.36), and  $\text{Nb}^{5+}$  (0.64 Å, 1.60) [92, 61]. The  $B_6$  cations interact with the central  $\text{Nb}^{5+}$  cation by electrostatic interactions, and can also modify the orientation, size, and shape of  $\text{O}_6$  octahedra and  $\text{Pb}_8$  hexahedra by electrostatic, covalent and steric effects (section 5.3.2). It is also reported that, in several lead based perovskite relaxor ferroelectrics, size mismatch of B cations combined with the strong  $\text{Pb}^{2+}$  off-centering (up

to 0.2 Å against B<sub>6</sub> octahedra and up to 0.5 Å against O<sub>12</sub> icosahedra) causes O<sub>6</sub> octahedra to rotate or tilt by as much as 18° [38]. As a result, the precise configuration and ordering of the three types of cations strongly affect the electron density and electric field gradient at the location of the central <sup>93</sup>Nb nuclei. These are manifested in the NMR chemical shift and quadrupolar coupling parameters. Thus it is reasonable to assign <sup>93</sup>Nb MAS spectral components according to the nBn configurations. The feasibility of this interpretation is strengthened by the fact that it gives consistent and sensible results for the concentration dependence of the relative integrated peak intensities.

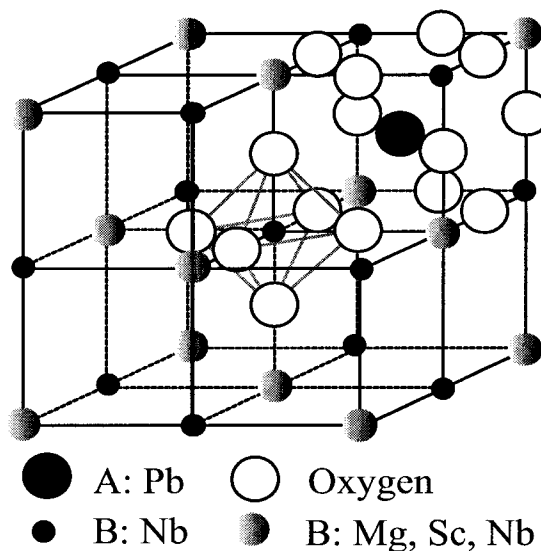


**Figure 6.5:** Perovskite structure and B-lattice for PMN-PSN. Only one complete perovskite cube and one BO<sub>6</sub> octahedron are displayed, so as to highlight the B-site lattice. Random B-site ordering in the [111] direction consists of alternating pure (Nb) and mixed (Mg, Sc, and Nb at random) planes.

Nearest B neighbor configurations will be designated by the numbers of Mg, Sc, and Nb cations,  $(N_{\text{Mg}}, N_{\text{Sc}}, N_{\text{Nb}})$ ; each number ranges from 0 to 6 with the requirement that their sum is 6. Each of the 28 nBn configurations can be represented by a point on a triangular grid in Fig. 6.6. For a given grid point, the three vectors pointing to the axes indicate the

numbers of each type of cation, and thus the triplet coordinate  $(N_{\text{Mg}}, N_{\text{Sc}}, N_{\text{Nb}})$ .

We assign the seven narrow components of the spectra (lines 6–0, see Fig. 6.2) to the seven nBn configurations consisting of no  $\text{Nb}^{5+}$ . They are designated by  $(N_{\text{Mg}}, 6 - N_{\text{Mg}}, 0)$ , with  $N_{\text{Mg}} = 6, 5, \dots, 0$  and represented by the seven grid points on the bottom of the triangle in Fig. 6.6. Only for the concentrations  $x = 0.6, 0.7$  are there minor deviations; for good quantitative agreement with the intensities of the four narrow lines 3, 2, 1 and 0, the probabilities (predicted by random site model, see section 6.4) of configurations (3,2,1), (2,3,1), (1,4,1) and (0,5,1) are added to those of (3,3,0), (2,4,0), (1,5,0) and (0,6,0) respectively. The assignments are reasonable given that in strong contrast with  $\text{Nb}^{5+}$  cations,  $\text{Mg}^{2+}$  and  $\text{Sc}^{3+}$  cations have similar size and electronegativity, and the smallest charge difference. The nBn configurations with only  $\text{Mg}^{2+}$  and/or  $\text{Sc}^{3+}$  cation have closest to cubic symmetry, and thus small EFGs; consistent with the observed narrow linewidths.

On the other hand, size and electronegativity mismatch resulting from substituting  $\text{Nb}^{5+}$  for  $\text{Mg}^{2+}/\text{Sc}^{3+}$  severely distorts the cubic symmetry, leading to larger EFGs, consequently greater linewidths. These broad lines, which are associated with nBn configurations containing  $\text{Nb}^{5+}$ , cannot be resolved and they contribute to the two broad distributions  $\text{D}_1$  and  $\text{D}_2$ . The three grid points (5,0,1), (4,1,1), and (4,0,2) in the dotted triangle are assigned to the second broad component  $\text{D}_2$  (Fig. 6.6). The remaining eighteen grid points in the dotted trapezoid contribute to the broad distribution component  $\text{D}_1$  (Fig. 6.6). Similar to the case of the narrow lines, small adjustment is made for  $\text{D}_1$  at concentrations  $x = 0.6, 0.7$ ;  $\text{D}_1$  now consists of only 14 nBn configurations, excluding the four configurations on the bottom line of the trapezoid. This partition between  $\text{D}_1$  and  $\text{D}_2$  has been made in order to find reasonable match between integrated intensities of the broad components with the

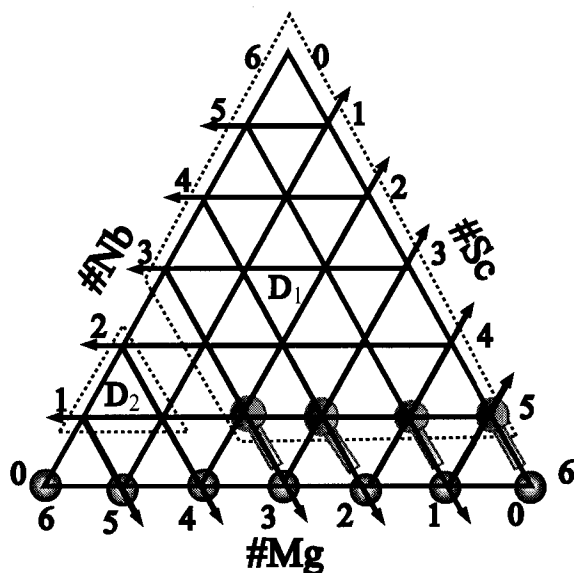


**Figure 6.6:** The twenty-eight nBn configurations of  $\text{Nb}^{5+}$  cations and their assignments. For a given grid point, the three vectors pointing to the axes indicate the numbers of each cation, and thus the triplet coordinate  $(N_{\text{Mg}}, N_{\text{Sc}}, N_{\text{Nb}})$ . The eighteen configurations in the dotted trapezoid are assigned to broad distribution component  $D_1$ . The three configurations in the dotted triangle are assigned to broad distribution component  $D_2$ . The seven configurations on the bottom line are assigned to the narrow resonance lines. Only for concentrations  $x = 0.6$  and  $0.7$ , do the four narrow lines  $(0,6,0)$ ,  $(1,5,0)$ ,  $(2,4,0)$  and  $(3,3,0)$  also include contributions from  $(0,5,1)$ ,  $(1,4,1)$ ,  $(2,3,1)$  and  $(3,2,1)$  respectively.

prediction by random site ordering model (see section 6.4). However, limited by the resolution of MAS spectra, the partition between  $D_1$  and  $D_2$  may be wrong and a new, less ambiguous partition between  $D_1$  and  $D_2$  will be made in the high-resolution 3QMAS study (see section 6.6).

In agreement with Fitzgerald et al. [43] the all-magnesium nBn configuration  $(6,0,0)$  corresponds to the high frequency narrow peak 6 (around  $-900$  ppm). Moreover, the all-niobium nBn configuration  $(0,0,6)$  contributes to the low frequency broad peak  $D_1$  (centered around  $-980$  ppm at 14 T, and  $-1020$  ppm at 9.4 T). The all-scandium configuration  $(0,6,0)$  is assigned to the low frequency narrow peak 0 (around  $-980$  ppm). These assignments are based on our experimental results and data from studies of two niobates [28, 84]. First, the

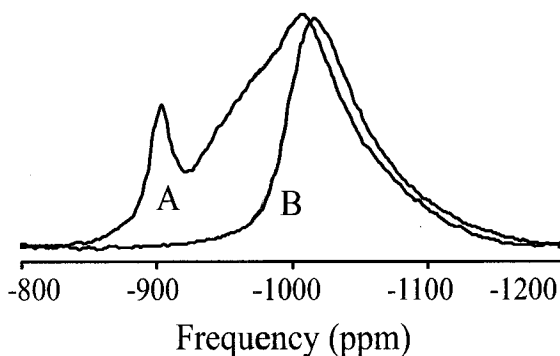


**Figure 6.7:** Comparison of MAS spectra of PMN (A) and Pyrochlore (B). Spectra were acquired at 9.4 T with sample spinning speed 32 kHz. Figure is modified from the work of Cruz et al.[28]. The chemical shift was referred to  $\text{Nb}_2\text{O}_5$  originally; and has been recalibrated to make  $\text{NbCl}_5/\text{MeCN}$  as zero ppm reference. (In our PMN spectrum at 9.4 T and spinning speed 12 kHz, the sharp peak occurs at  $-907$  ppm.)

all-magnesium configuration can be identified by comparing the MAS spectrum of PMN ( $\text{Mg}:\text{Nb} = 1:2$ ) to that of pyrochlore ( $\text{Pb}_{1.83}[\text{Mg}_{0.29}\text{Nb}_{1.71}]\text{O}_{6.39}$ ,  $\text{Mg}:\text{Nb}\sim 1:6$ ), see Fig. 6.7 [28]. In both crystalline materials, each  $\text{Nb}^{5+}$  is surrounded by six  $\text{Mg}^{2+}$  and/or  $\text{Nb}^{5+}$  cations; one notable difference, however, is that the pyrochlore has substantially lower  $\text{Mg}^{2+}$  content. Thus the population of the all-magnesium configuration (6,0,0) is predicted to be much lower in pyrochlore than that in PMN. It is obvious from Fig. 6.7 that the narrow peak of PMN around  $-907$  ppm must be attributed to the all-magnesium configuration (6,0,0), since no corresponding peak is present for pyrochlore. Second, the above analysis also leads to the conclusion that in pyrochlore the broad peak (around  $-1020$  ppm) consists of  $^{93}\text{Nb}$  species with  $\text{Nb}^{5+}$  as the majority in their nBn configurations; (0,0,6), (1,0,5), and (2,0,4). This hypothesis is further supported by the fact that four lead niobates ( $\text{Pb}_2\text{Nb}_2\text{O}_7$ ,  $\text{Pb}_3\text{Nb}_4\text{O}_{13}$ ,  $\text{Pb}_5\text{Nb}_4\text{O}_{15}$  and  $\text{Pb}_3\text{Nb}_2\text{O}_8$ ) consisting of corner sharing  $\text{NbO}_6$  octahedra have

$\delta_{\text{iso}}^{\text{CS}}$  ranging from  $-1003$  to  $-951$  ppm and  $P_Q$  ranging from  $13.6$  to  $20.6$  MHz (or  $\delta_{\text{iso}}^{2Q}$  from  $-27$  to  $-62$  ppm at  $9.4$  T) [84]. This confirms that the  $^{93}\text{Nb}$  species surrounded by six  $\text{Nb}^{5+}$  cations resonate on the low frequency side (from  $-978$  to  $-1065$  ppm at  $9.4$  T). Third, the lowest frequency narrow peak 0 is assigned to the all-scandium configuration (0,6,0). This is supported by the concentration dependence; the intensity of this peak increases monotonically with  $x$ . The largest intensity is observed in the  $x = 0.9$  spectrum (0.1 PMN - 0.9 PSN), where the concentration of scandium is largest (Fig. 6.2).

## 6.4 Models of cation disorder

We have assigned the components of MAS NMR spectra to the nearest B neighbor cation configurations, and established a relation between the integrated spectral intensities and the population of  $\text{Nb}^{5+}$  species with particular nBn configurations. Thus the experimental NMR results can be used to differentiate between various theoretical models of B-site order/disorder in perovskite ferroelectric solid solutions. The B-site ordering models can be used to predict the NMR spectral intensities, which can be directly compared to the NMR observations for all compositions,  $x$ . The two most relevant models are considered in detail: the completely random (CR) model, and the random site (RS) model (section 5.3.2).

### 6.4.1 Completely random model (CR)

In this simple model all B sites are assumed to be randomly occupied by  $\text{Mg}^{2+}$ ,  $\text{Sc}^{3+}$ , and  $\text{Nb}^{5+}$ , and the stoichiometry depends on the concentration  $x$ ;  $\text{Pb}[\text{Mg}_{(1-x)/3}\text{Sc}_{x/2}\text{Nb}_{(4-x)/6}]\text{O}_3$ . Assume that the three types of B cations have partial concentrations  $C_{\text{Mg}}$ ,  $C_{\text{Sc}}$  and  $C_{\text{Nb}}$  such that  $C_{\text{Mg}} + C_{\text{Sc}} + C_{\text{Nb}} = 1$ . Thus the partial concentrations are  $C_{\text{Mg}} = (1-x)/3$ ,  $C_{\text{Sc}} = x/2$ ,



and  $C_{\text{Nb}} = (4 - x)/6$ . For a given central  $\text{Nb}^{5+}$  ion the probability that it has a nBn configuration  $(N_{\text{Mg}}, N_{\text{Sc}}, N_{\text{Nb}})$  is

$$P_{\text{CR}}(N_{\text{Mg}}, N_{\text{Sc}}, x) = \frac{6!}{N_{\text{Mg}}!N_{\text{Sc}}!N_{\text{Nb}}!} (C_{\text{Mg}})^{N_{\text{Mg}}} (C_{\text{Sc}})^{N_{\text{Sc}}} (C_{\text{Nb}})^{N_{\text{Nb}}}. \quad (6.1)$$

In our assignments the narrow lines are configurations with no  $\text{Nb}^{5+}$  nearest B neighbors.

The probabilities are thus

$$P_{\text{CR}}(N_{\text{Mg}}, 6 - N_{\text{Mg}}, x) = \frac{6!}{N_{\text{Mg}}!(6 - N_{\text{Mg}})!} \left(\frac{1 - x}{3}\right)^{N_{\text{Mg}}} \left(\frac{x}{2}\right)^{6 - N_{\text{Mg}}}. \quad (6.2)$$

This formula gives negligible values ( $< 1.6\%$ ) for all narrow lines at all PSN concentrations. Since typical NMR intensities for the narrow lines are on the order of 10% (Table 6.1), this model fails to account for the observed NMR intensities and is an inappropriate description of B-site ordering. Moreover, it is important to appreciate that even in the disordered samples the NMR MAS spectral intensities cannot be described by the CR model (Table 6.1). This implies that there is significant short-range order even in the as sintered materials.

#### 6.4.2 Random site (RS)

This model assumes that along the [111] direction the layers of B cations alternate between pure  $\text{Nb}^{5+}$  and a random mixture of  $\text{Mg}^{2+}$ ,  $\text{Sc}^{2+}$  and the remaining  $\text{Nb}^{5+}$  (Fig. 6.5). The 1:1 ordering occurs along all four body diagonals. The name “random site” [31] is used instead of the previous “random layer” [2] since the word “layer” might suggest that the 1:1 ordering is only in one direction. The stoichiometric formula is  $\text{Pb}(\beta'_{1/2}\beta''_{1/2})\text{O}_3$ , with  $\beta' =$  random mixture  $[\text{Mg}_{2(1-x)/3}\text{Sc}_x\text{Nb}_{(1-x)/3}]$  and  $\beta'' = \text{Nb}$ . Half of the B cations are

on  $\beta'$  sites, and half are on  $\beta''$  sites, i.e.  $p_{\beta'} = 1/2, p_{\beta''} = 1/2$ . Within the mixed layer, the concentrations are  $C_{\beta'Mg} = 2(1-x)/3, C_{\beta'Sc} = x, C_{\beta'Nb} = (1-x)/3$ . The total  $Nb^{5+}$  concentration  $C_{Nb} = (4-x)/6$  is restored by calculating  $p_{\beta'}C_{\beta'Nb} + p_{\beta''}$ .

Each  $Nb^{5+}$  cation in the mixture layer ( $\beta'$ ) has six  $Nb^{5+}$  nearest B-site neighbors in the two adjacent pure  $Nb^{5+}$  layers ( $\beta''$ ). Therefore, the probability of having a B-cation which is  $\beta'$ -type  $Nb^{5+}$  with nBn configuration ( $N_{Mg}, N_{Sc}, N_{Nb}$ ) is

$$P_{\beta'Nb}(N_{Mg}, N_{Sc}, x) = p_{\beta'}C_{\beta'Nb} \delta(N_{Mg}, N_{Sc}), \quad (6.3)$$

where  $\delta = 1$  for  $N_{Mg} = 0$  and  $N_{Sc} = 0$ , 0 otherwise. Each  $Nb^{5+}$  cation in the pure layer ( $\beta''$ ) has 28 possible configurations of nearest B-neighbors from the two adjacent mixture layers ( $\beta'$ ). The probability of having a B-cation which is  $\beta''$ -type  $Nb^{5+}$  with nBn configuration ( $N_{Mg}, N_{Sc}, N_{Nb}$ ) is

$$P_{\beta''Nb}(N_{Mg}, N_{Sc}, x) = p_{\beta''} \frac{6!}{N_{Mg}!N_{Sc}!N_{Nb}!} (C_{\beta'Mg})^{N_{Mg}} (C_{\beta'Sc})^{N_{Sc}} (C_{\beta'Nb})^{N_{Nb}}. \quad (6.4)$$

The probability of having a B-cation which is  $Nb^{5+}$  with nBn configuration ( $N_{Mg}, N_{Sc}, N_{Nb}$ ) is the simply sum of equations 6.3 and 6.4,

$$P_{Nb}(N_{Mg}, N_{Sc}, x) = P_{\beta'Nb}(N_{Mg}, N_{Sc}, x) + P_{\beta''Nb}(N_{Mg}, N_{Sc}, x). \quad (6.5)$$

The summation of the probability over  $N_{Mg}$  and  $N_{Sc}$  is, not surprisingly,  $C_{Nb} = (4-x)/6$ . Thus normalization of Equation 6.5 gives the probability of having a  $Nb^{5+}$  cation with nBn configuration ( $N_{Mg}, N_{Sc}, N_{Nb}$ ),

$$P_{RS}(N_{Mg}, N_{Sc}, x) = \frac{6}{4-x} P_{Nb}(N_{Mg}, N_{Sc}, x). \quad (6.6)$$

For the narrow lines where  $N_{\text{Nb}} = 0$ , the RS prediction is found to be related to the completely random prediction [Eq. (6.2)] by

$$P_{\text{RS}}(N_{\text{Mg}}, 6 - N_{\text{Mg}}, x) = \frac{192}{4 - x} P_{\text{CR}}(N_{\text{Mg}}, 6 - N_{\text{Mg}}, x). \quad (6.7)$$

Therefore, for MAS spectral components assigned to  $(N_{\text{Mg}}, 6 - N_{\text{Mg}}, 0)$  configurations, it is obvious that the RS model yields much larger intensities than the CR model (48 times at  $x = 0$ , and 64 times at  $x = 1$ ).

The Random Site model is in very good qualitative agreement with the experimental MAS line intensities (see Table 6.2). The RS probabilities of the 28 configurations can be used to predict the integrated MAS intensities for all concentration  $x$ . In Table 6.2, the 28 probabilities for each concentration are arranged on triangular grid, as in Fig. 6.6. Theoretical intensities of the seven narrow lines and two broad lines are derived and compared with the experimental intensities (in parentheses) obtained by deconvolution of the MAS spectra obtained at 19.6 Tesla.

Although the NMR results strongly support the RS model, we would prefer to achieve quantitative agreement. Closer inspection of the overall lineshapes reveals that RS predicts intensities too low for the narrow lines with relatively large numbers of  $\text{Mg}^{2+}$  cations ( $\geq 3$ ) in the nBn configuration. For quantitative comparison, we predict the MAS lineshapes by using RS populations (from Table 6.2) and compare them with experimental spectra (FIG. 6.8). For high concentrations  $x = 0.7$  and  $0.9$ , the agreement is very good. However for the lower scandium concentrations, peak intensities corresponding to configurations  $(6,0,0)$ ,  $(5,1,0)$ ,  $(4,2,0)$ , and  $(3,3,0)$  are consistently underestimated. As illustrated in FIG. 6.8, such deficiencies cause a dramatic mismatch in the appearance of the spec-

**Table 6.2:** Random site prediction and experimental results of PMN and five ordered PMN-PSN solid solutions at 19.6 T. Contributions of twenty-eight configurations are arranged according to  $(N_{\text{Mg}}, N_{\text{Sc}}, N_{\text{Nb}})$  (see Fig. 6.6). The predicted line intensities (for the seven narrow lines and two broad distributions) are compared with experimental intensities which are in parentheses.

<p><math>x=0.0</math></p> <p style="text-align: center;"><b><math>6\text{Nb}</math></b></p> <p style="text-align: right;">D1: 49.0 (39.9)</p> <p>D2: 44.4 (45.3)</p> <p style="text-align: center;"><b><math>6\text{Mg}</math></b> 6.6 0.0 0.0 0.0 0.0 0.0 0.0 0.0 0.0 0.0 <b><math>6\text{Sc}</math></b></p> <p style="text-align: center;">(14.8 0.0 0.0 0.0 0.0 0.0 0.0)</p>	<p><math>x=0.6</math></p> <p style="text-align: center;"><b><math>6\text{Nb}</math></b></p> <p style="text-align: right;">D1: 28.0 (16.0)</p> <p>D2: 1.3 (0)</p> <p style="text-align: center;"><b><math>6\text{Mg}</math></b> 0.0 0.4 2.4 12.1 23.0 23.2 9.6 <b><math>6\text{Sc}</math></b></p> <p style="text-align: center;">(1.2 2.7 6.8 18.2 24.8 21.7 8.4)</p>
<p><math>x=0.1</math></p> <p style="text-align: center;"><b><math>6\text{Nb}</math></b></p> <p style="text-align: right;">D1: 57.7 (44.8)</p> <p>D2: 33.2 (32.6)</p> <p style="text-align: center;"><b><math>6\text{Mg}</math></b> 3.6 3.6 1.5 0.3 0.0 0.0 0.0 0.0 <b><math>6\text{Sc}</math></b></p> <p style="text-align: center;">(11.7 8.5 2.4 0.0 0.0 0.0 0.0)</p>	<p><math>x=0.7</math></p> <p style="text-align: center;"><b><math>6\text{Nb}</math></b></p> <p style="text-align: right;">D1: 19.4 (13.1)</p> <p>D2: 0.4 (0)</p> <p style="text-align: center;"><b><math>6\text{Mg}</math></b> 0.0 0.1 1.1 5.0 13.1 18.3 10.7 <b><math>6\text{Sc}</math></b></p> <p style="text-align: center;">(0.3 0.7 2.9 10.9 23.6 31.5 16.9)</p>
<p><math>x=0.2</math></p> <p style="text-align: center;"><b><math>6\text{Nb}</math></b></p> <p style="text-align: right;">D1: 65.2 (45.4)</p> <p>D2: 22.5 (28.6)</p> <p style="text-align: center;"><b><math>6\text{Mg}</math></b> 1.8 4.1 3.8 1.9 0.5 0.1 0.0 <b><math>6\text{Sc}</math></b></p> <p style="text-align: center;">(7.7 11.3 7.0 0.0 0.0 0.0 0.0)</p>	<p><math>x=0.9</math></p> <p style="text-align: center;"><b><math>6\text{Nb}</math></b></p> <p style="text-align: right;">D1: 20.7 (17.2)</p> <p>D2: 0 (0)</p> <p style="text-align: center;"><b><math>6\text{Mg}</math></b> 0.0 0.0 0.0 0.4 4.2 22.9 51.4 <b><math>6\text{Sc}</math></b></p> <p style="text-align: center;">(0.0 0.0 0.0 0.0 5.0 25.4 52.5)</p>

tra. This is particularly demonstrated in the sharp peak of the PMN associated with six  $\text{Mg}^{2+}$  neighbors,  $\text{Nb}(6,0,0)$ . These comparisons attest to the high specificity of NMR and its unique ability to probe local order and disorder in solids.

### 6.4.3 Modified RS model

We believe that the primary limitation of the RS model lies in its assumption that within the mixed layers all three types of cations ( $\text{Mg}^{2+}$ ,  $\text{Sc}^{3+}$ , and  $\text{Nb}^{5+}$ ) are distributed completely randomly. In fact their differences in valence charge, ionic size, and electronegativity are all possible driving forces for cation preference within the mixture layers. Pragmatically,

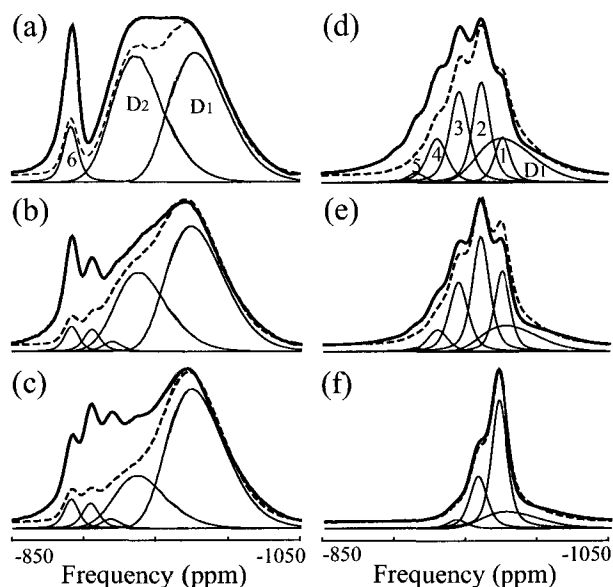


**Figure 6.8:** Random site predictions of line components (thin solid) and total intensities (dotted line), compared with MAS spectra (solid bold) at 19.6 T for  $(1-x)$ PMN- $x$ PSN samples. (a) PMN; (b-f) ordered samples with PSN concentration  $x = 0.1, 0.2, 0.6, 0.7,$  and  $0.9$  respectively.

it appears that there is some degree of  $\text{Mg}^{2+}$  clustering on the mixture layers, so as to enhance the intensities for the niobiums with relatively large numbers of  $\text{Mg}^{2+}$  in the nearest B-neighbor configuration.

This hypothesis can be most simply examined by Monte Carlo simulation of PMN, because the deviation of RS model is most serious at this concentration ( $x = 0$ ), it is simplest to simulate, and there is only one unlike-pair energy to consider,  $U_{\text{Mg},\text{Nb}}$  between  $\text{Mg}^{2+}$  and  $\text{Nb}^{5+}$ . The B-site lattice is initialized according to the random site model, that is, [111] planes alternate between pure  $\text{Nb}^{5+}$  ( $\beta''$ ) and random mixture of the  $\text{Mg}^{2+}$  and the remaining  $\text{Nb}^{5+}$  ( $\beta'$ ). The lattice size ( $30 \times 30 \times 30$ ) is large enough to ensure that the 28 nBn probabilities predicted by the RS model are reproduced by counting the nearest B configurations on the lattice. The  $[111]_{1:1}$  ordering, which is the compromise

between the long range electrostatic interactions among B cations and the local effect of large  $\text{Pb}^{2+}$  covalency (section 5.3.2), should be maintained throughout the simulation. For this purpose, the pure B sublattice ( $\beta''$ ) is fixed and the Monte Carlo algorithm is only applied on the mixed B sublattice ( $\beta'$ ). Since swapping two cations of the same type does not change energy, we may set like-pair energies to zero and only consider the unlike-pair energy between  $\text{Mg}^{2+}$  and  $\text{Nb}^{5+}$ . Thus, the Monte Carlo algorithm is: randomly pick a nearest neighbor pair on the mixture sublattice and then attempt to swap them. If the total energy decreases, accept the swap; otherwise, accept with probability  $\exp(-\Delta E/RT)$ , where  $\Delta E$  is the energy difference resulting from the swap,  $R$  is the universal gas constant, and  $T$  is temperature. Repeat the process for a large number of times ( $8.1 \times 10^8$ ) and then evaluate the 28 nBn probabilities over the whole B lattice. The experimental intensity (14%) of the all-magnesium (6, 0, 0) narrow line is reproduced when the unlike-pair energy is adjusted to  $U_{Mg,Nb} = -1.3 RT$ . At room temperature (300 K) this energy is  $-3.25$  kJ/mole, which is interestingly close to  $-3.14$  kJ/mole, the enthalpy change associated with the RS order-disorder transition [31]. Whatever their origin, whether differences in charge, size, or electronegativity, these driving forces bring the B lattice to the  $[111]_{1:1}$  ordering. They also result in the mixture layers exhibiting some degree of clustering, rather than complete randomness.

## 6.5 Higher Resolution Needed: 3QMAS NMR

In one-dimensional MAS spectra, it is very difficult to unambiguously and uniquely determine these two distribution functions independently because of spectral broadening and

overlap. Therefore, we chose a set of distribution parameters that consistently fit PMN line-shapes collected at two magnetic fields (14 and 19.6 Tesla), and all the subsequent fits were constrained to use the same parameter set for all PSN concentrations. This does not affect the accuracy for the narrow peak intensities; but it may not appropriately partition the distribution intensities in  $D_1$  and  $D_2$ . Thus the reported results of B-site ordering are valid, but the structural information derived for  $D_1$  and  $D_2$  using this over-simplified approach is prone to systematic errors and is intrinsically less accurate.

High-resolution two-dimensional 3-quantum MAS (3QMAS) NMR can provide more accurate and precise local structural information. With the additional isotropic dimension, both isotropic chemical shift and quadrupole coupling product can be determined from a 3QMAS experiment at a single magnetic field. Consequently, a distribution of chemical shifts can be disentangled from a distribution of quadrupole coupling products.

Because of fast  $T_1$  ( $< 50$  ms) and  $T_2$  ( $< 0.5$  ms) relaxation times the 3-pulse Z-filter 3QMAS sequence (see Section 4.6) was used to collect hypercomplex data at 19.6 T [5]. The optimized pulse widths were 2.5, 0.7, and 5  $\mu\text{s}$  respectively. The rf field strength was  $\nu_1 = 75$  kHz for the first two pulses, and  $\nu_1 = 10$  kHz for the third selective pulse. The interval between the second and third pulses was synchronized to one rotor period, 28  $\mu\text{s}$  (rotor of diameter 2 mm was spinning at 35.7 kHz); 512 complex data points were collected with dwell time 14  $\mu\text{s}$  in the direct acquisition dimension; 32 time increments ( $\Delta t_1 = 28$   $\mu\text{s}$ ) were used in the indirect acquisition dimension; 4000 scans were accumulated with 100 ms relaxation delay. A solution of  $\text{NbCl}_5$  in acetonitrile was used as the chemical shift reference ( $\delta_{\text{iso}}^{\text{CS}} = 0$  ppm).

Spectra were processed using customized NMRPIPE [35] following the steps (including

the shear transformation) described by Massiot et al. [73] Gaussian broadening of width 100 Hz was applied to the direct (or MAS) dimension following the echo centers; while no apodization was applied to the indirect (or isotropic) dimension. The two axes are defined in Eqs. (4.43) and (4.50).

## 6.6 3QMAS Results

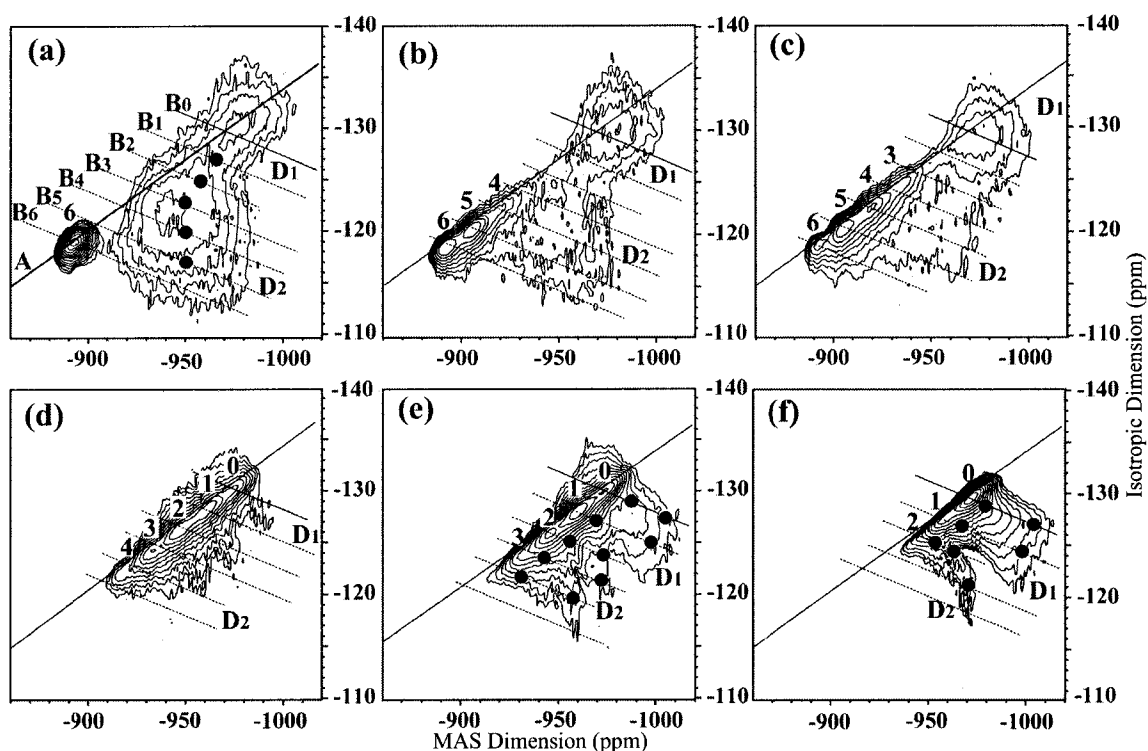


**Figure 6.9:**  $^{93}\text{Nb}$  3QMAS spectra for  $(1-x)$ PMN- $x$ PSN solid solutions, with concentrations  $x = 0$  (a), 0.1 (b), 0.2 (c), 0.6 (d), 0.7 (e), and 0.9 (f). Line A has slope 17/127; lines  $B_i$  ( $i = 0, 1, \dots, 6$ ) have slope  $-10/127$  and pass through positions of narrow peaks (see text for definitions). The contour levels start from 80% and decrease by factor 0.8. Different contour numbers are chosen so as to display signals with similar noise strength; 12 levels in (a) and (e) with 6.9% minimum, 9 in (b) with 13.4% minimum, 8 in (c) with 16.8% minimum, 10 in (d) with 10.7% minimum, and 14 in (f) with 4.4% minimum. Filled circles mark the sampling points whose coordinates are used to calculate NMR parameters (see text).



The  $^{93}\text{Nb}$  3QMAS spectra for six concentrations of the solid solutions  $(1-x)$ PMN- $x$ PSN are presented in Fig. 6.9. In the figure, line A is chemical shift distribution axis and a set of parallel lines  $B_i$  ( $i = 0, 1, \dots, 6$ ) are quadrupole distribution axes, as defined in section 4.8. For crystalline materials with well-defined crystal sites, the contours of each site should be parallel to the MAS dimension. However, in amorphous materials or in crystalline materials (such as the relaxor ferroelectrics) where many different cations can occupy crystallographically equivalent sites, there could be quasi-continuous distributions of NMR parameters. Any distribution of parameters results in contours that are slanted instead of parallel to the MAS dimension [12, 74]. Because of high correlation between the fitting parameters, the axes of distributions (A and  $B_i$ ) are central to the extraction of unique and unambiguous values  $\delta_{\text{iso}}^{\text{CS}}$ ,  $P_Q$ , and populations for the distributions  $D_1$  and  $D_2$ . Without this knowledge no meaningful interpretation of the changes of  $\delta_{\text{iso}}^{\text{CS}}$  and  $P_Q$  would be possible.

An example serves the purpose of reiterating the critical role of the distribution axes in interpreting the NMR parameters. In Fig. 6.10, we try to fit the lineshape of a slice taken from the PMN 3QMAS spectrum [Fig. 6.9(a)] at  $\delta_{\text{id}} = -120$  ppm. The slice appears to be an overlap of two peaks; for each peak, there are numerous pair of  $\delta_{\text{iso}}^{\text{CS}}$  and  $P_Q$  values which give acceptable fits to the lineshape, with appropriate amount of line broadening. Two equally good fits with rather different parameters are presented in Figs. 6.10(a) and 6.10(b). In Fig. 6.10(a), the narrow peak is fit with parameters  $\delta_{\text{iso}}^{\text{CS}} = -891.5$  ppm,  $P_Q = 10$  MHz, and lorentzian broadening of 3.5 ppm; the broad peak is fit with parameters  $\delta_{\text{iso}}^{\text{CS}} = -911$  ppm,  $P_Q = 31$  MHz, and lorentzian broadening of 6 ppm. In Fig. 6.10(b), the narrow peak is fit with parameters  $\delta_{\text{iso}}^{\text{CS}} = -894.5$  ppm,  $P_Q = 5$  MHz, and lorentzian broadening of 7 ppm; the

broad peak is fit with parameters  $\delta_{\text{iso}}^{\text{CS}} = -930$  ppm,  $P_Q = 20$  MHz, and lorentz broadening of 18 ppm. The failure of this slice-fitting approach, which is routinely used to extract NMR parameters ( $\delta_{\text{iso}}^{\text{CS}}$ ,  $C_Q$ ,  $\eta$ ) from MQMAS spectra of crystalline materials (cf Section 4.7), is due to the absence of characteristic features because of the disorder nature in the relaxor ferroelectrics (for a simple second order quadrupolar lineshape, there are usually two peaks and several discontinuities which sensitively depend on the value of  $\eta$ ).

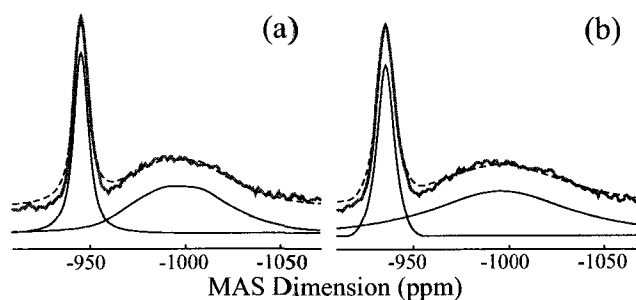


**Figure 6.10:** Lineshape fits for a slice taken from the PMN 3QMAS spectrum [Fig. 6.9(a) at  $\delta_{\text{id}} = -120$  ppm]. Bold solid line is the experimental spectrum, thin solid lines are fitting components, and dashed line is the sum of the two component lines. Equally good fits are obtained with very different parameters (see fitting parameters in text).

### 6.6.1 PMN

The PMN 3QMAS spectrum [Fig. 6.9(a)] reveals three sites; one narrow peak corresponding to  $^{93}\text{Nb}$  with six  $\text{Mg}^{2+}$  nearest B neighbors (label 6) and two broad peaks labeled  $D_1$  and  $D_2$ , respectively. One may compare their quadrupole products  $P_Q$  instantly by their distances from chemical shift axis (line A). The “mass centers” of peaks 6 and  $D_1$  are very close to line A, therefore these peaks have small and similar  $P_Q$ . The center of peak  $D_2$  is far from line A and thus a much larger  $P_Q$  is expected. The NMR parameters  $\delta_{\text{iso}}^{\text{CS}}$  and  $P_Q$  may be estimated from the coordinates of “mass centers” ( $\langle\delta_{\text{MAS}}\rangle$ ,  $\delta_{\text{id}}$ ) by solving Eqs. (4.43) and (4.50). These coordinates are best determined by varying contour spacing until a very

small closed contour is seen around a peak; spacing with factor 0.95 usually works. The results are summarized in Table 6.3. For peak 6,  $P_Q = 9.0$  MHz and  $\delta_{\text{iso}}^{\text{CS}} = -889.9$  ppm are calculated from coordinates  $(-892.6, -118.9)$  ppm. The quadrupole product 9.0 MHz agrees with the value 8.9 MHz found in another 3QMAS study by Cruz et al. [28], but is somewhat smaller than the value estimated ( $P_Q \sim 12$  MHz) in our previous analysis of the spinning-sideband manifold in a MAS spectrum [58]. Peak 6 has small distributions of NMR parameters and these distributions may be caused by effects of cations further than the nearest B cations. The evidence for distributions of  $\delta_{\text{iso}}^{\text{CS}}$  and  $P_Q$  is that the contours of this peak [Fig. 6.9(a)] are not parallel to the MAS dimension. For example, a point with coordinates  $(-892.6, -118.4)$  ppm, which is only 0.5 ppm away from the “mass center”, gives  $P_Q = 12.3$  MHz and  $\delta_{\text{iso}}^{\text{CS}} = -887.5$  ppm.

**Table 6.3:** NMR parameters for the narrow peak (6) and the two broad peaks (D<sub>1</sub> and D<sub>2</sub>) of PMN.

	$(\langle \delta_{\text{MAS}} \rangle, \delta_{\text{id}})$ (ppm)	$\delta_{\text{iso}}^{\text{CS}}$ (ppm) <sup>a</sup>	$P_Q$ (MHz) <sup>b</sup>
6	(-892.6, -118.9)	-889.9, -907 <sup>c</sup>	9.0, 8.9 <sup>c</sup>
D <sub>2</sub>	(-944.0, -121.0)	-918.8, -925 <sup>c</sup>	27.3, 21.5 <sup>c</sup>
D <sub>1</sub>	(-976.0, -130.0)	-973.0	9.4

<sup>a</sup> Errors are estimated as 0.5 ppm for  $\delta_{\text{iso}}^{\text{CS}}$ .

<sup>b</sup> Errors are estimated as 1 MHz for  $P_Q$ .

<sup>c</sup> Values quoted from another 3QMAS study of PMN [28], where chemical shift was originally referred to solid Nb<sub>2</sub>O<sub>5</sub> and has been re-calculated to refer to NbCl<sub>5</sub>/MeCN solution (cf caption of Fig. 6.7).

In the 3QMAS spectrum for PMN obtained by Cruz et al. (at 9.4 T with rotor speed 14 kHz), only one broad peak is identified with  $P_Q = 21.5$  MHz [28]. This is closet to the broad peak D<sub>2</sub> in our spectrum ( $P_Q = 27.3$  MHz obtained by the “mass center” of the peak, Table 6.3). High magnetic field strength (19.6 T) and fast sample spinning speed (35.7 kHz) in our 3QMAS experiment help to unambiguously resolve the other broad peak.

This additional peak D<sub>1</sub> has  $P_Q = 9.4$  MHz and  $\delta_{\text{iso}}^{\text{CS}} = -973$  ppm (Table 6.3).

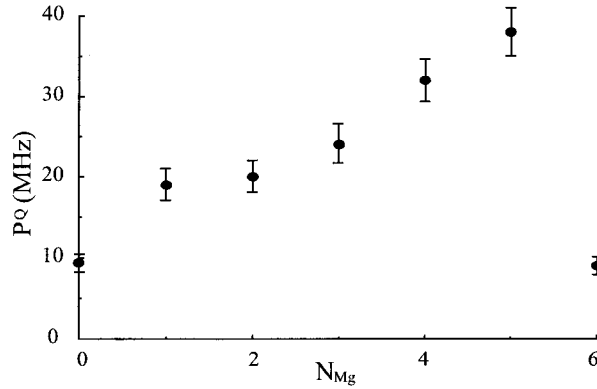


**Figure 6.11:**  $^{93}\text{Nb}$  quadrupole products of the nearest B neighbor configurations with only  $\text{Mg}^{2+}$  and  $\text{Nb}^{5+}$ ,  $(N_{\text{Mg}}, 0, 6 - N_{\text{Mg}})$ .

Large distributions of NMR parameters are evident for peaks D<sub>1</sub> and D<sub>2</sub> since the lineshapes are very broad and featureless. In PMN, there are seven nBn configurations;  $(N_{\text{Mg}}, 0, 6 - N_{\text{Mg}})$ , with  $N_{\text{Mg}} = 0, 1, \dots, 6$ . Later in Section 6.6 we will show that the isotropic chemical shift of any nBn configuration  $(N_{\text{Mg}}, N_{\text{Sc}}, N_{\text{Nb}})$  is mainly determined by the number of  $\text{Mg}^{2+}$  cations ( $N_{\text{Mg}}$ ) and is independent of the ratio  $N_{\text{Sc}}/N_{\text{Nb}}$ . Along each of the seven quadrupole distribution axes B<sub>*i*</sub> ( $i = 0, 1, \dots, 6$ ) shown in Fig. 6.9, the  $\delta_{\text{iso}}^{\text{CS}}$  value is solely determined by  $N_{\text{Mg}} = i$ . The quadrupole products of configurations with  $N_{\text{Mg}} = 6$  and 0 have been determined to be 9.0 and 9.4 MHz (Table 6.3). The quadrupole products of the remaining 5 configurations may be estimated from the coordinates of the 5 sampling points [marked by filled circles in Fig. 6.9(a)];  $P_Q = 38, 32, 24, 20$ , and 19 MHz for  $N_{\text{Mg}} = 5, 4, 3, 2$ , and 1, respectively. The quadrupole products of the seven configurations (with  $N_{\text{Sc}} = 0$  since there is no Scandium in PMN) are plotted against the number of  $\text{Mg}^{2+}$ ,  $N_{\text{Mg}}$  in Fig. 6.11. The pure-magnesium (6,0,0) and pure-niobium (0,0,6) configurations have small  $P_Q$  because of high symmetry. For configurations with both  $\text{Mg}^{2+}$  and  $\text{Nb}^{5+}$  the mismatch

lowers the symmetry, and therefore larger  $P_Q$  values are reasonable. It is interesting to notice that the (5,0,1) configuration has the largest  $P_Q$ . The large quadrupole effect of this configuration causes the resonance to shift in the lower-left direction along the quadrupole distribution axis  $B_5$  (Fig. 6.9); this explains the gap between narrow peak 6 and the broad peak  $D_2$  (also observed in the MAS spectrum of PMN).

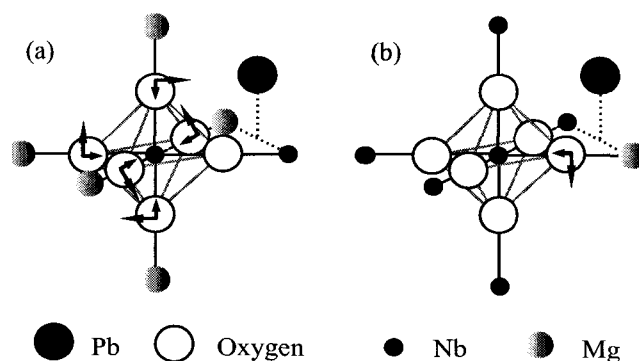


**Figure 6.12:** The two Sc-deficient nearest B-site (nBn) configurations: (5,0,1) with five Mg, one Nb (a) and (1,0,5) with one Mg, five Nb (b). The larger  $Mg^{2+}$  cation pushes oxygen ion toward the smaller cation  $Nb^{5+}$  in the center; moreover, size mismatch of the ions, which means the sum of ionic radii  $r_{Mg^{2+}} + 2r_{O^{2-}} + r_{Nb^{5+}} = 4.16 \text{ \AA}$  is greater than the cell parameter (for PMN)  $a = 4.05 \text{ \AA}$ , results in the transverse displacement of the oxygen ions. According to Bonneau et al., [13] the longitudinal displacement is  $0.07 \text{ \AA}$  and the transverse displacement is  $0.13 \text{ \AA}$ . The more distorted  $O_6$  octahedron in (a) results in larger electric field gradients than in (b).

The configuration (5, 0, 1) has  $P_Q$  double that of configuration (1, 0, 5); 40 MHz versus 19 MHz. The distortion of the  $O_6$  octahedron, which is the immediate surrounding of the center niobium, has the greatest influence on the electric field gradients. The environments of the two nBn configurations are shown in Fig. 6.12. According to Chen et al. the larger  $Mg^{2+}$  cation pushes the oxygen ion toward the smaller  $Nb^{5+}$  cation in the center. [21] Moreover, size mismatch, which here means the sum of ionic radii  $r_{Mg^{2+}} + 2r_{O^{2-}} + r_{Nb^{5+}} = 4.16 \text{ \AA}$  is greater than the cell parameter  $a = 4.05 \text{ \AA}$ , results in the transverse displacement of the

oxygen ions. [38] According to the results of the powder neutron diffraction refinements of PMN at 307°C, [13] the longitudinal displacement is 0.07 Å and the transverse displacement is 0.13 Å. These result in a larger O<sub>6</sub> distortion in the (5, 0, 1) configuration than in the (1, 0, 5) configuration (Fig. 6.12). This distortion is consistent with the much larger electric field gradient and quadrupole product in the (5, 0, 1) configuration.

### 6.6.2 (1 - x)PMN-xPSN: Narrow Peaks

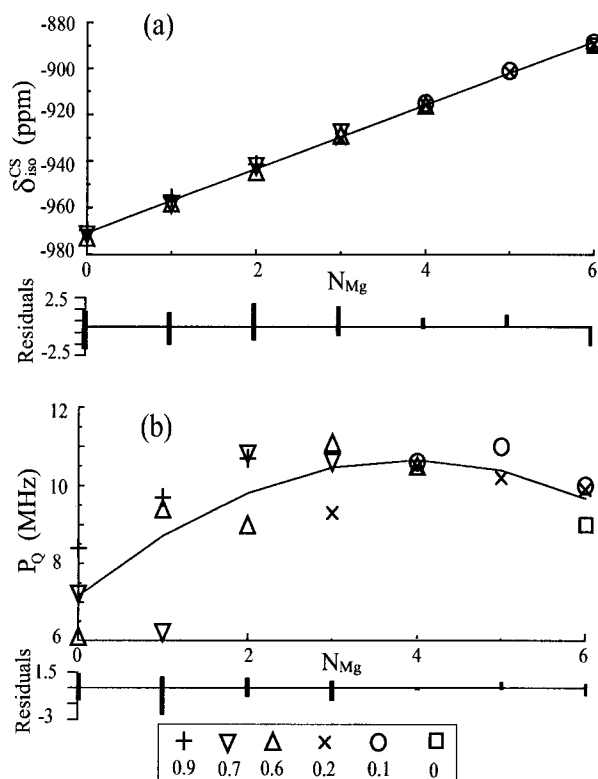


**Figure 6.13:** Isotropic chemical shifts (a) and quadrupole products (b) of the seven narrow peaks in  $^{93}\text{Nb}$  3QMAS spectra of  $(1 - x)\text{PMN}-x\text{PSN}$ . Each concentration  $x$  is marked with a unique symbol (see legend at the bottom). These peaks have only  $\text{Mg}^{2+}$  and  $\text{Sc}^{3+}$  cations as their nearest B-site neighbors,  $(N_{Mg}, 6 - N_{Mg}, 0)$ . Linear fit in (a):  $\delta_{iso}^{CS} = 13.7(\pm 0.1)N_{Mg} - 970.7(\pm 0.4)$  ppm (correlation coefficient  $R = 0.998$ ). Quadratic fit in (b):  $P_Q = -0.23(\pm 0.06)N_{Mg}^2 + 1.8(\pm 0.4)N_{Mg} + 7.2(\pm 0.5)$  MHz ( $R = 0.663$ ). The residuals are plotted below each sub-figure.

In the spectrum of the solid solution with  $x = 0.1$  [Fig. 6.9(b)], two more narrow peaks (labeled 5 and 4) are observed in addition to the narrow peak 6, which is the only narrow peak observed in PMN spectrum. For  $x = 0.2$  [Fig. 6.9(c)], one more narrow peak 3 is observed. For  $x = 0.6$  [Fig. 6.9(d)], peak 6 disappears completely and peak 5 is very weak. Meanwhile, new narrow peaks 2, 1, and 0 are observed. For  $x = 0.7$  [Fig. 6.9(e)], intensity of peak 5 disappears completely and peak 4 becomes weak. For  $x = 0.9$  [Fig. 6.9(f)], narrow peak 3 also disappears. The NMR parameters ( $\delta_{\text{iso}}^{\text{CS}}$  and  $P_Q$ ) of these peaks are calculated from their coordinates in the spectra; the results are summarized in Fig. 6.13. The seven narrow peaks have been assigned to the seven  $\text{Nb}^{5+}$ -deficient configurations ( $N_{\text{Mg}}, 6 - N_{\text{Mg}}, 0$ ), with  $N_{\text{Mg}} = 0, 1, \dots, 6$ ;  $N_{\text{Mg}}$  coincides with the number labelling each peak. The isotropic chemical shift is linearly correlated with the number of  $\text{Mg}^{2+}$  cations in the nBn configuration,

$$\delta_{\text{iso}}^{\text{CS}} = 13.7(\pm 0.1)N_{\text{Mg}} - 970.7(\pm 0.4) \text{ ppm.} \quad (6.8)$$

This means replacing each  $\text{Mg}^{2+}$  ion by a  $\text{Sc}^{3+}$  ion causes a  $-13.7$  ppm shift. An analogous linear dependence has been observed for  $^{207}\text{Pb}$  isotropic chemical shift in mixed crystals of lead/strontium nitrate  $[(\text{Pb},\text{Sr})(\text{NO}_3)_2]$  and lead/barium nitrate  $[(\text{Pb},\text{Ba})(\text{NO}_3)_2]$  [67]. In each of the mixed crystals, thirteen  $^{207}\text{Pb}$  resonance lines were observed due to lead ions with 0 to 12  $\text{Pb}^{2+}$  nearest-neighbor cations replaced by  $\text{Sr}^{2+}$  or  $\text{Ba}^{2+}$ . The average shift is 22 ppm per  $\text{Sr}^{2+}$  ion and 19 ppm per  $\text{Ba}^{2+}$  ion.

For the quadrupole product the data, though more scattered with concentration  $x$ , can

be fit to a quadratic dependence on the number of  $\text{Mg}^{2+}$  cations,

$$P_Q = -0.23(\pm 0.06)N_{\text{Mg}}^2 + 1.8(\pm 0.4)N_{\text{Mg}} + 7.2(\pm 0.5) \text{ MHz.} \quad (6.9)$$

The fitting curve [Fig. 6.13(b)] shows that mixing  $\text{Mg}^{2+}$  and  $\text{Sc}^{3+}$  cations in a nBn configuration slightly increases the electric field gradient at the central  $^{93}\text{Nb}$  site, which seems intuitively reasonable.

The applicability of the empirical relationship between  $\delta_{\text{iso}}^{\text{CS}}$  and  $N_{\text{Mg}}$  [Eq. (6.8)] deduced for the  $\text{Nb}^{5+}$ -deficient nBn configurations may be generalized to  $\text{Nb}^{5+}$ -containing nBn configurations. This generalization is based on the observation that the highest contour of 0.1PMN-0.9PSN, where locates the all scandium nBn configuration [(0,6,0), peak 0], almost coincides with the  $D_1$  “mass center” of PMN, which corresponds to the all niobium configuration [(0,0,6)] [see Figs. 6.9(a) and (f)]. These two configurations have similar NMR parameters;  $P_Q = 8.4, 9.4$  MHz and  $\delta_{\text{iso}}^{\text{CS}} = -969.6, -973$  ppm for the 6-scandium and 6-niobium configurations respectively. The two configurations have small  $P_Q$  values implying that they are both highly symmetric and ion displacements must be small. However, without detailed ab initio calculations it can not be understood why the two configurations should have such similar  $\delta_{\text{iso}}^{\text{CS}}$  values. Nevertheless, the applicability of the empirical relation [Eq. (6.8)] may be generalized based on this observation. That is, the isotropic chemical shift of any nBn configuration ( $N_{\text{Mg}}, N_{\text{Sc}}, N_{\text{Nb}}$ ) is determined by  $N_{\text{Mg}}$ , while the ratio  $N_{\text{Sc}}/N_{\text{Nb}}$  only results in minor adjustment. This generalization will soon be proven to be very important in interpreting the NMR parameters of other nBn configurations (and in fact, it has been used in Section 6.6 to interpret the configurations with only  $\text{Mg}^{2+}$  and  $\text{Nb}^{5+}$  in them).



### 6.6.3 $(1-x)$ PMN- $x$ PSN: Broad Distribution Peaks

In PMN, the two distributions  $D_1$  and  $D_2$  which were severely overlapped in the one-dimensional MAS spectra, are clearly resolved in the high-resolution two-dimensional 3QMAS spectrum [Fig. 6.9(a)]. As PSN concentration  $x$  [ $(1-x)$ PMN- $x$ PSN] increases from 0 to 0.1, 0.2, and 0.6 [Figs. 6.9(b), 6.9(c), and 6.9(d)],  $D_1$  and  $D_2$  intensities progressively decrease. However, at  $x = 0.6$  [Fig. 6.9(d)] the  $D_1$  intensity starts growing back but with a new shape. The new  $D_1$  has very strong intensities in 3QMAS spectra of concentrations  $x = 0.7$  and 0.9 [Figs. 6.9(e) and 6.9(f)]. In addition, the  $D_2$  distribution also has a new shape at high concentrations [ $x = 0.7$  and 0.9, Figs. 6.9(e) and 6.9(f)].

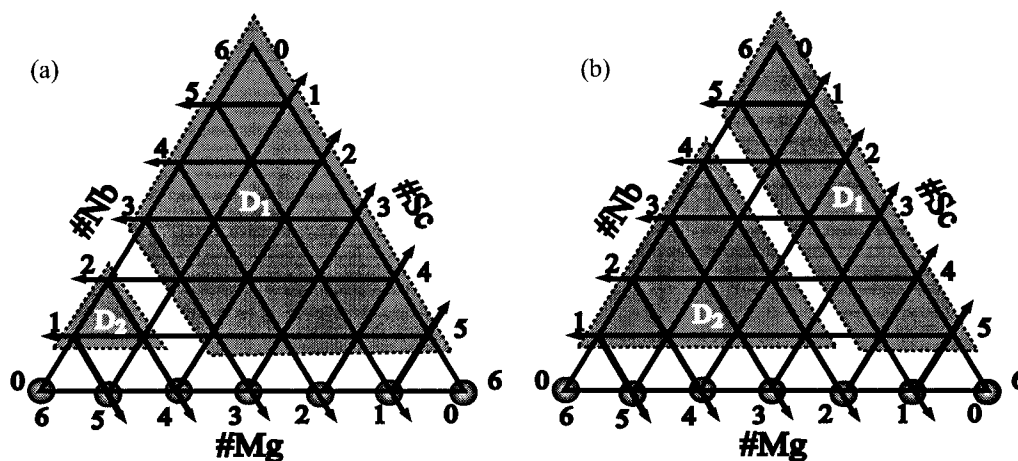


**Figure 6.14:** Assignments according to MAS (a) and 3QMAS (b) studies. The higher resolution of 3QMAS NMR allow the unambiguous partition between the two broad distributions  $D_1$  and  $D_2$ . See Fig. 6.6 for interpretation of the grids.

By inspection of the 3QMAS spectra of all solid solutions (Fig. 6.9), it seems a quadrupole distribution axis positioned midway between lines  $B_1$  and  $B_2$  marks an appropriate boundary between the two distributions  $D_1$  and  $D_2$ . With the assistance of the generalized relationship between isotropic chemical shift and the number of  $Mg^{2+}$  in

the configuration [Section 6.6, Eq. (6.8)], it is reasonable to assign  $D_1$  to configurations  $(N_{\text{Mg}}, N_{\text{Sc}}, N_{\text{Nb}})$  with  $N_{\text{Mg}} = 0, 1$  and  $N_{\text{Nb}} \neq 0$ .  $D_2$  has the rest of  $N_{\text{Nb}} \neq 0$  configurations with  $N_{\text{Mg}} = 2, 3, 4, 5$ . These assignments are somewhat different from the previous ones based on the MAS spectra, where  $D_1$  was assigned to configurations with  $N_{\text{Mg}} = 0, 1, 2, 3$  and  $N_{\text{Nb}} \neq 0$  and  $D_2$  to  $N_{\text{Mg}} = 4, 5$  and  $N_{\text{Nb}} \neq 0$ . Clearly, the new, unambiguous assignments supersede the old ones, which suffer from uncertainty and ambiguity in deconvolving the one-dimensional MAS spectra (in section 6.3). Both the old and new assignments are shown in Fig. 6.14.

Analyses of spectra for  $x = 0.7$  and  $0.9$  [Figs. 6.9(e) and 6.9(f)] provide NMR parameters for more nBn configurations. Along quadrupole distribution axis  $B_0$  [in both Figs. 6.9(e) and 6.9(f)], two points are sampled (marked with filled circles in the figures) to give an estimated  $P_Q$  range of 20–32 MHz for nBn configurations with  $(0, N_{\text{Sc}}, 6 - N_{\text{Sc}})$  and  $N_{\text{Sc}} = 1, 2, \dots, 5$ .

Along line  $B_1$  [in both Figs. 6.9(e) and 6.9(f)], two points are sampled (marked with filled circles in the figures) to give an estimated  $P_Q$  range of 20–37 MHz for nBn configurations with  $(1, N_{\text{Sc}}, 5 - N_{\text{Sc}})$  and  $N_{\text{Sc}} = 0, 1, \dots, 4$ .

Along line  $B_2$  in Fig. 6.9(e) for  $x = 0.7$ , the  $P_Q$  range 20–29 MHz is found for nBn configurations  $(2, N_{\text{Sc}}, 4 - N_{\text{Sc}})$  with  $N_{\text{Sc}} = 0, 1, 2, 3$ ; in Fig. 6.9(f) for  $x = 0.9$ , the range is 20–25 MHz. The smaller range at concentration 0.9 is probably caused by the disappearance of configurations with smaller number of  $\text{Sc}^{3+}$  [(2,0,4) and (2,1,3)], while the configurations with more  $\text{Sc}^{3+}$  cations [(2,2,2) and (2,3,1)] persist and probably increase. Therefore, the configurations (2,0,4) and (2,1,3) have  $P_Q$  range 25–30 MHz and configurations (2,2,2) and (2,3,1) have  $P_Q$  ranging from 20 to 25 MHz.

Along line B<sub>3</sub> in Fig. 6.9(e) for  $x = 0.7$ , the  $P_Q$  range 20–35 MHz is found for nBn configurations (3,0,3), (3, 1, 2), and (3,2,1); in Fig. 6.9(f) for  $x = 0.9$ , only intensity with large  $P_Q = 35$  MHz persists. Again, this intensity is assigned to the configuration with relatively more Sc<sup>3+</sup> cations, (3,2,1).

Along line B<sub>4</sub> in Fig. 6.9(e) for  $x = 0.7$ , the  $P_Q$  range 20–35 MHz is found for nBn configurations (4,0,2) and (4, 1, 1); in Fig. 6.9(f) for  $x = 0.9$ , only intensity with large  $P_Q = 35$  MHz persists. Again, this intensity is assigned to the configuration with relatively more Sc<sup>3+</sup> cations, (4,1,1).

Along line B<sub>5</sub> in Fig. 6.9(e) for  $x = 0.7$ , only a little intensity appears.  $P_Q \sim 40$  MHz is found for nBn configurations (5,0,0), which agrees with the value 38 MHz (Fig. 6.11) found by sampling a point in PMN spectrum [Fig. 6.9(a)]. In Fig. 6.9(f) for  $x = 0.9$ , this intensity disappears.

In summary, D<sub>1</sub> has  $\delta_{\text{iso}}^{\text{CS}}$  ranging from  $-970$  to  $-957$  ppm [Eq. (6.8) with  $N_{\text{Mg}} = 0, 1$ ],  $P_Q$  ranging from 20 to 37 MHz. D<sub>2</sub> has  $\delta_{\text{iso}}^{\text{CS}}$  ranging from  $-943$  to  $-902$  ppm [Eq. (6.8) with  $N_{\text{Mg}} = 2-5$ ],  $P_Q$  ranging from 25 to 40 MHz.

## 6.7 Fit of 3QMAS Spectra

We have identified most of the underlying sites and calculated their NMR parameters for the <sup>93</sup>Nb 3QMAS spectra of the PMN-PSN solid solutions. We are now able to simulate 3QMAS spectra based on these NMR parameters and to use these to extract relative populations for each configuration. For instance, in the simple case of PMN, the parameters of all six nBn configurations have been estimated [see Fig. 6.11 for quadrupole products and

Eq. (6.8) for isotropic chemical shifts] and they are used to simulate the two-dimension spectrum using program DMFIT [74], this is presented in Fig. 6.15. In addition to the intensities the line broadening in both isotropic and MAS dimensions are allowed to vary. Since the large number of parameters involved in fitting such a two-dimensional spectrum put high demand for the efficiency and robustness on the program, the fit shown in Fig. 6.15 is not well optimized. The fractional % intensities for configurations  $(N_{\text{Mg}}, 0, 6 - N_{\text{Mg}})$  with  $N_{\text{Mg}} = 0 \dots 6$  are respectively 17, 4, 5, 24, 10, 31, and 8%, respectively. The narrow peak 6 (configuration  $N_{\text{Mg}} = 6$ ) is not well-fitted using a single set of  $P_Q$  and  $\delta_{\text{iso}}^{\text{CS}}$  values, since it actually consists of small distribution of NMR parameters. This peak should have slightly higher intensity than 8%; in the previous MAS study, this peak has intensity 14.8%. Although these partial intensities may not be accurate, an interesting comparison can be made to the values 25.1, 1.2, 6.2, 16.5, 24.7, 19.8, and 6.6% for  $(N_{\text{Mg}}, 0, 6 - N_{\text{Mg}})$  with  $N_{\text{Mg}} = 0 \dots 6$  respectively, which are predicted by random B-site model (see TABLE II of the MAS work).

For higher PSN concentrations, there are more contributing configurations and it is not possible to extract the  $P_Q$  values of every configuration from the data. All these factors further complicate the modelling of two-dimensional spectra. Moreover for sites with different quadrupole coupling product  $P_Q$ , the pulse efficiency in a MQMAS experiment is not as uniform as in a MAS experiment. A more efficient, tractable algorithm for obtaining more accurate partial intensities is to deconvolute a MAS spectrum with the structural information  $(\delta_{\text{iso}}^{\text{CS}}, P_Q)$  obtained by analyzing a MQMAS spectrum. In the previous MAS study, we have already obtained reliable partial intensities for the narrow peaks by deconvoluting  $^{93}\text{Nb}$  MAS spectra for the PMN-PSN solid-solutions. Using these intensities we have been

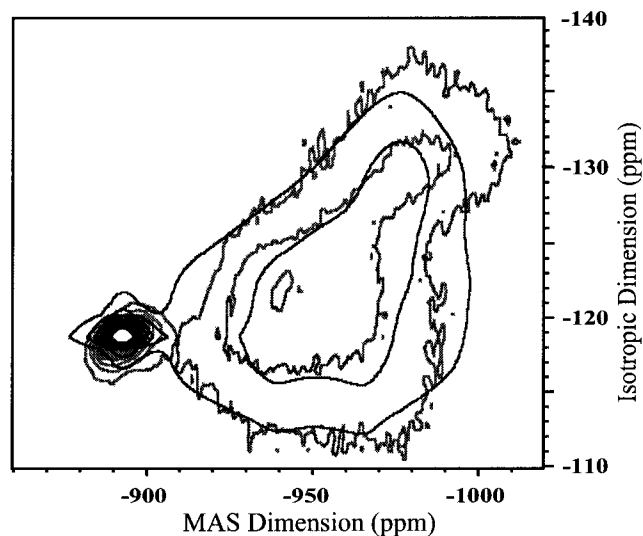


**Figure 6.15:** Fit of the 3QMAS spectrum of PMN using the NMR parameters calculated for the seven configurations [see Fig. 6.11 for quadrupole products and Eq. (6.8) for isotropic chemical shifts].

able to rule out the completely random B-site model and support a modified random site model.

## 6.8 Conclusions

$^{93}\text{Nb}$  MAS and 3QMAS NMR experiments have been performed on perovskite relaxor ferroelectric PMN-PSN solid solutions at high magnetic fields and fast sample spinning speeds. The resolution of the experiments is sufficient to allow assignments of MAS spectral components to  $^{93}\text{Nb}$  sites in 28 nearest B neighbor configurations. Seven narrow peaks and two broad components have been identified. The seven narrow peaks have been assigned to the seven configurations devoid of  $\text{Nb}^{5+}$ ; and are labelled 0–6 according to the number of  $\text{Mg}^{2+}$  in the configurations. The two broad components  $D_1$  and  $D_2$  have been respectively assigned to 11 and 10 configurations containing  $\text{Nb}^{5+}$ . These spectral assignments facilitate

quantitative evaluation of, and differentiation between, different models of B-site (chemical) disorder. The “completely random” model was ruled out and the “random site” model is shown to be in qualitative agreement with the NMR experiments. However, at compositions with low PSN concentration, the RS model underestimates intensities for the narrow spectral components corresponding to nearest B neighbor configurations with large  $\text{Mg}^{2+}$  number ( $N_{\text{Mg}} > 3$ ). This remaining small discrepancy from predictions of the RS model is most probably the result of its assumption of complete compositional randomness within the mixed layers. To explain this observation and obtain quantitative agreement with observed NMR intensities, we propose an enthalpic contribution which promotes clustering of  $\text{Mg}^{2+}$  cations on the mixed B sub-lattice. Monte Carlo simulations on PMN confirm that when the unlike-pair energy between  $\text{Nb}^{5+}$  and  $\text{Mg}^{2+}$  is  $-3.2$  kJ/mole, quantitative agreement of intensities are achieved.

The higher resolution achievable in the two-dimensional experiment, together with the systematic investigation of concentration dependence, provides abundant structural information in these materials. Moreover, systematic analyses of the  $(1-x)\text{PMN}-x\text{PSN}$  3QMAS spectra have enabled these  $\text{Nb}^{5+}$  containing configurations to be isolated and identified. NMR parameters have been calculated for most of the 28 possible nBn configurations. An empirical linear relationship has been established between the observed isotropic chemical shift and the number of  $\text{Mg}^{2+}$  cations in the configuration;  $\delta_{\text{iso}}^{\text{CS}} = 13.7(\pm 0.1)N_{\text{Mg}} - 970.7(\pm 0.4)$ . Enhanced 3QMAS resolution permits, for the first time, the quadrupole coupling product  $P_Q$  values to be determined for most of the 28 possible nBn configurations. The seven  $\text{Nb}^{5+}$ -deficient configurations  $(N_{\text{Mg}}, 6 - N_{\text{Mg}}, 0)$  and the pure niobium configuration  $(0, 0, 6)$  have small  $P_Q$  in the range 6–12 MHz. These have the smallest EFG due to the highly

symmetric environment of the central niobium and indicate structural displacements and distortions must be small or dynamically averaged. The configurations mixed with  $\text{Mg}^{2+}$  and  $\text{Nb}^{5+}$ , or with  $\text{Sc}^{3+}$  and  $\text{Nb}^{5+}$ , or with all three types of B-cations have large  $P_Q$  in the range 19–40 MHz. It is interesting to notice that configuration (5, 0, 1) has much larger  $P_Q$  (40 MHz) than that of (1, 0, 5) (19 MHz); this has been explained on the basis of ion size mismatch.

With these values of NMR parameters, the relative displacement of ions in the solid-solutions may be ultimately calculated from ab initio computational modelling. To understand  $^{93}\text{Nb}$  chemical shift in perovskites, especially the intriguing observation that the 6-niobium and 6-scandium configurations have similar  $\delta_{\text{iso}}^{\text{CS}}$  values, ab initio calculations have to be carried out using density function theory (DFT) and the gauge-including atomic orbital (GIAO) method, which have been applied to chemical shifts of  $^1\text{H}$ ,  $^{13}\text{C}$ ,  $^{87}\text{Rb}$ , etc. [110, 111, 65, 32]. To better understand the effects of nBn configurations on  $P_Q$ , for instance why configuration (5, 0, 1) (5  $\text{Mg}^{2+}$  and 1  $\text{Nb}^{5+}$ ) has  $P_Q$  double that of configuration (1, 0, 5) (1  $\text{Mg}^{2+}$  and 5  $\text{Nb}^{5+}$ ), ab initio calculations of electric field gradient should be carried out using either the MO LCAO-SCF or LDA LAPW approach. The former approach has been successfully applied to calculate the EFGs at the transition-metal sites in  $\text{LiNbO}_3$  and  $\text{LiTaO}_3$  crystals and at the aluminium sites in mixed ionic crystals  $\text{CaREAlO}_4$  (RE = La, Pr, Eu, Y); [93, 103] the latter approach has been applied to calculate the EFGs at the cation sites in  $\text{BaTiO}_3$  and  $\text{KNO}_3$  [94, 9].

In conclusion, the 3QMAS study [117] has confirmed and refined the assignment of spectral components to nearest B-site neighbor configurations, which was first proposed in our MAS NMR study [58]. Moreover, the superb fidelity and refined assignment of the

two broad distributions ( $D_1$  and  $D_2$ ) of 3QMAS allow unprecedented detailed structural information and distribution of local disorder in complex materials. Thus MAS and 3QMAS NMR techniques combined can be used to quantitatively study local structures and B-site cation ordering, which are very important for the relaxor properties of these materials.



## Chapter 7

# $^{45}\text{Sc}$ NMR Studies of PMN-PSN

$^{45}\text{Sc}$  NMR has been used to study the PMN-PSN system. The same MAS and 3QMAS techniques are used as in the studies of  $^{93}\text{Nb}$  NMR (Chapter 6). The  $^{93}\text{Nb}$  spectra has been assigned to the nBn configuration  $\text{Nb}(N_{\text{Mg}}, N_{\text{Sc}}, N_{\text{Nb}})$  (see Chapter 6), where the beginning Nb denotes the type of the center ion. Likewise there are a variety of nBn configurations  $\text{Sc}(N_{\text{Mg}}, N_{\text{Sc}}, N_{\text{Nb}})$ , where the beginning Sc for central  $\text{Sc}^{3+}$  ion. However, for both ordered and disordered samples, the central transition ( $+1/2 \leftrightarrow -1/2$ ) can be consistently fit with only one relatively narrow and one broad gaussian peak.  $^{45}\text{Sc}$  spectra do not resolve the expected seven narrow peaks as seen in the  $^{93}\text{Nb}$  spectra; this prevents order/disorder to be quantitatively studied using  $^{45}\text{Sc}$  NMR. Therefore, the first issue to understand is why  $^{45}\text{Sc}$  spectra have lower resolution than  $^{93}\text{Nb}$  spectra.

Large isotropic chemical shift differences tend to separate resonance peaks and hence improve spectral resolution, on the other hand, large second order quadrupole broadening tends to reduce resolution. Thus the decreased resolution is either because because  $^{45}\text{Sc}$  nuclei experience larger second order quadrupole interactions than  $^{93}\text{Nb}$  nuclei do and/or the chemical shift of  $^{45}\text{Sc}$  nuclei is less sensitive to the different nearest B-site neighbor (nBn) configurations.

According to Eq. (4.42), the second order quadrupole interaction should be

$$\delta^{2Q} \propto \frac{P_Q^2 [I(I+1) - 3/4]}{[2I(2I-1)]^2}. \quad (7.1)$$

[The magnetogyric ratios  $\gamma$  of the two nuclei are very close and have been ignored (see Table 2.1).] Spin  $I = 9/2$  and  $7/2$  for  $^{93}\text{Nb}$  and  $^{45}\text{Sc}$ , respectively. Therefore,  $\delta^{2Q} \propto 0.0046P_Q^2$  and  $0.0085P_Q^2$  for  $^{93}\text{Nb}$  and  $^{45}\text{Sc}$ , respectively. For PMN-PSN, the quadrupole coupling products  $P_Q$  range from 6 to 41 MHz for  $^{93}\text{Nb}$  (see Chapter 6) and from 5 to 16 MHz for  $^{45}\text{Sc}$  (see in the following subsection 7.2). The linewidth produced by  $P_Q = 6.8$  MHz for  $^{93}\text{Nb}$  is the same as that by  $P_Q = 5$  MHz for  $^{45}\text{Sc}$ . If the largest  $P_Q$  values are used, then the linewidth of  $^{93}\text{Nb}$  is much larger; the Nb:Sc ratio is 3.6. Therefore, in PMN-PSN the  $^{45}\text{Sc}$  linewidth is usually narrower than that of  $^{93}\text{Nb}$  and quadrupole interaction is not responsible for the lower resolution in  $^{45}\text{Sc}$  spectra.

Chemical shift interaction is the effect of the induced magnetic fields of the surrounding electron clouds. The electronegativity, which is the power of an atom when in a molecule to attract electrons to itself, may indicate the sensitivity of chemical shift. The Pauling electronegativities are 2.33, 1.60, 1.36, and 1.31 for  $\text{Pb}^{2+}$ ,  $\text{Nb}^{5+}$ ,  $\text{Sc}^{3+}$ , and  $\text{Mg}^{2+}$ , respectively [61]. The chemical shifts of  $^{207}\text{Pb}$  in relaxor ferroelectrics span several hundreds of ppm (Chapter 8), those of  $^{93}\text{Nb}$  span approximately 80 ppm, and those of  $^{45}\text{Sc}$  only span 40 ppm (see the following section 7.2); this follows the order in their electronegativities.  $^{25}\text{Mg}$  spectra (not shown) are similar to  $^{45}\text{Sc}$  and also have low resolution. Therefore, it is likely that the insensitivity of  $^{45}\text{Sc}$  chemical shift is responsible for lower spectral resolution of MAS and 3QMAS experiments.

## 7.1 MAS

Single pulse  $^{45}\text{Sc}$  MAS spectra were collected at two magnetic fields 14 and 19.6 T (proton frequencies of 600 and 833 MHz respectively). For experiments at 14 T, the  $^{45}\text{Sc}$  Larmor frequency  $\nu_L = 145.8$  MHz, rotor diameter was 2.5 mm, sample spinning speed  $\nu_R = 34$  kHz, rf field strength  $\nu_1 = 50$  kHz, pulse duration  $t_p = 1 \mu\text{s}$ , and recycle delay  $d = 100$  ms. For experiments at 19.6 T, the experiment parameters have the following values;  $\nu_L = 201.7$  MHz, rotor diameter was 2 mm,  $\nu_R = 35$  kHz,  $\nu_1 = 71$  kHz,  $t_p = 0.7 \mu\text{s}$ , and  $d = 100$  ms. The number of scans acquired was 2000, the full spectral width was 1 MHz (dwell time  $1 \mu\text{s}$ ), 4096 complex data points were collected, and  $\text{ScCl}_3$  aqueous solution (with one or two drops of HCl) was used as the chemical shift reference ( $\delta_{\text{iso}}^{\text{CS}} = 0$  ppm). Spectra are processed using similar procedures as for  $^{93}\text{Nb}$  MAS (Section 6.1).

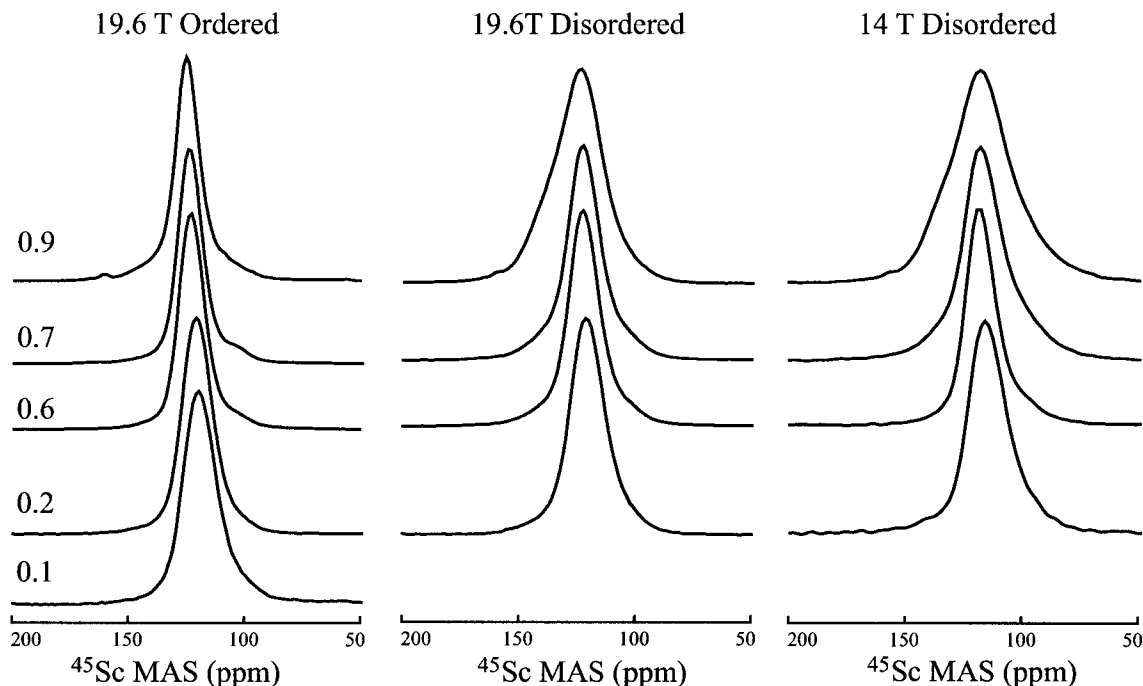


**Figure 7.1:** Central transition ( $+1/2 \leftrightarrow -1/2$ ) of  $^{45}\text{Sc}$  single pulse MAS spectra of  $(1 - x)\text{PMN}-x\text{PSN}$  solid solutions.

The central transition ( $+1/2 \leftrightarrow -1/2$ ) of the MAS spectra is shown in Fig. 7.1 for PMN-PSN samples: ordered at 19.6 T, disordered at 19.6 T, and disordered at 14 T. Clearly the higher magnetic field does narrow the MAS lineshape somewhat. At the same magnetic fields, spectra of ordered samples are narrower than those of disordered samples of the same PSN concentration ( $x$ ).

The simplest spectral decomposition is to consider the central transitions to be composed of two Gaussian lineshapes A and B, see Fig. 7.2. The quality of fit is very good for all spectra and fit parameters are given in Table 7.1. As scandium concentration  $x$  increases, the position of both A and B moves toward higher frequency for both ordered and disordered samples. For ordered samples, component A becomes narrower, while component B becomes wider with increasing  $x$  (with one exception at  $x = 0.1$ ).

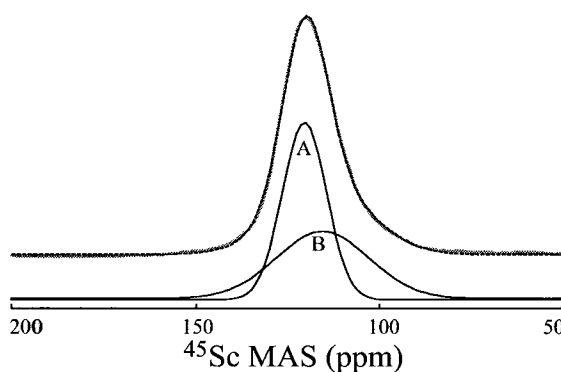


**Figure 7.2:** Decomposition of  $^{45}\text{Sc}$  MAS central transition of ordered 0.9PMN-0.1PSN solid solution. The experimental MAS spectrum (bold solid line in gray), two gaussians A and B (thin solid lines, see parameters in Table 7.1), and the sum of A and B (dotted line).

It is difficult to use these decomposition results to make a more physical interpretation analogous to the cation ordering information extracted from  $^{93}\text{Nb}$  MAS studies (Chapter 6). We are limited by the lower spectral resolution. Glinchuk et al. have ascribed the intensity of the narrower A component to the  $^{45}\text{Sc}$  nuclei in  $[111]_{1:1}$  ordered (micro)regions,

**Table 7.1:** Decomposition parameters for  $^{45}\text{Sc}$  MAS central transitions of  $(1-x)\text{PMN}-x\text{PSN}$  solid solutions.

$x$	A			B		
	$\mu$ (ppm) <sup>a</sup>	$\Delta$ (ppm) <sup>b</sup>	I (%) <sup>c</sup>	$\mu$ (ppm) <sup>a</sup>	$\Delta$ (ppm) <sup>b</sup>	I (%) <sup>c</sup>
ordered samples, 19.6 T						
0.1	121.0	14.2	55.7	116.1	29.8	44.3
0.2	122.2	13.1	59.6	118.8	28.2	40.4
0.6	123.9	11.5	66.0	119.1	29.0	34.0
0.7	125.0	11.1	65.8	120.3	30.6	34.2
0.9	125.9	10.4	53.9	123.8	34.4	46.1
disordered samples, 19.6 T						
0.2	121.3	14.1	48.7	119.1	31.4	51.3
0.6	123.0	12.9	52.5	121.2	34.2	47.5
0.7	123.4	13.0	45.8	122.2	34.9	54.2
0.9	124.1	14.0	19.3	127.2	32.9	80.7
disordered samples, 14 T						
0.2	117.4	15.0	46.8	113.0	35.9	53.2
0.6	119.3	13.4	44.7	114.4	34.4	55.3
0.7	119.1	14.1	35.9	115.1	39.6	64.1
0.9	119.7	22.0	36.1	117.5	47.4	63.9

<sup>a</sup> Center of Gaussian lineshape, error  $\pm 0.2$  ppm. <sup>b</sup> Full width at half maximum (FWHM) of Gaussian lineshape, error  $\pm 0.2$  ppm. <sup>c</sup> Percentage integrated intensity.

while that of the broader B component to the  $^{45}\text{Sc}$  nuclei in disordered (micro)regions; they then use the partial intensity of component A as an indicator of the degree of ordering [48]. This interpretation leads to the unphysical conclusion that the degrees of ordering depends on the magnetic fields. For example, for  $x = 0.9$  disordered sample (Table 7.1), the “ordered regions” (component A) intensity is calculated to be 19% and 36% at 19.6 and 14 T, respectively! Therefore, the intensity of narrow peak is not a direct measure of the extent of the  $[111]_{1:1}$  ordered regions.

William Brouwer (Department of Physics, College of William and Mary) has been able to fit all the MAS spectra with five gaussians at fixed positions (not shown). But no easy physical interpretation can be made either.

## 7.2 3QMAS

The two-dimensional 3QMAS spectra presented in this chapter were acquired using the 3-pulse Z-filter sequence (see Section 4.6.3). Hypercomplex data was collected at 19.6 T using optimized pulse widths of 2.5, 0.7, and 5  $\mu\text{s}$  respectively. The rf field strength was  $\nu_1 = 75$  kHz for the first two hard pulses, and  $\nu_1 = 10$  kHz for the third selective pulse. The interval between the second and third pulses was synchronized to one rotor period, 28  $\mu\text{s}$  (rotor of diameter 2 mm was spinning at 35.7 kHz); 512 complex data points were collected with dwell time 14  $\mu\text{s}$  in the direct acquisition dimension; 32 time increments ( $\Delta t_1 = 28$   $\mu\text{s}$ ) were used in the indirect acquisition dimension; 256 scans were accumulated with 100 ms relaxation delay. A  $\text{ScCl}_3$  aqueous solution was used as the chemical shift reference ( $\delta_{\text{iso}}^{\text{CS}} = 0$  ppm). Spectra are processed using the same procedures as for  $^{93}\text{Nb}$  3QMAS (Section 6.5).

### 7.2.1 NMR Parameters

The  $^{45}\text{Sc}$  3QMAS spectra for five well-ordered  $(1-x)\text{PMN}-x\text{PSN}$  solid solutions are shown in Fig. 7.3. The first thing to notice is that the S/N ratio of  $x = 0.1$  spectrum is very low because of the low scandium content in this sample. For this concentration, the maximum intensity is located at (121.0, 29.3) ppm, which gives NMR parameters  $\delta_{\text{iso}}^{\text{CS}} = 124.0$  ppm,  $\delta_{\text{iso}}^{2\text{Q}} = -3.0$  ppm, and  $P_Q = 7.0$  MHz [Eqs. (4.43) and (4.50)]. The intensities are mainly distributed along the chemical shift distribution axis with slope 17/73 (defined in Section 4.8); the range of the isotropic chemical shift,  $\delta_{\text{iso}}^{\text{CS}}$ , is estimated to be from 100 to 140 ppm. This 40 ppm range is smaller compared to the 82 ppm range of  $^{93}\text{Nb}$  chemical shift

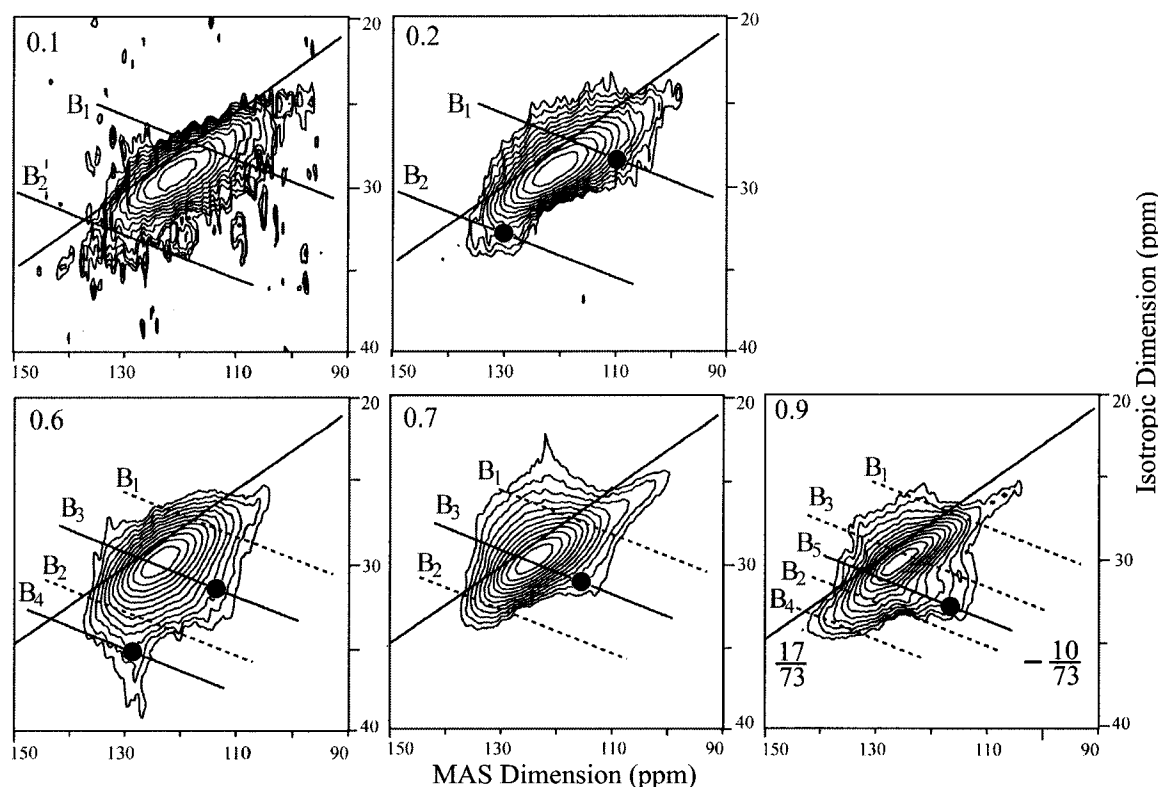


**Figure 7.3:**  $^{45}\text{Sc}$  3QMAS spectra for well-ordered  $(1-x)\text{PMN}-x\text{PSN}$  solid solutions, with concentrations  $x = 0.1, 0.2, 0.6, 0.7,$  and  $0.9$ . For spin  $I = 7/2$ , the chemical shift distribution axis has slope  $17/73$ , and the quadrupole distribution axes have slope  $-10/73$ . The contour levels start from 80% and decrease by factor 0.8. Twelve contour levels are plotted, and the lowest level is 6.9%. Filled circles mark the sampling points whose coordinates are used to calculate NMR parameters (see text).

(see Chapter 6) and does confirm the speculation in the beginning of this chapter that the low spectral resolution is a result of the insensitivity of  $^{45}\text{Sc}$  chemical shift to the nBn configurations.

For PSN concentration  $x = 0.2$ , the maximum intensity is located at  $(121.3, 28.8)$  ppm, which gives estimates  $\delta_{\text{iso}}^{\text{CS}} = 122.8$  ppm and  $P_Q = 4.9$  MHz. In addition to the chemical shift distributions similar to those seen at  $x = 0.1$ , quadrupole distribution along lines  $B_1$  and  $B_2$  are clearly revealed; estimate of parameters  $\delta_{\text{iso}}^{\text{CS}} = 116.4$  and  $137.4$  ppm, and  $P_Q = 10.1$  and  $10.8$  MHz are obtained for sample points on  $B_1$  and  $B_2$  respectively (filled circles in

Fig. 7.3).

For concentration  $x = 0.6$ , the maximum intensity is located at (123.8, 30.0) ppm, from which  $\delta_{\text{iso}}^{\text{CS}} = 127.0$  ppm and  $P_Q = 7.1$  MHz are estimated. The overall shape of contour levels are rounder than at lower concentrations; this is caused by both a smaller chemical shift distribution and larger quadrupole distributions. Two points (filled circles in Fig. 7.3) are sampled on quadrupole distribution axes  $B_3$  and  $B_4$ , they give  $\delta_{\text{iso}}^{\text{CS}} = 128.4$  and 142.4 ppm, and  $P_Q = 15.7$  and 14.6 MHz, respectively.

For concentration  $x = 0.7$ , the maximum intensity is located at (124.1, 29.7) ppm, from which  $\delta_{\text{iso}}^{\text{CS}} = 126.3$  ppm and  $P_Q = 5.9$  MHz are estimated. Intensity along  $B_4$  disappears and contours along  $B_2$  get narrower. A point (filled circles in Fig. 7.3) along  $B_3$  is sampled to give  $\delta_{\text{iso}}^{\text{CS}} = 126.8$  ppm, and  $P_Q = 13.1$  MHz.

For concentration  $x = 0.9$ , the maximum intensity is located at (125.1, 29.9) ppm, from which  $\delta_{\text{iso}}^{\text{CS}} = 127.2$  ppm and  $P_Q = 5.8$  MHz are estimated. Intensity along  $B_4$  appears again. A point (filled circles in Fig. 7.3) along  $B_5$  is sampled to give  $\delta_{\text{iso}}^{\text{CS}} = 132.2$  ppm, and  $P_Q = 16.1$  MHz.

### 7.2.2 Assignments

Unlike the  $^{93}\text{Nb}$  3QMAS NMR spectra, there are no well-defined narrow peaks in the  $^{45}\text{Sc}$  spectra shown in Fig. 7.3. This makes the complete spectral assignments and interpretation very difficult, if not impossible. Nevertheless, a few insights can still be obtained. For PSN concentration  $x = 0.1$ , where scandium content is low, most of the populated nBn configurations contain no  $\text{Sc}^{3+}$  or at most have 1 or 2  $\text{Sc}^{3+}$  cations occupying the 6 nBn positions ( $N_{\text{Sc}} = 0, 1, 2$ ). Statistically the nBn configurations with no Sc,  $\text{Sc}(N_{\text{Mg}}, 0, 6 - N_{\text{Mg}})$ , are



responsible for most of the intensity in the 3QMAS spectrum, which is characterized by a chemical shift distribution but no obvious quadrupole distribution. This result is counter-intuitive since it implies that configurations consisting of combinations of only  $\text{Mg}^{2+}$  and  $\text{Nb}^{5+}$  cations (which are very different in charge, size, and electronegativity) produce small and nearly constant electric field gradients!

On increasing the PSN concentration a little to  $x = 0.2$ , configurations with  $N_{\text{Sc}} = 1$  and 2 are increasingly populated. Intensities along  $B_1$  or  $B_2$  shall be assigned to those configurations with  $N_{\text{Sc}} = 1, 2$  and predominant  $\text{Nb}^{5+}$  cations,  $N_{\text{Nb}} > 3$ ,  $N_{\text{Mg}} = 0$  (or predominant  $\text{Mg}^{2+}$  cations  $N_{\text{Mg}} > 3$ ,  $N_{\text{Nb}} = 0$ , the correct correspondence will become clear shortly).

The uncertainty between the two assignments can be solved by investigating the spectrum at  $x = 0.9$ . Since the magnesium content is extremely low in this sample, configurations with predominance of  $\text{Mg}^{2+}$  cations should only be populated sparsely or not at all. Intensities above and along line  $B_1$ , which is strong at  $x = 0.2$ , become very weak. Therefore, the following assignments are reasonable: configurations with predominant  $\text{Mg}^{2+}$  cations, 1 (or 2)  $\text{Sc}^{3+}$ , and no  $\text{Nb}^{5+}$  cations produce intensities along  $B_1$ ; configurations with predominant  $\text{Nb}^{5+}$  cations, 1 (or 2)  $\text{Sc}^{3+}$ , and no  $\text{Mg}^{2+}$  cations produce intensities along  $B_2$ .

Large intensities along (and between) lines  $B_3$  and  $B_5$  at high PSN concentration ( $x = 0.6, 0.7$ , and  $0.9$ ) tell that they are contributed from configurations with predominant (but less than 6)  $\text{Sc}^{3+}$  cations. The pure scandium configuration  $\text{Sc}(0,6,0)$  should be assigned to the point with maximum intensity, where  $\delta_{\text{iso}}^{\text{CS}} = 127.2$  ppm and  $P_Q = 5.8$  MHz have been estimated above for  $x = 0.9$ .

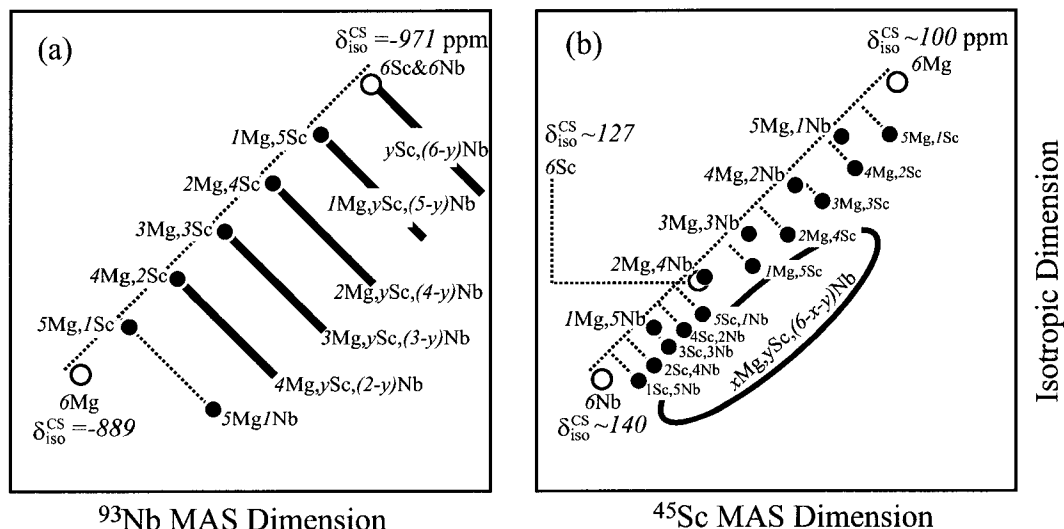


**Figure 7.4:** Schematic 3QMAS spectra of  $^{93}\text{Nb}$  (a) and  $^{45}\text{Sc}$  (b) in PMN-PSN system. Empty circles denote pure nearest B-site neighbor configurations, filled circles denote mixed configurations, solid lines in (a) denote distribution of more than one configuration, and the ellipse in (b) represents configurations consisting of all three types of cation. The numbers of Mg, Sc, and Nb should add up to six. In (a), for those configurations with  $y$  as the number of Sc, all three numbers should be greater than zero. In (b), for those configurations with  $x$  and  $y$  and the number of Mg and Sc respectively, also all numbers of the three ion types should be positive.

If it is assumed that the empirical linear relationship between  $\delta_{\text{iso}}^{\text{CS}}$  and the numbers of cations exists, then

$$\delta_{\text{iso}}^{\text{CS}}(N_{\text{Mg}}, N_{\text{Sc}}, N_{\text{Nb}}) = [N_{\text{Mg}}\delta_{\text{iso}}^{\text{CS}}(6, 0, 0) + N_{\text{Sc}}\delta_{\text{iso}}^{\text{CS}}(0, 6, 0) + N_{\text{Nb}}\delta_{\text{iso}}^{\text{CS}}(0, 0, 6)]/6. \quad (7.2)$$

For  $^{93}\text{Nb}$ , we have also assumed such linear dependence in section 6.6.2, where the fortuitous relationship

$$\delta_{\text{iso}}^{\text{CS}}(0, 6, 0) = \delta_{\text{iso}}^{\text{CS}}(0, 0, 6)$$

simplifies

$$\begin{aligned}\delta_{\text{iso}}^{\text{CS}}(N_{\text{Mg}}, N_{\text{Sc}}, N_{\text{Nb}}) &= \delta_{\text{iso}}^{\text{CS}}(0, 6, 0) + N_{\text{Mg}} [\delta_{\text{iso}}^{\text{CS}}(6, 0, 0) - \delta_{\text{iso}}^{\text{CS}}(0, 6, 0)] / 6 \\ &= 13.7N_{\text{Mg}} - 970.7 \text{ ppm}.\end{aligned}$$

For  $^{45}\text{Sc}$  in PMN-PSN system, the isotropic chemical shifts have been estimated for the pure nBn configurations,

$$\delta_{\text{iso}}^{\text{CS}}(6, 0, 0) \sim 100 \text{ ppm}, \delta_{\text{iso}}^{\text{CS}}(0, 6, 0) \sim 127 \text{ ppm}, \delta_{\text{iso}}^{\text{CS}}(0, 0, 6) \sim 140 \text{ ppm}. \quad (7.3)$$

Assisted with these relationships, we may schematically represent the spectral assignments to the nBn configurations in the  $^{45}\text{Sc}$  3QMAS spectra. For comparison, we also do this for  $^{93}\text{Nb}$  in Fig. 7.4(a). The assignments for  $^{93}\text{Nb}$  (a) and  $^{3+}\text{Sc}$  (b) clearly reveal the reasons why  $^{93}\text{Nb}$  spectra have higher resolution than  $^{45}\text{Sc}$  spectra:

1. The isotropic chemical shift of  $^{93}\text{Nb}$  has larger span (82 ppm) than that of  $^{45}\text{Sc}$  (40 ppm).
2. For  $^{93}\text{Nb}$ , the coincidence of isotropic chemical shifts of the 6-Sc and 6-Nb configurations simplifies the spectra, since this results in the alignment of all the 28 configurations along only seven quadrupole distribution axes. However, the  $^{45}\text{Sc}$  isotropic chemical shifts are more distributed, and the intensities from various configurations overlap more seriously.

### 7.3 Conclusion

In parallel to  $^{93}\text{Nb}$  NMR study (Chapter 6),  $^{45}\text{Sc}$  MAS and 3QMAS experiments have been performed on PMN-PSN solid solutions. However, the resolution is disappointingly low and B-site ordering information could be extracted. In MAS spectra, the intensities of the 28 possible nBn configurations are lumped into only two overlapping spectral components: the comparatively narrow A and broad B components. But physical interpretation is difficult to make.

Though in  $^{45}\text{Sc}$  3QMAS spectra no isolated narrow peak is observed either (analogous to the seven narrow peaks in  $^{93}\text{Nb}$  spectra), systematic concentration-dependent analyses identify the three pure nBn configurations (six-Mg, six-Sc, and six-Nb). Assuming that the isotropic chemical shift of any configuration is a linear combination of those of the three pure configurations, we may roughly locate each nBn configurations in the  $^{45}\text{Sc}$  3QMAS spectra. The reasons for low  $^{45}\text{Sc}$  resolution is also understood: the  $^{45}\text{Sc}$  isotropic chemical shift spans a smaller range than  $^{93}\text{Nb}$ , and no two pure nBn configurations has the same isotropic chemical shifts analogous to  $^{93}\text{Nb}$ .

Even though assignments have been suggested for the 3QMAS spectra, the limited resolution precludes the assignment of the A and B MAS components and still no physical interpretation can be made about their relative intensities.

However, these studies have significance for NMR spectroscopy. We have understand that the chemical shifts of  $^{45}\text{Sc}$  is less sensitive to environment than  $^{93}\text{Nb}$ , and the empirical linear interpolation of isotropic chemical shifts seems very useful when making spectral assignments.

## Chapter 8

# $^{207}\text{Pb}$ NMR Studies of PMN-PSN

The lead ion has large covalency and lone-pair electrons and should play an important role in determining ferroelectric behavior. For example in perovskites ( $A=\text{Ba}^{2+}$ ,  $\text{Pb}^{2+}$ ;  $B'=\text{Mg}^{2+}, \text{Ca}^{2+}, \text{Zn}^{2+}$ ;  $B''=\text{Nb}^{5+}, \text{Ta}^{5+}$ ), 1:2 ordering of the two B cations is found along the [111] direction when the A ion is  $\text{Ba}^{2+}$ , while 1:1 ordering when A is  $\text{Pb}^{2+}$  [19]. The Pb-based perovskites also have lower order-disorder transition temperatures than the Ba-based perovskites [19]. These phenomena have been attributed to the enhanced Pb-O hybridization between the Pb 6s and O 2p states of the underbonded oxygens in the  $\text{B}^{2+}\text{-O-B}^{2+}$  and  $\text{B}^{2+}\text{-O-B}^{5+}$  environments [19, 18]. Similarly, the large covalency of  $\text{Pb}^{2+}$  compared to  $\text{Ba}^{2+}$  has been modelled by an environment-dependent effective A-site charge and it is able to explain the observed different ordering behaviors [114].

In order to accommodate their lone-pair electrons,  $\text{Pb}^{2+}$  ions usually shift from high symmetry positions. An X-ray diffraction (XRD) study of  $\text{Pb}(\text{Mg}_{1/3}\text{Nb}_{2/3})\text{O}_3$  (PMN) shows that even at relatively high temperatures ( $\sim 300^\circ\text{C}$ ) lead ions are displaced from the perovskite cubic center [100]. The displacements may be random in both length and direction, but a spherical layer model (radius 0.285 and 0.259 Å for 20 and  $300^\circ\text{C}$  respectively) adequately describe the observed data [100]. However in  $\text{Pb}(\text{Sc}_{1/2}\text{Ta}_{1/2})\text{O}_3$  (PST),

pair distribution function analysis (PDF) using neutron scattering and X-ray scattering shows that  $\text{Pb}^{2+}$  ions move (by 0.2 Å) in the [100] direction rather than the macroscopic polarization direction [111] [38]. These results are very different and we hope  $^{207}\text{Pb}$  NMR study may shed some light on this issue.

In this chapter, the  $^{207}\text{Pb}$  NMR of the solid solutions  $(1-x)\text{PMN}-x\text{PSN}$  is used to investigate the important role of  $\text{Pb}^{2+}$  ion. However for these relaxor ferroelectric materials, the  $\text{Pb}^{2+}$  ions are in a variety of local environments due to B-site disorder, therefore there are large distributions of both isotropic and anisotropic  $^{207}\text{Pb}$  chemical shifts. The distributions of chemical shifts obscure the characteristic anisotropic lineshape seen for simple crystalline materials and result in a broad and featureless NMR lineshape; this has been observed for PMN-PSN [49]. To separate the distribution of isotropic shifts from anisotropic shifts, inaccessibly high magic-angle spinning speeds ( $\sim 50$  kHz) would be required. But in effect the two-dimensional phase-adjusted spinning sidebands technique (2D-PASS, introduced in Chapter 3) is able to achieve “infinite spinning speed” spectra in the sense of isolating isotropic chemical shift information in one dimension, while preserving valuable anisotropic chemical shift information in the second dimension. The 2D-PASS technique has been successfully applied to study chemical bonding of lead in  $\text{P}_2\text{O}_5\text{-PbO}$  glasses [41]. This technique is also able to provide valuable insight on the lead chemical bonding and displacements of PMN-PSN perovskites [118].

## 8.1 Experimental Setting

NMR experiments were carried out using a TECMAG APOLLO console with a 7 T OXFORD magnet. A 0.5 M aqueous  $\text{Pb}(\text{NO}_3)_2$  solution was used to tune the spectrometer (Larmor frequency 62.589 MHz), then the carrier frequency was increased by 100 kHz before working on the PMN-PSN samples. The duration of a  $\pi/2$  pulse was 3  $\mu\text{s}$  and the spectral width was  $\pm 100$  kHz. Depending on the amount of sample, 1000 to 4000 scans were collected. Lead chemical shifts are reported referenced to tetramethyl lead [ $\text{Pb}(\text{CH}_3)_4$ ] at 0 ppm, this was done by using the 0.5 M aqueous  $\text{Pb}(\text{NO}_3)_2$  solution as the working reference sample [ $-2941$  ppm on the  $\text{Pb}(\text{CH}_3)_4$  scale] [67].

A Varian-Chemagnetics triple-resonance MAS probe with a spinning control module enables the achievement of spinning speeds up to 12 kHz within  $\pm 2$  Hz error. The spinning speeds were  $\nu_R = 10$  and 5 kHz for MAS and 2D-PASS experiments, respectively. Teflon spacers were placed on both sides of the rotor to keep the samples in the middle, since the amount of sample was not enough to fill the 5 mm rotor. Boil-off from high-pressure liquid-nitrogen dewars was used for bearing and driving gas as well as for temperature control. A LAKESHORE temperature controller (model DRC-91CA) and a Varian-Chemagnetics VT stack, which sat on top of the probe, were used to control the sample temperature; the temperature sensor was located near the lower end of the VT stack. In MAS and 2D-PASS experiments, viscous drag by the driving gas causes sample heating. Temperature calibration was performed making use of the sensitive chemical shifts and narrow linewidth of lead nitrate  $\text{Pb}(\text{NO}_3)_2$  [10]. The corrections were  $T(^{\circ}\text{C}) = 3(\pm 3) + 0.95(\pm 0.1)T_{\text{read}}^{\circ}\text{C}$  and  $T(^{\circ}\text{C}) = 15(\pm 3) + 0.93(\pm 0.1)T_{\text{read}}^{\circ}\text{C}$  for  $\nu_R = 5$  and 10 kHz, respectively. This

calibration has been implicitly performed and all temperatures reported in this paper are actual corrected values.

Longitudinal relaxation times ( $T_1$ ) were measured on static samples using a saturation-recovery sequence; the saturation was created by a comb consisting of twenty  $\pi/2$  pulses separated by 100 ms [45]. A refocusing  $\pi$  pulse was applied before detection to shift the signal by 200  $\mu\text{s}$  so as to acquire the full echo. The intensity at the top of echo,  $I(t)$ , where  $t$  was the recovery time, were fit to the equation  $I(t) = I_0[1 - \exp(-t/T_1)]$  using a least-square algorithm. The relaxation of the broad frequency-domain lineshapes is anisotropic and the error of the  $T_1$  values was estimated to be  $\pm 0.5$  s.

For MAS experiments at  $\nu_R = 10$  kHz, Hahn-echo sequence was used with  $\tau = 200$   $\mu\text{s}$  separating the  $\pi/2$  and the  $\pi$  pulses.

In a 2D-PASS pulse sequence, five  $\pi$  pulses follow the initial  $\pi/2$  pulse (see Chapter 3). We used the shifted echo version of the pulse sequence since the free induction decay (FID) dies out extremely fast ( $T_2^* < 20$   $\mu\text{s}$ ) [41]; a duration of two rotor periods (with rotor period  $T_R = 200$   $\mu\text{s}$ ) was added to the delay before the last  $\pi$  pulse, and a duration of one rotor period was added to the delay after that pulse. Sixteen pitches were used to create sixteen  $t_1$  increments. The spinning speed of 5 kHz was sufficiently low to obtain enough spinning sidebands for reliable extraction of anisotropy parameters, yet it must be sufficiently large so that  $16\nu_R$  covers all spinning sidebands. The simplified phase-cycling scheme introduced in Chapter 3 consisting of only 3 steps was used. The recycle delays were at least  $3T_1$  for all 2D-PASS experiments.



## 8.2 Static and MAS spectra, and $T_1$ Measurements

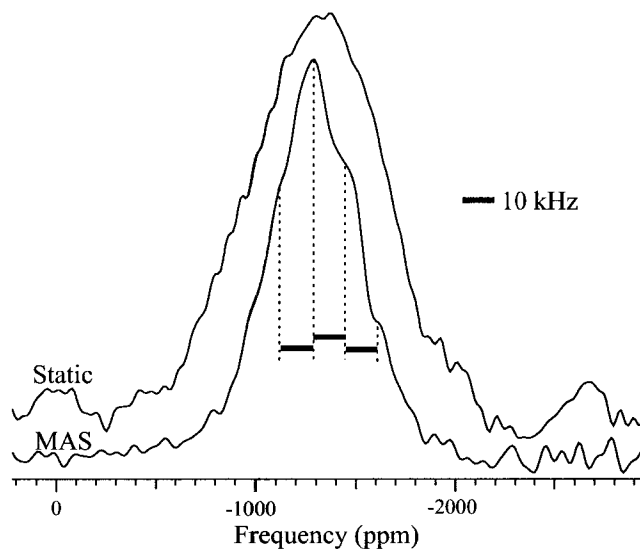


**Figure 8.1:** Static and MAS (10 kHz)  $^{207}\text{Pb}$  spectra at  $25^\circ\text{C}$  for ordered 0.3PMN-0.7PSN. Actual sample temperature in MAS experiment was  $38^\circ\text{C}$  due to frictional heating (see Section 8.1). Gaussian line broadening of 1 kHz was applied to both before Fourier transform.

Static and MAS spectra are shown in Fig. 8.1 for the ordered sample of  $x = 0.7$ . The static spectrum is very broad (full width at half height 800 ppm, or 50 kHz at 7 T). Unlike a simple crystalline sample (e.g.  $\text{PbSO}_4$ ), whose asymmetric lineshape of chemical shielding anisotropy shows characteristic features, this relaxor ferroelectric has a nearly symmetric lineshape due to its disordered nature. Magic-angle spinning does significantly narrow the linewidth (reducing it to FWHH 500 ppm); spinning sidebands with spacing of 10 kHz rotor speed may also be identified as inflections on the lineshape. Due to the complexity of the system, there is a distribution of chemical shift anisotropy parameters. MAS speeds of 50 kHz, which exceed the limit of current technology, would be required to completely separate the sidebands from the centerband.

The  $^{207}\text{Pb}$  longitudinal relaxation times  $T_1$  in  $(1 - x)\text{PMN}-x\text{PSN}$  are shown in Fig.

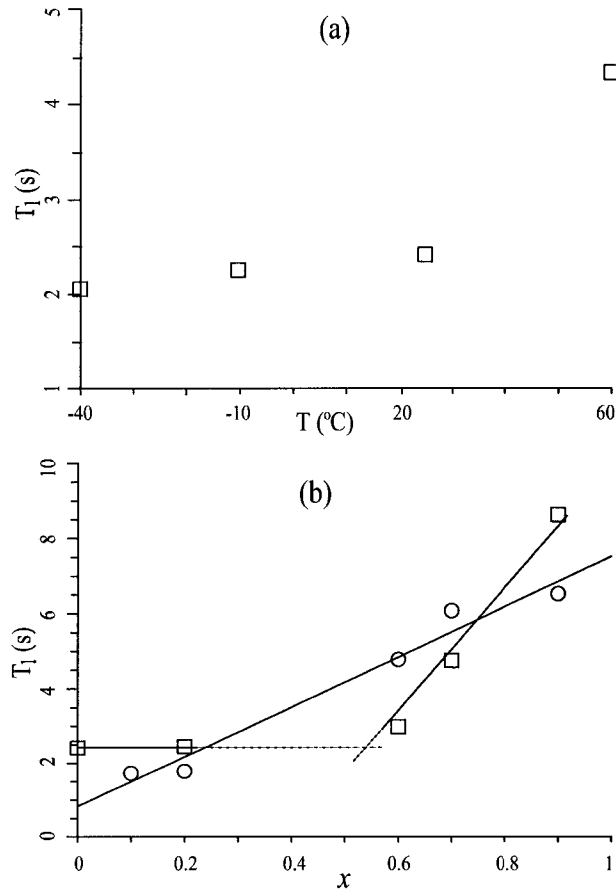


**Figure 8.2:** Lead relaxation time  $T_1$  of  $(1-x)$ PMN- $x$ PSN. Temperature dependence for PMN (a); concentration dependence at 25°C (b). Circles are data from ordered samples and squares from disordered materials. The lines in (b) are to guide the eye. Deviation may be  $\pm 0.5$  s due to relaxation anisotropy.

8.2. For PMN within the temperature range investigated ( $-40$  to  $60^\circ\text{C}$ ),  $T_1$  decreases with temperature [Fig. 8.2(a)]; the variation becomes very slow around the temperature for dielectric-maximum ( $-10^\circ\text{C}$ ) [22]. For the ordered samples,  $T_1$  has a linear dependence on concentration  $x$ ;  $T_1(\text{s}) = 0.8(\pm 0.4) + 6.7(\pm 0.7)x$  (with correlation coefficient  $R = 0.985$ , number of data points  $n = 5$ ) [Fig. 8.2(b)]. For disordered samples with available concentrations,  $T_1$  is constant 2.4 s at low concentrations ( $x < 0.5$ ) and grows rapidly at higher concentrations;  $T_1(\text{s}) = -8.4(\pm 0.3) + 18.9(0.9)x$ , ( $R = 0.999$ ,  $n = 3$ ) [Fig. 8.2(b)].

## 8.3 2D-PASS: Isotropic Chemical Shift

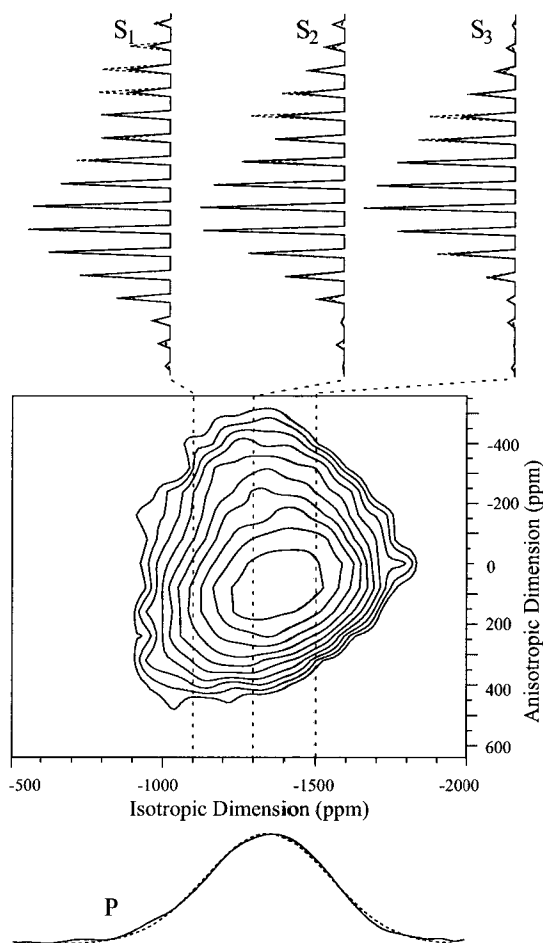


**Figure 8.3:**  $^{207}\text{Pb}$  2D-PASS spectrum of PMN at  $27^\circ\text{C}$ . Gaussian line broadening of 500 Hz was applied in the isotropic dimension. Ten contour levels start with 80% and decrease by factor 0.8. The projection (solid line) onto the isotropic dimension (P) is plotted with a Gaussian fit (dotted line) with center  $-1343$  ppm and FWHH 484 ppm. Three slices along the anisotropic dimension ( $S_1$ ,  $S_2$ , and  $S_3$  at  $\delta_{\text{iso}} = -1100$ ,  $-1300$ , and  $-1500$  ppm, respectively) are plotted with fits (in dotted lines) to the spinning sidebands using program DMFIT [74]; the anisotropic chemical shift parameters are  $\delta_{\text{aniso}} = -574$ ,  $-455$ ,  $-367$  ppm and  $\eta = 0.6$ ,  $0.65$ ,  $0.85$  for  $S_1$ ,  $S_2$ , and  $S_3$ , respectively.

In the 2D-PASS spectrum, the chemical shift isotropy and anisotropy are separated into horizontal and vertical dimensions, respectively. The spectrum of PMN at  $27^\circ\text{C}$  (Fig. 8.3) reveals a continuous distribution of chemical shift parameters; projection onto the

isotropic dimension offers the distribution of isotropic chemical shifts, which may be fit by a Gaussian lineshape with mean  $\mu(\delta_{\text{iso}}) = -1343$  ppm and standard deviation  $\sigma(\delta_{\text{iso}}) = 206$  ppm (or FWHH=484 ppm, which is much narrower than the MAS linewidth FWHH $\approx$ 700 ppm). Based on twenty one crystalline compounds, Fayon et al. have established empirical correlations between isotropic chemical shift and structural parameters,

$$\begin{aligned}\delta_{\text{iso}}(\text{ppm}) &= 20854 - 8669.0r_{\text{Pb-O}}(\text{\AA}), \\ \delta_{\text{iso}}(\text{ppm}) &= 622.8 - 349.7\text{CN},\end{aligned}\tag{8.1}$$

where  $r_{\text{Pb-O}}$  is the effective Pb-O bond length and CN is the effective coordination number [40]. The linear dependence on CN has been observed only for  $\text{CN} \geq 7$  while  $\delta_{\text{iso}}$  is more scattered for materials with lower coordination number [40]. However, for the PMN-PSN solid solutions, all of which have perovskite structure, the effective coordination number thus calculated should be reasonable. For the isotropic projection of PMN at 27°C,  $\mu(\delta_{\text{iso}}) = -1343$  ppm and  $\sigma(\delta_{\text{iso}}) = 206$  ppm of the Gaussian fit can be translated [Eq. (8.1)] into distributions of effective bond lengths and coordination numbers;  $\mu(r_{\text{Pb-O}}) = 2.56$  Å,  $\sigma(r_{\text{Pb-O}}) = 0.02$  Å and  $\mu(\text{CN}) = 5.6$ ,  $\sigma(\text{CN}) = 0.6$ .

The isotropic projections of the 2D-PASS spectra are shown in Fig. 8.4 for PMN at  $-35$ ,  $-6.5$ ,  $27$ ,  $60^\circ\text{C}$ , for  $x = 0.2$  both ordered and disordered at  $60^\circ\text{C}$ , and for  $x = 0.7$  ordered at  $27^\circ\text{C}$ . There are small inflections indicating more structural detail. If these features are ignored, all but one projections may be fit with one Gaussian lineshape; only for PMN at  $-35^\circ\text{C}$  is a second Gaussian lineshape needed to simulate the broad underlying distribution. The fit parameters are listed in Table 8.1. For PMN at temperatures from  $-6.5$  to  $60^\circ\text{C}$ , the mean isotropic chemical shift has a temperature coefficient of  $+0.15$  ppm/ $^\circ\text{C}$ .

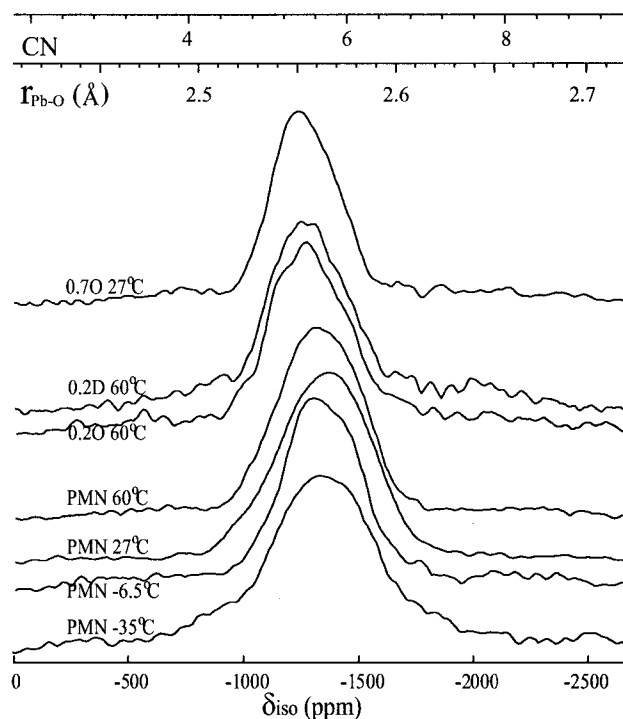


**Figure 8.4:** Isotropic projections of  $^{207}\text{Pb}$  2D-PASS spectra for  $(1-x)\text{PMN}-x\text{PSN}$  solid solutions. Experiments were performed with spinning speed 5 kHz at  $-35$ ,  $-6.5$ ,  $27$ ,  $60^\circ\text{C}$  for PMN, at  $60^\circ\text{C}$  for ordered and disordered samples of  $x = 0.2$ , and at  $27^\circ\text{C}$  for ordered sample of  $x = 0.7$ ; temperatures have been calibrated as stated in Section 8.1. The two axes on top are for conversions to the effective Pb-O distance and coordination number according to Eq. (8.1).

Similar temperature coefficient of  $+0.126$  ppm/ $^\circ\text{C}$  for  $\text{PbTiO}_3$  has been reported (over the range  $-150$  to  $60^\circ\text{C}$ ); this is attributed to a very small volume expansion that results in the slight changes of Pb-O distance [20]. The standard deviation  $\sigma(\delta_{\text{iso}})$  has a temperature coefficient of  $+0.18$  ppm/ $^\circ\text{C}$  over the range  $-6.5$  to  $60^\circ\text{C}$ . Lowering the temperature results in larger mean effective Pb-O distance  $\mu(r_{\text{Pb-O}})$  [and effective coordination number  $\mu(\text{CN})$ ] but smaller distribution width  $\sigma(r_{\text{Pb-O}})$  [and  $\sigma(\text{CN})$ ]. For PMN at  $-35^\circ\text{C}$ , the distribution curve has to be fit with two components, each with about 50% percent integral intensity. Both components have the same  $\mu(\delta_{\text{iso}}) = -1347$  ppm, which is very close to  $-1348$  ppm

determined at  $-6.5^\circ\text{C}$ ; this agrees with the fact that the perovskite unit cell parameters of PMN barely change below room temperature [13]. Component A is narrow and has  $\sigma(\delta_{\text{iso}}) = 0.0221$  ppm, while component B is broad and has  $\sigma(\delta_{\text{iso}}) = 0.0490$  ppm. The existence of two components may be related to the the para- to ferroelectric phase transition point  $-10^\circ\text{C}$  [22].

We emphasize that the variation of the mean isotropic chemical shift,  $\mu(\delta_{\text{iso}})$ , is only  $-10$  ppm over the range  $+60$  to  $-6.5^\circ\text{C}$ , and the empirical correlation is not accurate enough to estimate the real variation of bond length corresponding to a 10 ppm shift. The correlation is probably good enough to be used for larger chemical shift variations observed in the concentration dependence.

The concentration dependence may be found by comparing isotropic projections at identical temperatures; PMN and  $x = 0.2$  at  $60^\circ\text{C}$ , and PMN and  $x = 0.7$  at  $25^\circ\text{C}$ . Both mean  $\mu(r_{\text{Pb-O}})$  and distribution  $\sigma(r_{\text{Pb-O}})$  decrease as the PSN concentration  $x$  increases. This means that the Pb-O length does not scale in proportion to the perovskite cell parameter, which increases with  $x$  (perovskite cell parameter 4.050 and 4.075 Å for PMN and PSN respectively) [38, 13]. This tells that as the perovskite cell becomes larger, the  $\text{Pb}^{2+}$  shifts further away from the ideal position reflecting an increase of the local polar character due to the  $\text{Mg}^{2+}/\text{Sc}^{3+}$  substitution (which results in shortening the shortest Pb-O bond lengths and increasing the longest Pb-O bond lengths.).

The parameters for ordered and disordered samples of  $x = 0.2$  are close. Disorder seems to result in slight increases by around 0.001 Å in both the mean  $\mu(r_{\text{Pb-O}})$  and distribution  $\sigma(r_{\text{Pb-O}})$  of bond lengths.

**Table 8.1:** Gaussian fit parameters for the isotropic projections of 2D-PASS spectra for  $(1-x)$ PMN- $x$ PSN (see Fig. 8.4 for example).

Sample and Temperature	$\delta_{\text{iso}}$ (ppm) <sup>a</sup>		$r_{\text{Pb-O}}$ (Å) <sup>b</sup>		CN <sup>b</sup>		
	$\mu$	$\sigma$	$\mu$	$\sigma$	$\mu$	$\sigma$	
0.7O 27°C	-1265	169	2.5515	0.0195	5.40	0.48	
0.2D 60°C	-1279	206	2.5531	0.0238	5.44	0.59	
0.2O 60°C	-1273	199	2.5524	0.0230	5.42	0.57	
0D 60°C	-1338	213	2.5599	0.0246	5.61	0.61	
0D 27°C	-1343	206	2.5605	0.0238	5.62	0.59	
0D -6.5°C	-1348	201	2.5611	0.0232	5.64	0.58	
0D -35°C <sup>c</sup>	A	-1347	192	2.5610	0.0221	5.63	0.55
	B	-1347	425	2.5610	0.0490	5.63	1.22

<sup>a</sup> Error for  $\delta_{\text{iso}}$  is estimated as 5 ppm, which propagates to  $6 \times 10^{-4}$  Å for  $r_{\text{Pb-O}}$  and 0.01 for CN, according to Eq. (8.1).

<sup>b</sup> The mean  $\mu(\delta_{\text{iso}})$  and standard deviation  $\sigma(\delta_{\text{iso}})$  for isotropic chemical shift distribution are translated into distribution parameters of effective Pb-O bond length  $r_{\text{Pb-O}}$  and effective coordination number CN using Eq. (8.1).

<sup>c</sup> Only PMN at -35°C needs two components; 49% A + 51% B.

## 8.4 Measurement of the shortest Pb-O bond length

As the nearest neighbors, the 12 oxygens have the greatest influence on the chemical shifts of lead. To accommodate its lone-pair electrons,  $\text{Pb}^{2+}$  is usually displaced from the  $\text{O}_{12}$  center. Being unequally distant from the  $\text{Pb}^{2+}$ , the 12 oxygens have different degrees of influence on the  $^{207}\text{Pb}$  chemical shielding tensor. Thus the effective Pb-O bond length deduced from the isotropic chemical shift is a sort of weighted-average over the 12 crystallographically inequivalent Pb-O bond lengths. The simple ferroelectric and well-studied  $\text{PbTiO}_3$  (PT), which is also a perovskite, may help us to build such connections. It is well known that at room temperature PT is tetragonal; lattice parameters  $a = 3.904$  Å,  $c = 4.105$  Å (Fig. 8.5) [62]. In the [001] direction with respect to the Ti sublattice, oxygen ions are displaced by 0.3 Å and Pb is displaced by -0.1 Å according to neutron TOF (time of flight) Rietveld

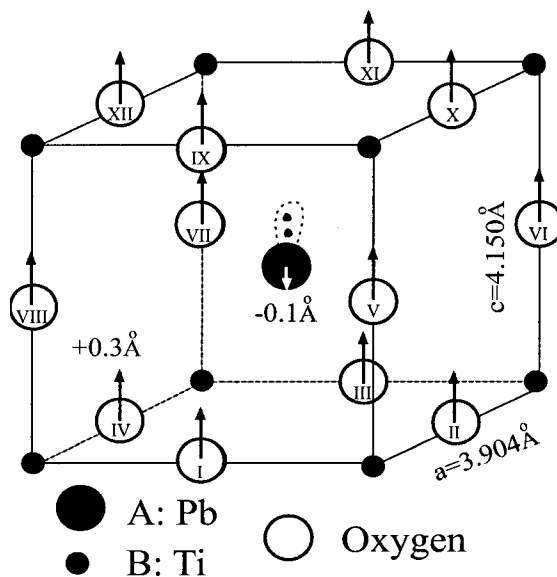


**Figure 8.5:** Tetragonal structure of  $\text{PbTiO}_3$  at room temperature. Lattice parameters  $a = 3.904 \text{ \AA}$ ,  $c = 4.105 \text{ \AA}$  [62]. With respect to Ti sublattice, oxygen ions are displaced by  $+0.3 \text{ \AA}$  in  $[001]$  direction and Pb ions are displaced by  $-0.1 \text{ \AA}$  [38]. The 6s lone-pair electrons of  $\text{Pb}^{2+}$  are schematic depicted.

refinement [38]. The Pb-O distances split into three values:  $2.5 \text{ \AA}$  for  $\text{Pb-O}_{\text{I-IV}}$ ,  $2.8 \text{ \AA}$  for  $\text{Pb-O}_{\text{V-VIII}}$ , and  $3.2 \text{ \AA}$  for  $\text{Pb-O}_{\text{IX-XII}}$  (see Fig. 8.5 for oxygen labels). The isotropic chemical shift of PT at room temperature is around  $-1420 \text{ ppm}$ , [20] which corresponds to an effective Pb-O distance  $2.57 \text{ \AA}$  according to Eq. (8.1). Thus, the effective Pb-O distance seen by NMR is almost solely determined by the shortest Pb-O distance. For PMN-PSN this shortest Pb-O distance is in the range  $2.5$  to  $2.6 \text{ \AA}$ , except for PMN at  $-35^\circ\text{C}$ , where the range is  $2.45$  to  $2.65 \text{ \AA}$  (Fig. 8.4). From Fig. 8.5, it seems  $\text{CN}=4$  is appropriate to account for the four closest oxygens on the bottom plane. But the effective coordination number  $\text{CN}=5.8$  [according to Eq. (8.1)] is also very reasonable since the four second-closest oxygens on the middle plane also influence to the isotropic chemical shift. Thus, the effective coordination number is slightly bigger than its crystallographic counterpart. The



effective CN for PMN-PSN is in the range 4.4 to 6.8, except for PMN at  $-35^{\circ}\text{C}$  where the range is 3.6 to 6.8 (Fig. 8.4).

## 8.5 Lead displacement models

In order to accommodate their lone-pair electrons,  $\text{Pb}^{2+}$  ions usually shift from high symmetry positions; a shift of about 0.3–0.4 Å is often seen [38]. An X-ray diffraction (XRD) study of  $\text{Pb}(\text{Mg}_{1/3}\text{Nb}_{2/3})\text{O}_3$  (PMN) shows that the lead displacements may be random in both length and direction; but a single layer spherical model (radius 0.285 and 0.259 Å for 20 and  $300^{\circ}\text{C}$  respectively) adequately describes the XRD data [100]. However in  $\text{Pb}(\text{Sc}_{1/2}\text{Ta}_{1/2})\text{O}_3$  (PST), pair distribution function analysis (PDF) using neutron scattering and X-ray scattering shows that  $\text{Pb}^{2+}$  ions move (by 0.2 Å) in the [100] direction rather than the macroscopic polarization direction [111] [38]. These results are inconsistent. The isotropic projection of 2D-PASS NMR directly measures the distribution of the shortest Pb-O bond length and this allows us to examine the two lead displacement models; their major difference is whether the Pb displacement is in a random direction or unique direction.

### 8.5.1 Shell model

In the shell model, which is the generalization of the single layer spherical model, the direction of Pb displacement is random, while the distance from the ideal position has a gaussian distribution with mean  $r_0$  and standard deviation  $\sigma$ . This was simulated by constructing an ensemble of perovskites with Pb displacements as described, and other ions in their ideal positions. The shortest Pb-O bonds were identified and the distribution of the shortest Pb-O distance was plotted. The simulation results are shown in Fig. 8.6. The mean  $r_0 = 0.336$

$\text{\AA}$  was chosen to roughly align the middle of the simulated curves with the experimental distribution curve for PMN at  $27^\circ\text{C}$ . Simulations were performed with  $\sigma = 0.00, 0.01, 0.02, 0.03,$  and  $0.05$ . The  $\sigma = 0.00$  case corresponds to the single layer spherical model proposed in the XRD study [100]. However, the simulated distribution curve has several discontinuities and very asymmetric; it does not resemble the NMR experimental distribution at all. If a small radial distribution is introduced, e.g.  $\sigma = 0.01$  and  $0.02$ , the discontinuities become round but the curves are too wide. Increasing radial distribution (e.g.  $\sigma = 0.05$ ) further broadens the simulated distribution curves and this does not help to match the experimental curve. Thus, shell model is unable to reproduce the experimental distribution.

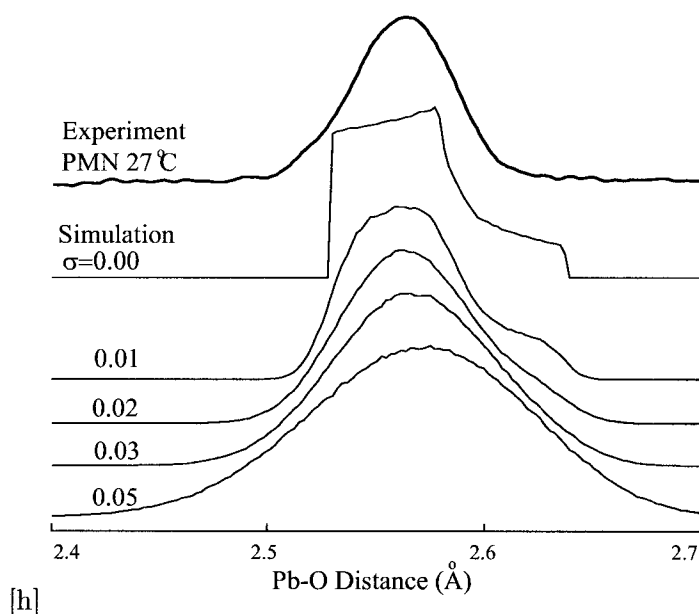


**Figure 8.6:** Shell distribution model for Pb displacement. In the shell model, the direction of Pb displacement is random, while the distance (from the ideal position) has a gaussian distribution with mean  $r_0$  and standard deviation  $\sigma$ . To roughly align the simulated curves with the experimental distribution curve for PMN at  $27^\circ\text{C}$ ,  $r_0 = 0.336 \text{ \AA}$  is chosen. Simulation has been done for  $\sigma = 0.00, 0.01, 0.02, 0.03,$  and  $0.05 \text{ \AA}$ . Shell model is unable to reproduce the experimental distribution.

### 8.5.2 Unique direction model

In the unique direction model, Pb displacement, which is only allowed in a given direction, assumes a gaussian distribution of mean  $r_0$  and standard deviation  $\sigma$ . The resulting distribution of the shortest Pb-O bond length has a nearly gaussian lineshape. The simulated lineshapes fit NMR experiments very well; two examples are shown in Fig. 8.7 for PMN at 27°C and -35°C. All fit parameters are listed in Table 8.2. It turns out that we are unable to discern the direction of the Pb displacement; this model fits experiments equally well with any of the three directions [001], [011], and [111]. However, the distribution parameters strongly depend on the direction; for PMN at 27°C,  $r_0(\sigma) = 0.455(0.039)$ ,  $0.302(0.023)$ , and  $0.381(0.030)$  Å for [001], [011], and [111], respectively.

**Table 8.2:** Parameters of unique direction model for Pb displacement. For  $(1-x)$ PMN- $x$ PSN ordered and disordered samples, the NMR experimental shortest Pb-O distribution are fit with this model at three special directions (see Fig. 8.7 for example).

Sample and Temperature	[001]		[011]		[111]		
	$r_0^a$	$\sigma^b$	$r_0$	$\sigma$	$r_0$	$\sigma$	
0.7O 27°C	0.473	0.032	0.313	0.020	0.394	0.025	
0.2D 60°C	0.468	0.038	0.310	0.022	0.391	0.030	
0.2O 60°C	0.468	0.038	0.310	0.022	0.391	0.030	
0D 60°C	0.456	0.041	0.303	0.025	0.382	0.033	
0D 27°C	0.455	0.039	0.302	0.023	0.381	0.030	
0D -6.5°C	0.454	0.037	0.302	0.022	0.380	0.029	
0D -35°C <sup>c</sup>	A	0.454	0.035	0.301	0.021	0.380	0.028
	B	0.454	0.080	0.301	0.055	0.380	0.067

<sup>a</sup> The mean of the gaussian distribution of the displacement, precision 0.001 Å.

<sup>b</sup> The standard deviation of the gaussian distribution of the displacement, precision 0.001 Å.

<sup>c</sup> Only PMN at -35°C needs two components; 49% A + 51% B.

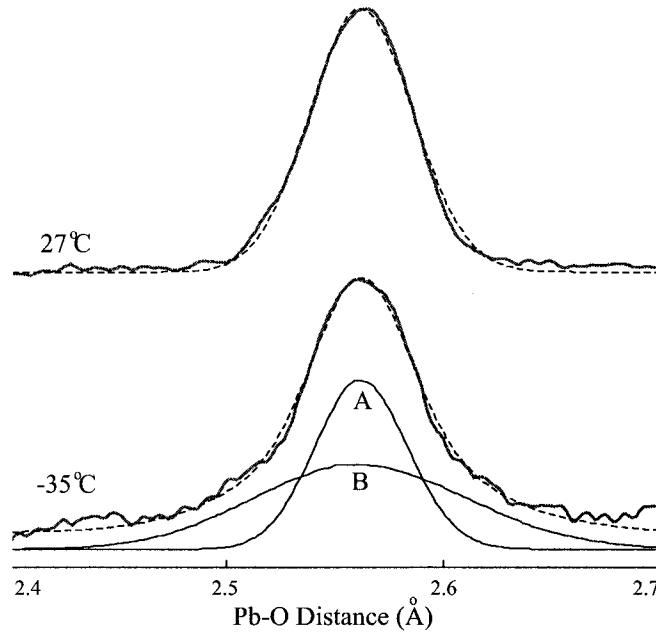


**Figure 8.7:** Unique direction model for the distribution of the Pb displacement. In this model, the displacement of Pb is along a single specified direction and has a gaussian distribution in distance from ideal position: mean  $r_0$  and standard deviation  $\sigma$ . For PMN at 27°C (bold line), the NMR experimental distribution of the shortest Pb-O distances is fit with model (dashed line) specified in [001] direction and parameters  $r_0 = 0.455 \text{ \AA}$  and  $\sigma = 0.039 \text{ \AA}$ . For PMN at -35°C, the experimental distribution (bold line) is fit with model (dashed line) in [001] direction and the two components (49%A+51%B, thin solid lines) have parameters  $r_0 = 0.454 \text{ \AA}$  and  $\sigma = 0.035 \text{ \AA}$  for A and  $r_0 = 0.454 \text{ \AA}$  and  $\sigma = 0.080 \text{ \AA}$  for B.

## 8.6 2D-PASS: Anisotropic Chemical Shift

To retrieve chemical shift anisotropy (CSA) from a 2D-PASS spectrum, slices are taken along the anisotropic dimension and catenated with zeroes to give spinning sidebands; the intensities of sidebands are then fit with the Herzfeld-Berger algorithm [56]. For example for PMN at 27°C in Fig. 8.3, the fitted CSA parameters ( $\delta_{\text{aniso}}$ ,  $\eta$ ) are (-574 ppm, 0.6), (-455 ppm, 0.65), (-367 ppm, 0.85) for slices taken at  $\delta_{\text{iso}} = -1100$ , -1300, and -1500 ppm, respectively. With increasing  $\delta_{\text{iso}}$ , that is, decreasing bond length  $r_{\text{Pb-O}}$  [Eq. (8.1)], the chemical shift anisotropy  $|\delta_{\text{aniso}}|$  increases. This correlation implies that the Pb-O

bonds vary from a more ionic environment (longer bond length, lower anisotropy) to a more covalent environment (shorter bond length, higher anisotropy) [41]. Thus the chemical shift tensor provides detailed information on electronic bonding.

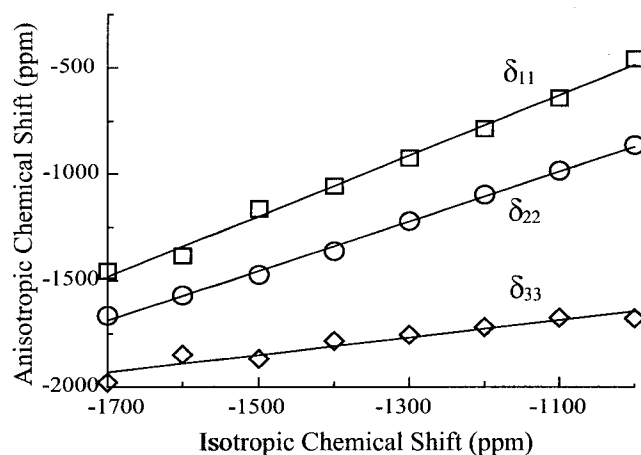


**Figure 8.8:** Correlation between anisotropic and isotropic chemical shifts. Data are sampled every 100 ppm from  $\delta_{\text{iso}} = -1700$  to  $-1000$  ppm from the 2D-PASS spectrum of PMN at  $27^\circ\text{C}$  (Fig. 8.3). Errors are about the size of symbol. The regressions are  $\delta_{11} = 940(\pm 60) + 1.42(\pm 0.05)\delta_{\text{iso}}$ ,  $\delta_{22} = 300(\pm 30) + 1.17(\pm 0.02)\delta_{\text{iso}}$ , and  $\delta_{33} = -1230(\pm 70) + 0.41(\pm 0.05)\delta_{\text{iso}}$ .

The principal values of the CSA tensor for PMN are calculated using Eqs. (3.4) and (3.7) and plotted with respect to  $\delta_{\text{iso}}$  in Fig. 8.8. Very good linear correlations are found between the individual tensor components  $\delta_{ii}$ ,  $i = 1, 2, 3$  and the isotropic chemical shift  $\delta_{\text{iso}}$ ; regression analyses give  $\delta_{11} = 940(\pm 60) + 1.42(\pm 0.05)\delta_{\text{iso}}$ ,  $\delta_{22} = 300(\pm 30) + 1.17(\pm 0.02)\delta_{\text{iso}}$ , and  $\delta_{33} = -1230(\pm 70) + 0.41(\pm 0.05)\delta_{\text{iso}}$  with  $R = 0.99$  for  $\delta_{11}$  and  $\delta_{22}$ ,  $R = 0.97$  for  $\delta_{33}$ .

For PMN at  $-6.5$ ,  $27$ , and  $60^\circ\text{C}$ , the CSA principal components  $\delta_{11}$  and  $\delta_{22}$  increase while  $\delta_{33}$  decreases as temperature increases; the maximum difference is around 80 ppm. The principal components at  $-35^\circ\text{C}$  are between those at  $-6.5$  and  $27^\circ\text{C}$ . In Fig. 8.9 the temperature dependence of the  $\delta_{22}$  component is shown.

However, no clear concentration dependence is seen. The principal components at  $60^\circ\text{C}$

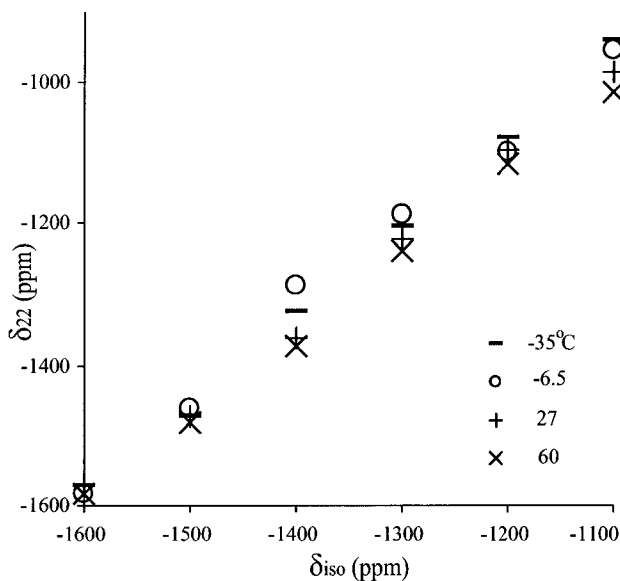


**Figure 8.9:** The temperature dependence of the  $\delta_{22}$  component of the chemical shielding tensor for PMN at four different temperatures.

for PMN are larger at some  $\delta_{\text{iso}}$  values but smaller at other values than those for  $x = 0.2$  (both ordered and disordered). The same pattern is seen when comparing PMN at 27°C and  $x = 0.7$  (ordered).

## 8.7 Pb-O bonding environments

For PMN-PSN, the measured isotropic and anisotropic chemical shifts suggest that the Pb-O bonds in the system are not strongly covalent. For ionic compounds, weak chemical shift anisotropies and large negative  $^{207}\text{Pb}$  isotropic shifts in the range from  $-2000$  to  $-3500$  ppm are observed. In contrast, a more covalent bonding state (found, for example, oxides and silicates) gives rise to more positive isotropic shifts in the range from  $-500$  to  $+1500$  ppm associated with very large chemical shift anisotropies  $\delta_{\text{aniso}} \sim -2000$  ppm, which reflect the steric effect of the  $\text{Pb}^{2+}$  lone-pair electrons which preclude a (spherical) symmetric

environment with short Pb-O bond lengths [40]. Thus for PMN-PSN, the  $\delta_{\text{iso}}$  range from  $-1800$  to  $-900$  ppm and the  $\delta_{\text{aniso}}$  range  $-700$  to  $-230$  ppm indicate that the Pb-O bonding environments are midway between typical ionic and typical covalent.

The asymmetry parameter  $\eta$  in PMN-PSN ranges from 0.5 to 1; this also supports the above statement concerning Pb-O bonding environments. For example in lead oxides and silicates (typical covalent compounds), Pb lies at the apex of a  $\text{PbO}_4$  pyramid (one-sided coordination) and the shielding tensor is close to axially symmetric ( $\eta \approx 0$ ). On the other hand, in lead nitrate (a typical ionic compound), Pb is 12-fold coordinated by oxygen atoms with large Pb-O bond lengths but the shielding tensor is also axially symmetric.

For each sample, the distributions of chemical shift parameters ( $\delta_{\text{iso}}$ ,  $\delta_{\text{aniso}}$ , and  $\eta$ ) agree with the fact that there is a variety of  $\text{B}^x\text{-O-B}^y$  environments, where  $\text{B}^x$  and  $\text{B}^y$  can be any of  $\text{Mg}^{2+}$ ,  $\text{Sc}^{3+}$ , and  $\text{Nb}^{5+}$ . In the  $\text{ABO}_3$  perovskite structure of  $\text{Pb}(\text{Mg}_{1/3}\text{Nb}_{2/3})\text{O}_3$  -  $\text{Pb}(\text{Sc}_{1/2}\text{Nb}_{1/2})\text{O}_3$ , the A ion ( $\text{Pb}^{2+}$ ) is in the center of a distorted perovskite cube, the B ions ( $\text{Mg}^{2+}$ ,  $\text{Sc}^{3+}$ , and  $\text{Nb}^{5+}$ ) are on the eight corners, and the oxygen ions are in the middle of the 12 edges. Thus each  $\text{Pb}^{2+}$  is surrounded by 12 edges of  $\text{B}^x\text{-O-B}^y$ ; the total number of such configurations is huge. For  $\text{Mg}^{2+}\text{-O-Mg}^{2+}$ ,  $\text{Sc}^{3+}\text{-O-Sc}^{3+}$ ,  $\text{Mg}^{2+}\text{-O-Sc}^{3+}$ , and  $\text{Mg}^{2+}\text{-O-Nb}^{5+}$ , the average B ion valence is less than four [ $(x+y)/2 < 4$ ]; the Pb-O hybridization is enhanced between the Pb 6s and O 2p states of such underbonded oxygens [19, 18]. For the remaining cases, the Pb-O hybridization is weaker. Therefore, the distribution of mixed B ions will produce a distribution of Pb-O bond covalence.

## 8.8 Conclusion

The  $^{207}\text{Pb}$  static, MAS, and 2D-PASS NMR experiments have been performed on  $(1 - x)\text{PMN}-x\text{PSN}$  relaxor ferroelectrics as a function of concentration  $x$ ; temperature dependence is also studied especially on PMN. The inherent chemical and positional disorder in these materials results in very low resolution in the static and MAS spectra. Only in 2D-PASS spectra can isotropic and anisotropic chemical shifts be separated. The isotropic chemical shift  $\delta_{\text{iso}}$  ranges from  $-1800$  to  $-900$  ppm; the anisotropic chemical shift  $\delta_{\text{aniso}}$  ranges from  $-700$  to  $-230$  ppm; the asymmetry parameter  $\eta$  ranges from 0.5 to 1, thus the shielding tensor is far from axially symmetric. The isotropic chemical shift is empirically related to the effective NMR Pb-O distance, which decreases upon increasing the perovskite cell parameter by increasing either the concentration  $x$  or temperature. This is because the Pb ion moves further away off center as the cell parameter increases. Strong linear correlations between isotropic and anisotropic chemical shifts show that Pb-O bonds vary from more ionic to more covalent environments. The existence of various Pb-O bonds is a result of the distribution of mixed B ions.

By comparing the crystallographic and NMR study for  $\text{PbTiO}_3$ , the NMR effective Pb-O distance is found to correlate with the shortest Pb-O bond length (among the 12 Pb-O bonds in a perovskite cell). Thus the distribution of isotropic chemical shifts is essentially the distribution of the shortest Pb-O bond length. This distribution is used to examine two competing models of Pb displacement; the direction of displacement is random in the spherical model but specific in the unique direction model. The spherical model yields an asymmetric distribution curve which is unable to fit the observed distribution of the shortest



Pb-O bond length. The unique direction model yields a gaussian distribution curve which can fit the observed distribution. However, it is unable to discern the direction of the Pb displacement; this model fits experiments equally well with any given direction. The distribution parameters strongly depend on the direction; for PMN at 27°C,  $r_0(\sigma) = 0.455(0.039)$ ,  $0.302(0.023)$ , and  $0.381(0.030)$  Å for [001], [011], and [111] respectively, where  $r_0$  and  $\sigma$  are respectively the mean and standard deviation of the gaussian distribution of the Pb displacement from the ideal position. For PMN at -35°C (below the para- to ferroelectric phase transition point -10°C), the distribution curve has to be fit with two components with the same  $r_0$  but different  $\sigma$ ; the [011] direction model gives  $r_0 = 0.301$  Å and  $\sigma = 0.021$  and  $0.055$  Å for the narrow and broad components respectively.

# Chapter 9

## Conclusion

In this work, we have used versatile solid state NMR techniques to study the important relaxor ferroelectric materials. The solid solutions  $(1-x) \text{Pb}(\text{Mg}_{1/3}\text{Nb}_{2/3})\text{O}_3-x \text{Pb}(\text{Sc}_{1/2}\text{Nb}_{1/2})\text{O}_3$  (PMN-PSN) have been chosen since PMN and PSN represent two classes with 1:2 and 1:1 B stoichiometries, respectively. Local structure and order/disorder are important to the macroscopic relaxor behavior.

Systematic multinuclear NMR together with concentration dependence have proven to be worthwhile. For the first time, local disorder is quantitatively described by  $^{93}\text{Nb}$  NMR, and possible B-site ordering models have been examined. Short range ordering is very important for the relaxor properties like the diffused and dispersed para- to ferroelectric transition. The  $^{93}\text{Nb}$  and  $^{45}\text{Sc}$  chemical shielding tensors and quadrupole coupling products have been determined for most of the 28 possible nearest B-site neighbor (nBn) configurations,  $B(N_{\text{Mg}}, N_{\text{Sc}}, N_{\text{Nb}})$ , where B can be Nb or Sc as the central nucleus, and  $N_{\text{Mg}}$  is the number of  $\text{Mg}^{2+}$  ions in the nBn configurations. Chemical shielding tensor is a probe to local electronic densities. For  $^{93}\text{Nb}$ , the isotropic chemical shifts of Nb(0,6,0) and Nb(0,0,6) fortuitously coincide; this results in good resolution in  $^{93}\text{Nb}$  MAS and 3QMAS spectra. For  $^{45}\text{Sc}$ , there is no such coincidence and its chemical shift is less sensitive to the local envi-

ronment. Resonances from various nBn configurations are very crowded, and this results in a very broad and featureless MAS lineshape. Quadrupole coupling product is a probe to the electric field gradient (EFG). The observed  $^{93}\text{Nb}$  quadrupole coupling products  $P_Q \sim 40$  and  $19$  MHz for Nb(5,0,1) and Nb(1,0,5) nBn configurations, respectively. This parallels that size-mismatch between  $\text{Mg}^{2+}$  and  $\text{Nb}^{5+}$  ions results in a much larger oxygen octahedral distortion in the Nb(5,0,1) configuration. More information and further understanding may be obtained by comparison of experiments and ab initio calculations of chemical shift and EFG tensors.

Lead is very unique for its large covalence and lone-pair electrons and plays an important role in determining the B-site ordering and phase transition temperature. It may also be responsible for the large dielectric and mechanical responses in these Pb-based relaxor ferroelectrics. It tends to shift away from its ideal position in order to accommodate the lone-pair electrons. The chemical shift of  $^{207}\text{Pb}$  is very sensitive to local environments and usually span hundreds or thousands of ppm, since it has high atomic weight and polarity. This poses difficulties on the traditional static and MAS NMR experiments. The problem is solved by 2D-PASS NMR experiments which isolate isotropic from anisotropic chemical shifts. There is an empirical linear correlation between the  $^{207}\text{Pb}$  isotropic chemical shift and the shortest Pb-O bond length. The observed distribution of isotropic chemical shift is essentially the distribution of the shortest Pb-O distance. One possible model of Pb displacement is that its direction is random. However, simulation results show that this model predicts a Pb-O distance distribution that is very different from what is observed. In another model, the Pb displacement direction is preferentially along a unique axis. This model is able to reproduce the experimentally observed Pb-O distance distribution. However, it is not

possible to discern along which direction the lead displacement occur.

Future NMR studies on these materials should include variable temperature  $^{45}\text{Sc}$  and  $^{93}\text{Nb}$  NMR to elucidate possible dynamics.  $^{17}\text{O}$  NMR is also desirable since the oxygens are the nearest neighbors to both A and B sites; oxygen octahedron distortions and rotations may be revealed by  $^{17}\text{O}$  NMR. This will require isotopic labelling of these ceramic materials, which is far from trivial [15, 97].

The relaxor ferroelectric materials have attracted the attention of many experimentalists and theoreticians. Many spectroscopy methods and computer simulations have been performed in order to discover and understand the origin of the relaxor behavior and the useful properties. The joint efforts from various perspectives will finally be able to identify the origin of the piezoelectric response which is crucial to the design of devices with desired high performance properties. We hope NMR will continue to make important contributions to such collaborative efforts.

# Appendix A

## Rotation Matrices

When describing NMR interaction the principal axes system (PAS) is easy to use; but the lab frame (LF) is convenient for describing the observed spectra. Moreover, an intermediate reference rotor frame (RF) is introduced by spinning the sample at the magic-angle (54.7° with the static magnetic field). To facilitate the transformation from one reference frame to another, cartesian rotation matrices and Wigner matrices are used.

The operation  $\mathbf{R}(\alpha\beta\gamma)$  (with  $\alpha, \beta, \gamma$  as Euler angles) in changing from  $(x, y, z)$  to  $(x', y', z')$  is executed as following: first rotation  $R(00\gamma)$  around  $z$ -axis, second rotation  $R(0\beta0)$  around  $y$ -axis, and third rotation  $R(\alpha00)$  around  $z$ -axis. The Cartesian rotation matrix  $\mathbf{R}(\alpha\beta\gamma) =$

$$\begin{pmatrix} \cos \alpha \cos \beta \cos \gamma - \sin \alpha \sin \gamma & -\cos \alpha \cos \beta \sin \gamma - \sin \alpha \cos \gamma & \cos \alpha \sin \beta \\ \sin \alpha \cos \beta \cos \gamma + \cos \alpha \sin \gamma & -\sin \alpha \cos \beta \sin \gamma + \cos \alpha \cos \gamma & \sin \alpha \sin \beta \\ -\sin \beta \cos \gamma & \sin \beta \sin \gamma & \cos \beta \end{pmatrix}. \quad (\text{A.1})$$

And its inverse is the transpose,  $\mathbf{R}^{-1} = \mathbf{R}^\dagger$  [55].

The elements of Wigner matrix are given by [55]

$$\mathcal{D}_{mn}^j(\alpha\beta\gamma) = d_{mn}^j(\beta)e^{-i(m\alpha+n\gamma)}, \quad (\text{A.2})$$

with the reduced Wigner matrix defined as

$$d_{mm}^j(\beta) = \sum_{k=0}^j (-1)^k \frac{\sqrt{(j+m)!(j-m)!(j+n)!(j-n)!}}{(j+m-k)!k!(j-n-k)!(n-m+k)!} \times \left(\cos \frac{\beta}{2}\right)^{2j+m-n-2k} \left(\sin \frac{\beta}{2}\right)^{n-m+2k}. \quad (\text{A.3})$$

In this work, we are concerned with tensors of rank 0, 2 and 4. Rank 0 has only one entry,  $d^0(\beta) = 1$ . Rank 2 matrix  $d^2(\beta) =$

$$\begin{pmatrix} \left(\frac{1+\cos\beta}{2}\right)^2 & -\frac{(1+\cos\beta)\sin\beta}{2} & -\sqrt{\frac{3}{8}}\sin^2\beta & -\frac{(1-\cos\beta)\sin\beta}{2} & \left(\frac{1-\cos\beta}{2}\right)^2 \\ \frac{(1+\cos\beta)\sin\beta}{2} & \frac{(1+\cos\beta)(2\cos\beta-1)}{2} & -\sqrt{\frac{3}{2}}\sin\beta\cos\beta & \frac{(1-\cos\beta)(2\cos\beta+1)}{2} & -\frac{(1-\cos\beta)\sin\beta}{2} \\ \sqrt{\frac{3}{8}}\sin^2\beta & \sqrt{\frac{3}{2}}\sin\beta\cos\beta & \frac{3\cos^2\beta-1}{2} & -\sqrt{\frac{3}{2}}\sin\beta\cos\beta & \sqrt{\frac{3}{8}}\sin^2\beta \\ \frac{(1-\cos\beta)\sin\beta}{2} & \frac{(1-\cos\beta)(2\cos\beta+1)}{2} & \sqrt{\frac{3}{2}}\sin\beta\cos\beta & \frac{(1+\cos\beta)(2\cos\beta-1)}{2} & -\frac{(1+\cos\beta)\sin\beta}{2} \\ \left(\frac{1-\cos\beta}{2}\right)^2 & \frac{(1-\cos\beta)\sin\beta}{2} & \sqrt{\frac{3}{8}}\sin^2\beta & \frac{(1+\cos\beta)\sin\beta}{2} & \left(\frac{1+\cos\beta}{2}\right)^2 \end{pmatrix}. \quad (\text{A.4})$$

The indice  $m$  runs from +2 on top to -2 on bottom, and  $n$  runs from +2 on left to -2 on right. (Note that several entries for  $d^2(\beta)$  have errors in Harter's book [55], which are corrected here.) For rank 4, only those entries with  $n = 0$  are of interest,

$$\begin{aligned} d_{00}^4(\beta) &= \frac{1}{64}(35\cos 4\beta + 20\cos 2\beta + 9), \\ d_{\pm 10}^4(\beta) &= \mp \frac{\sqrt{5}}{32}(7\sin 4\beta + 2\sin 2\beta), \\ d_{\pm 20}^4(\beta) &= \frac{\sqrt{10}}{64}(-7\cos 4\beta + 4\cos 2\beta + 3), \\ d_{\pm 30}^4(\beta) &= \pm \frac{\sqrt{35}}{32}(\sin 4\beta - 2\sin 2\beta), \\ d_{\pm 40}^4(\beta) &= \frac{\sqrt{70}}{128}(\cos 4\beta - 4\cos 2\beta + 3). \end{aligned} \quad (\text{A.5})$$

These matrices have been employed in Chapters 3 and 4 to deduce spectra under the chemical shielding anisotropy and quadrupole interaction, respectively.

## Appendix B

# Coherence Transfer Pathway and Phase Cycling

In high-field NMR, the magnetic quantum number  $m_i$  is a good quantum number for each eigenstate  $|i\rangle$  of the Zeeman Hamiltonian, and a coherence order  $p = m_i - m_j$  characterizes each coherence  $|i\rangle\langle j|$ . In a multi-pulse, multi-quantum NMR experiment, only certain elements of the density matrix are desirable to keep during each free evolution period, while others need to be removed. Typically only one or a few coherence transfer pathways are selected.

Phase cycling refers to changing the phases of rf pulses in a sequence in a such a way as to select one particular coherence transfer pathway(s). Phase cycling is routinely used in modern pulse NMR spectroscopy to solve problems due to instrumental artifacts: receiver baseline error, quadrature ghosts, and imperfect pulses [89]. It is also important to phase cycle in most multi-pulse, multi-quantum NMR experiments.

## B.1 Traditional Scheme

The principles of phase cycling have been worked out and are well described in the book of Ernst et al. [39]. The rf phase of the  $i$ th pulse incrementally takes these  $N_i$  values  $\phi_i = k_i 2\pi/N_i$ , with  $k_i = 0, 1, \dots, N_i - 1$ . The change of coherence order is defined as  $\Delta p_i = p(\tau_i^+) - p(\tau_i^-)$ , where  $\tau_i^-$  and  $\tau_i^+$  refer to immediately before and after the application of the  $i$ th pulse. In this appendix, only three rules are described; they are necessary and sufficient for the design of a phase cycling scheme.

1. By selecting  $\Delta p_i$ , then  $\Delta p_i \pm lN_i$ ,  $l = 0, 1, 2, \dots$  are automatically selected.
2. Only  $n - 1$  of the  $n$  pulses are needed to be phase-cycled independently.
3. The receiver phase is determined by  $\phi^{\text{recv}} = -\sum_i^n \Delta p_i \phi_i$ .

The prototype MQMAS pulse sequence in section 4.5 is used as an example, see Fig. B.1. For spin  $I$ , the possible coherence orders are  $2I, 2I - 1, \dots, -2I$ . For example consider  $I = 3/2$ , the desired echo coherence transfer pathway is  $0 \rightarrow -3 \rightarrow -1$ , and the anti-echo pathway is  $0 \rightarrow +3 \rightarrow -1$ .

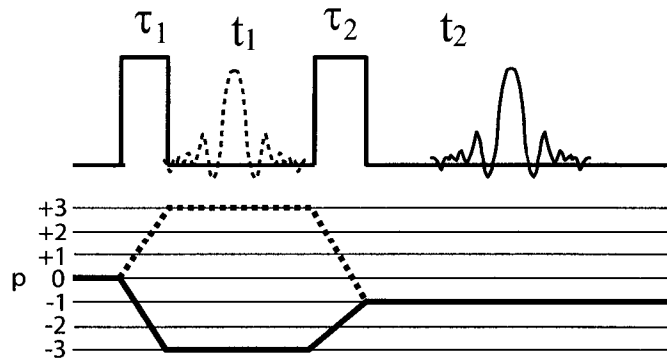


**Figure B.1:** A prototype MQMAS sequence. Echo (solid line) or/and anti-echo (dotted line) appear with appropriately chosen coherence pathway(s).



If only the echo pathway is to be chosen, then  $N_1 > 6$  so that  $\Delta p_1 = +3$  (equivalently  $p_1(\tau_1^+) = +3$  since  $p_1(\tau_1^-) = 0$ ) should not be selected when  $\Delta p_1 = -3$  is selected; let  $N_1 = 12$ ,  $\phi_1 = 0^\circ, 30^\circ, \dots, 330^\circ$ . Since there are only two pulses in the sequence, the second pulse may assume constant phase  $\phi_2 = 0$ . The receiver phase is  $\phi^{\text{recv}} = 3\phi_1$ , which repeatedly cycles through these four values  $0^\circ, 90^\circ, 180^\circ, 270^\circ$ . We didn't chose  $N_1 = 7$  because the receiver phase can only have these four values corresponding to four ways of data routing.

If only the anti-echo pathway is to be chosen, the phases of the two pulses are the same as above. But the receiver phase becomes  $\phi^{\text{recv}} = -3\phi_1$ , which repeatedly cycles through the four values  $0^\circ, 270^\circ, 180^\circ, 90^\circ$ .

If both pathways are to be chosen, then  $N_1 = 6$  is suitable;  $\phi_1 = 0^\circ, 60^\circ, \dots, 300^\circ$ ;  $p = +3$  is chosen at the same time when  $p = -3$  is chosen according to the first rule. Still keep  $\phi_2 = 0$ . The receiver phase may be calculated by either  $\phi^{\text{recv}} = 3\phi_1$  or  $-3\phi_1$ , they give the same result:  $\phi^{\text{recv}} = 0^\circ, 180^\circ$ . If the second pulse has a flip angle of  $90^\circ$  then the two pathways have equal pulse efficiency (this is true only for  $I = 3/2$ ) [4], therefore this produces a *cosine* signal.

In order to separate the echo and anti-echo signals, the *sine* signal should also be acquired. This may be achieved by shifting the phase of the first pulse by  $90^\circ/|p_1(\tau_1^+)| = 30^\circ$ . The corresponding receiver phase is  $\phi_{\text{recv}} = 90^\circ, 270^\circ$ .

## B.2 Simplification of Phase Cycling

The traditional scheme described above may not result in a phase cycle with minimal steps. For instance in the 2D-PASS sequence described in Chapter 3, the traditional scheme cycles each of the five  $\pi$  pulses independently in three steps; this results in 243 total steps. But by clever design, the phase cycling can be reduced to only three steps (see Chapter 3). The short cycling can be advantageous in these situations: (1) If the signal is strong, only three or 30 scans may be collected instead of 243. This saves experiment time. (2) When setting up the experiment, the performance can only be checked after a phase cycle is completed. Assuming a recycle delay of 5 s and a 16-pitch 2D-PASS experiment, one needs to wait for at least 5.4 hours simply to check whether the setting is right if the original cycle is used, but only 4 minutes are needed using the simplified cycle.

The simplification for the 2D-PASS sequence has been made by cycling the first three and the last two  $\pi$  pulses in a coordinated way (see Section 3.5). Recently, Levitt et al. have proposed a similar idea: the “cogwheel” phase cycle scheme [68]. The phases of two or more pulse blocks are incremented simultaneously, as opposed to the traditional “nested” scheme, in which the block phases are incremented independently. The cogwheel phase cycles achieve the same selectivity as traditional phase cycles in many cases.

## B.3 Summary

The effective selection of a particular coherence transfer pathway is essential in designing new pulse sequences. In this appendix, the three simple design guidelines are summarized for the traditional nested scheme. Moreover, the recent development of the cogwheel scheme

is briefly introduced. In a coordinated way, which is similar to the idea of the cogwheel scheme, we have independently simplified the 2D-PASS phase cycle from 243 to three steps to significantly save experiment time and to ease the experimental setup.



# Bibliography

- [1] A. ABRAGAM. *The Principles of Nuclear Magnetism*. The International Series of Monographs on Physics. Clarendon Press, Oxford, 1978.
- [2] MEHMET A. AKBAS AND PETER K. DAVIES. Domain growth in  $\text{Pb}(\text{Mg}_{1/3}\text{Ta}_{2/3})\text{O}_3$  perovskite relaxor ferroelectric oxides. *J. Am. Ceram. Soc.*, 80(11):2933–2936, 1997.
- [3] J.-P. AMOUREUX AND C. FERNANDEZ. Triple, quintuple and higher order multiple quantum MAS NMR of quadrupolar nuclei. *Solid State NMR*, 10:211–223, 1998.
- [4] J.-P. AMOUREUX, C. FERNANDEZ, AND L. FRYDMAN. Optimized multiple-quantum magic-angle spinning NMR experiments on half-integer quadrupoles. *Chemical Physics Letters*, 259:347–355, 1996.
- [5] J-P AMOUREUX, C. FERNANDEZ, AND S. STEURNAGEL. Z filtering in MQMAS NMR. *Journal of Magnetic Resonance, Series A*, 123:116–118, 1996.
- [6] JEAN-PAUL AMOUREUX. High-resolution solid-state NMR for spin 3/2 and 9/2: the multi-quantum transitions method. *Solid State Nuclear Magnetic Resonance*, 2:83–88, 1993.
- [7] OLEG N. ANTZUTKIN, S. C. SHEKAR, AND MALCOLM H. LEVITT. Two-dimensional sideband separation in magic-angle-spinning NMR. *Journal of Magnetic Resonance. Series A*, 115:7–19, 1995.
- [8] MAD S. BAK, JIMMY T. RASMUSSEN, AND NIELS CHR. NIELSEN. Simpson: A general simulation program for solid-state nmr spectroscopy. *J. Magn. Res.*, 147(2):296–330, 2000.
- [9] T. J. BASTOW AND H. J. WHITFIELD.  $^{137}\text{Ba}$  and  $^{47,49}\text{Ti}$  NMR: Electric field gradients in the non-cubic phases of  $\text{BaTiO}_3$ . *Solid State Communications*, 117:483–488, 2001.

- [10] ANTHONY BIELECKI AND DOUGLAS P. BURUM. Temperature dependence of  $^{207}\text{Pb}$  mas spectra of solid lead nitrate. an accurate, sensitive thermometer for variable-temperature mas. *J. Magn. Reson. A*, 116:215–220, 1995.
- [11] R. BLINC, J. DOLINSEK, A. GREGOROVIC, B ZALAR, C. FILIPIC, Z. KUTNJAK, A. LEVSTIK, AND R. PIRC. Local polarization distribution and Edwards-Anderson order parameter of relaxor ferroelectrics. *Phys. Rev. Lett.*, 83(2):424–427, 1999.
- [12] PHILIPPE R. BODART. Distributions of the quadrupolar and isotropic chemical shift interactions in two-dimensional multiple-quantum MAS NMR spectra. *J. Magn. Resn.*, 133:207–209, 1998.
- [13] P. BONNEAU, P. GARNIER, G. CALVARIN, E. HUSSON, J. R. GAVARRI, A. W. HEWAT, AND A. MORELL. X-ray and neutron diffraction studies of the diffuse phase transition in pmn ceramics. *Journal of Solid State Chemistry*, 91:350–361, 1991.
- [14] S. P. BROWN AND S. WIMPERIS. Two-dimensional multiple-quantum MAS NMR of quadrupolar nuclei: A comparison of methods. *Journal of Magnetic Resonance*, 128:42–61, 1997.
- [15] L. M. BULL, B. BUSSEMER, T. ANUPOLD, A. REINHOLD, A. SAMOSON, J. SAUER, A. K. CHEETHAM, AND R. DUPREE. A high-resolution  $^{17}\text{O}$  and  $^{29}\text{Si}$  nmr study of zeolite siliceous ferrierite and ab initio calculations of nmr parameters. *J. Am. Chem. Soc.*, 122:4948–4958, 2000.
- [16] GERALD BURNS. *Introduction to Group Theory with Applications*. Academic Press, New York, 1977.
- [17] B. P. BURTON. Empirical cluster expansion models of cation order-disorder in  $\text{A}(\text{B}'_{1/3}\text{B}''_{2/3})\text{O}_3$  perovskites. *Phys. Rev. B*, 59(9):6087–6091, 1999.
- [18] B. P. BURTON. Why  $\text{Pb}(\text{B}_{1/2}\text{B}'_{2/3})\text{O}_3$  perovskites disorder more easily than  $\text{Ba}(\text{B}_{1/3}\text{B}'_{2/3})\text{O}_3$  perovskites and the thermodynamics of 1:1-type short-range order in PMN. *J. Phys. Chem. Solids*, 61:327–333, 2000.
- [19] B. P. BURTON AND E. COCKAYNE. Why  $\text{Pb}(\text{B}, \text{B}')\text{O}_3$  perovskites disorder at lower temperatures than  $\text{Ba}(\text{B}, \text{B}')\text{O}_3$  perovskites. *Physical Review B*, 60(18):R12542–R12545, 1999.
- [20] D.A. BUSSIAN AND G.S. HARBISON. Variable temperature  $^{207}\text{Pb}$  NMR of  $\text{PbTiO}_3$ . *Solid State Communications*, 115:95–98, 2000.

- [21] I-WEI CHEN, PING LI, AND YING WANG. Structural origin of relaxor perovskites. *J. Phys. Chem Solids*, 57(10):1525–1536, 1996.
- [22] JIE CHEN, HELEN M. CHAN, AND MARTIN P. HARMER. Ordering structure and dielectric properties of undoped and La/Na-doped  $\text{Pb}(\text{Mg}_{1/3}\text{Nb}_{2/3})\text{O}_3$ . *J. Am. Ceram. Soc.*, 72(4):593–598, 1989.
- [23] M. H. COHEN AND F. REIF. *Quadrupole Effects in Nuclear Magnetic Resonance Studies of Solids*, volume 5 of *Solid State Physics: Advances in Research and Applications*. Academic Press, New York, 1957.
- [24] E. V. COLLA, E. YU. KOROLEVA, N. M. OKUNEVA, AND S. B. VAKHRUSHEV. Long-time relaxation of the dielectric response in lead magnoniobate. *Phys. Rev. Lett.*, 74:1681–1684, 1995.
- [25] R. M. COTTS AND W. D. KNIGHT. Nuclear resonance of  $^{93}\text{Nb}$  in  $\text{KNbO}_3$ . *Physical Review*, 96(5):1285–1293, 1954.
- [26] L. ERIC CROSS. Relaxor ferroelectrics. *Ferroelectrics*, 76(3-4):241–267, 1987.
- [27] L. ERIC CROSS. Relaxor ferroelectrics: an overview. *Ferroelectrics*, 151:305–320, 1994.
- [28] LUISA P. CRUZ, JOAO ROCHA, JULIO D. PEDROSA DE JESUS, JEAN M. SAVARIAULT, AND JEAN GALY. Solid-state single and triple-quantum  $^{93}\text{Nb}$  MAS NMR studies of ferroelectric  $\text{Pb}(\text{Mg}_{1/3}\text{Nb}_{2/3})\text{O}_3$  and a related pyrochlore. *Solid State NMR*, 15:153–158, 1999.
- [29] T. P. DAS AND E. L. HAHN. *Nuclear Quadrupole Resonance Spectroscopy*, volume Supplement 1 of *Solid State Physics*. Academic Press, New York, 1958.
- [30] P. K. DAVIES AND M. A. AKBAS. chemical order in PMN-related relaxors: structure, stability, modification, and impact on properites. *J. Phys. Chem. Solids*, 61:159–166, 2000.
- [31] PETER K. DAVIES, L. FARBER, M. VALANT, AND M. A. AKBAS. cation ordering and dielectric properties of PMN-PSN relaxors. *AIP Conf. Proc.*, 535:38–46, 2000.
- [32] ANGEL C. DE DIOS, ANN WALLING, IAN CAMERON, CHRISTOPHER I. RATCLIFFE, AND JOHN A. RIPMEESTER. Alkali metal NMR chemical shielding as a probe of local structure: An experimental and theoretical study of  $\text{Rb}^+$  in halide lattices. *J. Phys. Chem. A*, 104:908–914, 2000.
- [33] F. W. DE WETTE. Electric field gradients in point-ion and uniform-background lattices. *Phys. Rev.*, 123(1):103–112, 1961.

- [34] F. W. DE WETTE AND G. E. SCHACHER. Internal field in general dipole lattices. *Phys. Rev.*, 137(1A):A78–A91, 1965.
- [35] FRANK DELAGLIO, GEERTEN W. VUISTER, GUANG ZHU, AND JOHN PFEIFER. Nmrpipe: a multidimensional spectral processing system based on UNIX pipes. *J. Biomol. NMR*, 6:277–293, 1995.
- [36] W. THOMAS DIXON. Spinning-sideband-free NMR spectra. *J. Mag. Res.*, 44:220–223, 1981.
- [37] W. THOMAS DIXON. Spinning-sideband-free and spinning-sideband-only NMR spectra in spinning samples. *Journal of Chemical Physics*, 77(4):1800–1809, 1982.
- [38] W. DMOWSKI, M. K. AKBAS, PETER K. DAVIES, AND T. EGAMI. Local structure of  $\text{Pb}(\text{Sc}_{1/2}\text{Ta}_{1/2})\text{O}_3$  and related compounds. *J. Phys. Chem. Solids*, 61:229–237, 2000.
- [39] RICHARD R. ERNST, GEOFFREY BODENHAUSEN, AND ALEXANDER WOKAUN. *Principles of nuclear magnetic resonance in one and two dimensions*. The international series of monographs on chemistry. Clarendon Press, Oxford, 1987.
- [40] F. FAYON, I. FARNAN, C. BESSADA, J. COUTURES, D. MASSIOT, AND J. P. COUTURES. Empirical correlations between 207 pb nmr chemical shifts and structure in solids. *J. Am. Chem. Soc.*, 119:6837–6843, 1997.
- [41] FRANCK FAYON, CATHERINE BESSADA, ANDRE DOUY, AND DOMINIQUE MASSIOT. Chemical bonding of lead in glasses through isotropic vs anisotropic correlation: PASS shifted echo. *Journal of Magnetic Resonance*, 137:116–121, 1999.
- [42] RICHARD B. FIRESTONE, VIRGINIA S. SHIRLEY, CORAL M. BAGLIN, S.Y. FRANK CHU, AND JEAN ZIPKIN. *The 8th edition of the Table of Isotopes (also 1998 and 1999 updates)*. John Wiley & Sons, Inc., 1996.
- [43] JOHN J. FITZGERALD, SUBRAMANIAN PRASAD, JIONG HUANG, AND JAY S. SHORE. Solid-state  $^{93}\text{Nb}$  NMR and  $^{93}\text{Nb}$  nutation studies of polycrystalline  $\text{Pb}(\text{Mg}_{1/3}\text{Nb}_{2/3})\text{O}_3$  and  $(1-x)\text{Pb}(\text{Mg}_{1/2}\text{Nb}_{2/3})\text{O}_3/x\text{PbTiO}_3$  solid-solution relaxor. *J. Am. Ceram. Soc.*, 122:2556–2566, 2000.
- [44] LUCIO FRYDMAN AND JOHN S. HARWOOD. Isotropic spectra of half-integer quadrupolar spins from bidimensional magic-angle-spinning NMR. *J. Am. Chem. Soc.*, 117:5367–5368, 1995.



- [45] EIICHI AND FUKUSHIMA AND STEPHEN B. ROEDER. *Experimental Pulse NMR: A Nuts and Bolts Approach*. Addison-Wesley Publishing Company, Inc., London, 1981.
- [46] ZHEHONG GAN. Isotropic NMR spectra of half-integer quadrupolar nuclei using satellite transitions and magic-angle spinning. *J. Am. Chem. Soc.*, 122(13):3242–3243, 2000.
- [47] A. E. GLAZOUNOV AND A. K. TAGANETSEV. A breathing model for the polarization response of relaxor ferroelectrics. *Ferroelectrics*, 221:57–66, 1999.
- [48] M. D. GLINCHUK, V. V. LAGUTA, I. P. BYKOW, S. NOKHRIN, V. P. BOVTUN, M. A. LESCHENKO, J. ROSA, AND L. JASTRABIK. nuclear magnetic resonance study of ion ordering and ion shifts in relaxor ferroelectrics. *J. Appl. Phys.*, 81(8):3561–3569, 1997.
- [49] M. D. GLINCHUK, V. V. LAGUTA, I. P. BYKOW, S. NOKHRIN, V. P. BOVTUN, M. A. LESCHENKO, J. ROSA, AND L. JASTRABIK. nuclear magnetic resonance study of ion ordering and ion shifts in relaxor ferroelectrics. *J. Appl. Phys.*, 81(8):3561–3569, 1997.
- [50] A. GOLDBOURT, P. K. MADHU, AND S. VEGA. Enhanced conversion of triple to single-quantum coherence in the triple-quantum MAS NMR spectroscopy of spin-5/2 nuclei. *Chemical Physics Letters*, 320:448–456, 2000.
- [51] HONG GUI, BINGLIN GU, AND XIAOWEN ZHANG. Distribution of relaxation times in perovskite-type relaxor ferroelectrics. *J. Appl. Phys.*, 78(3):1934–1939, 1995.
- [52] HONG GUI, BINGLIN GU, AND XIAOWEN ZHANG. Dynamics of the freezing process in relaxor ferroelectrics. *Phys. Rev. B.*, 52(5):3135–3142, 1995.
- [53] HONG GUI, XIAOWEN ZHANG, AND BINGLIN GU. Possible order-disorder phase transitions in  $(A'_x A''_{1-x})\text{BO}_3$  and  $A(B'_x B''_{1-x})\text{O}_3$  complex perovskites. *J. Phys.: Condens. Matter*, 8:1491–1501, 1996.
- [54] A. A. GUSEV, I. M. REZNIK, AND V. A. TSITRIN. Electron-electron interaction and antishielding constants of core shells of atoms. *J. Phys.: Condens. Matter*, 7:4855–4863, 1995.
- [55] WILLIAM G. HARTER. *Principles of Symmetry, Dynamics, and Spectroscopy*. John Wiley & Sons, Inc., New York, 1993.

- [56] JUDITH HERZFELD AND ALAN E. BERGER. Sideband intensities in NMR spectra of samples spinning at the magic angle. *J. Chem. Phys.*, 73(12):6021, 1980.
- [57] R. R. HEWITT AND T. T. TAYLOR. Nuclear quadrupole resonance and the electric field gradient in metallic indium. *Phys. Rev.*, 125(2):524532, 1962.
- [58] GINA L. HOATSON, DONGHUA H. ZHOU, F. FAYON, D. MASSIOT, AND ROBERT L. VOLD.  $^{93}\text{Nb}$  MAS NMR study of perovskite relaxor ferroelectrics PMN-PSN. *Phys. Rev. B*, 66:224103, 2002.
- [59] E. HUSSON, L. ABELLO, AND A. MORELL. Short-range order in  $\text{PbMg}_{1/3}\text{Nb}_{2/3}\text{O}_3$  ceramics by RAMAN spectroscopy. *Mater. Res. Bull.*, 25:539–545, 1990.
- [60] E. HUSSON, M. CHUBB, AND A. MORELL. Superstructure in  $\text{PbMg}_{1/3}\text{Nb}_{2/3}\text{O}_3$  ceramics revealed by high resolution electron microscopy. *Mater. Res. Bull.*, 23:357–361, 1988.
- [61] A. M. JAMES AND M. P. LORD. *Macmillan's Chemical and Physical Data*. Macmillan, London, UK, 1992.
- [62] G. JONA, FRANCO AND SHIRANE. *Ferroelectric Crystals*. Volume 1 of the International Series of Monographs on Solid State Physics. Pergamon Press, New York, 1962.
- [63] WERNER KANZIG. *Ferroelectricity and Antiferroelectrics*. Solid State Physics. Academic Press, New York, 1957.
- [64] A. P.M. KENTGENS AND R. VERHAGEN. Advantages of double frequency sweeps in static, MAS and MQMAS NMR of spin  $I=3/2$  nuclei. *Chemical Physics Letters*, 300:435–444, 1999.
- [65] DONG HEE KIM, HEUI MAN EUN, AND HO-SOEB CHOI. Density functional theory/GIAO/CSGT studies of the  $^{13}\text{C}$  NMR chemical shifts in 1-chlorosilatrane. *Bull. Korean Chem. Soc.*, 21(1):148–150, 2000.
- [66] H. B. KRAUSE, J. M. COWLEY, AND J. WHEALEY. Short-range ordering in  $\text{Pb}(\text{Mg}_{1/3}\text{Nb}_{2/3})\text{O}_3$ . *Acta Crystallogr. A*, 35:1015–1017, 1979.
- [67] YOUNG-SIK KYE, BRUNO HERREROS, AND GERARD S. HARBISON.  $^{207}\text{Pb}$  NMR and Monte Carlo studies of ionic solid solutions. *Mat. Res. Soc. Symp. Proc.*, 547:339–344, 1999.
- [68] M. H. LEVITT, P. K. MADHU, AND C. E. HUGHES. Cogwheel phase cycling. *J. Magn. Reson.*, 155(2):300–306, 2002.

- [69] A. LLOR AND J. VIRLET. Towards high-resolution NMR of more nuclei in solids: Sample spinning with time-dependent spinner axis angle. *Chemical Physics Letters*, 152(2, 3):248–253, 1988.
- [70] P. K. MADHU, A. GOLDBOURT, L. FRYDMAN, AND S. VEGA. Sensitivity enhancement of the MQMAS NMR experiment by fast amplitude modulation of the pulses. *Chemical Physics Letters*, 307:41–47, 1999.
- [71] P. K. MADHU, A. GOLDBOURT, L. FRYDMAN, AND S. VEGA. Fast radio-frequency amplitude modulation in multiple-quantum magic-angle-spinning nuclear magnetic resonance: Theory and experiments. *J. Chem. Phys.*, 12:2377–2391, 2000.
- [72] D. MASSIOT. Sensitivity and lineshape improvements of mq-mas by rotor-synchronized data acquisition. *J. Magn. Res. A* 122, 122:240–244, 1996.
- [73] D MASSIOT, B TOUZO, D TRUMEAU, J. P. COUTURES, J. VIRLET, ET AL. Two-dimensional magic-angle spinning isotropic reconstruction sequences for quadrupolar nuclei. *Solid State NMR*, 6:73–83, 1996.
- [74] DOMINIQUE MASSIOT, FAYON FRANCK, MICKAEL CAPRON, IAN KING, STEPHANIE LE CALVE, BRUNO ALONSO, JEAN-OLIVIER DURAND, BRUNO BUJOLI, ZHEHONG GAN, AND GINA HOATSON. Modelling one- and two-dimensional solid-state NMR spectra. *Magnetic Resonance in Chemistry*, 40:70–76, 2002.
- [75] VINCENT J. MCBRIERTY AND KENNETH J. PACKER. *Nuclear Magnetic Resonance in Solid Polymers*. Cambridge Solid State Science Series. Cambridge University Press, New York, 1993.
- [76] ALES MEDEK, JOHN S. HARWOOD, AND LUCIO FRYDMAN. Multiple-quantum magic-angle spinning NMR: A new method for the study of quadrupolar nuclei in solids. *J. Am. Chem. Soc.*, 117:12779–12787, 1995.
- [77] K. T. MUELLER, B. Q. SUN, G. C. CHINGAS, J. W. ZWANZIGER, T. TERAQ, ET AL. Dynamic-angle spinning of quadrupolar nuclei. *Journal of Magnetic Resonance*, 86:470–487, 1990.
- [78] R. E. NEWNHAM. Tunable transducers: Nonlinear phenomena in electroceramics. *NIST Spec. Publ.*, 804:39–52, 1996.
- [79] G. E. PAKE. *Solid State Physics Advances in Research and Applications*, volume 2. Academic Press, New York, 1956.

- [80] SEUNG-EEK PARK AND THOMAS R. SHROUT. Ultrahigh strain and piezoelectric behavior in relaxor based ferroelectric single crystals. *J. Appl. Phys.*, 82(4):1804–1811, 1997.
- [81] WILLIAM W. PAUDLER. *Nuclear Magnetic Resonance—General Concepts and Applications*. Wiley, John & Sons, Incorporated, New York, 1987.
- [82] R. PIRC AND R. BLINC. Spherical random-bond-random-field model of relaxor ferroelectrics. *Phys. Rev. B*, 60(19):13470–13478, 1999.
- [83] R. PIRC, R. BLINC, AND V. BOBNAR. Dynamics of relaxor ferroelectrics. *Phys. Rev. B*, 63:054203, 2001.
- [84] S. PRASAD, P. ZHAO, J. HUANG, J. J. FITZGERALD, AND J. S. SHORE. Niobium-93 MQMAS NMR spectroscopic study of alkali and lead niobates. *Solid State NMR*, 19:45–62, 2001.
- [85] S. PRASAD, P. ZHAO, J. HUANG, AND J. S. SHORE. pure-phase two-dimensional niobium-93 nutation spectroscopic study of lead metaniobate and the piezoelectric lead magnesium niobate. *Solid State NMR*, 14:231–235, 1999.
- [86] NORMAN F. RAMSEY. *Nuclear Moments*. John Wiley & Sons, Inc., New York, 1953.
- [87] AHMAD SAFARI, RAJESH K. PANDA, AND VICTOR F. JANAS. Ferroelectric ceramics : Processing, properties & applications. <http://www-rci.rutgers.edu/rkpanda/ferroelectric/ferroelectric.html>, 2002. Serve Date: 2002.
- [88] A. SAMOSON, E. LIPPMAA, AND A. PINES. High resolution solid-state NMR. averaging of second-order effects by means of a double-rotor. *Mol. Phys.*, 65(4):1013–1018, 1988.
- [89] JEREMY K. M. SANDERS AND BRIAN K. HUNTER. *Modern NMR Spectroscopy: A Guide for Chemists*. Oxford University Press, Oxford, 1993.
- [90] P. C. SCHMIDT, K. D. SEN, T. P. DAS, AND ALARICH WEISS. Effect of self-consistency and crystalline potential in the solid state on nuclear quadrupole sternerheimer antishielding factors in closed-shell ions. *Physical Review B*, 22(9):4167–4179, 1980.
- [91] K. SCHMIDT-ROHR AND H. W. SPIESS. *Multidimensional Solid-State NMR and Polymers*. Academic Press, London, 1994.

- [92] R. D. SHANNON. Revised effective ionic radii and systematic studies of interatomic distances in halides and chalcogenides. *Acta Cryst.*, A32:751–767, 1976.
- [93] MARINA G. SHELYAPINA, VALENTINA S. KASPEROVICH, BORIS F. SHCHEGOLEV, AND ELENA V. CHARNAYA. Ab initio cluster calculations of electric-field-gradients at the transition-metal sites in the ferroelectric LiNbO<sub>3</sub> and LiTaO<sub>3</sub> crystals. *Proceedings of the 15th European Experimental NMR Conference*, 2000.
- [94] DAVID J. SINGH. Electric field gradients in BaTiO<sub>3</sub> and KNbO<sub>3</sub>. *Ferroelectrics*, 153:183–187, 1994.
- [95] CHARLES P. SLICHTER. *Principles of Magnetic Resonance*. Solid-State Science 1. Springer-Verlag, New York, 3 edition, 1990.
- [96] G. A. SMOLENSKII, I. G. SINY, R. V. PISAREV, AND E. G. KUZMINOV. Raman scattering in ordered and disordered perovskite type crystals. *Ferroelectrics*, 12:135, 1976.
- [97] J.F. STEBBINS, LIN-SHU DU, S. KROEKER, NEUHOFF P., D. RICE, J. FRYE, AND H.J. JAKOBSEN. New opportunities for high-resolution solid-state nmr spectroscopy of oxide materials at 21.1 and 18.8 t fields. *Solid State Nuclear Magnetic Resonance*, 21(1-2):105–115, 2002.
- [98] N. J. STONE. Table of nuclear magnetic dipole and electric quadrupole moments. [http://www.nndc.bnl.gov/nndc/stone\\_moments/](http://www.nndc.bnl.gov/nndc/stone_moments/), 2001.
- [99] K. UCHINO. *Piezoelectric Actuators and Ultrasonic Motors*. Kluwer Academic Publishers, Boston, 1996.
- [100] S. VAKHRUSHEV, S. ZHUKOV, G. FETISOV, AND V. CHERNYSHOV. The high-temperature structure of lead magnoniobate. *J. Phys.: Condens. Matter*, 6:4021–4027, 1994.
- [101] D. VIEHLAND, S.J. JANG, L. ERIC CROSS, AND M. WUTTIG. Freezing of the polarization fluctuations in lead magnesium niobate relaxors. *Journal of Applied Physics*, 68(6):2916–21, 1990.
- [102] DWIGHT VIEHLAND, S. J. JANG JANG, L. ERIC CROSS, AND MANFRED WUTTIG. Deviation from curie-weiss behavior in relaxor ferroelectrics. *Phys. Rev. B*, 46(13):8003–8006, 1992.
- [103] L. S. VOROTILOVA, O. E. KVIATKOVSKI, A. A. LEVIN, AND B. F. SHCHEGOLEV. Nonempirical cluster calculations of the electric field gradient tensor at the <sup>27</sup>Al nuclei in YAlO<sub>3</sub> and HoAlO<sub>3</sub> and refinement of the crystal structure of HoAlO<sub>3</sub>. *Physics of the Solid State*, 35(2):143–145, 1993.

- [104] T. VOSEGAARD, P. FLORIAN, P. J. GRANDINETTI, AND D. MASSIOT. Pure absorption-mode spectra using a modulated rf mixing period in MQMAS experiments. *J. Magn. Res.*, 143:217–222, 2000.
- [105] THOMAS VOSEGAARD, PIERRE FLORIAN, DOMINIQUE MASSIOT, AND PHILIP J. GRANDINETTI. Multiple quantum magic-angle spinning using rotary resonance excitation. *J. Chem. Phys.*, 114:4618–4624, 2001.
- [106] B. E. VUGMEISTER AND H. RABITZ. Dynamics of interacting clusters and dielectric response in relaxor ferroelectrics. *Phys. Rev. B*, 57(13):7581–7585, 1998.
- [107] B. E. VUGMEISTER AND H. RABITZ. Coexistence of the critical slowing down and glassy freezing in relaxor ferroelectrics. *Phys. Rev. B*, 61(21):14448–14453, 2000.
- [108] V. WESTPHAL, W. KLEEMANN, AND M. D. GLINCHUK. Diffuse phase transitions and random-field-induced domain states of the “relaxor” ferroelectric  $\text{PbMg}_{1/3}\text{Nb}_{2/3}\text{O}_3$ . *Phys. Rev. Lett.*, 68(6):847–850, 1992.
- [109] MARK WINTER. Webelements. <http://www.webelements.com/>, 1993. Serve Date: Oct 27, 2002.
- [110] S. K. WOLFF AND T. ZIEGLER. Calculation of DFT-GIAO NMR shifts with the inclusion of spin-orbit coupling. *Journal of Chemical Physics*, 109(3):895–905, 1998.
- [111] S. K. WOLFF, T. ZIEGLER, E. VAN LENTHE, AND E. J. BAERENDS. Density functional calculations of nuclear magnetic shieldings using the zeroth-order regular approximation (zora) for relativistic effects: Zora nuclear magnetic resonance. *Journal of Chemical Physics*, 110(16):7689–7698, 1999.
- [112] E. A. WOOD. Polymorphism in potassium niobate, sodium niobate, and other  $\text{ABO}_3$  compounds. *Acta Crystallographica*, 4(4):353–362, 1951.
- [113] G. WU, D. ROVNYAK, AND R. G. GRIFFIN. Quantitative multiple-quantum magic-angle-spinning NMR spectroscopy of quadrupolar nuclei in solids. *J. Am. Chem. Soc.*, 118:9326–9332, 1996.
- [114] ZHIGANG WU AND H. KRAKAUER. Charge-transfer electrostatic model of compositional order in perovskite alloys. *Phys. Rev. B*, 63:184113, 2001.
- [115] ZHI YAO, HYUNG-TAE KWAK, DIMITRIS SAKELLARIOU, LYNDON EMSLEY, AND P. J. GRANDINETTI. Sensitivity enhancement of the central transition NMR signal of quadrupolar nuclei under magic-angle spinning. *Chemical Physics Letters*, 327:85–90, 2000.

- [116] PEIDONG ZHAO, SUBRAMANIAN PRASAD, JIONG HUANG, JOHN J. FITZGERALD, AND JAY S. SHORE. Lead-207 NMR spectroscopic study of lead-based electronic materials and related lead oxides. *J. Phys. Chem. B*, 103:10617–10626, 1999.
- [117] DONGHUA H. ZHOU, GINA L. HOATSON, AND ROBERT L. VOLD. The local structures of perovskite relaxor ferroelectrics by high-resolution  $^{93}\text{Nb}$  3QMAS NMR. *Phys. Rev. B*, submitted, 2003.
- [118] DONGHUA H. ZHOU, GINA L. HOATSON, ROBERT L. VOLD, AND FRANCK FAYON. Local structure in relaxor ferroelectrics by  $^{207}\text{Pb}$  NMR. *Phys. Rev. B*, submitted, 2003.

## VITA

Donghua Zhou

The author was born on December 30, 1974 in Linhai, Zhejiang Province, China. He received a B.S. degree in June, 1997 from Peking University in Beijing with a major in Physics and a minor in Electric Engineering; a M.S. degree in May, 1999 and a Ph.D. degree in March, 2003 from the Department of Physics, College of William and Mary in Virginia. In April, 2003 he will start to solve biological issues using NMR as a postdoctoral fellow in the University of Illinois at Urbana-Champaign. He and Lingjin Xiang were married in June, 2000.